YSCAT BACKSCATTER DISTRIBUTIONS

by

Benjamin E. Barrowes

A thesis submitted to the faculty of

Brigham Young University

in partial fulfillment of the requirements for the degree of

Master of Science

Department of Electrical and Computer Engineering

Brigham Young University

August 1999

BRIGHAM YOUNG UNIVERSITY

GRADUATE COMMITTEE APPROVAL

of a thesis submitted by

Benjamin E. Barrowes

This thesis has been read by each member of the following graduate committee and by majority vote has been found to be satisfactory.

Date	David G. Long, Chair
Date	David V. Arnold
Date	Michael A. Jensen

BRIGHAM YOUNG UNIVERSITY

As chair of the candidate's graduate committee, I have read the thesis of Benjamin E. Barrowes in its final form and have found that (1) its format, citations, and bibliographical style are consistent and acceptable and fulfill university and department style requirements; (2) its illustrative materials including figures, tables, and charts are in place; and (3) the final manuscript is satisfactory to the graduate committee and is ready for submission to the university library.

Date

David G. Long
Chair, Graduate Committee

Accepted for the Department

A. Lee Swindlehurst
Graduate Coordinator

Accepted for the College

Douglas M. Chabries
Dean, College of Engineering and Technology

ABSTRACT

YSCAT BACKSCATTER DISTRIBUTIONS

Benjamin E. Barrowes

Department of Electrical and Computer Engineering

Master of Science

YSCAT is a unique ultrawideband microwave scatterometer developed to investigate the sea surface under a variety of environmental and radar parameters. The YSCAT94 experiment consisted of a six month deployment on the WAVES research tower operated by the Canada Center for Inland Waters (CCIW). Over 3500 hours of data were collected at 2, 3.05, 5.3, 10.02, and 14 GHz and at a variety of wind speeds, relative azimuth angles, and incidence angles.

A low wind speed "rolloff" of the normalized radar cross section (σ°) in YSCAT94 data is found and quantified. The rolloff wind speed, Υ, is estimated through regression estimation analysis using an Epanechnikov kernel. For YSCAT94 data, the rolloff is most noticeable at mid-range incidence angles with Υ values ranging from 3 to 6 m/s.

In order to characterize YSCAT94 backscatter distributions, a second order polynomial in log space is developed as a model for the probability of the radar cross

section, $p(\sigma^\circ)$. Following Gotwols and Thompson, $p(\sigma^\circ)$ is found to adhere to a log-normal distribution for horizontal polarization and a generalized log-normal distribution for vertical polarization. If $p(a|\sigma^\circ)$ is assumed to be Rayleigh distributed, the instantaneous amplitude distribution $p(a)$ is found to be the integral of a Rayleigh/generalized log-normal distribution.

A robust algorithm is developed to fit this probability density function to YSCAT94 backscatter distributions. The mean and variance of the generalized log-normal distribution are derived to facilitate this algorithm. Over 2700 distinct data cases sorted according to five different frequencies, horizontal and vertical polarizations, upwind and downwind, eight different incidence angles, 1-10 m/s wind speeds, and 0.1-0.38 mean wave slope are considered. Definite trends are recognizable in the fitted parameters a_1, a_2, and C of the Rayleigh/generalized log-normal distribution when sorted according to wind speed and mean wave slope.

At mid-range incidence angles, the Rayleigh/generalized log-normal distribution is found to adequately characterize both low and high amplitude portions of YSCAT94 backscatter distributions. However, at higher incidence angles (50° and 60°) the more general Weibull/generalized log-normal distribution is found to better characterize the low amplitude portion of the backscatter distributions.

ACKNOWLEDGMENTS

I would like to thank Drs. David G. Long, David V. Arnold, and all those who constructed and operated the YSCAT instrument. A special thanks goes to Dr. Long who kept a tight reign on a slack rope. Without them and their hard work, this thesis would have been impossible. Thanks also goes to Dr. Mark Donelan for the use of the CCIW WAVES research platform and wave staff data.

Finally, my love and gratitude go to my wife who has sacrificed greatly for our family and for this thesis. The people I love give merit to the work I love.

Contents

List of Tables

List of Figures

Chapter 1

Introduction

The study of microwave remote sensing began in the 1960's with the advent of space exploration [1]. The obvious advantages of microwave remote sensing from space such as near real-time information and global coverage has motivated much research [2]. Yet despite 30 years of research on the subject there are still many outstanding questions about the air-sea interface and the interaction between the wind and the waves.

Tower mounted scatterometers, such as the YSCAT scatterometer, are a cost-effective way to study the air-sea interface. The understanding gained from scatterometers such as YSCAT will enable us to better understand data collected by spaceborne scatterometers such as the European Space Agency's Earth Remote Sensing satellites (ERS-1 and ERS-2), Japan's Advanced Earth Observing Satellite (ADEOS-II), and the QuikSCAT scatterometer to be launched later this year [3].

1.1 Statement of Problem

The relationship between the environmental parameters of the air-sea interface and the observed radar cross section (σ°) is referred to as the geophysical model function (GMF). Understanding the geophysical model function is central in interpreting scatterometer data [4]. However, it remains poorly understood due to the complexity of the air-sea interface. The normalized radar cross section, σ°, of the sea surface is dependent on many parameters including incidence angle, microwave frequency, transmit and receive polarizations, wind direction, long wave field, salinity of the water, water temperature, air temperature, and other factors. Tower mounted

scatterometers such as YSCAT are deployed in an effort to more fully describe the geophysical model function and forge a connection between environmental parameters and radar backscatter. This thesis increases our understanding of the GMF through analysis of YSCAT94 data.

1.2 Contributions

The backscatter distributions from the YSCAT94 experiment are analyzed in this thesis in an effort to increase our understanding of the air-sea interface and to increase our ability to predict environmental parameters based on microwave backscatter data. Specific contributions of this thesis include:

- Identifying qualitatively the low wind speed rolloff previously observed only in wave tank and air ship experiments
- Using linear estimation techniques to estimate the low wind speed rolloff (Υ)
- Reporting logged and unlogged σ° statistics according to both wind speed and mean wave slope
- Finding the analytical mean and variance of the generalized log-normal distribution in order to facilitate data analysis
- Parameterizing data histograms in log space with the log-normal and generalized log-normal distributions according to both wind speed and mean wave slope
- Parameterizing data histograms by the Rayleigh/generalized log-normal distribution according to both wind speed and mean wave slope
- Identifying trends in distribution parameters fitted to YSCAT94 data
- Constructing the Weibull/generalized log-normal distribution in order to account for the non-Rayleigh low amplitude portions of empirical backscatter distributions at high incidence angles

1.3 Overview

The remainder of this thesis is organized as follows. A brief background to scatterometry and a review of the current research in this field is provided in Chapter 2. A description of the YSCAT scatterometer instrument used to collect the data analyzed in this thesis is also provided. This is followed by details of the YSCAT94 experiment which lasted for six months (June-November, 1994) and was conducted on the Canada Centre for Inland Waters (CCIW) WAVES research tower located on Lake Ontario. The data set collected from the YSCAT94 experiment is described and data processing methods are discussed.

Chapter 3 provides a qualitative description of the low wind speed rolloff in the normalized radar cross section observed in YSCAT94 data. Possible explanations for this phenomenon are discussed, and some examples of this rolloff in YSCAT94 data are presented. Plots showing this rolloff for all YSCAT94 data sets is included as appendix A. Linear regression data smoothing techniques are used to estimate the low wind speed rolloff (Υ). This low wind speed rolloff of σ° has been reported for carefully controlled wave tank experiments [5] and for air ship scatterometer experiments [6], but this is the first time this effect has been reported for tower mounted scatterometer data.

Chapter 4 presents the method used to extract mean wave slope estimates from a wire wave gauge array. This wire wave gauge array gathered 10 Hz sampled surface height measurements simultaneously with YSCAT94. The method proposed by Cox and Munk [7] is used to estimate the mean wave slope (s_x) to which YSCAT94 data is compared. The results of this comparison to wind speed, as well as the results of the comparison of YSCAT94 data to mean wave slope s_x, are presented in Appendices B and C respectively.

Chapter 5 presents the model for backscatter amplitude and explains the theory used in this thesis in some detail. The compound probability model proposed most recently by Gotwols and Thompson [8] is developed and used to parameterize the full YSCAT94 data set. The log-normal and generalized log-normal distributions are developed and described, and the mean and variances of both distributions are

derived. The Rayleigh/generalized log-normal distribution is also described, though no analytic solution is found. The procedures used to fit probability distribution functions to empirical data histograms, including the metric used to fit them, is described Section 5.4. Finally, results of fitting the log-normal and generalized leg-normal distributions to logged YSCAT94 data, and fitting Weibull and Rayleigh/generalized log-normal distributions to unlogged YSCAT94 data, along with statistical parameters such as the mean and variance of both the logged and unlogged data are presented and trends are discussed.

These chapters are followed by a summary and conclusion. Implications of the results as well as possibilities for future research are presented. Appendix A shows plots of the low wind speed rolloff (Υ). Appendices B and C are comprised of plots showing the parameters associated with the entire YSCAT94 data set according to wind speed and wave slope. Appendix D contains β values resulting from fitting the Weibull/generalized log-normal distribution to YSCAT94 data.

Chapter 2

Background

2.1 The Air-Sea Interface

The air-sea interface is a complex, constantly changing boundary layer between the atmosphere and Earth's oceans. Much research has been devoted to understanding this interface and the role it plays in global weather and in the natural environment (for an overview, see [2]). In spite of this research, our understanding of the mechanisms involved at this interface remains poor.

The primary application of spaceborne scatterometers such as the SEASAT Scatterometer (SASS) and the NASA Scatterometer (NSCAT) is microwave anemometry [4]. The relationship between the wind and the waves generated on the sea surface is of primary importance. As the wind speed over the water increases, first small capillary waves, then longer wavelength gravity waves are generated [9]. Eventually a wave spectrum emerges and the wind and waves reach a steady state called a fully developed sea [9] [10] (see Fig. 2.1). The process through which this generation occurs, including when and what wavelength of waves are generated by a given wind speed, is still debated [4].

Radar scatterometry has been an effective tool used to increase our understanding of the air-sea interface since the 1960's [1] [2]. Tower mounted scatterometers such as YSCAT provide a cost effective way to study the air-sea interface. Results of this research help to more fully understand the data collected by spaceborne scatterometers such as NSCAT, ERS-1, and the soon to be launched QuikSCAT [3].

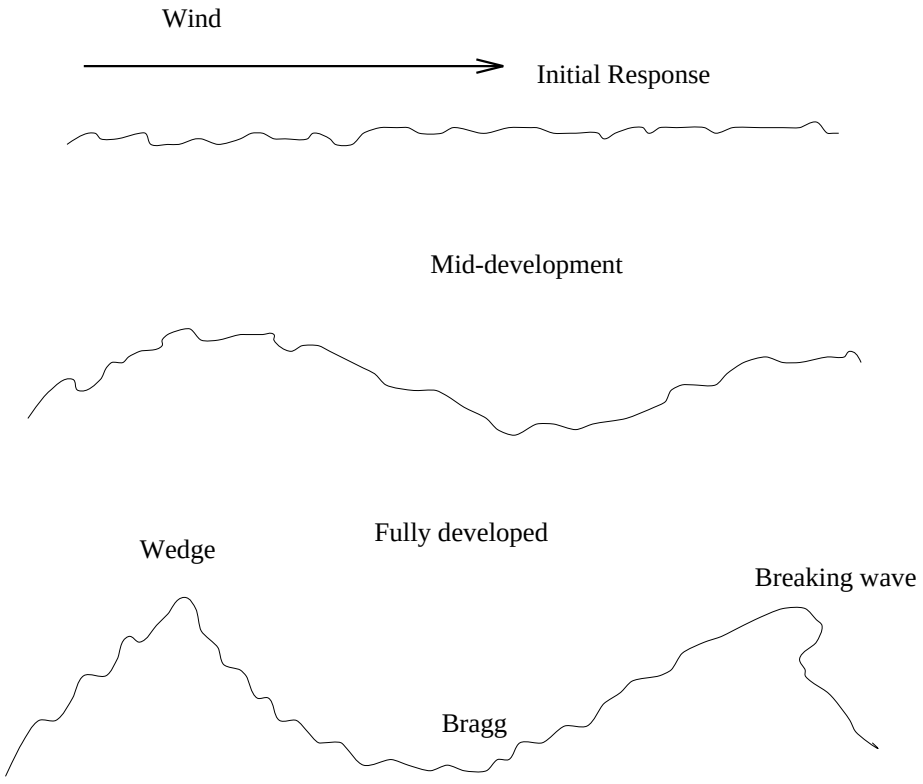

Figure 2.1: Cross section of ocean surface at different stages of growth.

Scatterometers transmit electromagnetic (**E** and **H**) impulses toward the surface and record the reflected electric field. The electric field scattered by an arbitrary surface can theoretically be calculated using Huygen's equation [11]

$$\mathbf{E}_r = \iint\limits_{S'} \left\{ i\omega\mu\overline{\overline{G}}(\bar{r},\bar{r}) \cdot [\hat{n} \times \mathbf{H}(\bar{r}')] + \nabla \times \overline{\overline{G}}(\bar{r},\bar{r}) \cdot [\hat{n} \times \mathbf{E}(\bar{r}')] \right\} dS' \tag{2.1}$$

where $\overline{\overline{G}}$ is the dyadic green function and is given by [11]

$$\overline{\overline{G}}(\bar{r},\bar{r}') = \left(\overline{\overline{I}} + \frac{\nabla\nabla}{k^2} \right) \frac{e^{ik|\mathbf{r}-\mathbf{r}'|}}{4\pi|\mathbf{r}-\mathbf{r}'|}. \tag{2.2}$$

This approach for calculating the scattered fields is impractical for real scatterometers since a detailed description of the sea surface is not available. Instead, scatterometers record the normalized radar cross section (σ°) of the water surface [4] (see Fig. 2.2 for a typical scatterometer geometry).

Small Perturbation Theory (SPT) gives a scattering model for σ° called the the composite model [Eq. (2.9)] after simplification of Huygen's equation [Eq. (2.1)] under certain assumptions. A more detailed description of the composite model will be presented in Ch. 5. Using the composite model as a form for σ°, the air-sea interface is studied in this thesis to more fully understand relationship between the wind and the waves.

A typical scatterometer configuration is schematically illustrated in Fig. 2.2. The scatterometer antenna transmits a radar signal at an incidence angle, θ, to the surface. The amount of backscatter power is a function of the roughness of the surface, polarization, frequency of the transmitted wave, and many other factors [12]. The rougher the surface, the more power that is scattered back to the antenna. The relationship between the the power transmitted, P_t, the power received, P_r, and σ° is given by the radar equation [12]

$$\sigma^o = \frac{(4\pi)^3 R^4 L P_r}{P_t G^2 \lambda^2 A_{eff}}, \tag{2.3}$$

where R is the range to the surface, L is the system loss, G is the gain of the antenna, λ is the microwave wavelength and A_{eff} is the effective area of the antenna. From this equation it is apparent that the value of σ° is essentially the ratio of the power

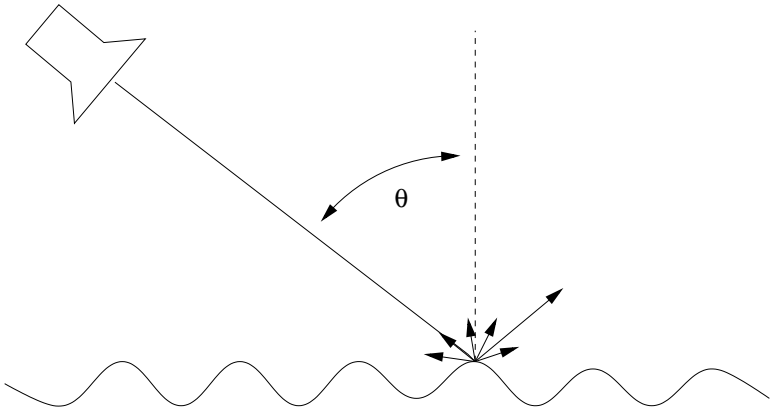

Figure 2.2: A scatterometer transmits a radar beam incident to the surface at an angle θ. The amount of radiation reflected back to the antenna is related to the roughness of the surface

returned (adjusted for spreading and system losses) to the power transmitted. While not explicitly stated, it is also important to note that σ° is dependent on θ.

For mid-range incidence angles (20° - 50°) at microwave frequencies, the sea surface scattering is primarily dependent on small scale (1-15 cm) gravity/capillary waves due to Bragg scattering [8]. This thesis will focus primarily on mid-range incidence angles though statistics for 0° (nadir), 10°, and 60° will also be documented. In Bragg scattering theory, the backscatter return is assumed to be primarily from the water wave component in resonance with the incident radiation. In first order Bragg theory, the resonant water wavelength Λ is related to electromagnetic wavelength λ by

$$\Lambda = \frac{\lambda}{2\sin(\theta)}. \tag{2.4}$$

where θ is the incidence angle.

For microwave frequencies of 2 - 18 GHz, and mid-range incidence angles, the Bragg wavelength varies from approximately 1 cm to 20 cm, a range which includes capillary and short gravity waves. Table 2.1 shows the water Bragg wavelengths measured in the YSCAT94 experiment. The Bragg wavelength can be a useful, compact parameter to examine the backscatter versus radar parameters; however, it must be

Table 2.1: Bragg wavelength in cm as a function of frequency and incidence angle.

Frequency (GHz)	Incidence Angle				
	20°	25°	30°	40°	50°
2.00	21.93	17.75	15.00	11.67	9.79
3.05	14.38	11.64	9.84	7.65	6.42
5.30	8.27	6.70	5.66	4.40	3.69
10.02	4.38	3.54	3.00	2.33	1.96
14.00	3.13	2.54	2.14	1.67	1.40

noted that while Bragg scattering may be the dominate scattering mechanism, other scattering mechanisms and hydrodynamic modulation also affect the radar backscatter.

2.2 Theoretical Background

The study of the air-sea interface and the Geophysical Model Function (GMF) have been the subject of much research for the past 30 or more years. Two prominent topics of research in this area are the wave height spectrum and the electro-magnetic scattering models used to predict the σ° of the water surface. Both of these topics are central to the focus of this thesis.

Various mathematical expressions for the wave height spectrum have been proposed. One popular and simple model is the Phillips model [13] which assumes a wave height spectrum of the form

$$\Psi(k) = Bk^{-4} \tag{2.5}$$

where k is the wavenumber and B is a function at most of the angle between the wind vector and the wave propagation. The k^{-4} falloff is characteristic of observed spectra (including YSCAT94 spectra, see Fig. 4.1), making this a simple approximation of the wave height spectra.

Another model for the wave height spectrum is the Durden and Vesecky model [14] which extends the Phillips model to account for rotational fluids. The Durden

and Vesecky model is expressed as

$$\Psi(k,\phi) = \frac{0.004k^{-4}}{2\pi} \cdot \begin{cases} e^{-0.74(K_c/k)^2}(1 + c(1 - e^{-sk^2}))\cos 2\phi & k < 2 \\ \left(\frac{bku_*^2}{g}\right)^{a\log(k/2)}(1 + c(1 - e^{-sk^2}))\cos 2\phi & k > 2 \end{cases} \tag{2.6}$$

where k is the wavenumber, ϕ is the angle between the waves and the look direction, K_c is a cutoff wavenumber which depends on wind speed, u_* is the friction velocity, and s, b, and a are constants determined by fitting to empirical data. Other models for the wave height spectrum include the Pierson-Moskowitz spectrum [15], the Plant model [16], the JONSWAP spectrum for fetch-limited seas [17], and others including various gamma spectra. All of these models attempt statistically describe a fully developed sea. The periods of time during significant wave growth or decay is remain poorly understood and largely ignored.

In this thesis the frequency spectrum (related to the wave height spectrum through the dispersion relation [Eq. (4.3)]) is assumed to be a Donelan spectrum [18] which is expressed as

$$\Phi(\omega) = \alpha g^2 \frac{\omega^{-4}}{\omega_p} e^{-\frac{\omega_p}{\omega}} \gamma^{\Gamma} \tag{2.7}$$

$$\Gamma = e^{-(\omega-\omega_p)^2/2\sigma^2\omega_p^2} \tag{2.8}$$

where ω_p is the spectral peak, α is the equilibrium range parameter, γ is the peak enhancement factor, and σ is the peak width factor. This spectrum was chosen because it was developed from wave height measurements taken at the same site as YSCAT94's deployment. This spectrum is described in more detail in Section 5.2.2.

The other major topic of research upon which this thesis relies is the electromagnetic scattering models used to predict the σ° of the water surface. The most popular electromagnetic scattering model for ocean scattering is the composite model. This model proposes that the water surface is composed of small independent "patches" whose individual cross sections are given by small perturbation theory (SPT), *i.e.*

$$\sigma^\circ = 16\pi k_m^4 |g_{pp}(\theta_i)|^2 \Psi(2k_m \sin\theta_i, 0) \tag{2.9}$$

where σ° is the normalized radar cross section, θ_i is the incidence angle, $g_{pp}(\theta_i)$ is a polarization dependent reflection coefficient with pp being hh or vv, k_m is the microwave wavenumber ($\omega\sqrt{\mu\epsilon}$ or $\frac{2\pi}{\lambda}$), and Ψ is the wave height spectrum [19]. The composite model including the reflection coefficients $g_{hh}(\theta_i)$ and $g_{vv}(\theta_i)$ [16] are explained in more detail in Section 5.1.

With a model for $\Psi(k)$ and an expression for σ°, this thesis proposes a quadratic approximation (in log space) for σ° which captures the behavior of σ° over varying radar parameters. This model concludes that the probability distribution for the amplitude of the radar backscatter may be expressed as

$$p(a) = \int_{-\infty}^{\infty} \underbrace{2aCe^{a_1 s_x + a_2 s_x^2} e^{-a^2 C e^{a_1 s_x + a_2 s_x^2}}}_{p(a|\sigma_\circ(s_x))} \underbrace{\frac{e^{\frac{-s_x^2}{2\sigma_x^2}}}{\sqrt{2\pi}\sigma_x}}_{p(s_x)} ds_x. \tag{2.10}$$

where s_x is the mean wave slope and a_1, a_2, σ_x, and C are constants determined by fitting to empirical data (see Section 5.4). Equation (2.10) is a combination of a Rayleigh and a generalized log-normal distribution expressed in terms of the mean wave slope s_x instead of σ°. Equation (2.10) is expressed in terms of σ° in Eq. (5.19). This thesis characterizes YSCAT94 data by finding a_1, a_2, σ_x, and C values which fit YSCAT94 backscatter amplitude data. The development of Eq. (2.10) is an extension of work done by B. L. Gotwols and D. R. Thompson [8].

While Eq. (2.10) characterizes backscatter distributions at mid-range incidence angles quite well, if fails to capture the behavior in the extremely low amplitude portion of backscatter distributions at higher incidence angles. Rather than a Rayleigh/generalized log-normal distribution, a more general distribution based in a Weibull distribution for $p(a|\sigma^\circ)$ is developed. This Weibull/generalized log-normal distribution reduces to the Rayleigh/generalized log-normal distribution at mid-range incidence angles, but also captures the behavior of the extremely low amplitude portion of the amplitude backscatter distribution where the Rayleigh/generalized log-normal distribution fails.

Figure 2.3: The Canada Centre for Inland Waters (CCIW) WAVES research platform. YSCAT is the crane-like structure on the upper deck. Also visible are the two anemometers on the support legs and the bivane anemometer on the tower in the center of the platform.

2.3 YSCAT Instrument

YSCAT was a tower mounted microwave scatterometer designed by Brigham Young University to collect normalized radar cross section (σ°) measurements under varying radar and environmental parameters in order to study the air-sea interface (see Fig. 2.3). YSCAT operated at primary frequencies of 2 GHz (S-band), 3 GHz (S-band), 5 GHz (C-band), 10 GHz (X-band), and 14 GHz (Ku-band) and at incidence angles of 0° (nadir), 10°, 20°, 25°, 30°, 40°, 50°, and 60°. YSCAT's antenna was specially designed to provide a near-constant beamwidth (and therefore a near-constant footprint of approximately 1 m size at mid-range incidence angles) of five

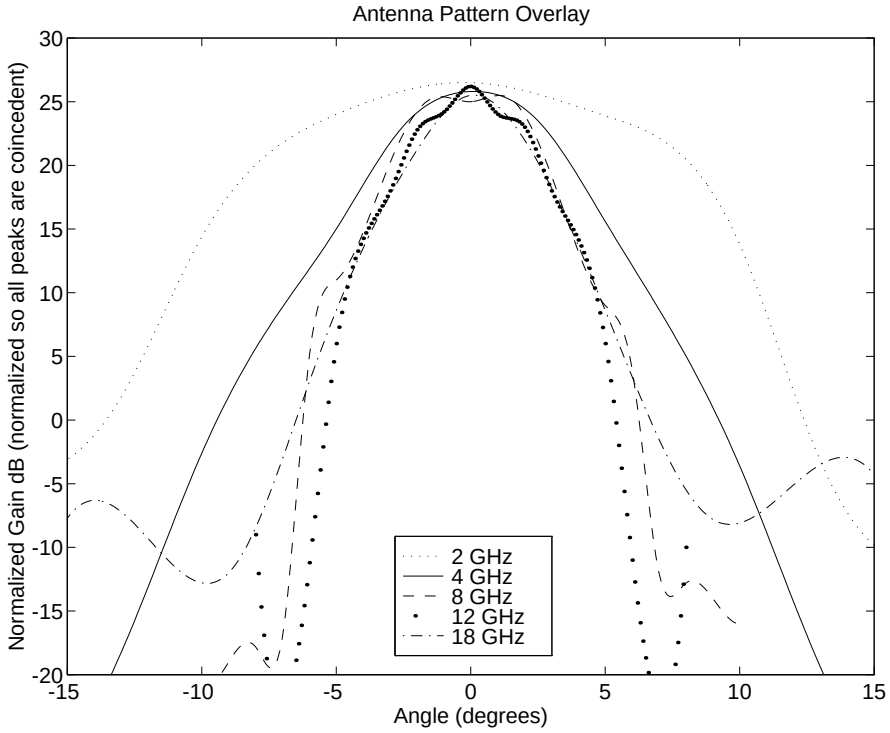

Figure 2.4: Two-way antenna patterns.

degrees over most of the operating bandwidth (4-18 GHz, see Fig. 2.4). In addition, YSCAT operated at both h-pol and v-pol. A summary of YSCAT's RF parameters is provided in Table 2.2 while a more detailed description of the YSCAT instrument is provide in [20] and [21].

2.4 YSCAT94 Experiment

The YSCAT94 experiment consists of data collected by the YSCAT instrument in 1994 when it was deployed for a period of six months, from June to November, 1994, on Lake Ontario. It was mounted on the Canada Center for Inland Waters (CCIW) WAVES research platform about 1.1 km from the western shore of Lake Ontario (see Fig. 2.5). Water depth at this site is about 12 m, and YSCAT was mounted 10 m above the water surface (c.f. to Fig. 2.3). The annual variation in water depth is less that 0.5 m and there are no significant tides, seiches, or associated

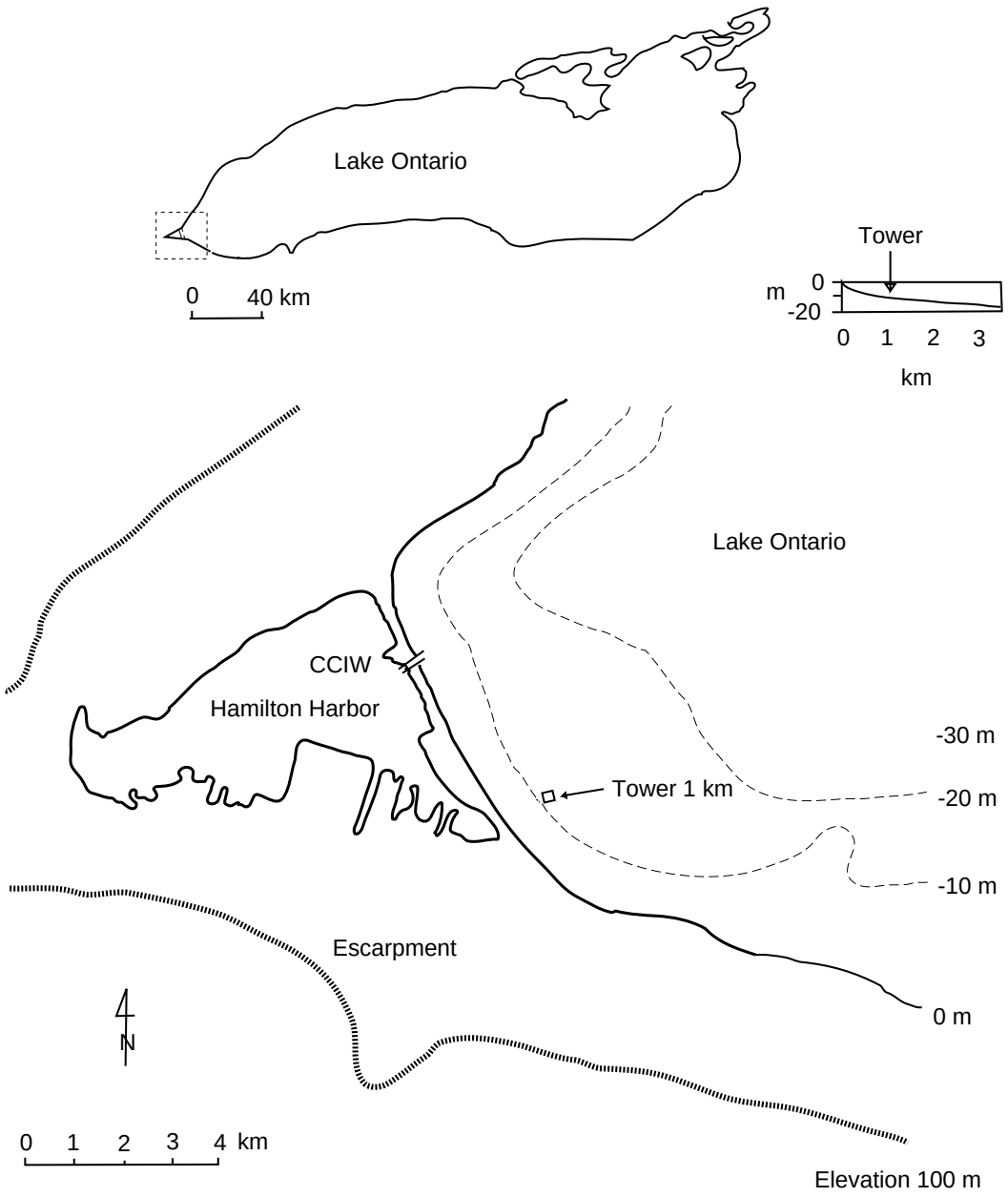

Figure 2.5: Location of the Lake Ontario deployment site [20].

Table 2.2: YSCAT RF System Parameters

Center Frequency	2-18 GHz
Peak Output Power	23 dBm
Transmit Polarization	V or H (selectable)
Two-Way Antenna Beam width	5-10 degrees (varies with frequency)
Receive Polarization	V and H (selectable)
Polarization Isolation	15-20 dB
LO-IF	166 MHz
Dynamic Range	50-110 dB
Baseband Signal Bandwidth	900 Hz

currents. Other random currents are typically less than 10 cm/s. The CCIW tower was designed to minimize both wind and wave disruption and therefore no effort is given to account for turbulent effect on the wind and the waves due to the tower in this thesis. Prevailing winds in this area were westerly which provided fetches from 1.1-2 km. Due to this short fetch, waves with periods of four seconds are common, while waves with periods of eight seconds are rare [21].

YSCAT's goal was to provide normalized radar cross section (σ°) measurements under a wide variety of environmental and radar parameters. In addition to collecting data at multiple frequencies, incidence angles, and polarizations, YSCAT had the ability to track the wind direction with the aid of simultaneous weather data acquired at the site. In this thesis, "upwind" and "downwind" include 20° azimuth angle allowance on either side of the true wind direction. Wind speed, wind direction, rainfall, and water temperature measurements were collected so that comparison could be performed later. Additionally, a wave staff array was installed midway through the summer.

Data which was collected during or after rainy periods was contaminated and was removed from later analysis. Data corrupted by equipment failures or other sources of error (e.g., ships, birds) were also removed. As well, especially during a three day period from October 4^{th} through the 7^{th}, 1994, and at other spurious short intervals, the 10 Hz amplitude backscatter measurements exhibited a "flat" response

Table 2.3: Number of measurements for various wind speed, frequency, and polarization cases after rain contaminated and instrument malfunction data records were discarded.

WS (m/s) / Frequency (GHz)		0-5	5-7.5	7.5-10	> 10
H-Pol	2	4245	1196	516	587
	3	3808	810	388	299
	5	7263	1756	791	806
	10	3739	833	369	308
	14	6775	1763	744	828
V-Pol	2	4315	1502	511	396
	3	4658	1539	555	366
	5	10083	3319	1179	622
	10	6176	2001	636	310
	14	8595	3064	1034	499

(see Section 3.2 for a discussion of these records). These flat data records were not considered in the present analysis.

After binning the data according to frequency, polarization, direction (upwind or downwind), incidence angle, and wind speed or wave slope, the mean of each data case was found. Data measurements with 1 minute means far removed from the aggregate mean were generally found to have fluctuating wind speed records which led to unstable σ° measurements, and were also discarded. Table 2.3 summarizes the resulting number of measurements in each data case after rain contaminated and instrument malfunction data records were discarded.

2.5 Data Quality Analysis

Each different data case (frequency, polarization, wind direction, wind speed, incidence angle, and mean wave slope, see Table 2.4) of YSCAT94 data was analyzed for data quality prior to computing a histogram. This analysis included removing any "flat" responses from the data set (see section 3.2), and then removing other records whose means are far (more than 4 times) removed from the aggregate mean. YSCAT94 data consists of one minute records of amplitude measurements sampled

Table 2.4: Summary of YSCAT94 data classification. 2,720 distinct data cases emerge from the YSCAT94 data set.

Parameter	**Classification Values**
frequency	2, 3, 5.3, 10, 14 GHz
polarization	horizontal, vertical
direction	upwind, downwind (40° swath)
inc. angle	0° (nadir), 10°, 20°, 25°, 30°, 40°, 50°, and 60°
wind speed	1-10 m/s
wave slope	0.1-0.38
Total	**2,720 distinct cases**

at 10 Hz for a total of 600 measurements each. Included with each record are environmental and radar parameters including frequency, transmit polarization, incidence angle, azimuth angle, received σ°, wind speed, wind direction, and water temperature. Except for the radar return amplitude data, these other 10 Hz sampled parameters are combined into one minute averages.

The amount of data records for different cases varies widely, ranging from only one (or in some cases zero) one minute records, to over 100 individual one minute records. For this reason, the number of bins used for a given histogram is varied to reflect the amount of data present. The number of bins used to compute each histogram is calculated using the following equation

$$\#ofbins = \begin{cases} 60 & : \quad N \leq 1000 \\ 60 + \left\lfloor \frac{(N-1000)}{25} \right\rfloor & : \quad N > 1000 \end{cases} \tag{2.11}$$

where N is the total number of 10 Hz samples for this data case and $\lfloor\rfloor$ indicates the floor operation.

In some cases, the number of bins calculated from Eq. (2.11) required too much computation to be analyzed practically (see Section 5.4.2 for more information). Therefore, after the histogram is computed using the number of bins given by Eq. (2.11), adjacent bins are averaged until the number of bins is below 300. Figure 2.6(a-b) shows two different cases with differing amounts of data for comparison. As with all histograms, extreme outlier values tend to reduce the resolution. For this

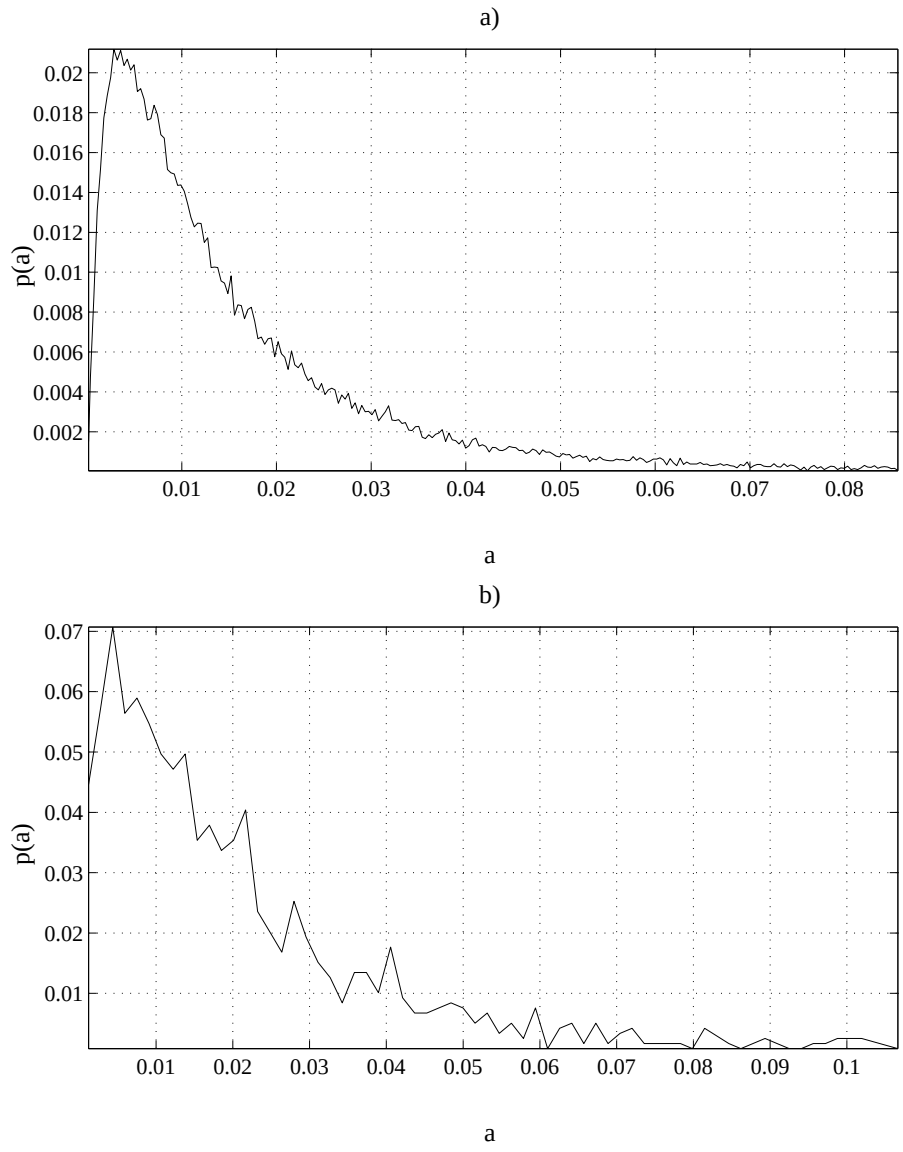

Figure 2.6: Example of Dense and Sparse Histograms. a) Dense histogram made from 46,000 individual measurements. Data is for 3 GHz, h-pol, downwind, 20° incidence angle, and 3 m/s wind speed. b) Sparse histogram made from 600 individual measurements. Data is for 2 GHz, h-pol, downwind, 20° incidence angle, and 9 m/s wind speed.

reason, the largest 0.1% of the amplitude measurements of each data case is discarded in order to provide needed resolution at lower amplitudes.

Two realizations of data are considered: the first realization is simply the raw data, while in the second realization the data is first normalized by dividing each one minute record by the mean of that record, then multiplying all data in that bin by the aggregate mean. This second method tended to reduce errors introduced by receiver gain fluctuation due to temperature changes, distance variations from the water surface, or other factors. Unless otherwise specified, the figures and discussion in this thesis refer to the normalized data, and only results for normalized parameters are provided in the Appendices. Figure 2.7 shows a comparison between the normalized and unnormalized data with the mean indicated by a straight dashed line. Data is for 3 GHz, v-pol, upwind, 25° incidence angle, 5 m/s wind speed.

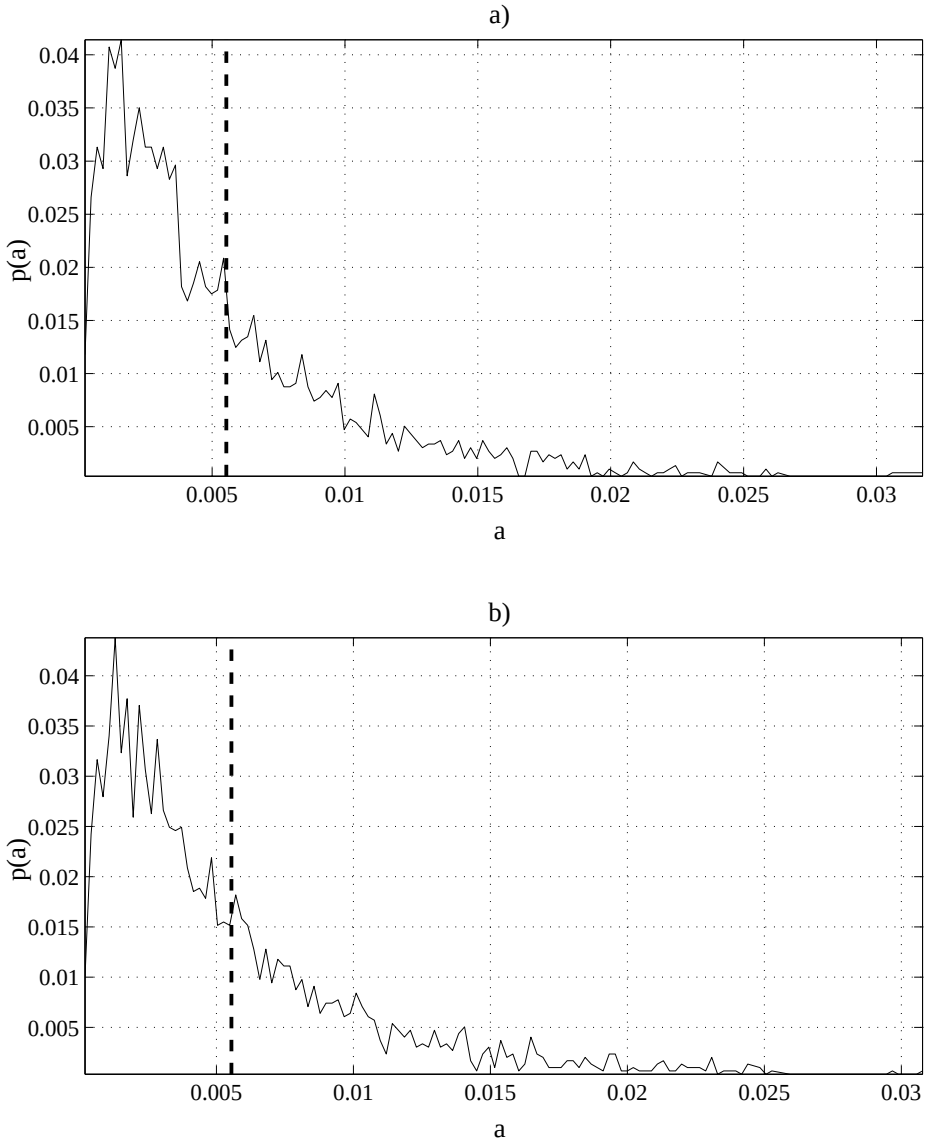

Figure 2.7: Comparison between the a) unnormalized and b) normalized and data with the mean indicated by a straight dashed line. a) Unnormalized data histogram. Aggregate mean=0.005533 b) Normalized data for the same case as a). Aggregate mean=0.005545.

Chapter 3

Low Wind Speed Rolloff

3.1 Rolloff Theory

Donelan and Pierson [22] postulated the existence of a rolloff in the normalized radar cross section (σ°) at low wind speeds. At very low wind speeds, the friction velocity, u_*, is too small to generate capillary waves, resulting in a smooth surface and therefore a small backscatter cross section. At higher wind speeds, the wind generates capillary waves and σ° closely follows a power-law relationship with wind speed. This effect has been observed in carefully controlled wave tank data where a hysteresis effect in $\sigma_\circ$ versus wind speed is observed [5]: as the wind speed is increased from zero, at a temperature-dependent threshold wave generation commences and $\sigma_\circ$ increases significantly. As the wind speed is decreased, waves are maintained at wind speeds below the startup threshold and finally fall off. The thresholds at which wave generation begins and ends is very temperature and long wave field sensitive.

While this effect has been observed in wave tank data [5] and in airship scatterometer data [6], it has not previously been reported in tower mounted scatterometer data. However, YSCAT94 data provides strong evidence to support this low wind speed rolloff over a wide range of frequencies. For example, Fig. 3.1 illustrates a typical plot of YSCAT94 σ° measurements versus wind speed. Each dot represents a one minute average of σ°. This example is for 5 GHz, 20° incidence angle, horizontal polarization, downwind and is typical of YSCAT94 data. Note that there is a dramatic rolloff in the received power at wind speeds less than about 4 m/s. The broad wind speed spread in the falloff region supports the existence of the hysteresis

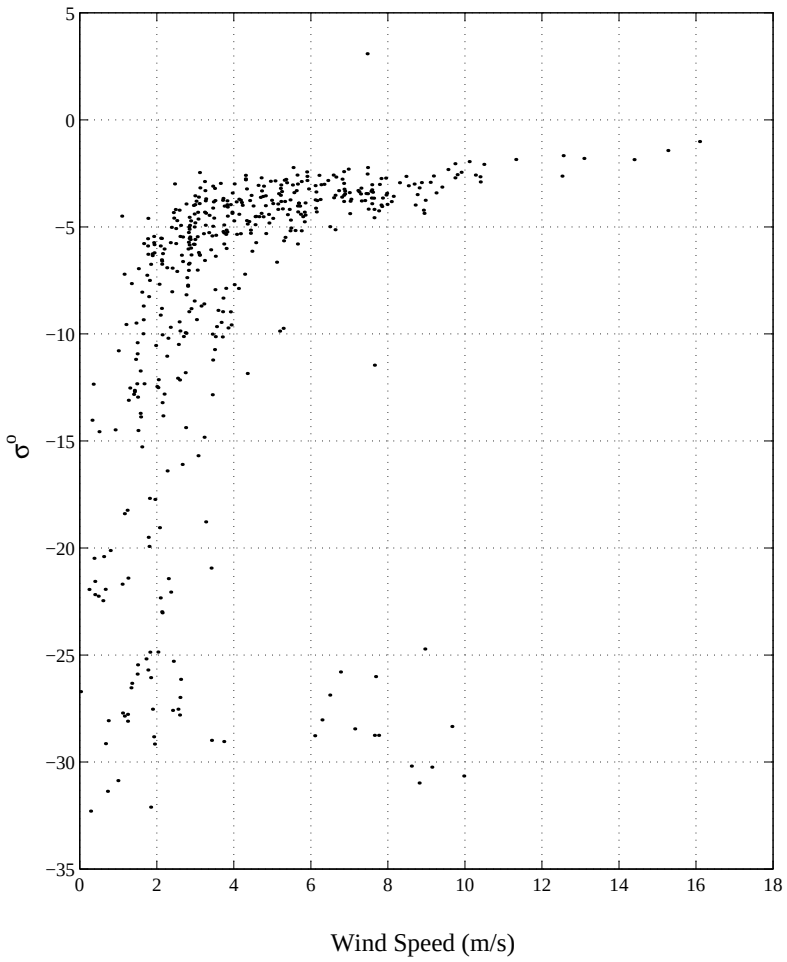

Figure 3.1: Typical YSCAT94 backscatter response illustrating the low wind speed rolloff of σ°. Each dot represents a one minute average of σ° measurements. Data is for 5 GHz, horizontal polarization, downwind, 20° incidence angle.

effect observed in wave tank data since there is a range of long wave and temperature conditions, as well as wind fluctuations, in the uncontrolled environment of the tower experiment. Over the range of frequencies and incidence angles observed by YSCAT, the fall off threshold varies from 3 to 6 m/s. The low wind speed rolloff (Υ) is quantified by a heuristic smoothing algorithm in Section 3.3.

3.2 "Flat" Responses

As noted in Chapter 2, for a three day period on Oct. 4^{th} through Oct. 7^{th} and at other times during the YSCAT94 experiment, "flat" backscatter amplitude data was recorded. Figure 3.2 illustrates typical normal and flat responses. The flat response of Fig. 3.2(a) has considerably less variance and amplitude than the typical normal response of Fig. 3.2(b).

The cause of such flat data records has not been determined for all cases by the author. One possibility may be that these responses represent data measurements taken below the low wind speed rolloff. This seems improbable because the rolloff at low wind speeds is clearly recognizable even after all flat responses are removed (see Fig. 3.3). On the other hand, these responses may have been due simply to equipment failure as seems to be the case for the three day contiguous period from Oct. 4^{th} through Oct. 7^{th} (see below).

In this thesis, flat data records, whatever their origin, are identified and discarded before performing the analysis presented in Chapters 4 and 5. Figure 3.3 shows the records remaining after removing these flat data records from the data set of Fig. 3.1 above using the method described below. A similar rolloff may be seen, but many of the extremely low σ° values have been discarded.

Flat data records are usually easy to detect due to the unusually low σ° values of these records in comparison to neighboring data. Such is the case for the erroneous data in Fig. 3.1. For the data case of 3 GHz, vertical polarization, upwind, 20° incidence angle presented in Fig. 3.4, the low σ° measurements around -35dB (denoted by asterisks in Fig. 3.4) all correspond to the time period between Oct. 4^{th} through Oct. 7^{th} and have flat responses similar to that shown in Fig. 3.2. While the flat data

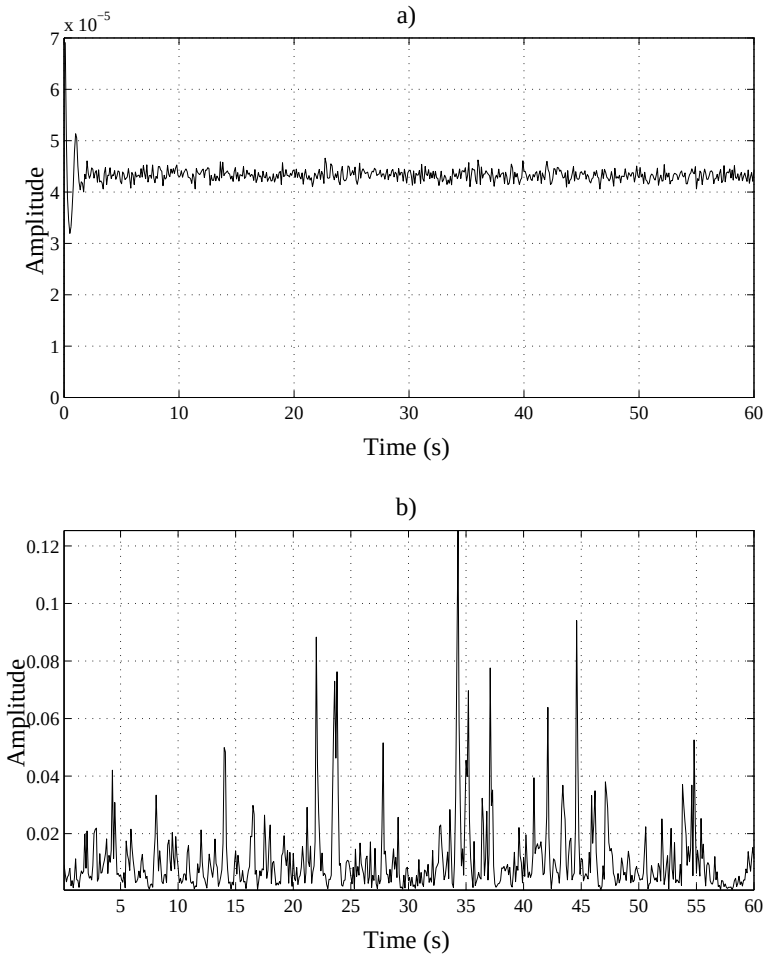

Figure 3.2: 5 GHz, h-pol, 20° example of of a) "flat" and b) "normal" data records. Notice the flat data record's measurements are on the order of two magnitudes lower than those of the normal response. For a) $\Delta^\circ = 13.57$ and for b) $\Delta^\circ = 393.5$ (see text).

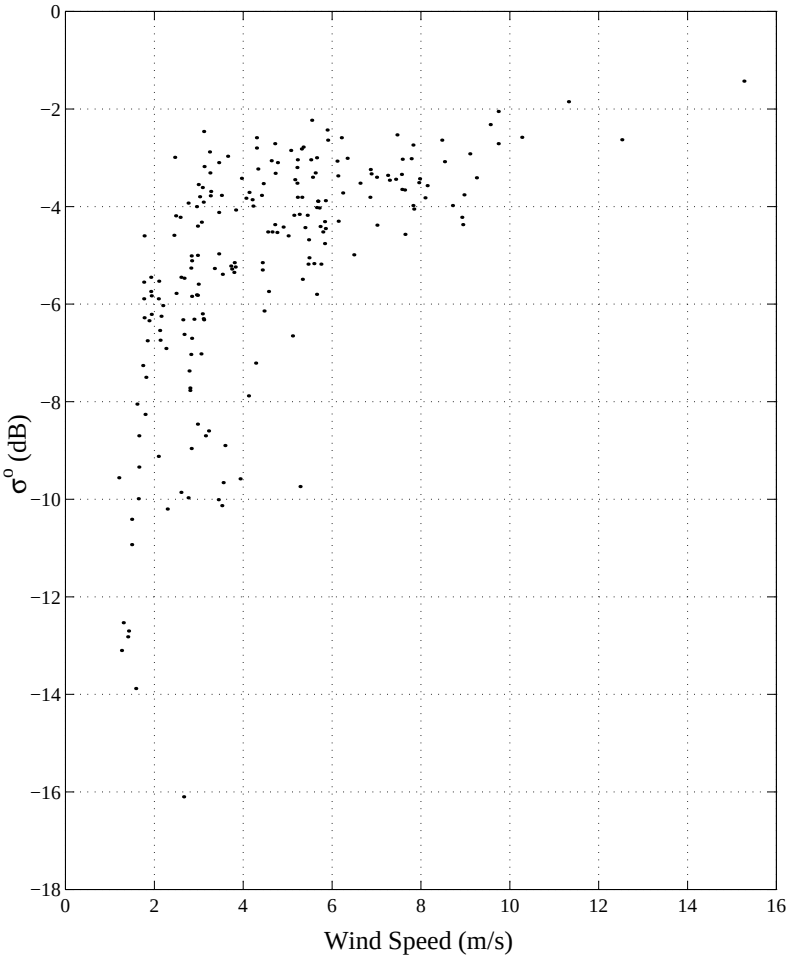

Figure 3.3: YSCAT94 backscatter of Fig. 3.1 with "Flat" responses removed. Many of the extremely low σ° values have been discarded.

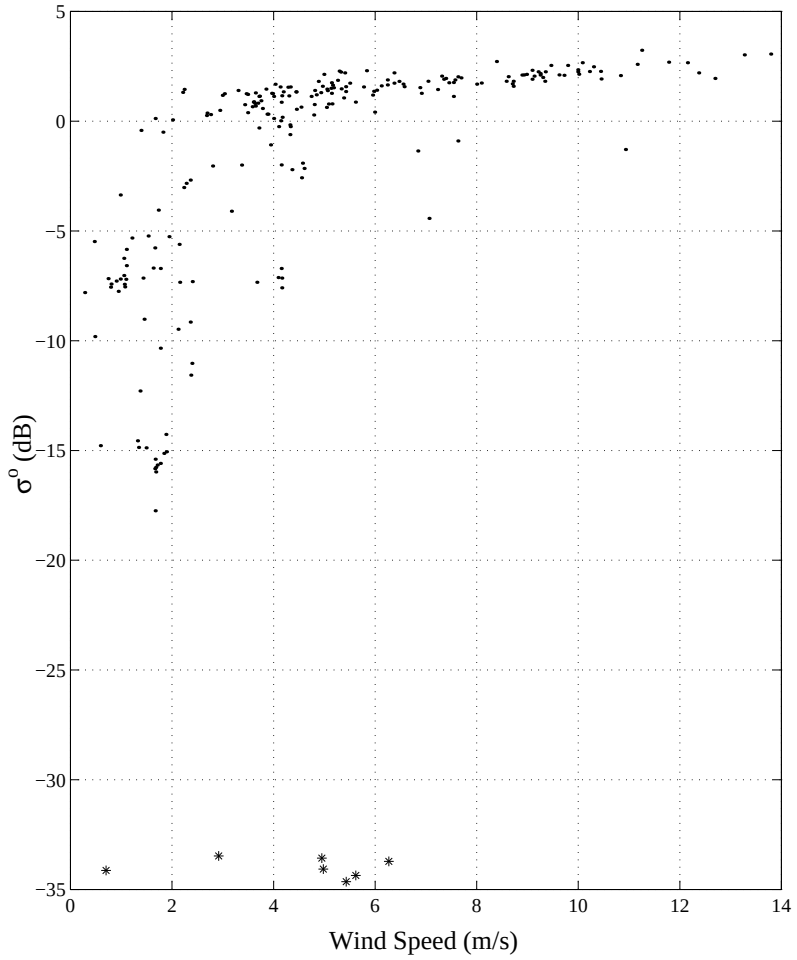

Figure 3.4: σ° measurements for 3 GHz, vertical polarization, upwind, 20° incidence angle. Flat responses between Oct. 4^{th} and Oct. 7^{th} are denoted by asterisks.

records during this three day period are easy to detect, there is the suspicion that flat data responses may have occurred at other times during the YSCAT94 experiment.

To find other flat responses, a test of the normalized deviation from the mean (Δ°) is calculated for each data record. As a measure of how flat each response is, Δ° is computed according to the following equation

$$\Delta^\circ = \frac{\sum_{n=1}^{N}(x_n - \bar{x})}{\bar{x}} \tag{3.1}$$

where x_n is each sample, $\bar{x}$ is the mean of each data record, and N is the number of total samples (600 for one minute of 10 Hz sampled measurements). Δ° for Fig. 3.2(a) is 13.57 and Δ° for Fig. 3.2(b) is 393.5. Thus a wide discrepancy in Δ° exists between the "normal" and the "flat" responses. Fig. 3.5 shows Δ° values for all of the one minute records for the 5 GHz, h-pol, 20° incidence angle data case. Data records with a Δ° value below 125 (indicated by the horizontal dashed line) are considered "flat". The value 125 was chosen empirically as a value midway between typical normal and flat response Δ° values. All of the YSCAT94 data is processed using this method in order to remove flat data records. Flat responses were observed at spurious times throughout the YSCAT94 experiment. While instrument failures may be responsible for many of these, it is possible that valid σ° data was discarded by this procedure.

3.3 Rolloff Analysis

Section 3.1 presented the theory of the rolloff of σ° at low wind speeds. In this section, a quantitative analysis of this rolloff is performed.

In order to quantify the rolloff of σ° at low wind speeds, an algorithm using statistical smoothing methods is implemented. A local polynomial regression algorithm with an Epanechnikov kernel is used to smooth the data [23]. A threshold is then calculated to determine at what wind speed this rolloff occurs. Many of the data cases do not exhibit a clear rolloff due either to insufficient data, or due to the noise floor. However, for many of the lower incidence angles and lower frequencies, there is a distinguishable rolloff wind speed (Υ) which is quantified by the method outlined in this section.

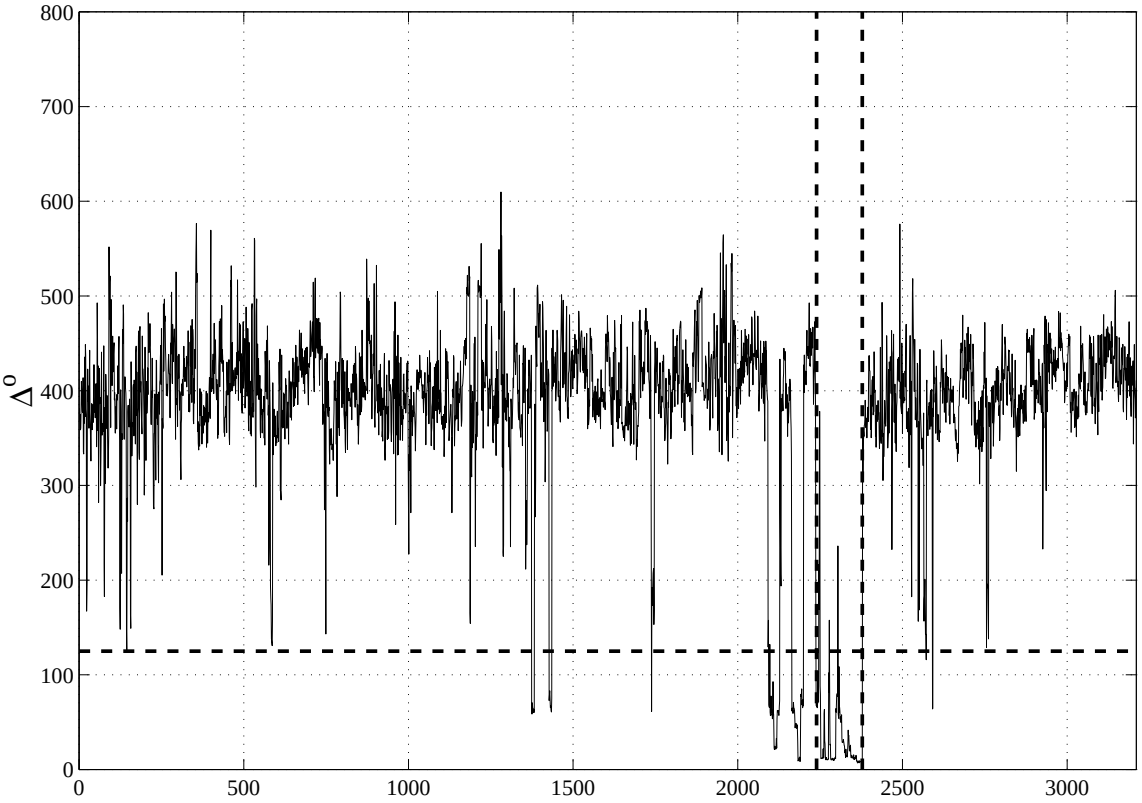

Figure 3.5: 5 GHz, h-pol, 20° normalized deviation from the mean ($\Delta°$). A value of $\Delta°$ below 125 (below the horizontal dashed line) is considered "flat". The time period between Oct. 4^{th} and Oct. 7^{th} is shown between the vertical dashed lines. x-axis values are only an index. This plot includes all wind directions.

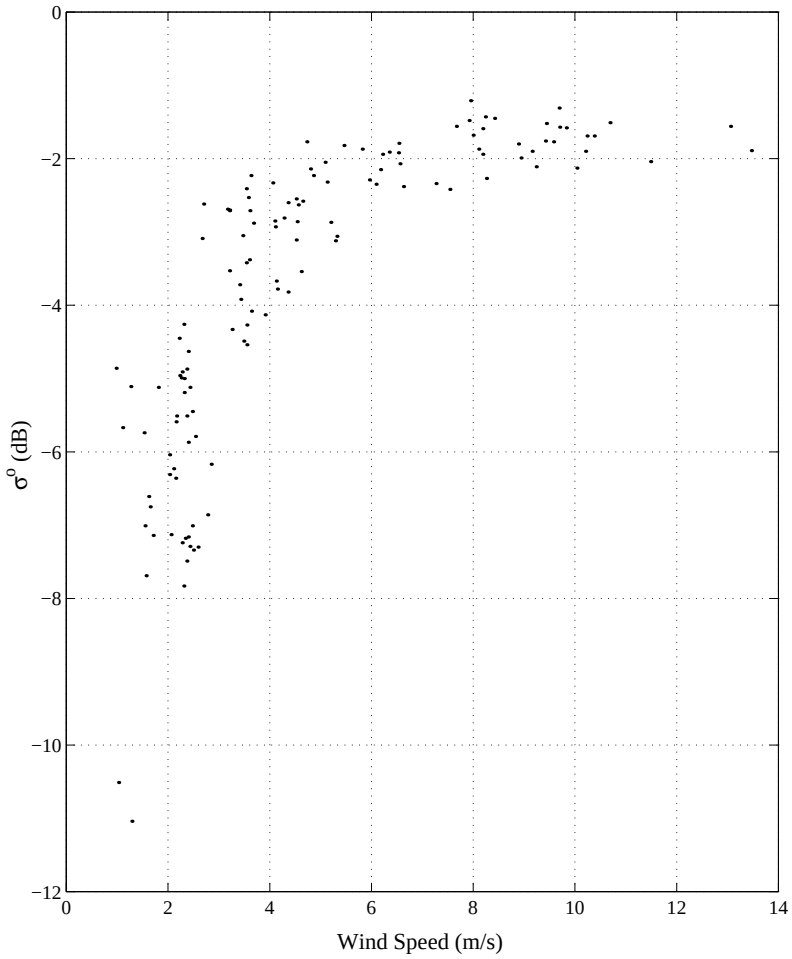

Figure 3.6: Data to be used for low wind speed rolloff quantification. Data is for 2 GHz, vertical polarization, upwind, and 20° incidence angle.

As an example of how this algorithm quantifies the low wind speed rolloff, consider the data presented in Fig. 3.6. The data presented is for 2 GHz, vertical polarization, upwind, and 20° incidence angle. The local polynomial regression algorithm estimates the p^{th} order polynomial regression fit for each data point using a kernel function to weight the nearby data. In this thesis, only a first order polynomial (linear) fit is calculated for each point.

The local linear regression algorithm yields the estimated regression fit and the estimated derivative of that fit. To accomplish this, a grid of equally spaced

points over which the estimation will be performed is determined. If the grid spacing is determined by

$$dx = \frac{10}{P}, \tag{3.2}$$

where P is the number of data points for that case, then the vector of grid points $\vec{x}$ (which corresponds to wind speed) is determined by

$$\vec{x}_n = \min(\vec{X}) + (n-1)dx \tag{3.3}$$

where $\vec{X}$ represents the wind speed values for that data case, and n ranges from 1 to n_{max} given by

$$n_{max} = \frac{\max(\vec{X}) - \min(\vec{X})}{dx}. \tag{3.4}$$

The estimated regression fit ($m(\vec{x})$) and the estimated derivative of that fit ($m'(\vec{x})$) at each grid point $\vec{x}_n$ are given by

$$\widehat{\beta}_n = (\mathcal{X}_n^T \mathcal{W}_n \mathcal{X}_n)^{-1} \mathcal{X}_n^T \mathcal{W}_n \vec{Y} = \begin{pmatrix} m(\vec{x}_n) \\ m'(\vec{x}_n) \end{pmatrix}. \tag{3.5}$$

In this equation,

$$\mathcal{X}_n = \begin{pmatrix} 1 & (\vec{X}_1 - \vec{x}_n) \\ 1 & (\vec{X}_2 - \vec{x}_n) \\ \vdots & \vdots \\ 1 & (\vec{X}_P - \vec{x}_n) \end{pmatrix} \tag{3.6}$$

where $\vec{x}_n$ is each grid point defined by Eq. (3.3) and $\vec{X}_{1...P}$ are the data points corresponding to wind speed. $\vec{Y}$ in Eq. (3.5) is the vector containing the σ° values corresponding to $\vec{X}$. $\mathcal{W}_n$ is given by

$$\mathcal{W}_n = \text{diag}\{K_h(\vec{X}_p - \vec{x}_n)\}. \tag{3.7}$$

K_h is an Epanechnikov kernel defined as

$$K_h(\vec{X}_p - \vec{x}_n) = \left(1 - \left(\frac{\vec{X}_p - \vec{x}_n}{h_x}\right)^2\right)_+ \tag{3.8}$$

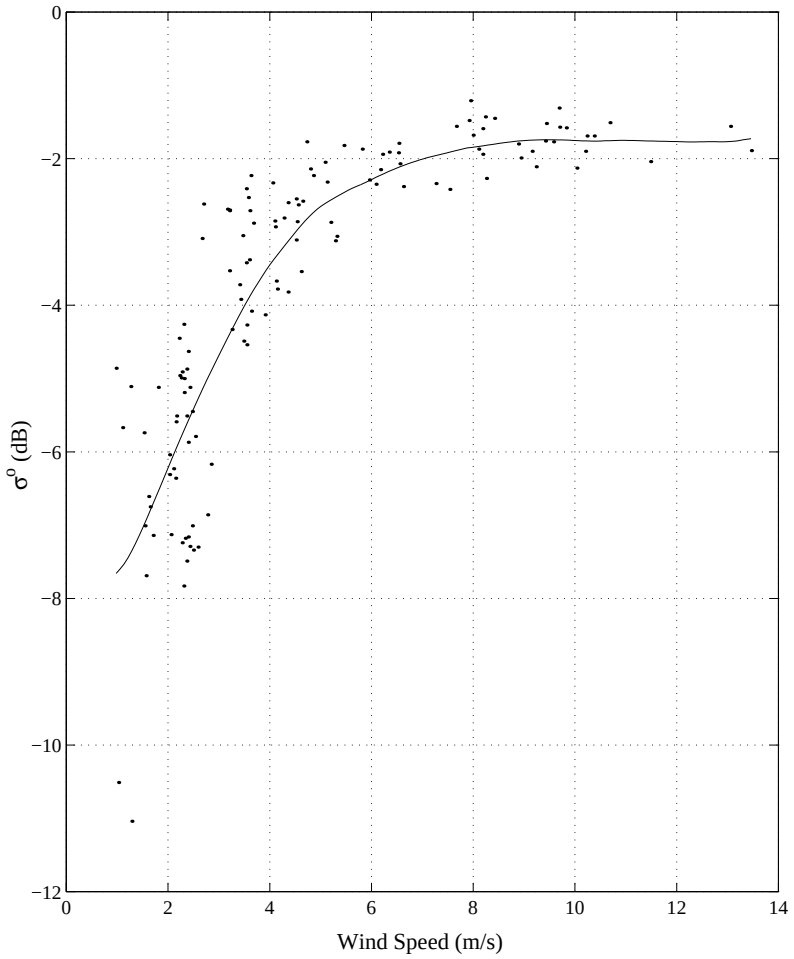

Figure 3.7: Local linear regression fit to the data in Fig. 3.6. Data is for 2 GHz, vertical polarization, upwind, and 20° incidence angle.

where the "+" indicates that only the positive values are used. h_x is the bandwidth parameter whose optimal value for the Epanechnikov kernel is given by [24]

$$h_x = 2.347\sigma_X N^{-1/5} \tag{3.9}$$

where N is the number of data points and σ_X is the standard deviation of the wind speed data vector $\vec{X}$.

Using the method described above, the local linear regression fit of the data in Fig. 3.6 is computed and shown in Fig. 3.7 as a solid curved line. Note that the estimate displays the same rolloff behavior as the data.

The next step in extracting the low wind speed rolloff estimate is to determine the point where the data starts to "roll off". This is done by fitting a line to the data at high wind speeds above the rolloff to determine the linear behavior of σ° versus wind speed. By extending this linear fit to lower wind speeds and comparing the actual low wind speed σ° values against this line, the rolloff can be more easily quantified (see Fig. 3.8).

The wind speed threshold at which the wind speed rolloff (Υ) occurs is determined as the wind speed closest to but smaller than 6 m/s at which the deviation of the estimated regression fit from the linear fit is farther than one fifth of the maximum distance between the mean of the five lowest data point (σ° value) and the σ° value predicted by the linear fit. This is expressed as

$$\Upsilon = \max_{\vec{x}<6m/s} \left[|\vec{y}_{i,est} - \vec{y}_{i,l}| > \left| \frac{\vec{y}_{i,l} - \overline{\vec{y}_{i,1:5}}}{5} \right| \right] \tag{3.10}$$

where $\vec{y}_{i,est}$ is the σ° value given by the linear regression estimation algorithm, $\vec{y}_{i,l}$ is the σ° value predicted by the linear fit to data at high wind speeds (over 6 m/s), and $\overline{\vec{y}_{i,1:5}}$ is the mean of the lowest five σ° values. An example of Υ is shown in Fig. 3.9 where $\Upsilon = 4.85$ m/s. All of YSCAT94 data is processed using the local linear regression algorithm. Plots similar to Fig. 3.9 for all data cases are provided in Appendix A.

This low wind speed rolloff was most noticable at lower incidence angles and lower wind speeds. At higher incidence angles, the data appears to follow a power law relationship for all wind speeds. For this reason, no low wind speed rolloff values are reported for 60° incidence angles. Table 3.1 summarizes (relatively) reliable Υ values for YSCAT94 data. Blank places in Table 3.1 indicate the rolloff was unreliable or undistinguishable. Υ tends to get lower toward higher incidence angles and higher frequencies.

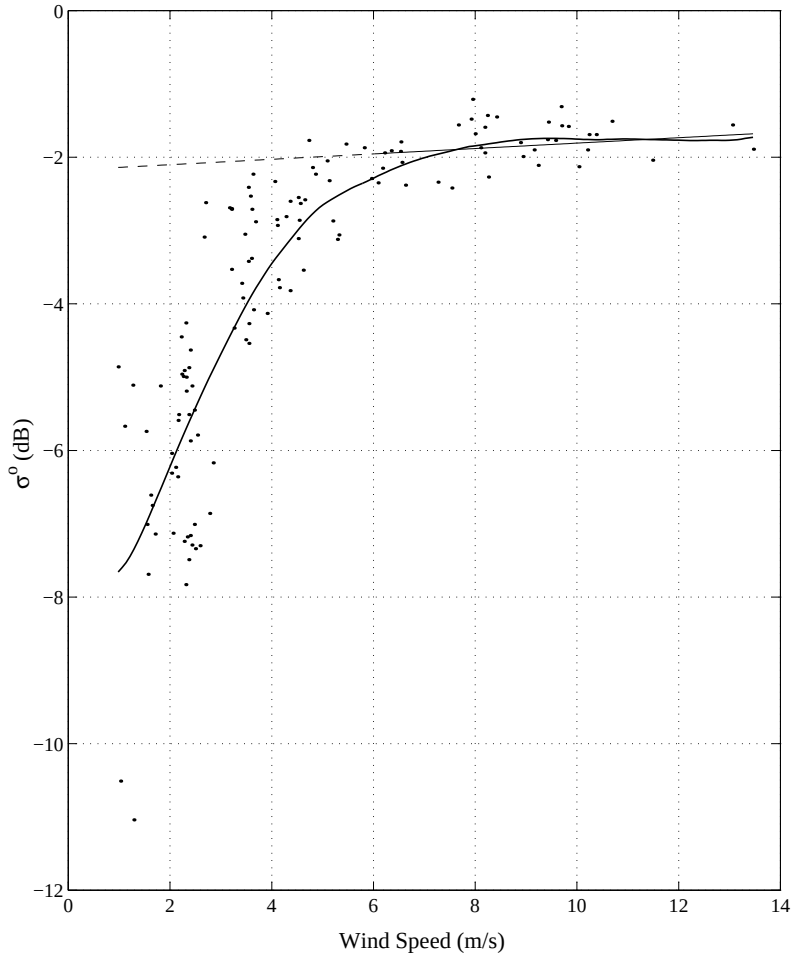

Figure 3.8: Epanechnikov smoothing and linear fit to data at high wind speeds. The linear fit is shown as the straight solid line with the part of the line left of 6 m/s indicated by a dashed line. The rolloff in the data and in the estimate is easily compared to this straight line. Result of the smoothing algorithm is indicated by the curved solid line. Data is for 2 GHz, vertical polarization, upwind, and 20° incidence angle.

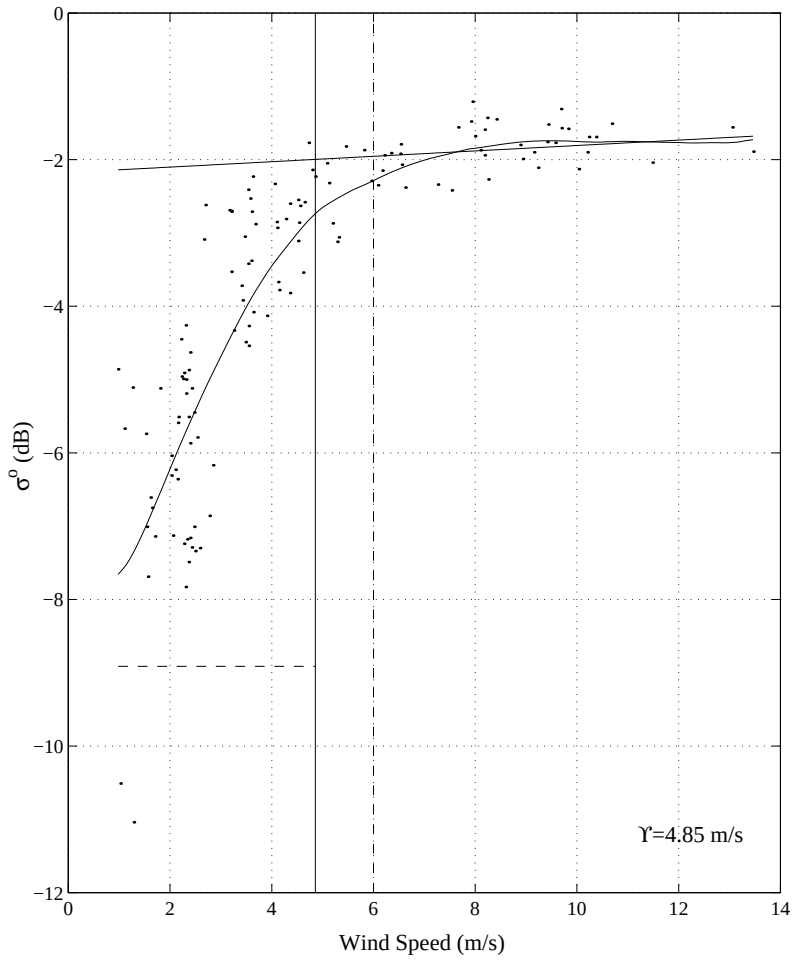

Figure 3.9: Low wind speed rolloff value, $\Upsilon = 4.85$ m/s. Υ is indicated by the solid vertical line. Solid curved line is the linear estimation regression fit. Dashed vertical line is high wind speed delineation at 6 m/s. Dashed horizontal line is $\overline{\vec{y}_{i,1:5}}$ for this case. Data is for 2 GHz, vertical polarization, upwind, and 20° incidence angle.

Table 3.1: Low Wind speed rolloff (Υ) summary. Blank entries indicate unreliable estimates. Values tend to be lower at higher incidence angles and higher frequencies. In each box are four entries, each corresponding to a differnent combination of polarization and direction (see key in top left box). "h/up" indicates a h-pol, upwind measurement. See Appendix A for a detailed plot of each data case.

	Frequency (GHz)											
h/up h/down v/up v/down			2			3.05			5.3			10.02			14.0	
0° (nadir)	5.16	5.00		4.28	4.53											
	4.86	5.46		5.59												
10°	4.17			4.17	4.65		3.98	3.58		4.1						
	4.61	2.97		5.32	3.34		3.64	4.02								
20°	4.49	3.1		3.02	4.15		4.74	3.86			3.93		3.69	4.19		
	4.85	3.18		4.53				2.95			4.01					
25°	3.63	3.54		4.81	5.02						2.99		3.66	3.88		
	4.87	2.69		3.86			3.15	3.15		3.75	3.92					
30°	3.08	4.44					2.7	3.58			2.54					
	3.51	3.41						3.84								
40°		3.55			2.87			3.09			3.76					
	2.87	4.61						3.56								
50°											2.79					

Chapter 4

Mean Wave Slope

In addition to studying trends in the Rayleigh/generalized log-normal distribution parameters as a function of wind speed, it is also useful to consider these parameters as a function of mean wave slope. While simultaneous weather records provide accurate wind speed measurements, wave slope must be calculated either from the radar return itself or from surface height measurements from an instrument such as a wave staff. Estimation of the mean wave slope has been accomplished based solely on radar return [25] [26]. However, for a good portion of YSCAT94's deployment period a wave staff array was in operation on the CCIW WAVES research platform. This eliminates the need to rely only on the radar return for mean wave slope estimates. Dr. Mark Donelan of CCIW made this wave staff data available to the Brigham Young University Microwave Earth Remote Sensing (MERS) lab to facilitate the research presented in this thesis.

Before proceeding with the calculation of the mean wave slope from wave staff data, some justification should be given as to why this slope estimate is used instead of using the variance of the slope distribution (σ_x^2) as a measure of the mean wave slope directly. It can be argued that σ_x^2, as the variance of the slope distribution (assumed to be Gaussian), is a more empirical measurement of the mean wave slope. However, in this thesis, the method outlined by C. Cox and W. H. Munk [7] is used to calculate the mean wave slope, mainly due to its stochastic and robust nature. Also, calculating a time-varying σ_x makes useful and direct comparison of the model parameters a_1, a_2, and C difficult, if not impossible. For these reasons, σ_x is considered constant

in this thesis and the Rayleigh/generalized log-normal distribution parameters are computed based on the mean wave slope calculated by the method in [7].

The first step in computing the mean wave slope using the method of [7] is to calculate the frequency spectrum of the sea surface. The frequency spectrum of the sea surface is calculated by splitting up contiguous 17 minute records of wave staff data into four overlapping sections 4096 points long. At the 10 Hz sampling rate this corresponds to approximately seven minutes of data for each estimate. A periodogram estimate is made using sixteen 256 point FFT's. Each of these sixteen windows is detrended to remove any slowly varying bias. All of the resulting sixteen periodogram estimates are then averaged to achieve the final periodogram. A sample frequency spectrum is shown in Fig. 4.1.

Once the frequency spectrum has been computed, the slope spectrum is computed using [7]

$$S(f_i) = \frac{(2\pi f_i)^4}{g^2}\Phi(f_i), \tag{4.1}$$

where f_i is the frequency, $S(f_i)$ is the slope spectrum, g is the gravitational acceleration constant, and $\Phi(f_i)$ is the surface height spectrum. A sample slope spectrum is presented in Fig. 4.2. The last step in the method is to calculate the mean wave slope from the slope spectrum [Eq. (4.1)] using the relation

$$s_x = \left[\frac{1}{N}\sum_{i=1}^{N}\frac{(2\pi f_i)^4}{g^2}\Phi(f_i)\right]^{\frac{1}{2}} \tag{4.2}$$

where N is the number of frequency bins.

Care must be taken when calculating Eq. (4.2) so the unreasonable slopes are not produced. By using only part of the spectrum specified by upper and lower cutoffs, this problem can be minimized. Upper and lower cutoffs must be decided upon before meaningful s_x (estimated by the mean wave slope) values are produced [27]. Because waves with periods on the order of five to eight seconds are quite rare [21], a lower cutoff in frequency corresponding to a period of ten seconds is used for YSCAT94 data. This choice for the lower cutoff is indicated by the left bold dashed line in Fig. 4.1.

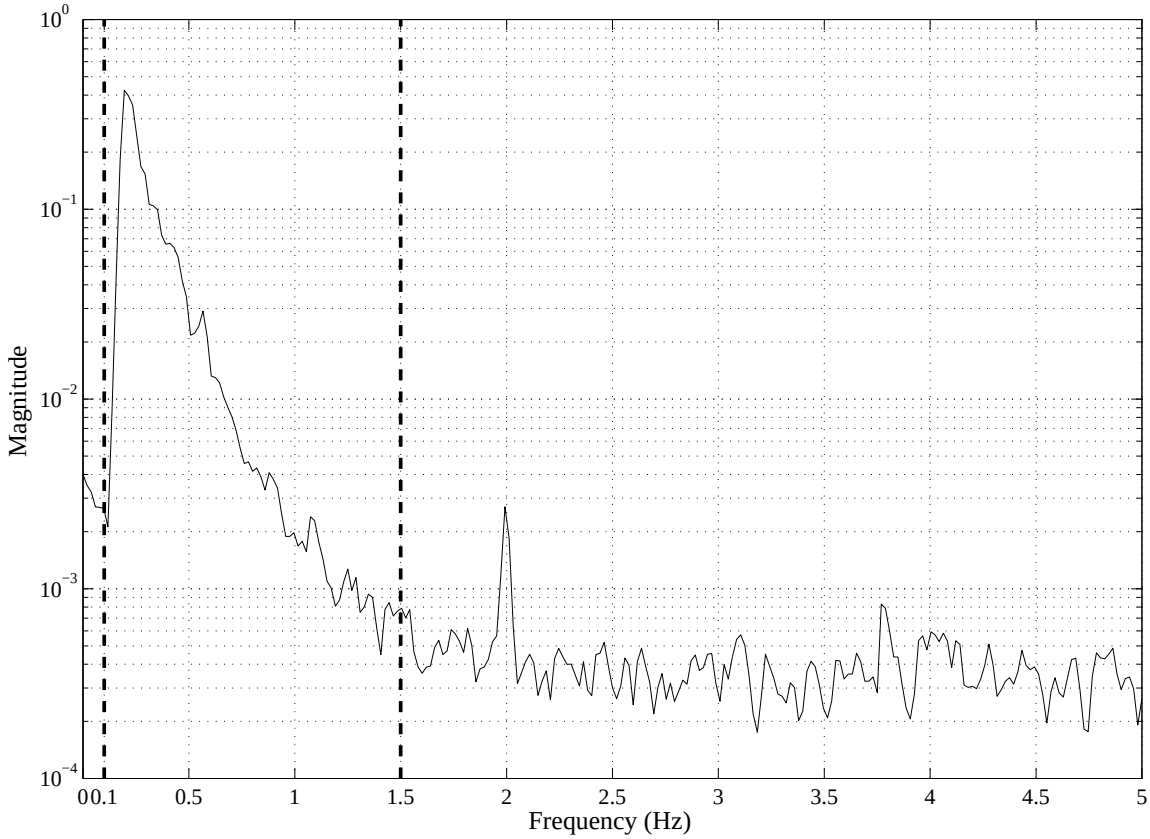

Figure 4.1: Wave height spectrum from wave staff data. Data is for 8:02-8:19 pm October 1, 1994. Upper (at 1.5 Hz) and lower (0.1 Hz) cutoffs are indicated by vertical dashed lines (see text for a discussion of frequency cutoffs).

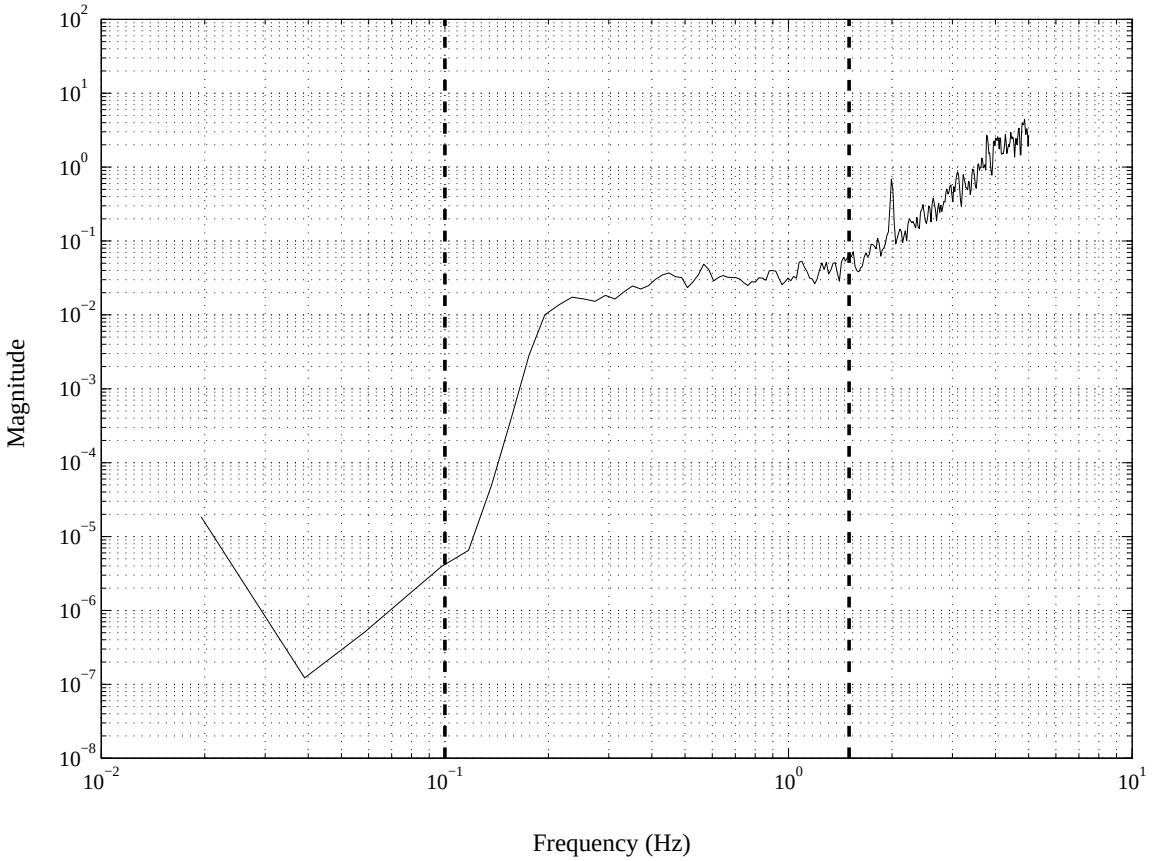

Figure 4.2: Mean wave Slope spectrum calculated from the surface height spectrum using Eq. (4.1). Upper (at 1.5 Hz) and lower (0.1 Hz) cutoffs are indicated by vertical dashed lines.

The relationship between frequency and wavelength is referred to as the dispersion relation. The deep water approximation of the dispersion relation is

$$\lambda = \frac{g}{2\pi f^2} \tag{4.3}$$

where λ is the wavelength, g is the acceleration of gravity, and f is the frequency of the wave. Thus a wave with a period of ten seconds ($f = \frac{1}{10} = 0.1s$) corresponds to a 156 m wavelength wave. The sizes of waves are impossible in such shallow water, so any energy below this frequency in the spectrum is untrustworthy.

The upper cutoff was chosen to be at 0.67 seconds (or f=1.5 Hz, λ=0.7 m) principally because waves much shorter than this do not contribute to the large scale wave slope as much as the much more energetic longer wavelength waves. Further, 0.7 m is on the same order as the footprint size of YSCAT.

The upper and lower cutoffs are illustrated as dashed lines in Fig. 4.1. Equation (4.2) must be modified to accommodate for upper and lower cutoffs as

$$s_x = \left[\frac{1}{N - M + 1} \sum_{i=M}^{N} \frac{(2\pi f_i)^4}{g^2} \Phi(f_i) \right]^{\frac{1}{2}} \tag{4.4}$$

where N is the frequency bin corresponding to the upper cutoff, and M is the frequency bin corresponding to the lower cutoff. In this thesis, s_x is calculated from wave staff measurements using Eq. (4.4).

Most of the energy in the spectrum is within the range of $0.1 < f < 1.5$ Hz (*c.f.* Fig. 4.1). The wave slope values for the 24-hour period starting November 13, 1994 at 12:28 pm are shown in Fig. 4.3, while the total histogram of mean wave slope values over the entire YSCAT94 deployment period is given in Fig. 4.4.

Using values calculated by the method described above, YSCAT94 data is sorted according to wave slope in addition to wind speed. To determine the location and position of mean wave slope bins, the data for 5 GHz, vertical polarization, 20° incidence angle is shown as a scatterplot in Fig. 4.5. While a definite relationship between wind speed and mean wave slope is observable for smaller mean wave slopes, there are many data with mean wave slopes greater than that suggested by this relationship. These data points strengthen the theory that, under certain conditions,

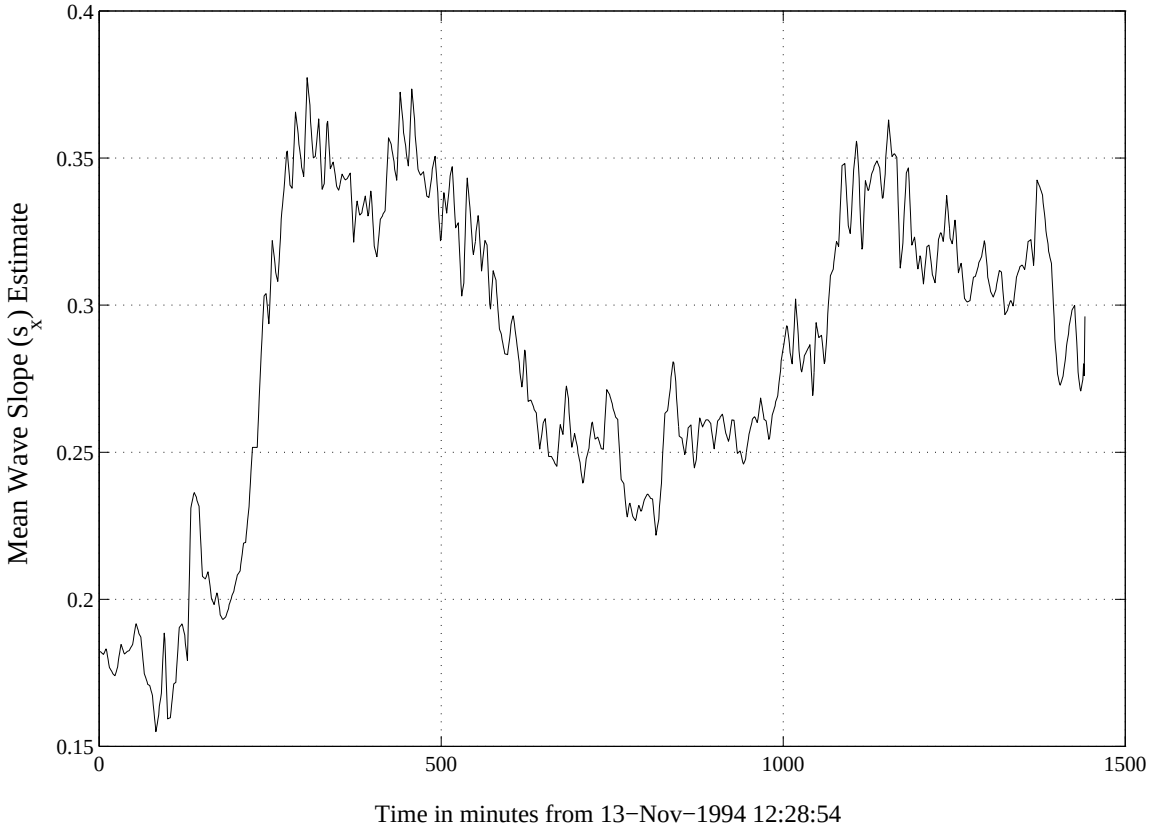

Figure 4.3: Time-varying mean wave slope estimate for an extended period. Data is for the 24-hour period starting November 13, 1994 at 12:28 pm.

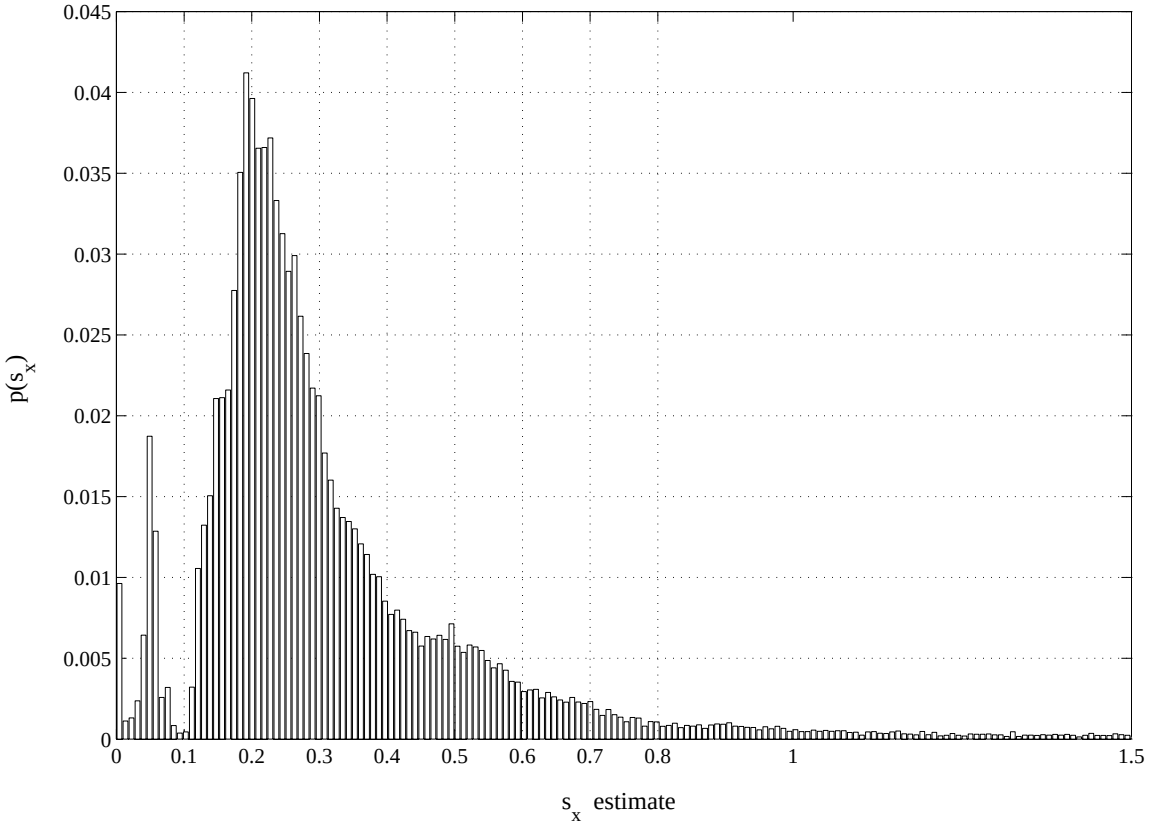

Figure 4.4: Slope distribution for the entire 6 months of YSCAT94 data.

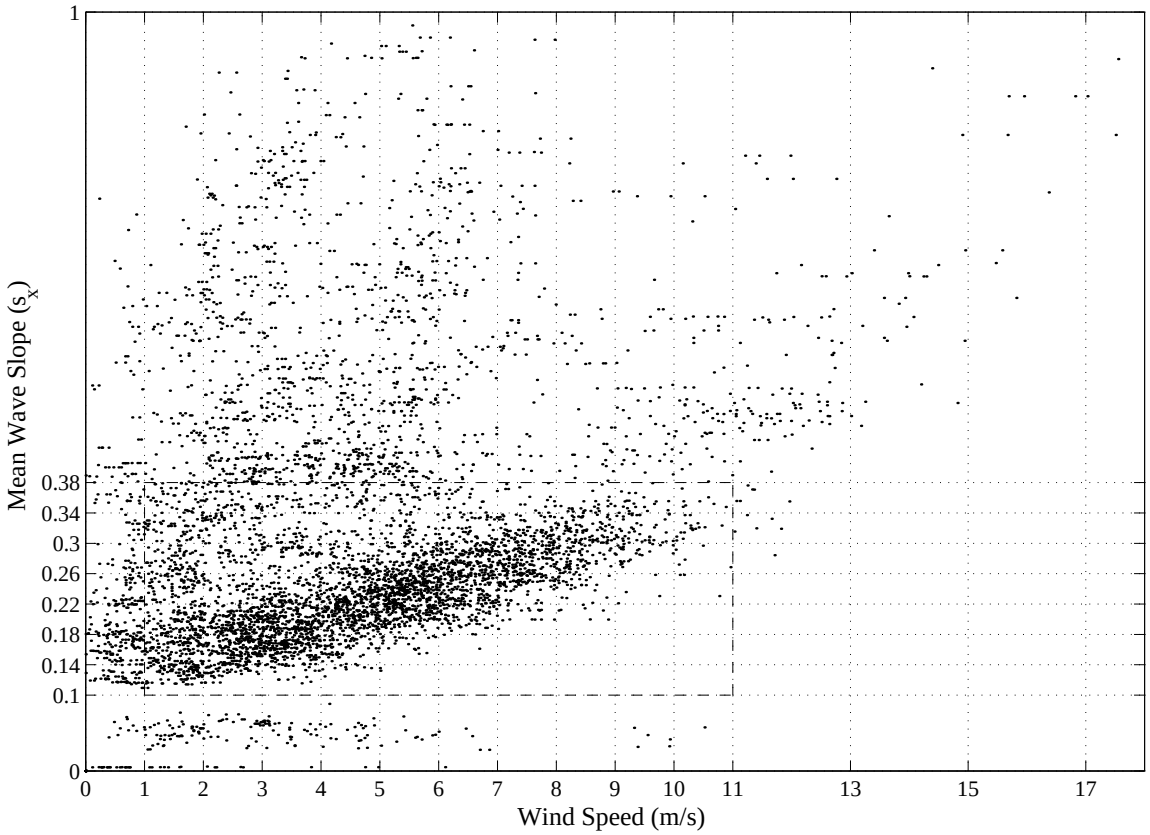

Figure 4.5: Wind speed vs. mean wave slope for 5 GHz, v-pol, 20° incidence angle. Includes data at all wind directions. Data inside the dashed box (1-10 m/s wind speed and 0.1-0.38 mean wave slope) is considered in this thesis. Note the wide spread of wind speeds for a given mean wave slope, especially in the dark band where the majority of the data lies.

mean wave slope is not directly related to wind speed. For example, a storm generates large waves which can propagate to calmer areas with lower wind speeds.

The region in Fig. 4.5 in which wind speed and mean wave slope have a distinct relationship is of primary concern. Therefore, bins based on this estimate of wave slope are delineated at successive 0.04 increments with data between 0.0 and 0.1 discarded. Wave slope is classified according to the seven cases of 0.1-0.14, 0.14-0.18, 0.18-0.22, 0.22-0.26, 0.26-0.30, 0.30-0.34, and 0.34-0.38. Results of this analysis are given later in Section B.

Chapter 5

YSCAT94 Power Distributions

5.1 Introduction

The most common model for sea scattered radar return at moderate incidence angles is the composite model. The composite model assumes that the sea surface is composed of small independent patches each of which has a normalized radar cross section (σ°) given by small perturbation theory (SPT) as,

$$\sigma^\circ = 16\pi k_m^4 |g_{pp}(\theta_i)|^2 \Psi(2k_m \sin\theta_i, 0) \tag{5.1}$$

where σ° is the normalized radar cross section, θ_i is the incidence angle, $g_{pp}(\theta_i)$ is a polarization dependent reflection coefficient with pp being hh or vv, k_m is the microwave wavenumber ($\omega\sqrt{\mu\epsilon}$ or $\frac{2\pi}{\lambda}$), and Ψ is the wave height spectral density [21].

These patches of relatively small waves (on the order of centimeters), are modulated, or tilted, by larger waves typically on the order on meters. Consequently, the radar backscatter distribution depends on the distribution of the larger waves present. This relationship is captured in the compound probability model. Following Gotwols and Thompson [8], this model is developed and compared to YSCAT94 backscatter distributions in this chapter.

5.2 Compound Probability Model

The compound probability model, originally proposed by Valenzuela and Laing [28], considers the aforementioned two scales of waves separately. Radar backscatter characteristics of the sea surface depend on waves on the order of or smaller than the radar footprint (the Bragg waves) and on the underlying tilt imposed from waves

with wavelengths much larger than the radar footprint. For the former case of shorter wavelength waves, σ° is considered constant but the amplitude of the return varys yielding the conditional probability $p(a|\sigma^\circ)$. For the latter case of longer wavelength waves, due to the relatively large scale of the waves, σ° is allowed to vary with probability $p(\sigma^\circ)$. We note that σ° is a function of the local wave slope. Thus the total distribution may be expressed as a conditional probability

$$p(a) = \int_0^\infty p(a|\sigma^\circ)p(\sigma^\circ)\ d\sigma^\circ. \tag{5.2}$$

The probability of measuring a given backscatter power a can be calculated by considering distributions on the orders of both scales.

5.2.1 Distribution of $p(a|\sigma^\circ)$

When the scatterometer footprint is large enough to encompass many patches of small waves, the scattered field should approach a normal distribution via the central limit theorem. In this case, the amplitude a of the radar return should be Rayleigh distributed [29]. On the other hand, when the scatterometer footprint is on the order of the intermediate to large size waves, this assumption is less valid, but should still hold if the footprint encompasses several correlation lengths. This conclusion has been debated [30] [31], with Thompson and Gotwols [8] concluding that for their data, $p(a|\sigma^\circ)$ was indeed Rayleigh distributed. The method used in [8] to arrive at this conclusion is to remove any underlying $p(\sigma^\circ)$ variation by normalizing successive 1/3 s amplitude records (corresponding to 333 samples for their data set) by dividing by the RMS amplitude of that 1/3 s record. While YSCAT's operational parameters, and most importantly footprint size, are similar to [8], YSCAT's backscatter sampling frequency of 10 Hz is too low to test its data by removing the underlying $p(\sigma^\circ)$ dependence in this way. Therefore, because of the similarity, the present analysis assumes that $p(a|\sigma^\circ)$ is Rayleigh distributed based on the theoretical justification above and the results in [8]. Because their analysis was for mid-range

incidence angles, this assumption may be less valid for 0°, 10°, and 60° incidence angles. In Section 5.6 it is shown that $p(a|\sigma^\circ)$ may be Weibull distributed under certain conditions.

The form of $p(\sigma^\circ)$ is shown in the next section to closely follow a generalized log-normal distribution. Once these two distributions are known, a form for $p(a)$ can be calculated by Eq. (5.2) and compared with empirical data collected during the YSCAT94 experiment.

5.2.2 Distribution of $p(\sigma^\circ)$

Referring back to Eq. (5.1), in order to completely determine σ°, expressions must be found for the reflection coefficients g_{pp} and the wave height spectral density $\Psi(2k_m \sin\theta_i, 0)$. From Plant [32] we find the reflection coefficients to be,

$$|g_{vv}(\theta_i)|^2 = \frac{\cos^4\theta_i(1+\sin^2\theta_i)^2}{(\cos\theta_i + 0.111)^4} \tag{5.3}$$

and

$$|g_{hh}(\theta_i)|^2 = \frac{\cos^4\theta_i}{(0.111\cos\theta_i + 1)^4} \tag{5.4}$$

where θ_i is the incidence angle between the radar and the water surface and the empirical permittivity of water ($\epsilon_r \approx 81$) is used.

Various wave height spectrums have been proposed and used (see Chapter 2). The wave height spectrum used in this thesis is calculated from from *in situ* wave staff measurements at Lake Ontario by Donelan et al [18]. The Donelan spectrum can be expressed as,

$$\Phi(\omega) = \alpha g^2 \frac{\omega^{-4}}{\omega_p} e^{-\frac{\omega_p}{\omega}} \gamma^\Gamma \tag{5.5}$$

$$\Gamma = e^{-(\omega-\omega_p)^2/2\sigma^2\omega_p^2} \tag{5.6}$$

where ω_p is the spectral peak, α is the equilibrium range parameter, γ is the peak enhancement factor, and σ is the peak width factor. The parameter α is given by

$$\alpha = 0.006(U\cos\theta/c_p)^{0.55} \tag{5.7}$$

where U is the wind speed and c_p is the phase velocity of the peak frequency wave. The peak enhancement factor (γ) is given by

$$\gamma = 1.7 + 6\ln(U/c_p). \tag{5.8}$$

The peak width parameter is given by

$$\sigma = 0.08\left(1 + \frac{4}{(U\cos\theta/c_p)^3}\right) \tag{5.9}$$

and the ratio $U\cos/c_p$ is given by

$$U\cos\theta/c_p = 11.6\tilde{x}^{-0.23} \tag{5.10}$$

where $\tilde{x}$ is the non-dimensional fetch.

The fetch (the distance over which the wind blows over the water) is approximated as a constant 6 km at the CCIW site [21]. Using the spectrum given by Eq. (5.6) and the reflection coefficients [Eqs. (5.3) and (5.4)] above, a plot of σ° versus incidence angle is generated and shown in Figure 5.1.

Figure 5.1 relates σ° to θ_i, the local incidence angle. Another representation is to plot σ° versus mean wave slope instead. The mean wave slope is related to θ_i (the angle between the incident radar wave and the mean level of the water) and the nominal incidence angle ($\theta_\circ$, the angle between the incident radar wave and the tilted water surface) by

$$\chi + \theta_i = \theta_\circ \tag{5.11}$$

where

$$\tan(\chi) = -s_x. \tag{5.12}$$

and where s_x can be expressed as the "rise" over the "run" as illustrated in Fig. 5.2. In Fig. 5.3 the radar cross section is plotted versus mean wave slope in a manner similar to Fig. 5.1.

Gotwols and Thompson [8] noted the highly linear nature of the h-pol return and the quadratic nature of the V-pol return over mid-range incidence angles (20° -

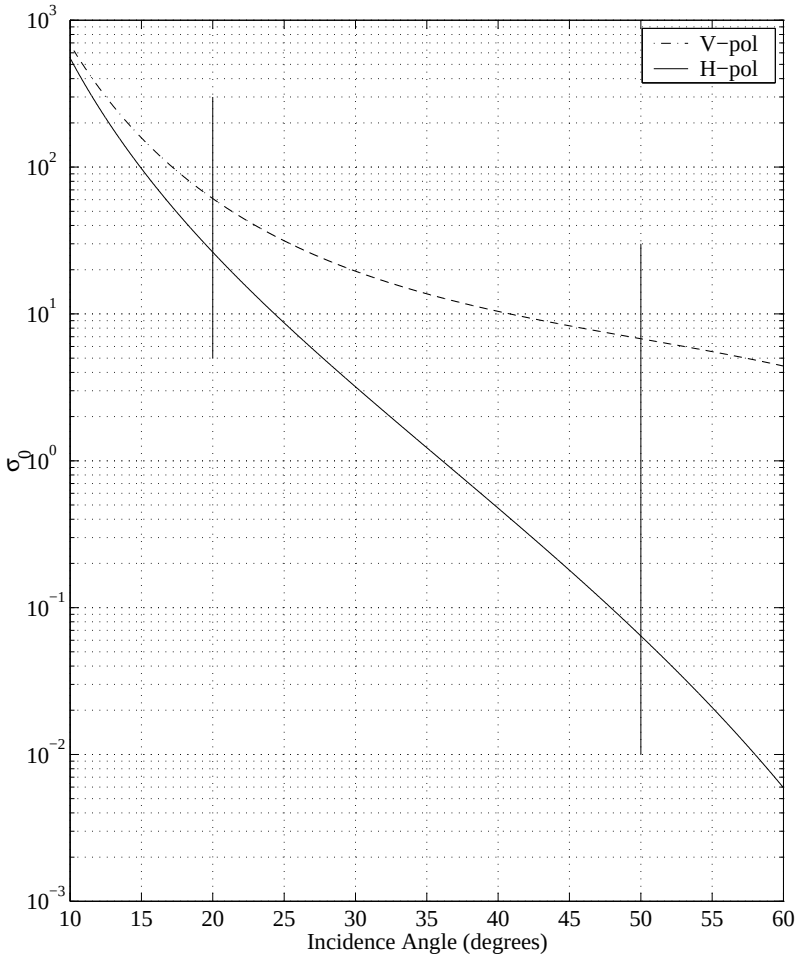

Figure 5.1: Incidence angle versus σ° plotted from the Donelan spectrum. Frequency is 14GHz, wind speed is 8m/s, fetch is 6 km, and λ_p=20 m. Note the linear nature of σ° for h-pol return, and the quadratic nature of σ° for v-pol. The vertical lines denote moderate incidence angles between 20° and 50°.

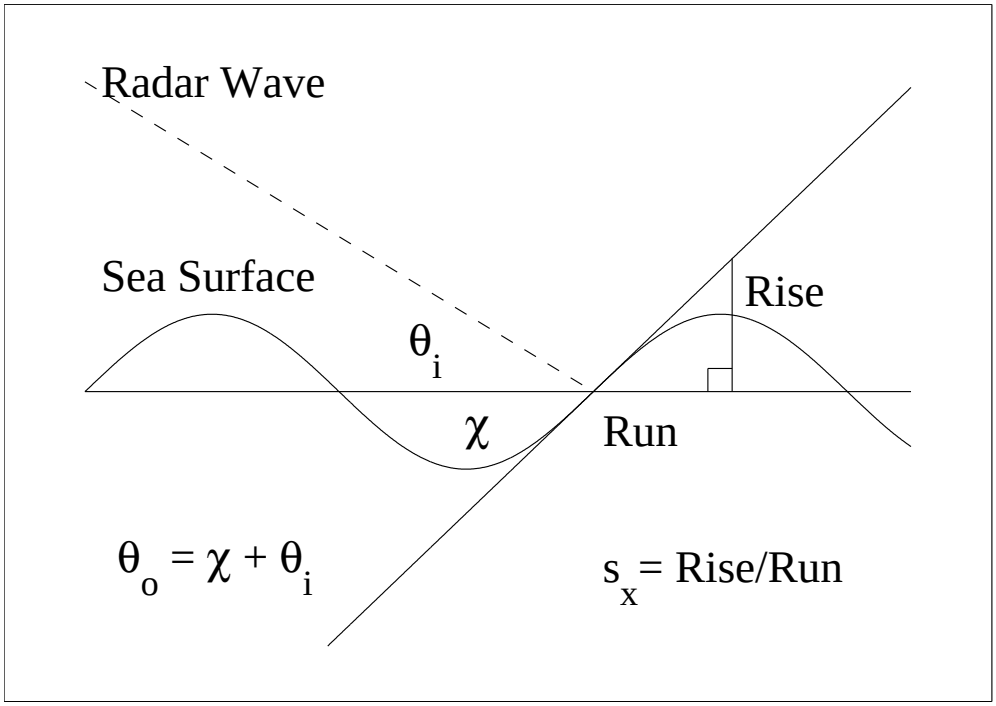

Figure 5.2: Relationship between χ, θ_i, and θ_0. Mean wave slope can be described by the "rise" over the "run".

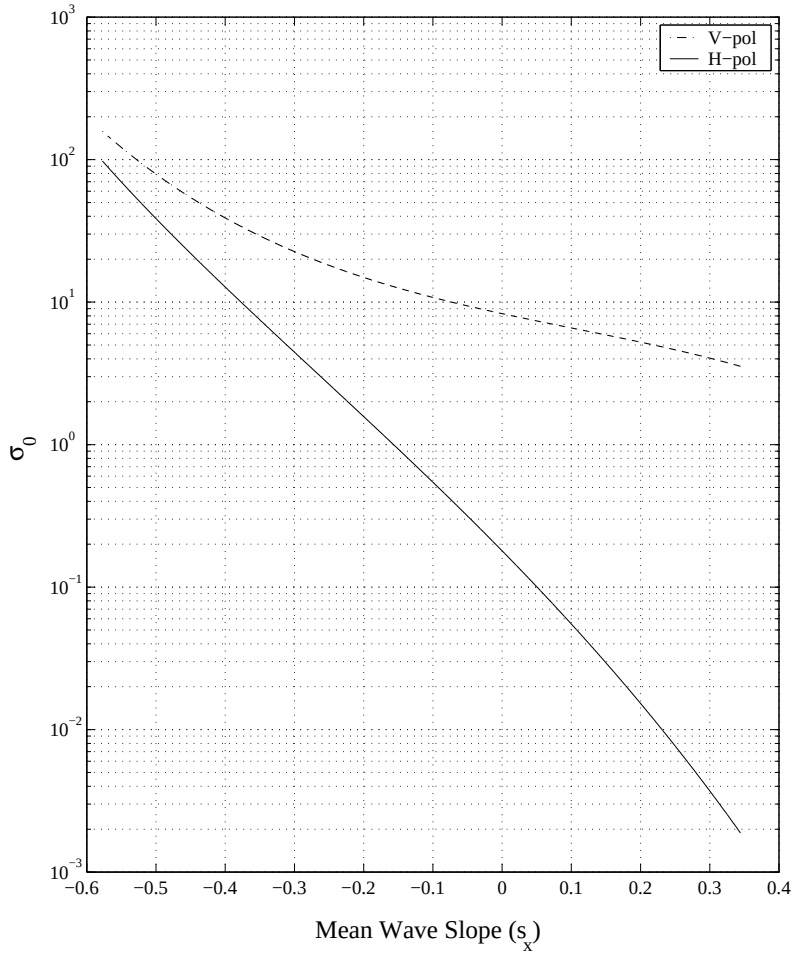

Figure 5.3: Mean wave slope versus σ° plotted from the Donelan spectrum. Frequency is 14GHz, wind speed is 8m/s, fetch is 6 km, and λ_p=20 m. Note the linear nature of σ° for h-pol return, and the quadratic nature of σ° for v-pol.

50°). As a result, they proposed a quadratic model (in log space) for σ° versus mean wave slope,

$$\sigma_p^\circ = Ce^{a_1 s_x + a_2 s_x^2} \tag{5.13}$$

where p is either v or h for v-pol and h-pol respectively. In theory, $a_2 = 0$ for σ_h° and $a_1, a_2 \neq 0$ for σ_v°.

This model for σ_p° is justified by the close agreements of the first and second order fits to σ° versus mean wave slope as can be seen from Fig. 5.3. Using Eq. (5.13) we can find an expression for $p(\sigma_p^\circ)$ by the transformation law for probability density

$$p(\sigma_p^\circ) = \frac{p(s_x)}{|d\sigma_p^\circ/ds_x|}. \tag{5.14}$$

and assuming $p(s_x)$ is normally distributed with variance σ_x^2 and zero mean. Noting that

$$\begin{aligned} |d\sigma_p^\circ/ds_x| &= C(a_1 + 2a_2 s_x)e^{a_1 s_x + a_2 s_x^2} \\ &= (a_1 + 2a_2 s_x)\sigma_p^\circ \end{aligned} \tag{5.15}$$

and

$$s_x = \frac{-a_1 \pm \sqrt{a_1^2 + 4a_2 ln(\frac{\sigma_p^\circ}{C})}}{2a_2}, \tag{5.16}$$

it can be shown that for horizontal polarization (a_2=0) [8],

$$p(\sigma_h^\circ) = \frac{1}{a_1 \sigma_x \sigma_h^\circ \sqrt{2\pi}} \exp\left\{\frac{-(ln\sigma_h^\circ - lnC)^2}{2a_1^2\sigma_x^2}\right\} \tag{5.17}$$

and for vertical polarization ($a_1, a_2 \neq 0$),

$$p(\sigma_v^\circ) = \frac{1}{\sigma_x(a_1 + 2a_2 s_x)Ce^{a_1 s_x + a_2 s_x^2}\sqrt{2\pi}} \exp\left\{\frac{-(s_x)^2}{2\sigma_x^2}\right\} \tag{5.18}$$

with s_x as defined by Eq. (5.16) and for the zero mean case. The probability distribution function (pdf) in Eq. (5.17) is referred to as the log-normal distribution. Equation (5.18), which describes the distribution for the case of $a_1, a_2 \neq 0$, has no common name but will be referred to as the generalized log-normal and is the focus of the next section. Equations (5.17) and (5.18) can serve as the backscatter distribution $p(\sigma_p^\circ)$ for a given slope distribution for the case of h-pol and v-pol respectively.

For the more general case of $a_1, a_2 \neq 0$, assuming $p(a|\sigma^\circ)$ to be Rayleigh distributed and expressing Eq. (5.18) in terms of σ°, Eq. (5.2) becomes

$$\begin{aligned} p(a) &= \int_0^\infty \underbrace{p(a|\sigma^\circ)}_{\text{Rayleigh}} \underbrace{p(\sigma^\circ)}_{Eq.\ (5.18)} \, d\sigma^\circ \\ &= \int_0^\infty \underbrace{\frac{2a\sigma^\circ}{e^{a^2\sigma^\circ}}}_{p(a|\sigma^\circ)} \underbrace{\left(\frac{\exp\left(\frac{a_1^2}{4\sigma_x^2 a_2^2}\right) \exp\left(\pm \frac{a_1\sqrt{a_1^2 + 4a_2 \ln\frac{\sigma^\circ}{C}}}{4\sigma_x^2 a_2^2}\right) \left(\frac{\sigma^\circ}{C}\right)^{\frac{1}{2a_2\sigma_x^2}}}{\sigma_x \sigma^\circ \sqrt{\pi}\sqrt{a_1^2 + 4a_2 \ln\frac{\sigma^\circ}{C}}} \right)}_{p(\sigma^\circ)\ \ [Eq.\ (5.18)]} d\sigma^\circ \end{aligned} \quad (5.19)$$

where polarization dependence has been dropped. Using Eqs. (5.13) and (5.14), Eq. (5.19) may be written as

$$p(a) = \int_{-\infty}^{\infty} \underbrace{2aCe^{a_1 s_x + a_2 s_x^2} e^{-a^2 C e^{a_1 s_x + a_2 s_x^2}}}_{p(a|\sigma_\circ(s_x))} \underbrace{\frac{e^{\frac{-s_x^2}{2\sigma_x^2}}}{\sqrt{2\pi}\sigma_x}}_{p(s_x)} ds_x. \quad (5.20)$$

Equation (5.20) provides a model which describes the amplitude pdf of backscatter from the sea surface at mid-range incidence angles. More is said about this distribution in Section 5.3.3, including an explanation of the techniques used to fit this integral equation to empirical histograms.

The assumption that the wave slopes are normally distributed is common when discussing backscatter distributions and necessary in this case in order to produce a tractable model for sea surface backscatter. To investigate the wave slope distribution at the CCIW site, wave staff data collected from a wave staff array installed on the CCIW tower in the summer of 1994 is used to calculate the wave slope distribution. A representative seventeen minute record of 10 Hz wave staff measurements is examined in Fig. 5.4. The slope is determined as the difference of successive samples. The resulting instantaneous slopes are binned into a histogram as illustrated in Fig. 5.4. A best fit ($\mathbf{L_2}$ norm) normal distribution is shown overlaid as a dashed line. As can be seen, for YSCAT94 data, the slope distribution is reasonably well approximated by

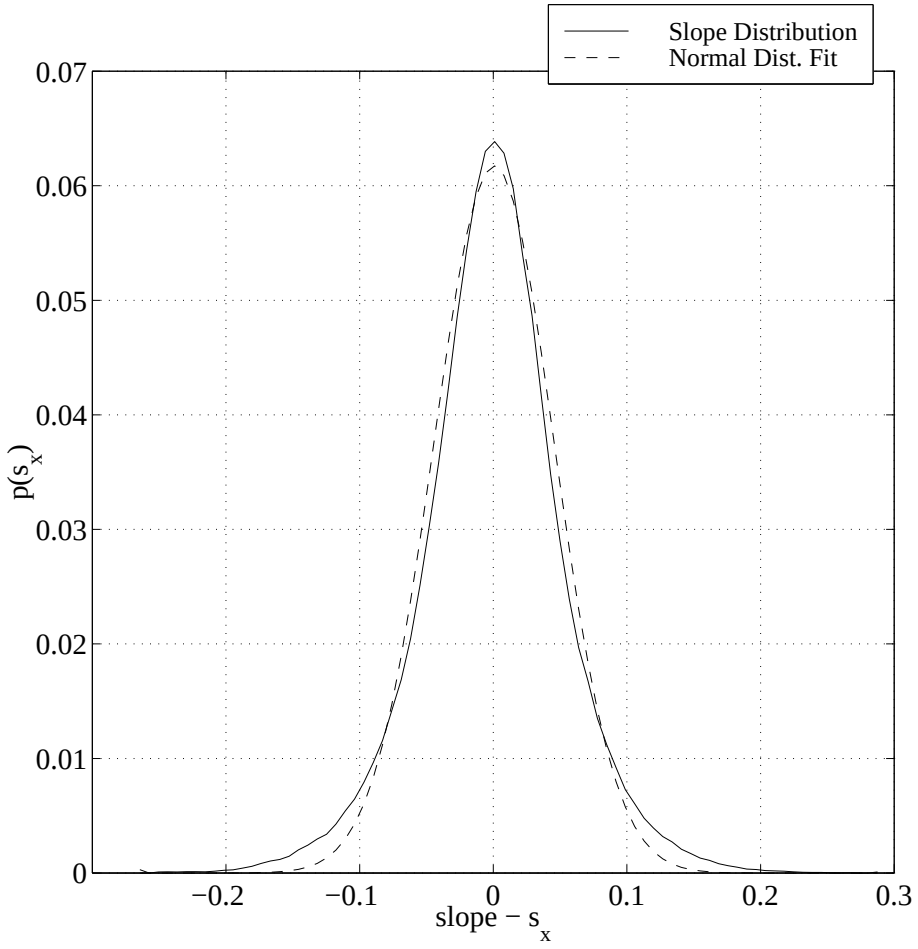

Figure 5.4: Typical slope distribution of YSCAT94 17 minute record. Data is for August 10, 10:01-10:18 A.M, 1994. σ_x=0.04515

a normal distribution. A Gram-Charlier series gives a more exact description of the slope distribution [33] and accounts for the peaked nature of the slope distribution when compared to a Gaussian, but in this thesis it is assumed that the wave slopes are indeed normally distributed.

In principle, real-time slope distribution variances (σ_x^2) can be calculated from wave staff measurements taken at the CCIW tower. However, in the present analysis, slope variance parameters are not calculated for each separate data case due to the lack of wave staff data for the full length of the YSCAT94 experiment and the desire to compare fitted distribution parameters a_1, a_2, and C. Variance parameters may be calculated in future analysis of YSCAT94 data, but for the purposes of this thesis $\sigma_x = 0.0914$ is used. The computed σ_x for the case of Fig. 5.4 is σ_x=0.04515 which is for calmer conditions than were normally present at the site during the YSCAT94 experiment. As discussed in Section 5.3, this dies not affect the generality of the results.

5.3 Distributions Definitions

5.3.1 The Log-normal Distribution

The expression for $p(\sigma_h^\circ)$ developed in Section 5.2.2 yields the log-normal distribution for the case of $a_2 = 0$ [Eq. (5.17)], and the generalized log-normal distribution for the case of $a_1, a_2 \neq 0$ [Eq. (5.18)]. The log-normal distribution is a common distribution with uses in many branches of science such as chemistry, estimation, and, as in the present case, microwave scatterometry. Two parameters dictate the shape of the log-normal distribution: in this case C and a_1. σ_x and a_1 combine to yield one parameter as can be seen by noting that a_1 and σ_x appear only as the combination $a_1\sigma_x$ in Eq. (5.17). Thus, even though σ_x is fixed in this thesis at 0.0914, Eq. (5.17) does not lose generality since a_1 is still a free parameter. A representative log-normal distribution fit to YSCAT94 data is shown in Fig. 5.5(a) with the mean identified by a dotted line. In the case of Eq. (5.17), the first moment (mean) of the log-normal

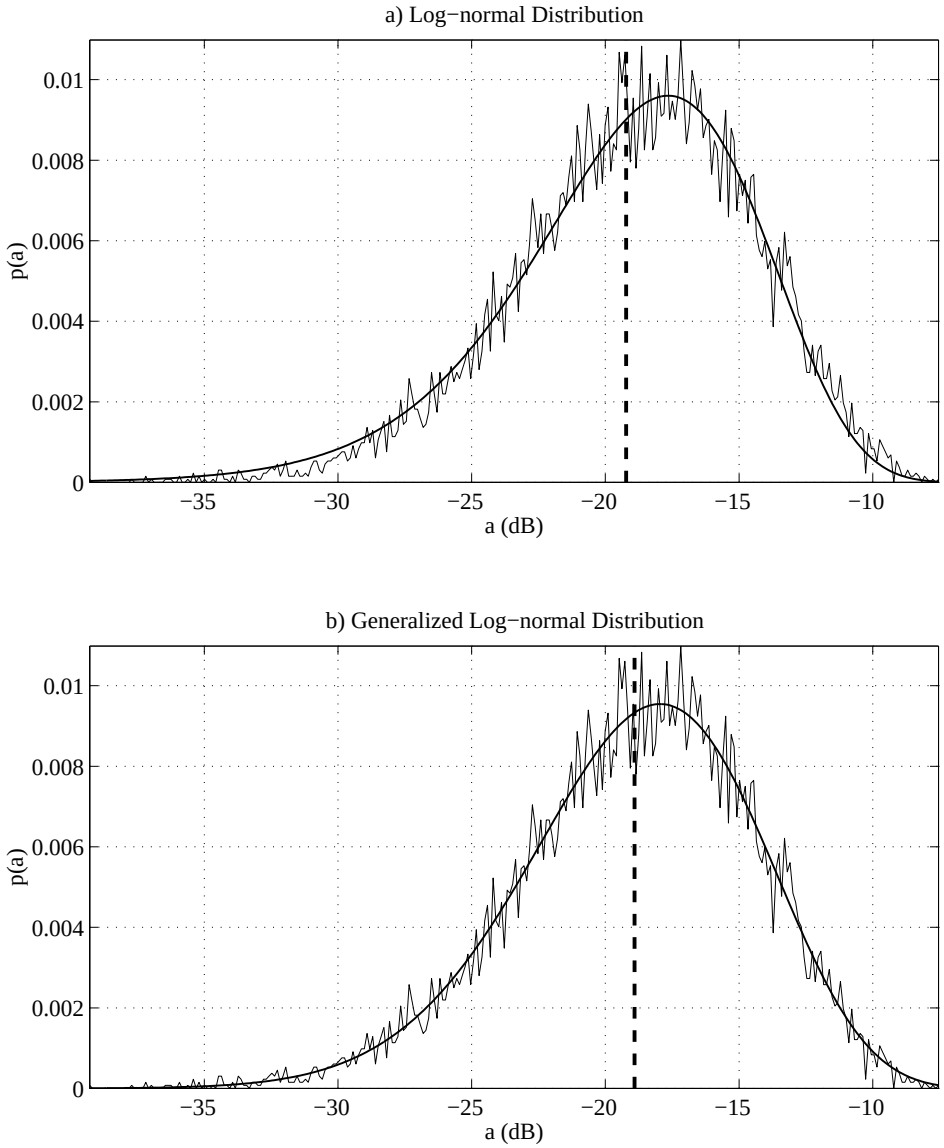

Figure 5.5: a) Log-normal distribution fit to YSCAT94 data. Log-normal distribution parameters are a_1=-2.621. σ_x=0.0914, and C=-18.698. The mean of this distribution is -19.22 dB (empirical). Using Eq. (5.21) μ_{ln}=-19.243 (indicated by the bold dashed line. Wavy line is the normalized histogram of the data for this case. Bold curved line is the fitted log-normal distribution. b) Generalized log-normal distribution fit to YSCAT94 data. Distribution parameters are a_1=2.603. a_2=-1.361, σ_x=0.0914, and C=-18.597. The fitted distribution is -19.22 dB (empirical). Using Eq. (5.27) μ_{2ln}=-18.905. Data is for 2 GHz, h-pol, downwind, 20° incidence angle, and wind speed 3m/s. Bold curved line is the fitted generalized log-normal distribution.

distribution is

$$\begin{aligned}
\mu_{ln} &= \lim_{a\to\infty} \int_0^a \frac{1}{\sigma_x a_1 \sqrt{2\pi}} \exp\left\{-\frac{(\ln\frac{\sigma_h^\circ}{C})^2}{2a_1^2\sigma_x^2}\right\} d\sigma_h^\circ \\
&= \lim_{a\to\infty} -\frac{1}{2} C e^{\frac{\sigma_x^2 a_1^2}{2}} \operatorname{erf}\left\{\frac{\sigma_x^2 a_1^2 - \ln\frac{\sigma_h^\circ}{C}}{\sigma_x a_1 \sqrt{2}}\right\}\Bigg|_{\sigma_h^\circ=0}^{\sigma_h^\circ=a} \\
&= C e^{\frac{\sigma_x^2 a_1^2}{2}} \qquad (5.21)
\end{aligned}$$

and the variance is

$$\begin{aligned}
\sigma_{ln}^2 &= \lim_{a\to\infty} \int_0^a \frac{\sigma_h^\circ}{\sigma_x a_1 \sqrt{2\pi}} \exp\left\{-\frac{(\ln\frac{\sigma_h^\circ}{C})^2}{2a_1^2\sigma_x^2}\right\} d\sigma_h^\circ \\
&= C^2(e^{2\sigma_x^2 a_1^2} - e^{\sigma_x a_1}). \qquad (5.22)
\end{aligned}$$

Figure 5.5(a) shows a log-normal distribution fit to a YSCAT94 backscatter distribution (in log space) for the case of 2 GHz, h-pol, downwind, 20° incidence angle, and wind speed 3m/s. The bold dashed line indicates the mean of the regular log-normal distribution. A generalized log-normal fit is also included as Fig. 5.5(b) with its mean also shown as a dashed line.

5.3.2 Generalized Log-normal Distribution

The generalized log-normal distribution in this case is defined in terms of s_x by Eq. (5.18) or in terms of σ_v° [using Eq. (5.13)] as

$$p(\sigma_v^\circ) = \frac{\exp\left(\frac{a_1^2}{4\sigma_x^2 a_2^2}\right) \exp\left(\pm\frac{a_1\sqrt{a_1^2+4a_2\ln\frac{\sigma_v^\circ}{C}}}{4\sigma_x^2 a_2^2}\right) \left(\frac{\sigma_v^\circ}{C}\right)^{\frac{1}{2a_2\sigma_x^2}}}{\sigma_x \sigma_v^\circ \sqrt{\pi}\sqrt{a_1^2 + 4a_2 \ln\frac{\sigma_v^\circ}{C}}}. \qquad (5.23)$$

Four parameters, a_1, a_2, C, and σ_x, dictate the shape of of the curves produced by generalized log-normal distributions. One of these parameters may not be combined with another [as can a_1 and σ_x in the one component case, refer to Eq. (5.17)]. However, the distribution is found to be degenerate (*i.e.* it has non-unique solutions) when all four parameters are left free. This can be seen by observing that the generalized log-normal distribution in Fig. 5.6 has several solutions as listed in Table 5.1 which generate the same distribution. Included in Table 5.1 is the percent error between the

Table 5.1: Different possible sets of generalized log-normal distribution parameters yielding the same distribution shown in Fig. 5.6. This underscores the need for fixing σ_x in order to aid in comparison.

Set #	a_1	a_2	C	σ_x	distribution % error from Set # 1
1	2.220	-3.226	-25.822	-0.0914	0
2	2.536	-4.211	-25.822	-0.080	4.745e-7
3	3.381	-7.487	-25.822	-0.060	1.001e-6
4	20.287	-269.527	-0.2582	-0.010	3.436e-8
5	202.873	-26,952.616	-0.00258	-0.001	1.975e-10

two distributions. The percent error is defined as the summed squared error between the distribution generated by those parameters and the distribution generated by the parameters of the first set listed in Table 5.1.

To alleviate this problem of degeneracy in YSCAT94 analysis, σ_x is fixed for all cases to be the representative slope standard deviation (σ_x) 0.0914. Thus unique a_1, a_2, and C values may be profitably contrasted. This value of σ_x was chosen because it is typical of slope variances found at the CCIW site.

Analytically, the mean of the generalized log-normal distribution [Eq. (5.23)] is given by

$$\mu_{2ln} = \lim_{a\to\infty} \int_0^a \frac{\exp\left(\frac{a_1^2}{4\sigma_x^2 a_2^2}\right) \exp\left(\pm \frac{a_1\sqrt{a_1^2+4a_2\ln\frac{\sigma_v^\circ}{C}}}{4\sigma_x^2 a_2^2}\right) \left(\frac{\sigma_v^\circ}{C}\right)^{\frac{1}{2a_2\sigma_x^2}}}{\sigma_x \sigma_v^\circ \sqrt{\pi}\sqrt{a_1^2+4a_2\ln\frac{\sigma_v^\circ}{C}}} \sigma_v^\circ \, d\sigma_v^\circ \qquad (5.24)$$

and by using a change of variables defined by

$$\begin{aligned} u &= \sqrt{a_1^2 + 4a_2 \ln\frac{\sigma_v^\circ}{C}} \quad \text{and} \\ du &= \frac{2a_2}{\sigma_v^\circ \sqrt{a_1^2+4a_2\ln\frac{\sigma_v^\circ}{C}}}, \end{aligned} \qquad (5.25)$$

Eq. (5.24) may be written as

$$\mu_{2ln} = \lim_{a\to\infty} \int_0^a \frac{C \exp\left(\frac{u^2(2\sigma_x a_2 - 1) + u(2a_1) - (a_1^2 + 2a_2\sigma_x^2 a_1^2)}{8\sigma_x^2 a_2^2}\right)}{\sigma_x a_2 2\sqrt{2\pi}} \, du \qquad (5.26)$$

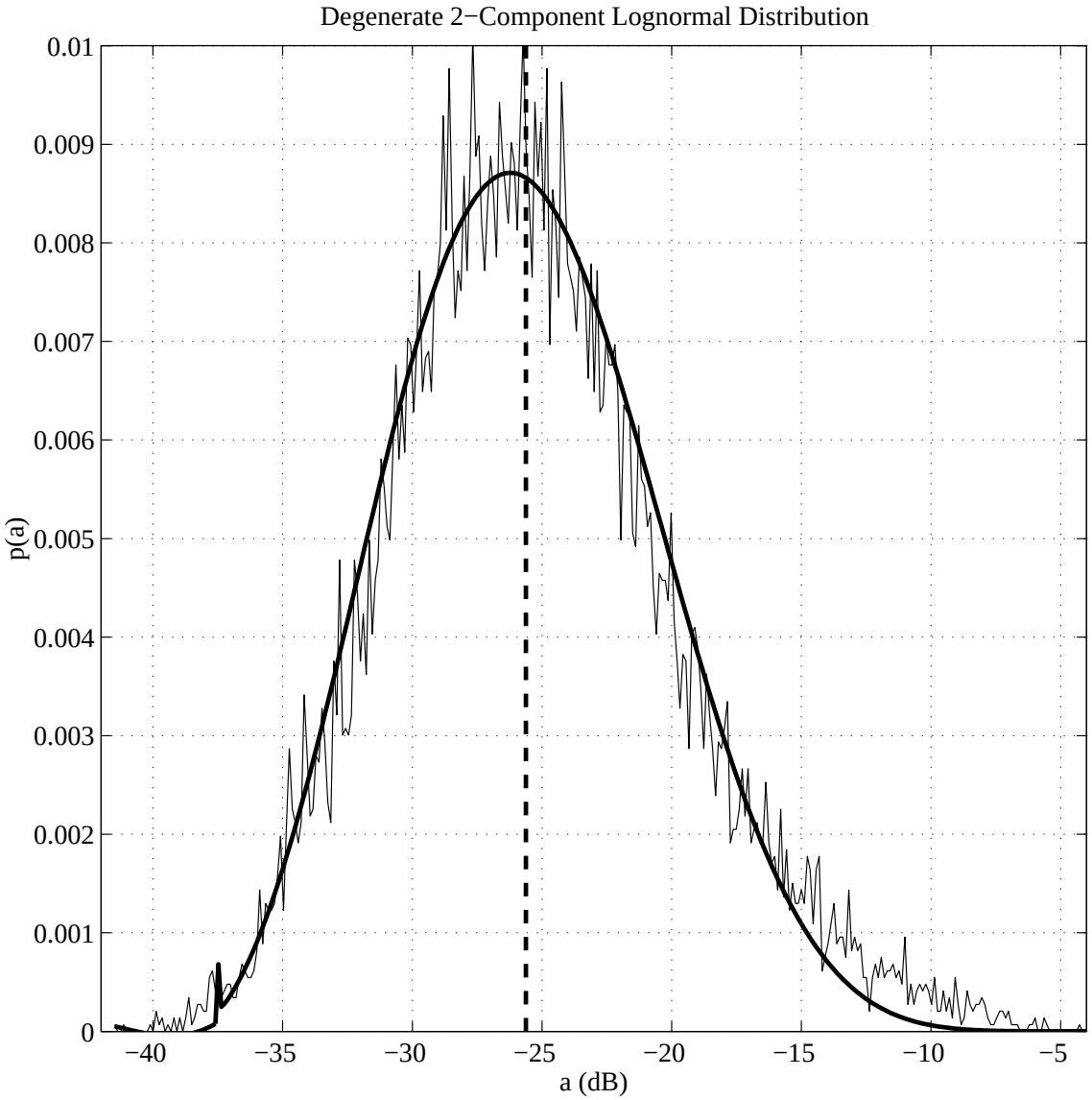

Figure 5.6: Example of the degenerate behavior of the generalized log-normal distribution. This same distribution (solid line) can be generated by the different possible sets of parameters given in Table 5.1. This demonstrates the degeneracy of the Rayleigh/generalized log-normal distribution when all parameters are free and hence the need to pick σ_x in order to aid in comparison. Data is for 10 GHz, h-pol, downwind, 20° incidence angle, and 4 m/s wind speed. Wave line is the data histogram. Bold solid line is the generalized log-normal fit. See Table 5.1 for the different possible parameter values which generate this distribution.

and thus the mean of the generalized log-normal distribution is given by

$$\mu_{2ln} = \frac{C \exp\left(\frac{a_1^2 \sigma_x^2}{1-2a_2\sigma_x^2}\right)}{\sqrt{1-2a_2\sigma_x^2}}. \tag{5.27}$$

By a similar method, the variance may be written as

$$\sigma_{2ln}^2 = \frac{C^2 \exp\left(\frac{2a_1^2 \sigma_x^2}{1-4a_2\sigma_x^2}\right)}{\sqrt{1-4a_2\sigma_x^2}}. \tag{5.28}$$

Individual cases illustrating how the generalized log-normal distribution changes as parameters change may be numerically produced as in Fig. 5.7. The parameter a_2 has less of an effect on the overall distribution location or width than either a_1 or C, however a_2 does effect the small-scale shape of the distribution amounting to "fine-tuning" the resulting distribution. The parameter a_2 is thus sensitive to small changes in distribution shape when this distribution is fit to data histograms.

The final note about the generalized log-normal distribution lies in its symmetry about a_1. The same distribution is generated regardless of the sign of a_1. This may be suspected from inspection of Eqs. (5.27) and (5.28) for the mean and variance of this distribution by noting that the parameter a_1 appears only as a squared quantity. Due to this, in Section 5.5 and in Appendices B and C, the absolute value of a_1 is plotted instead of a_1.

5.3.3 Rayleigh/Generalized Log-normal Distribution

The form for the probability of a given amplitude of microwave backscatter from the sea surface is now defined in terms of σ° by Eq. (5.19) (reproduced below).

$$p(a) = \int_0^\infty \underbrace{\frac{2a\sigma^\circ}{e^{a^2\sigma^\circ}}}_{p(a|\sigma^\circ)} \underbrace{\left(\frac{\exp\left(\frac{a_1^2}{4\sigma_x^2 a_2^2}\right) \exp\left(\pm \frac{a_1 \sqrt{a_1^2 + 4a_2 \ln \frac{\sigma_v^\circ}{C}}}{4\sigma_x^2 a_2^2} \right) \left(\frac{\sigma_v^\circ}{C}\right)^{\frac{1}{2a_2\sigma_x^2}}}{\sigma_x \sigma_v^\circ \sqrt{\pi} \sqrt{a_1^2 + 4a_2 \ln \frac{\sigma_v^\circ}{C}}} \right)}_{p(\sigma^\circ) \quad [Eq.\ (5.18)]} d\sigma^\circ, \tag{5.29}$$

or in terms of s_x as

$$p(a) = \int_{-\infty}^\infty \underbrace{2aCe^{a_1 s_x + a_2 s_x^2} e^{-a^2 C e^{a_1 s_x + a_2 s_x^2}}}_{p(a|\sigma_\circ(s_x))} \underbrace{\frac{e^{\frac{-s_x^2}{2\sigma_x^2}}}{\sqrt{2\pi}\sigma_x}}_{p(\sigma_\circ(s_x))} ds_x. \tag{5.30}$$

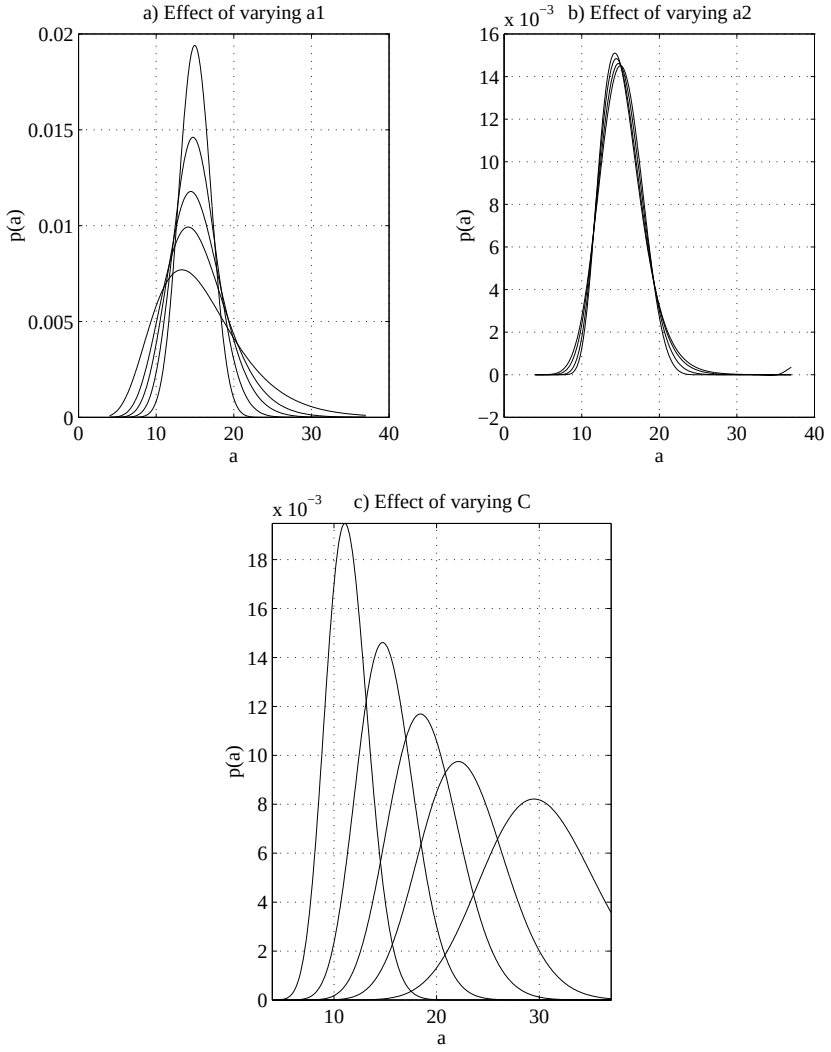

Figure 5.7: Effects of parameter variation on the generalized log-normal distributions. $a_1^o = 2.0$, $a_2^o =$ -1.0, and $C^o = 15.0$.
a) $a_1 = [1.5\ 2.0\ 2.5\ 3.0\ 4.0]\ a_1^o$ (upper to lower curve)
b) $a_2 = [1.0\ 0.2\ -1.0\ -2.0]\ a_2^o$ (upper to lower curve)
c) $C = [11.25\ 15.0\ 18.75\ 22.5\ 30.0]\ C^o$ (left to right).

Equation (5.29) is the multiplication of a Rayleigh distribution and a generalized log-normal distribution. The generalized log-normal distribution is defined by Eq. (5.23) and explained by the subsequent discussion. Equation (5.30) has the same functionality as Eq. (5.29) but is easier to work with.

The analytical solution to the integral in Eq. (5.30) has not been found by the author. However, Eq. (5.30) may be successfully integrated numerically over s_x for a given set of parameters. For example, Fig. 5.8 shows the value of the integrand of Eq. (5.30) plotted against s_x for a_1=12.037, a_2=-23.233, C=1.1297e6, σ_x=0.0914, and a=0.0001, 0.00025, 0.0005, 0.0013, and 0.002. In Fig. 5.9 these four curves have been integrated and normalized to yield the four probabilities $p(a)$= 7.6657e-4, 0.0013, 0.00104, and 4.4902e-5 denoted by asterisks, while the underlying curve represents the curve resulting from values of a between 0 and 0.004.

Care must be taken in the deciding of integration limits when numerically evaluating Eq. (5.30). Since slopes of (s_x) greater than 0.5 are rarely found in nature, the limits used for numerically integrating Eq. (5.30) are set at $s_x = \pm 1$ (*c.f.* Fig. 5.8). The numerical integration resolution, that is, the spacing between the evaluation points in Eq. (5.20) is also important. This spacing should be small to assure valid results, yet large to enable acceptably fast calculation. A spacing of 0.005 was chosen as a compromise to ensure both (percentage error between using 0.005 and 0.001 spacing was $<$ 1e-8).

To ensure that no significant area of $p(a)$ falls beyond these limits, two tests were conducted. The first test is calculating the ratio of the peak of each $p(a)$ curve to the value at $s_x = \pm 1$. Except at times when numerical singularities were encountered in the integration, the greatest observed value of this ratio was 1e-22. This demonstrates that the significant part of the curve $p(a)$ is within the bounds of $s_x = \pm 1$. This conclusion is also supported empirically in Fig. 5.8. All five of the curves in Fig. 5.8 attenuate to negligible levels by $s_x = \pm 0.5$.

A second test to insure valid integration is performed after fitting Eq. (5.20) to each data histogram (see Section 5.4.2 for a discussion of fitting Eq. (5.20) to data histograms). After finding a "best" fit (using the Kullback-Leibler test, see

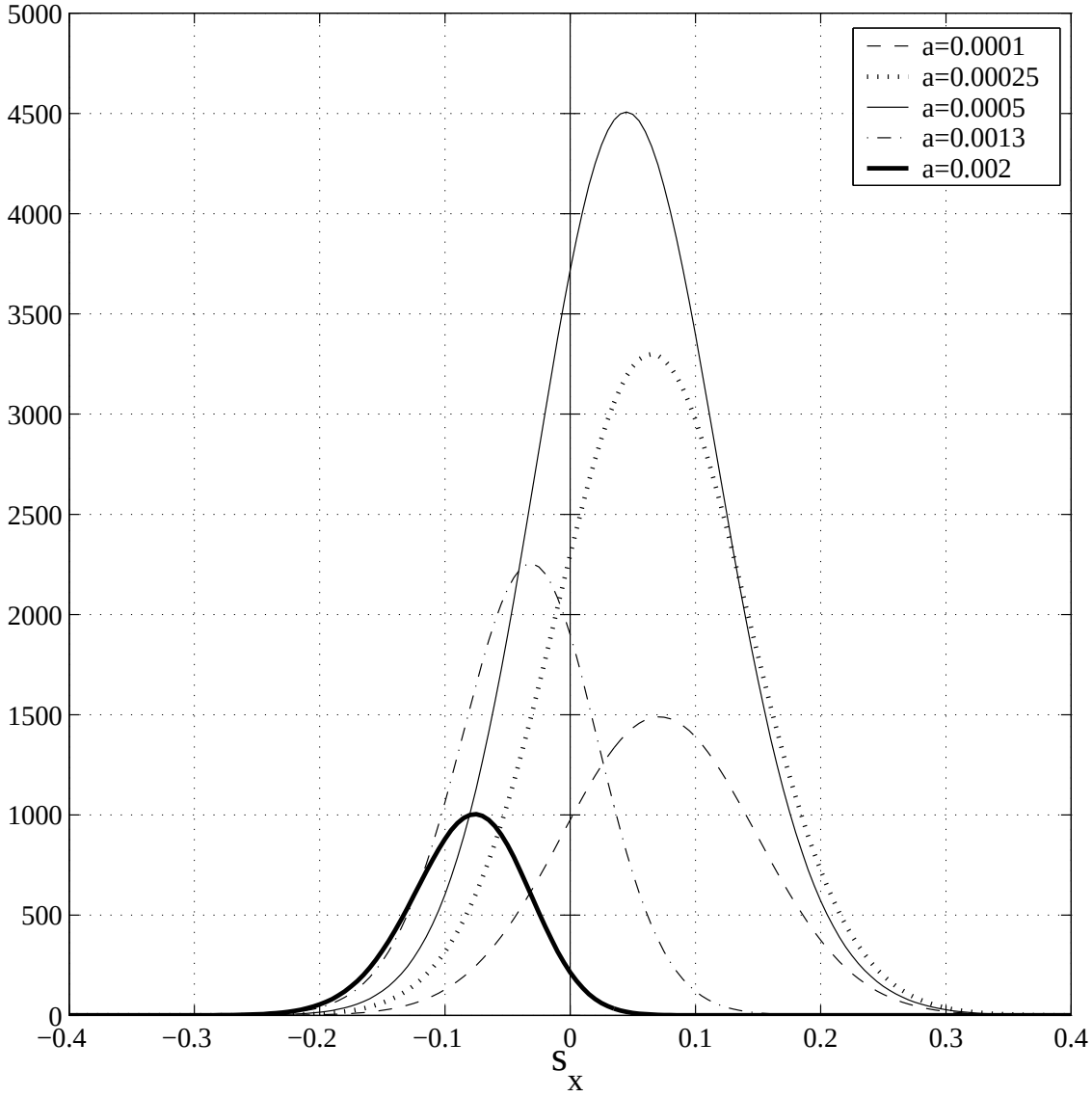

Figure 5.8: Evaluation of Eq. (5.30) for a=0.0001, 0.00025, 0.0005, 0.0013, and 0.002. After integration and normalization, these five curves map to the asterisks in Fig. 5.9. For this case, a_1=12.037, a_2=-23.233, C=1.1297e6, and σ_x=0.0914.

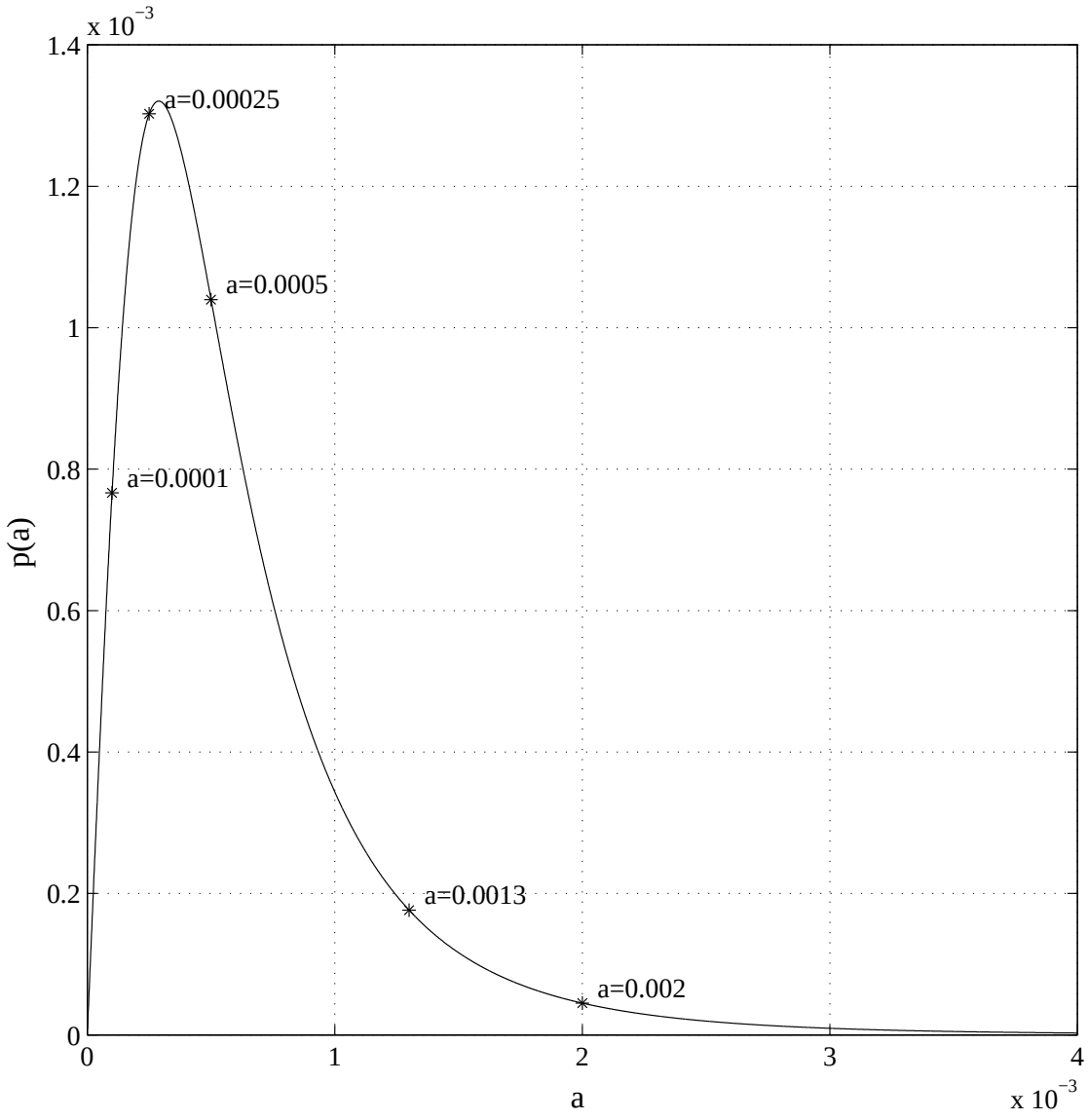

Figure 5.9: Rayleigh/generalized log-normal distribution for this case of a_1=12.037, a_2=-23.233, C=1.1297e6, and σ_x=0.0914. Asterisked values are normalized integrated values from Fig. 5.8 with a=0.0001, 0.00025, 0.0005, 0.0013, and 0.002.

Section 5.4.1) to the data histogram, the limits of integration for Eq. (5.20) were set to $s_x = \pm 2$, the integration spacing is also decreased 5 times to 0.001, and the resulting value is compared with integrating from $s_x = \pm 1$ with with spacing set to 0.005. The maximum deviation encountered by this second test was 107 parts per billion, and the mean deviation was 120 parts per trillion.

As stated above, the values for $p(a)$ produced by Eq. (5.30) curve may be numerically evaluated and fit to empirical histograms of backscatter amplitude data. The full method used to reliably fit this distribution to YSCAT94 backscatter distributions is detailed in Section 5.4.2, but an example is shown in Fig. 5.10. The combined Rayleigh/generalized log-normal distribution captures the trends in backscatter data extremely well, especially in the tails. The Rayleigh/generalized log-normal distribution fit to the data histogram in Fig. 5.10(a) is excellent to the point that the distribution lies directly over the data almost the entire length of the data histogram. If the y-axis is set to a log scale, the best-fit distribution lies on the center of the varying backscatter. For comparison, a best fit Weibull distribution is also shown as a dashed line in Fig. 5.10(a-b). As noted in [8], the data pdf closely follows a Weibull distribution for small amplitudes, but the agreement is not as good in the tails of the distributions.

5.4 Fitting the Distributions

YSCAT94 data was binned according to frequency, polarization, wind direction, incidence angle, wind speed, and estimated mean wave slope resulting in over 2700 distinct cases. Equation (5.30) was fit to the histogram (converted to a pdf) of the backscatter amplitude in normal (unlogged) space. The Weibull distribution was also fit to this same backscatter data. These fits were implemented so that YSCAT94 backscatter distributions could be characterized by Eq. (5.30). Trends in the parameters a_1, a_2, and C provide insight into the relationship between the environmental parameters of wind speed and slope to radar backscatter. Ultimately, it is hoped that environmental parameters such as wind speed and wave slope may be accurately deduced from the radar backscatter.

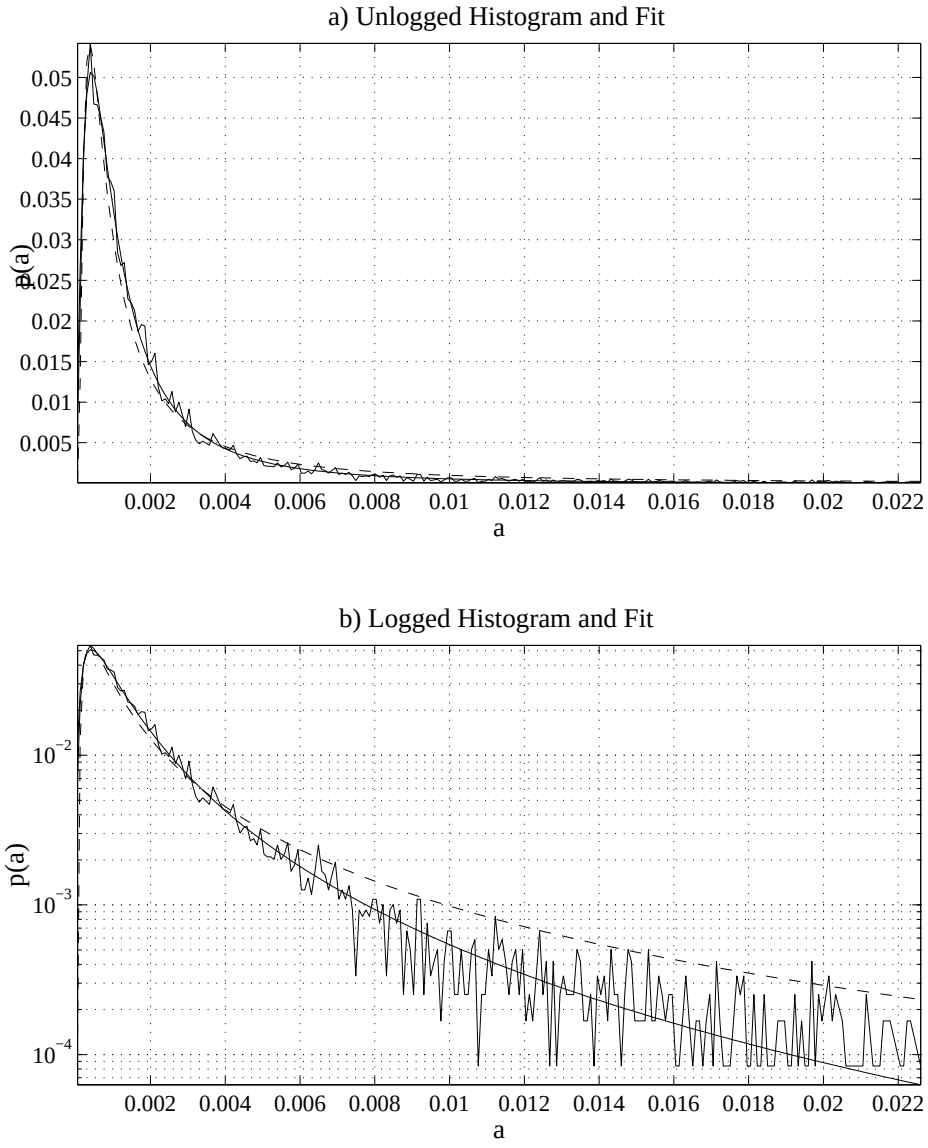

Figure 5.10: "Best" fit Rayleigh/generalized log-normal distribution to data at 5 GHz, h-pol, downwind, 30° incidence angle, and wind speed 5 m/s. Parameter values are a_1=20.81, a_2=-26.32, and C=4.4712e5. a) Unlogged scale, b) Log scale on y-axis.

The log of the individual amplitude measurements was also converted to a pdf in order to find the log-mean and log-variance of YSCAT94 data. A log-normal and a generalized log-normal distribution are fit to these distributions in log space. This was done to characterize these empirical data distributions according to more flexible statistical distributions (which are also supported by the physics of the situation) in addition to characterizing them by the traditional log-mean and log-variance statistics normally encountered in the literature [31] [32] [34] [35].

5.4.1 Fitting Metric

The metric used in this thesis to decide which fit is "best" is the Kullback-Leibler distance. The Kullback-Leibler distance is minimized in order to fit the backscatter distributions by the method outlined in Section 5.4.2. The Kullback-Leibler distance between two distributions is defined as [36]

$$p(f||g) = \int f(x) log \frac{f(x)}{g(x)} dx. \tag{5.31}$$

Minimizing the Kullback-Leibler distance provides a maximum entropy solution when finding the best fit. In Eq. (5.31), f(x) is the data, and g(x) is the fit though this could be reversed. In order to avoid unexpected minima, the following modification of Eq. (5.31) is used to sum discreet points of data

$$p(f||g) = \sum_{n=-\infty}^{\infty} \left| f(x_n) \log \frac{f(x_n)}{g(x_n)} \right|. \tag{5.32}$$

5.4.2 Fitting Algorithm

The parameters of the Rayleigh/generalized log-normal distribution (in the unlogged case) and the log-normal and generalized log-normal distributions (in the logged case) are very sensitive to small changes in distribution shape. Figure 5.11 illustrates this fact by showing three Rayleigh/generalized log-normal distributions seemingly close together, but with parameters varying as much as 35 times. For profitable comparison, the parameters a_1, a_2, and C for a given data case need to maintain a close relationship with parameters of nearby data cases. If the fits are optimal, trends in a_1, a_2, and C for different wind speeds, wave slopes, polarizations,

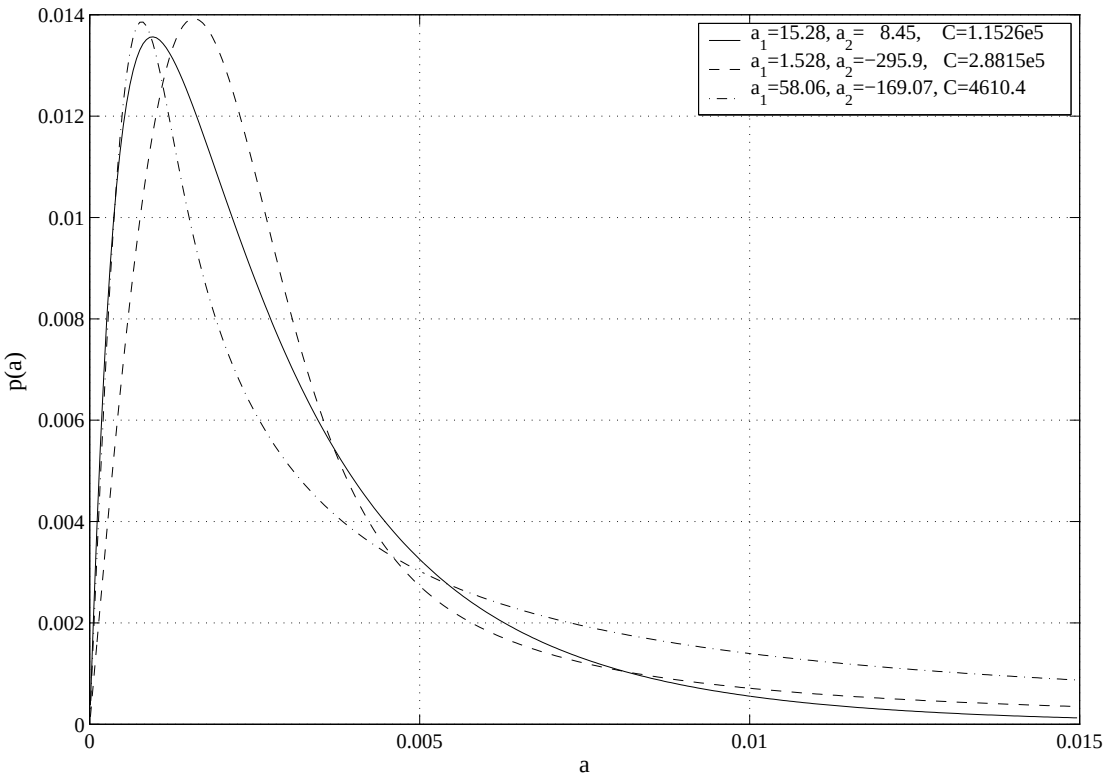

Figure 5.11: Demonstration of the sensitivity of the Rayleigh/generalized log-Normal distribution. Though the three curves are similar in shape, the parameter values vary as much as 35 times.

wind directions, frequencies, and incidence angles can be identified. Thus, there is a strong need to ensure the fits are indeed optimal when fitting the Rayleigh/generalized log-normal distribution to YSCAT94 backscatter distributions.

The workhorse of the fitting routines used in this thesis is an unconstrained Gauss-Newton search with upper and lower bounds on each of the parameters. This unconstrained search finds the minimum distance from the data histogram to a given pdf according to the Kullback-Leibler distance of Eq. (5.32). With sufficiently close "seed" values, or guesses, at which to begin the search, an unconstrained search using the Gauss-Newton procedure usually finds the global minimum of Eq. (5.32). The means and variances for the log-normal and generalized log-normal distributions (c.f. Eqs. (5.21), (5.22) and (5.27), (5.28), respectively) aid in making good initial guesses when attempting to fit pdfs to these distributions. On the other hand, the Rayleigh/generalized log-normal distribution has no known analytical statistical moments. The algorithm for finding Rayleigh/generalized log-normal fits to the backscatter amplitude must be robust and general.

The fitting method developed in this thesis to fit the Rayleigh/generalized log-normal distribution to the unlogged backscatter data is a mixture of powerful established extremization searching techniques and random perturbation techniques. When used in conjunction with the best nearby solution as the seed, the method outlined below yields the best fit for the majority of YSCAT94 data. Overall, the Rayleigh/generalized log-normal distribution produces an extremely close fit except in cases of higher frequencies (10-14 GHz), high incidence angles (50°-60°), and some very low wind speed (1-2 m/s) cases. See Section 5.6 for a discussion of these poor fits.

For the logged case, only the log-normal and generalized log-normal distributions are fit to the data. These fits converge much more quickly with fewer caveats than when fitting the Rayleigh/generalized log-normal distribution to the unlogged case. The log-normal and generalized log-normal fits to the logged data, as well as Weibull distribution fits to the unlogged data, all use the same metric [Eq. (5.32)] but

Table 5.2: Summary of data Types considered, distributions fitted, and parameters extracted from YSCAT94 data analysis.

Data Type	**Distribution**	**Parameters**
Wind Speed		
Logged Measurements	log-normal	a_1, C
	generalized log-normal	a_1, a_2, C
		mean, variance
Unlogged Measurements	Weibull	α
	Rayleigh/generalized log-normal	a_1, a_2, C
		mean, variance
Wave Slope		
Logged Measurements	log-normal	a_1, C
	generalized log-normal	a_1, a_2, C
		mean, variance
Unlogged Measurements	Weibull	α
	Rayleigh/generalized log-normal	a_1, a_2, C
		mean, variance

only the unconstrained search Gauss-Newton search method. Table 5.2 summarizes the distributions, data types, and parameters which result from this analysis.

The first step in fitting Eq. (5.32) to YSCAT unlogged amplitude measurements is to pick a good seed value. Because the Rayleigh/generalized log-normal distribution parameter solutions are usually close to other solutions, especially for adjacent data cases, nearby parameter solutions are tested. The set "closest," or the one that yields the minimum distance according to Eq. (5.32), becomes the seed for the present data case. In this thesis, "nearby" data cases are data cases with wind speed (or wave slope), polarization, or wind direction different but with other parameters the same. For example, to find a seed value for the case of 5 GHz, h-pol, upwind, 20° incidence angle, and 4 m/s wind speed, adjacent data cases of 1-10 m/s wind speed and 5 GHz, h-pol downwind, and v-pol up/downwind, 20° incidence angle, and at 4 m/s wind speed are all tested and the nearest selected. One benefit of this technique is the improvement of seed values as the algorithm progresses and solutions are found to nearby data cases.

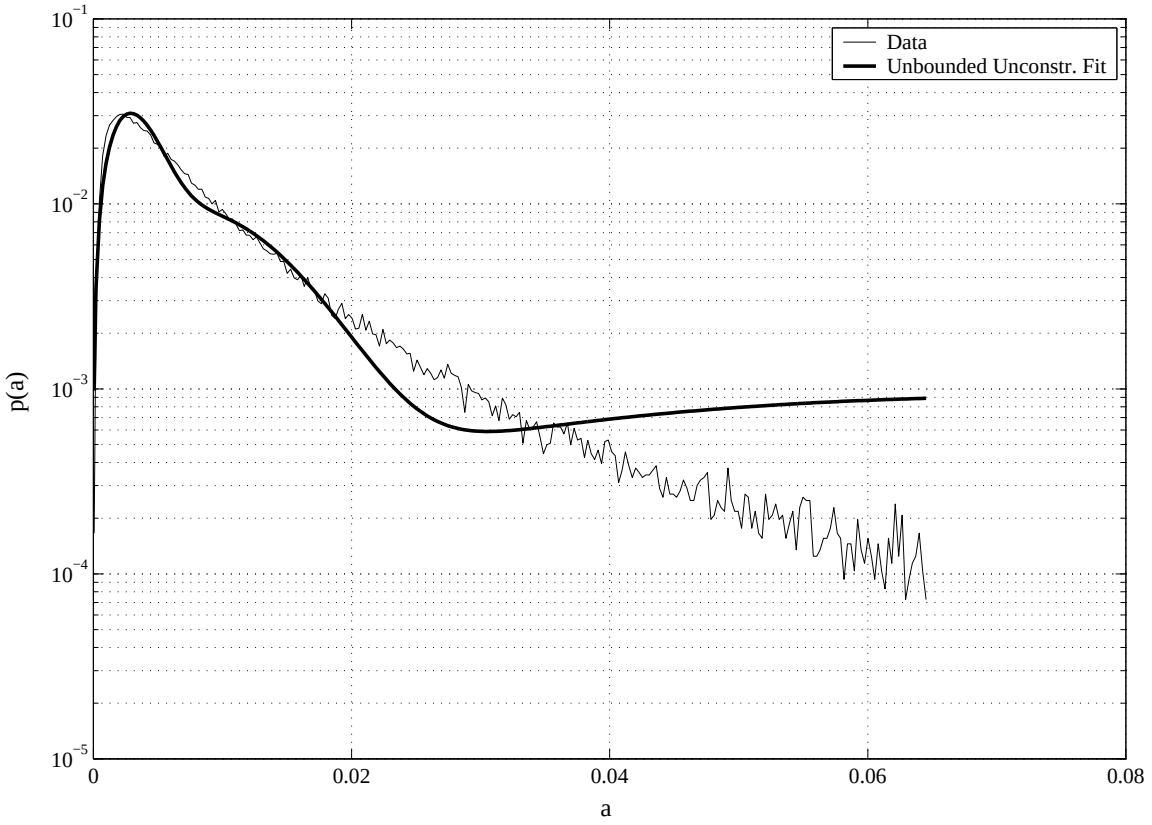

Figure 5.12: Demonstration of the inadequacy of the unbounded unconstrained Gauss-Newton search method alone. Initial guess: a_1=1, a_2=-300, and C=30. Parameters for the erroneous fit above: a_1=452.95, a_2=-177,643.7, and C=69,838.6. Kullback-Leibler distance=0.21. Data is for 5 GHz, v-pol, downwind, 20° incidence angle, and 4 m/s wind speed.

The resulting seed value is then passed to an unconstrained search which uses the Gauss-Newton method to find the minimum of Eq. (5.32). However, even after this minimization routine, a_1 and a_2 values may be incorrect with possible values in the 10^5 range such as illustrated in Fig. 5.12. Therefore, constraints of $|a_1|$ <100 and -200< a_2 <29.926 were added to the minimization routine. The upper limit on a_2 is a consequence of requiring the mean [Eq. (5.27)] and the variance [Eq. (5.28)] of the generalized log-normal distribution to be real. The other limits arise from empirical observations of a number of different cases. Some a_2 values ended up to be above this

Table 5.3: Constrained search perturbation factors (see text).

Perturbation # / Parameter	1	2	3	4	5	6	7
a_1	1	1	1	1	1.15	0.87	1
a_2	1	1	1.15	0.87	1	1	1
C	1.15	0.87	1	1	1	1	1

limit. This discrepancy is due to the fact that only the real part of Eq. (5.30) was used in fitting Eq. (5.30) to YSCAT94 data.

Equation (5.32) has many local minima, but the global minimum is desired. It is possible to "perturb" the output parameters of the constrained search above in order to break out of local minima on the road to the global minimum. After the constrained search finds a minimum, all seven perturbations listed in Table 5.3 are tried as new seed values of a new constrained search. If a new minima is found to be even 0.01% better, the cycle of perturbations repeats itself until there is no improvement. After implementing this constrained search methodology, the global minimum Kullback-Liebler distance is found about 90% of the time. The other 10% of the cases resulted in situations like that shown in Fig. 5.13 which is still not the optimal fit.

To improve any inaccurate parameter solutions remaining after the unconstrained search, a random perturbational method is introduced. This method involved scaling the resulting parameters a_1, a_2, and C by all 27 combinations of remaining the same, scaling larger, or scaling smaller by only the slight amount of 0.13%. The scale factors used are listed in Table 5.4. When any set of scaled parameters yield a better fit to the data ($> 0.001\%$ better), all 27 scale factors are tested again. In this way, this random perturbation method is similar to the method used in the constrained search.

This random perturbation method works in many cases where the first method fails. After implementing this procedure the global minimum is achieved for nearly all data cases. This search method works particularly well when the best descent path

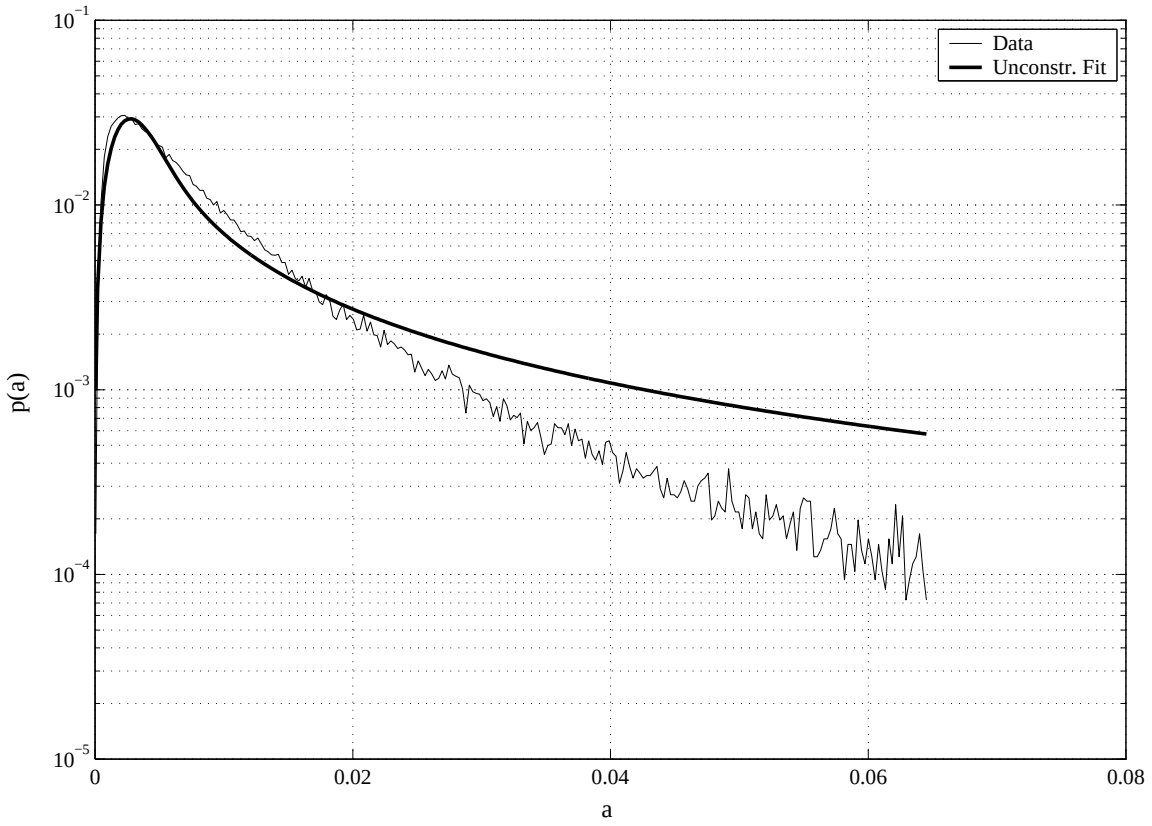

Figure 5.13: Demonstration of the inadequacy of the bounded unconstrained Gauss-Newton search method alone. Parameters for the erroneous fit above: a_1=50.91, a_2=-199.89, and C=4,255.35. Kullback-Leibler distance=0.19. Data is for 5 GHz, v-pol, downwind, 20° incidence angle, and 4 m/s wind speed.

Table 5.4: Random search perturbation factors. Each factor is tried in turn by the random optimization routine. Any improvement in error according to Eq. (5.32) results in testing all 27 factors again.

Parameter / Perturbation #	a_1	a_2	C
1	1	1	1
2	1	1	0.9987
3	1	1	1.0013
4	1	0.9987	1
5	1	0.9987	0.9987
6	1	0.9987	1.0013
7	1	1.0013	1
8	1	1.0013	0.9987
9	1	1.0013	1.0013
10	0.9987	1	1
11	0.9987	1	0.9987
12	0.9987	1	1.0013
13	0.9987	0.9987	1
14	0.9987	0.9987	0.9987
15	0.9987	0.9987	1.0013
16	0.9987	1.0013	1
17	0.9987	1.0013	0.9987
18	0.9987	1.0013	1.0013
19	1.0013	1	1
20	1.0013	1	0.9987
21	1.0013	1	1.0013
22	1.0013	0.9987	1
23	1.0013	0.9987	0.9987
24	1.0013	0.9987	1.0013
25	1.0013	1.0013	1
26	1.0013	1.0013	0.9987
27	1.0013	1.0013	1.0013

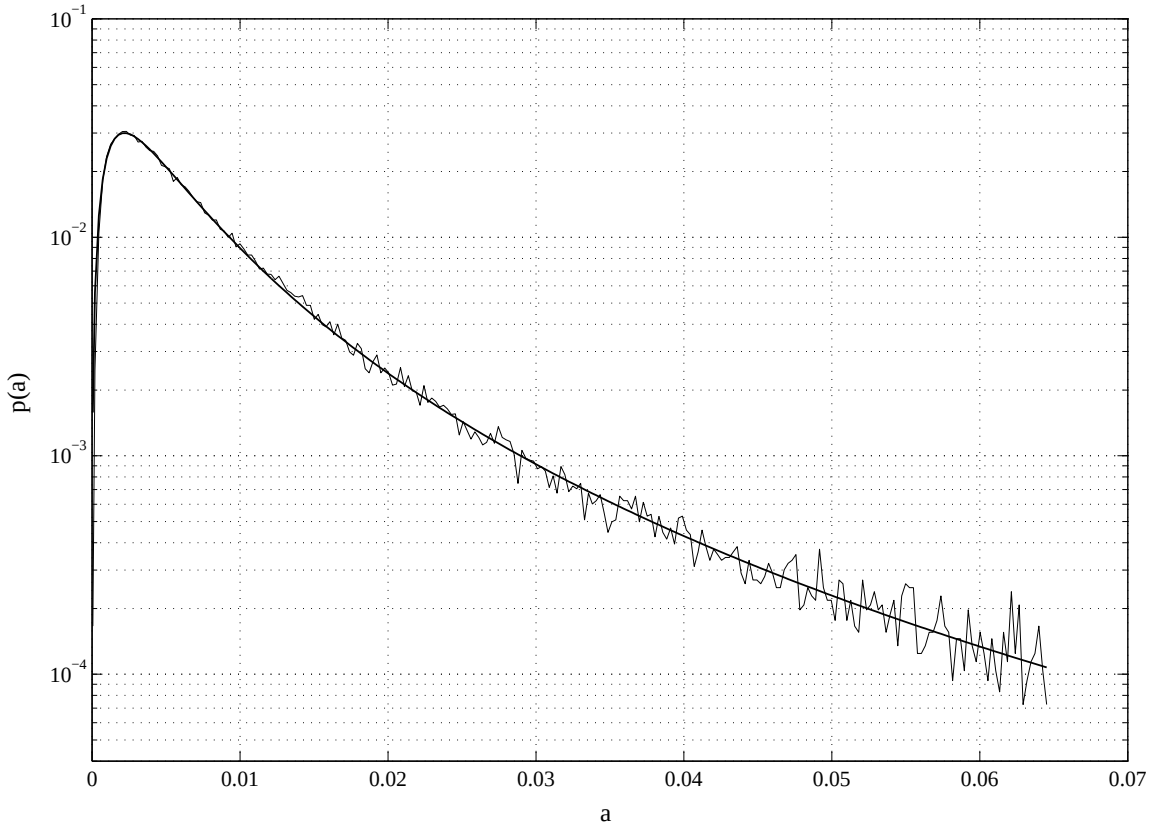

Figure 5.14: Demonstration of the effectiveness of the random perturbation search method. The following parameters result from implementing the random perturbation method on the vales from the constrained search: a_1=18.14, a_2=-13.08, and C=19,305.16. The parameter a_2 becomes -211.2 (outside the lower bound for a_2 set in the constrained search method) before settling down to the value above. Kullback-Leibler distance=0.034976. Data is for 5 GHz, v-pol, downwind, 20° incidence angle, and 4 m/s wind speed.

falls outside the bounds set in the first method (e.g., $a_2 <$ -200) to enable another variable (usually a_1) to change significantly toward its final value. Using this method, the failed case presented in Fig. 5.13 becomes the fit in Fig. 5.14.

As a final strategy to ensure the best fit possible, a search similar to the first unconstrained search is implemented without bounds on a_1 and a_2. This search tests 27 scale factors in a similar manner to the random perturbation method repeating the cycle if a new local minimum is found. Finally, using the full procedure of first,

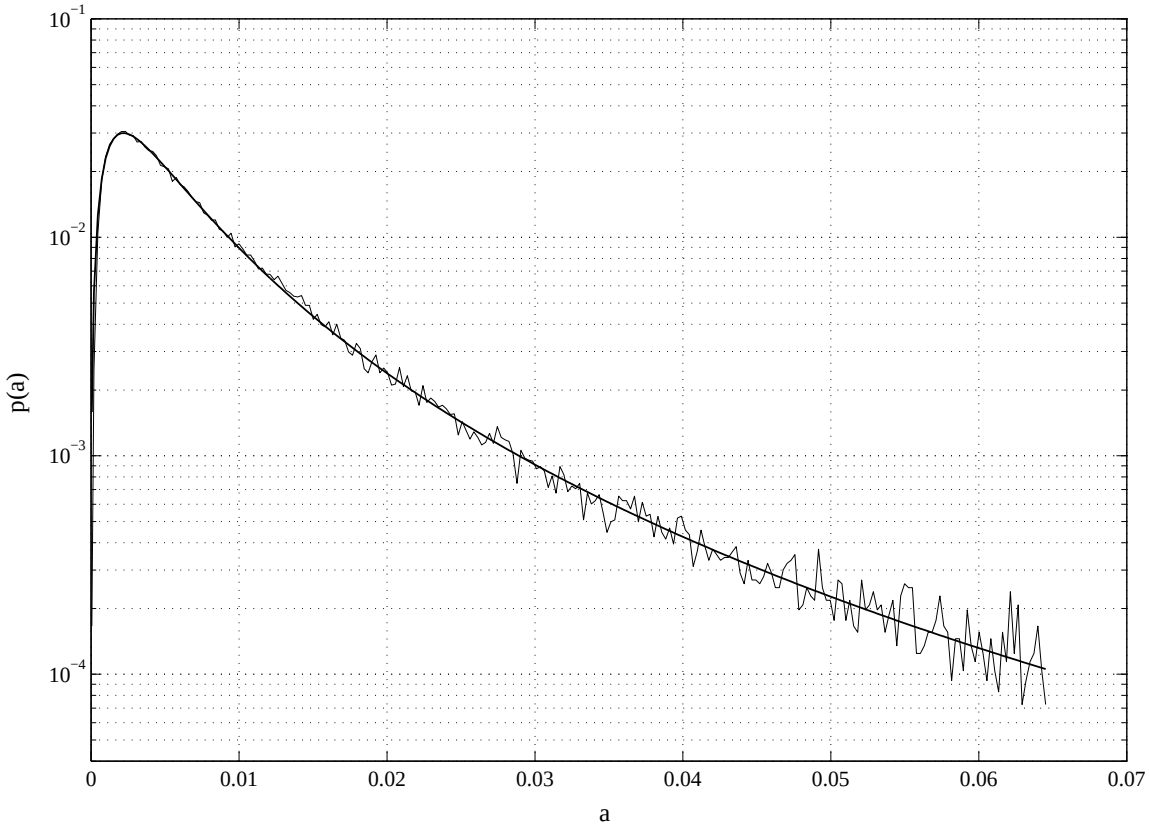

Figure 5.15: Demonstration of the combined perturbation fitting search method. The final parameters resulted from implementing the combined perturbation method were: a_1=18.102, a_2=-12.616, and C=19,304.98. Kullback-Leibler distance=0.034953. Data is for 5 GHz, v-pol, downwind, 20° incidence angle, and 4 m/s wind speed.

the bounded unconstrained search, then the random search, and last the unbounded unconstrained search, the global minimum occurs when a_1=18.102, a_2=-12.616, and C=19,304.98. The empirical distribution of Fig. 5.14 now has as its final fit shown in Fig. 5.15. The Kullback-Leibler distance started at 0.21 after the first phase of searching was performed and finished at 0.034953 which was an improvement in accuracy of over six times, and a difference in parameter values of up to 22 times. The combined perturbational method described above is effective in fitting Rayleigh/generalized log-normal distributions to YSCAT94 microwave backscatter data distributions.

5.5 Results

According to Table 5.2, the analysis presented in this thesis resulted in over 20 parameters which describe the behavior of the logged and unlogged amplitude backscatter distributions from the YSCAT94 experiment on Lake Ontario. A few select cases which serve to illustrate general trends in these parameters are presented here. For an exhaustive report of these results, the reader is referred to Appendix B and Appendix C for results sorted according to wind speed and wave slope respectively.

The general trends of each parameter are worthy of note. For example, the means of each data case showed a general trend of increasing with wind speed and mean wave slope though the increase is more gradual with mean wave slope. In general, the higher the frequency and the higher the incidence angle, the lower the mean value. The same (very) general statements may be said for the variances of the data, although for both the mean and variance a decreasing trend can be observed for 0° (nadir) scattering, especially at higher frequencies. Figure 5.16(a-d) shows the mean (a,b) and variance (c,d) respectively for different Bragg wavelengths in terms of wind speed (a,c) and mean wave slope (b,d).

For the Rayleigh/generalized log-normal distribution parameters a_1, a_2, and C, different trends are observed. In general, C values display trends reversed from those of the mean and variance. C values tend to decrease according to a log relationship with the exception of 0° (nadir) cases displaying a slight tendency to increase. Higher frequencies also tend to yield higher C values instead of lower as is the case for the mean and variance of the unlogged data. This is somewhat surprising since the mean and variance of the generalized log-normal distribution both have C as a multiplier. This relationship between the mean values and the values for C is illustrated in Fig. 5.17.

a_1 values for the Rayleigh/generalized log-normal distribution tend to stay in the same range of 5-25 for different frequencies and incidence angles. A slight upward trend can be seen in many cases when plotted versus wind speed as in Fig. 5.18. a_1 values also tend to decrease as incidence angle increases as can be seen in Fig. 5.18

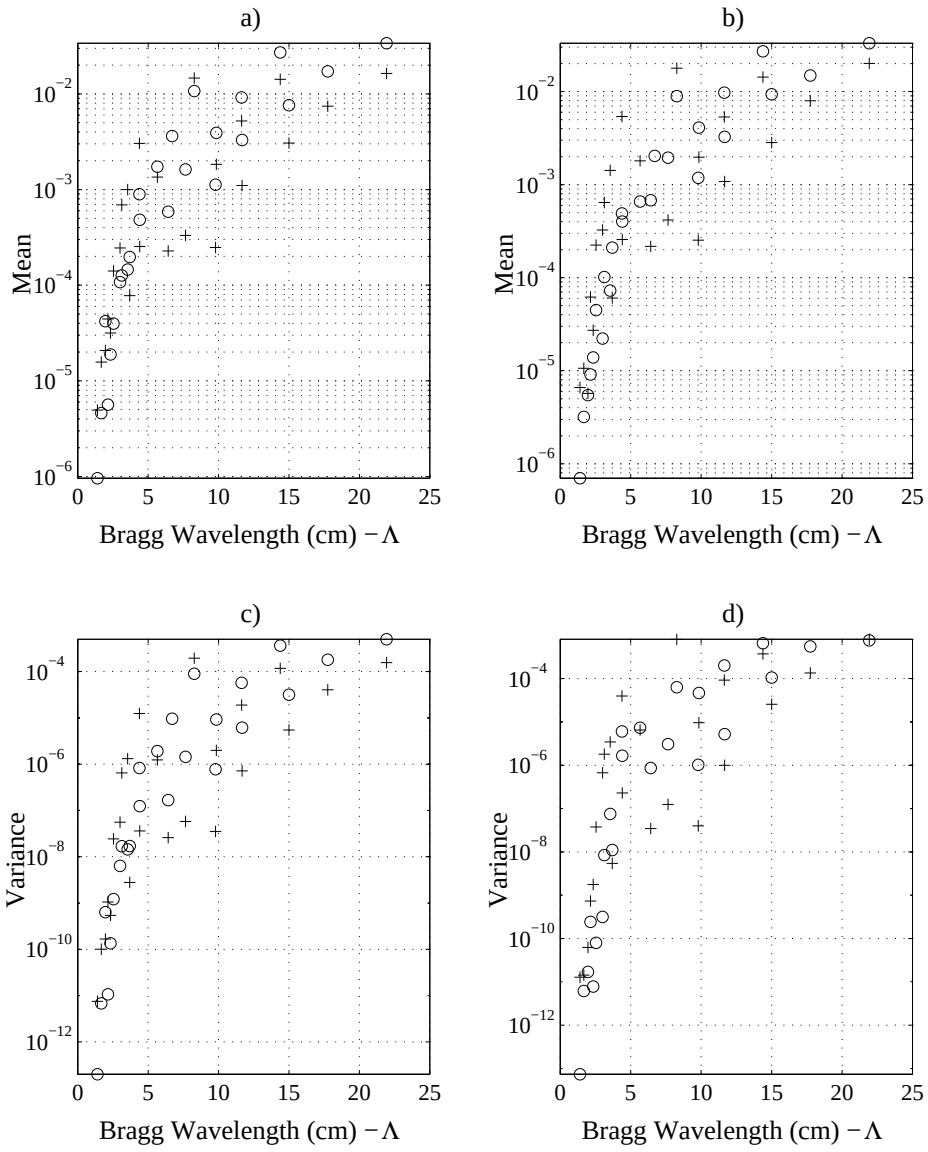

Figure 5.16: Mean (μ) and variance (σ^2) according to Bragg wavelength (Λ). The mean according to the Bragg wavelength for a) wind speed of 4 m/s, and b) mean wave slope of 0.2. The variance according to the Bragg wavelength for the same cases is shown in c) and d). Circles indicate v-pol, upwind values. Pluses indicate h-pol, upwind values.

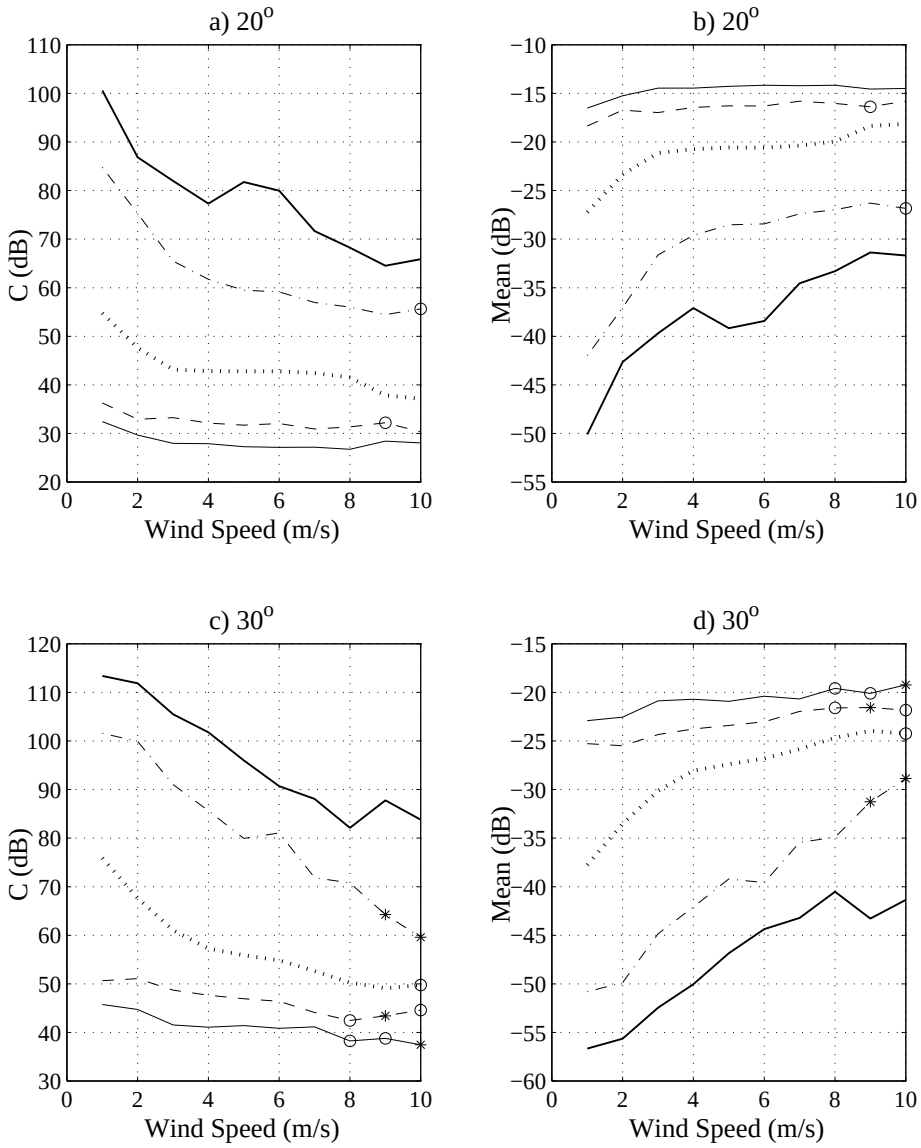

Figure 5.17: Comparison of mean values and C values from the Rayleigh/generalized log-normal distribution. a) and b) are for a 20° incidence angle. c) and d) are for a 30° incidence angle. Data is for v-pol, downwind case. Thin solid line corresponds to 2 GHz, dashed line corresponds to 3 GHz, dotted line corresponds to 5 GHz, dash/dot line corresponds to 10 GHz, and the bold solid line corresponds to 14 GHz. Asterisks correspond to interpolated values for bins with no data, and circles indicate bins with only one or two minutes of data.

above. a_2 values for the Rayleigh/generalized log-normal distribution display a decreasing trend when considered versus wind speed and mean wave slope. These a_2 values tend to be lower for higher frequencies and again lower for increasing incidence angles as illustrated in Fig. 5.19. A typical progression of the backscatter distributions through the eight different incidence angles YSCAT94 operated at is shown graphically in Figs. 5.20, 5.21, and 5.22. Figure 5.20 shows how the distribution shape changes as wind speed changes for the case of 5 GHz, vertical polarization, downwind, and 20° incidence angle. Figure 5.21 shows how the a_1, a_2, and C parameters change as wind speed changes for the same data case, and Fig. 5.22 shows how the a_1, a_2, and C parameters change as mean wave slope changes for the same data case.

The logged statistics display somewhat different behavior than the unlogged statistics. While the log-mean value rises in a similar fashion to their unlogged counterparts, the log-variance tends to neither increase nor decrease, but exhibits similar values at all wind speeds and mean wave slopes for a given frequency, polarization, incidence angle, and wind direction. This can be seen in Fig. 5.23 by plotting the log-mean and log-variance according to Bragg wavelength (Λ) for the case of 4 m/s wind speed and 0.2 mean wave slope. This failure of the log-variance to increase with increasing wind speed has been noticed by others, and seems to be true for YSCAT94 data.

After taking the log of YSCAT94 backscatter data, different distributions emerge. The log-normal and generalized log-normal distributions are fit to the logged data. Differing trends in these parameters are worth noting. The a_1 parameter either stays the same or has a slight downward trend for different wind speeds and mean wave slopes, with the exception of a slight upward trend in the 0° (nadir) case. a_1 values for the log-normal distribution are generally lower for higher frequencies, and as incidence angle increases, a_1 increases toward zero. A plot of a_1 values for the log-normal distribution according to wind speed and mean wave slope for 20°, 30°, and 40° incidence angle is given in Fig. 5.24.

The values of C for the log-normal distribution are almost identical to the log-mean values and exhibit the same trends, including the same flat trend when plotted

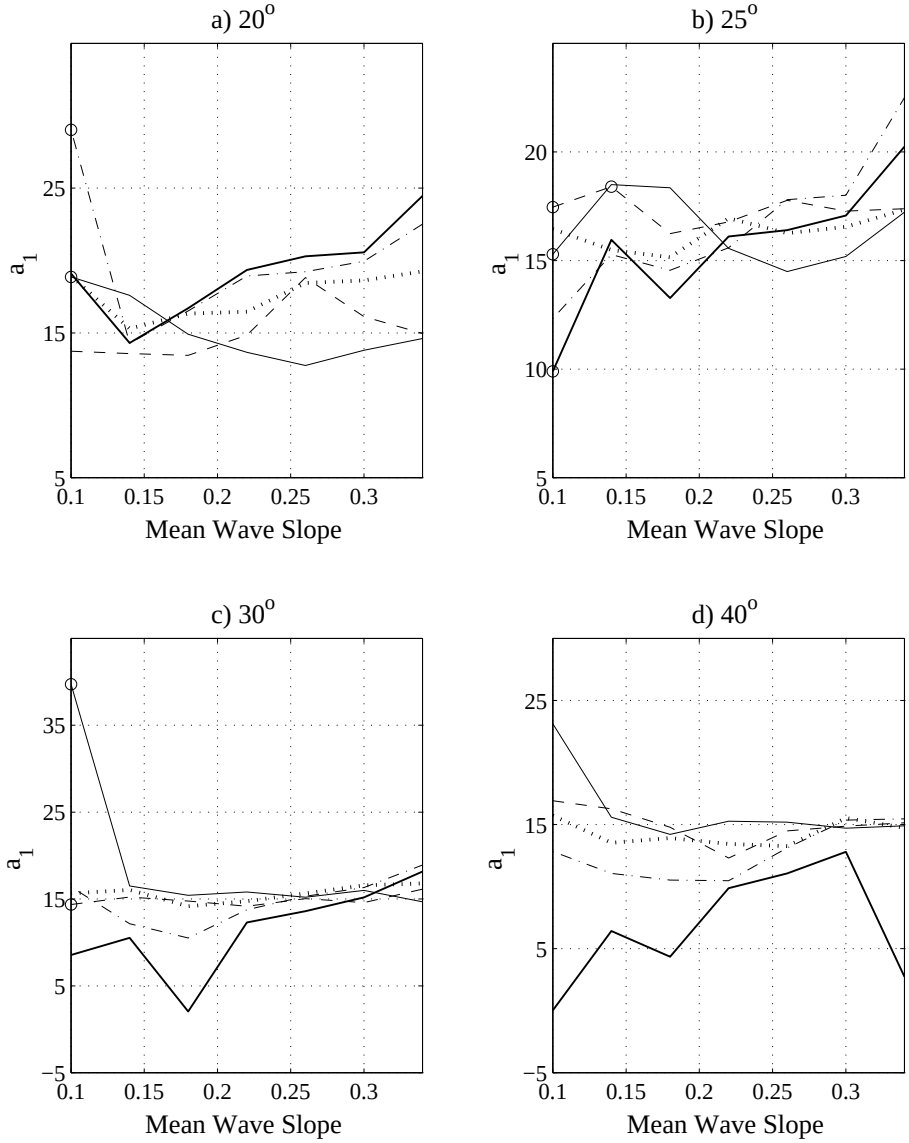

Figure 5.18: Upward trend in $|a_1|$ values versus mean wave slope from the Rayleigh/generalized log-normal distribution. a) is for 20°, b) is for 25°, c) is for 30°, and d) is for 40° incidence angle. Data is for v-pol, downwind case. Thin solid line corresponds to 2 GHz, dashed line corresponds to 3 GHz, dotted line corresponds to 5 GHz, dash/dot line corresponds to 10 GHz, and the bold solid line corresponds to 14 GHz. Asterisks correspond to bins with no data, and circles indicate bins with only one or two minutes of data.

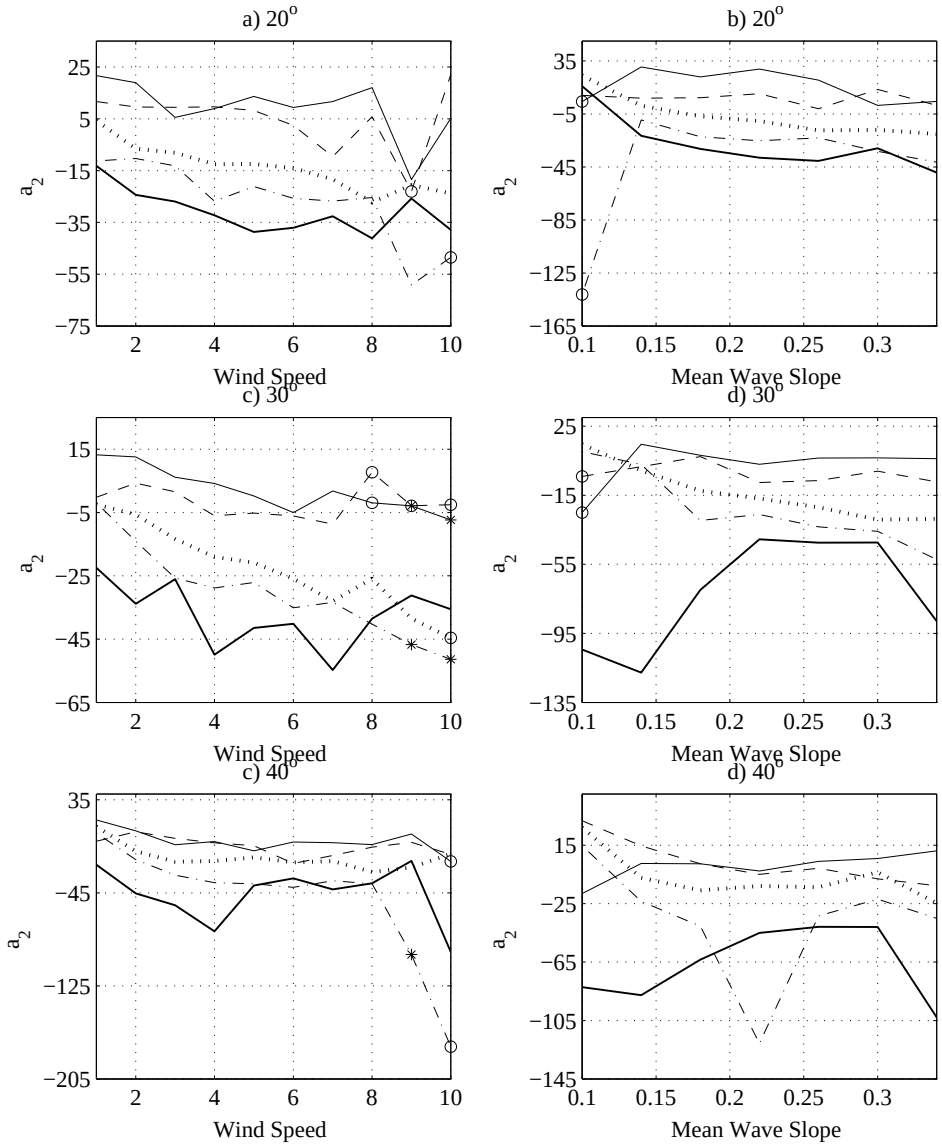

Figure 5.19: Downward trend in a_2 values versus a), c), e) wind speed and b), d), f) mean wave slope from the Rayleigh/generalized log-normal distribution. a) and b) are for 20°, c) and d) are for 30°, and e) and f) are for 40° incidence angle. Data is for v-pol, downwind case. Thin solid line corresponds to 2 GHz, dashed line corresponds to 3 GHz, dotted line corresponds to 5 GHz, dash/dot line corresponds to 10 GHz, and the bold solid line corresponds to 14 GHz. Asterisks correspond to bins with no data, and circles indicate bins with only one or two minutes of data.

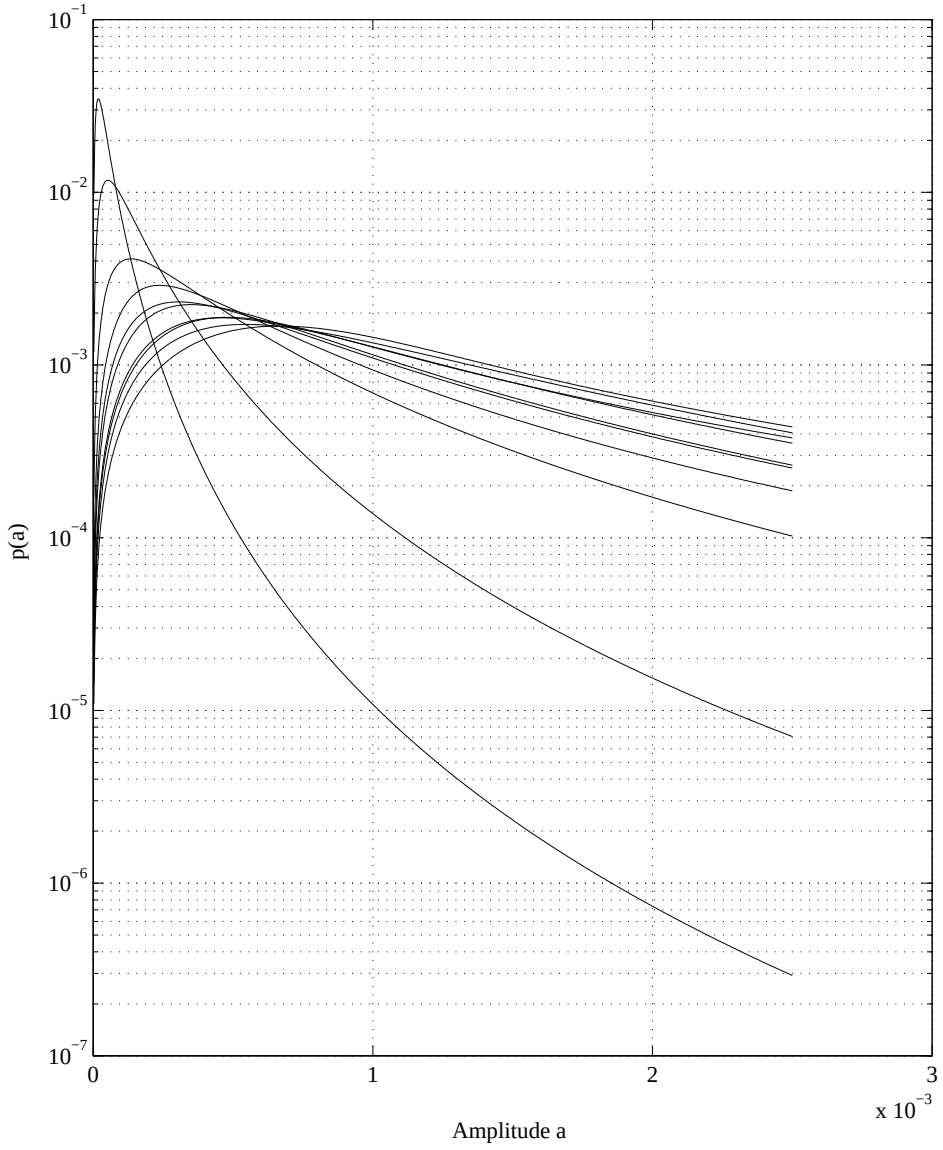

Figure 5.20: Distribution shape progression for the Rayleigh/generalized log-normal distribution according to wind speed. Data is for 10 GHz, v-pol, downwind, 20°, wind speed 1-10 m/s. Distribution with the lowest tail is for 1 m/s wind speed, highest tail is 10 m/s.

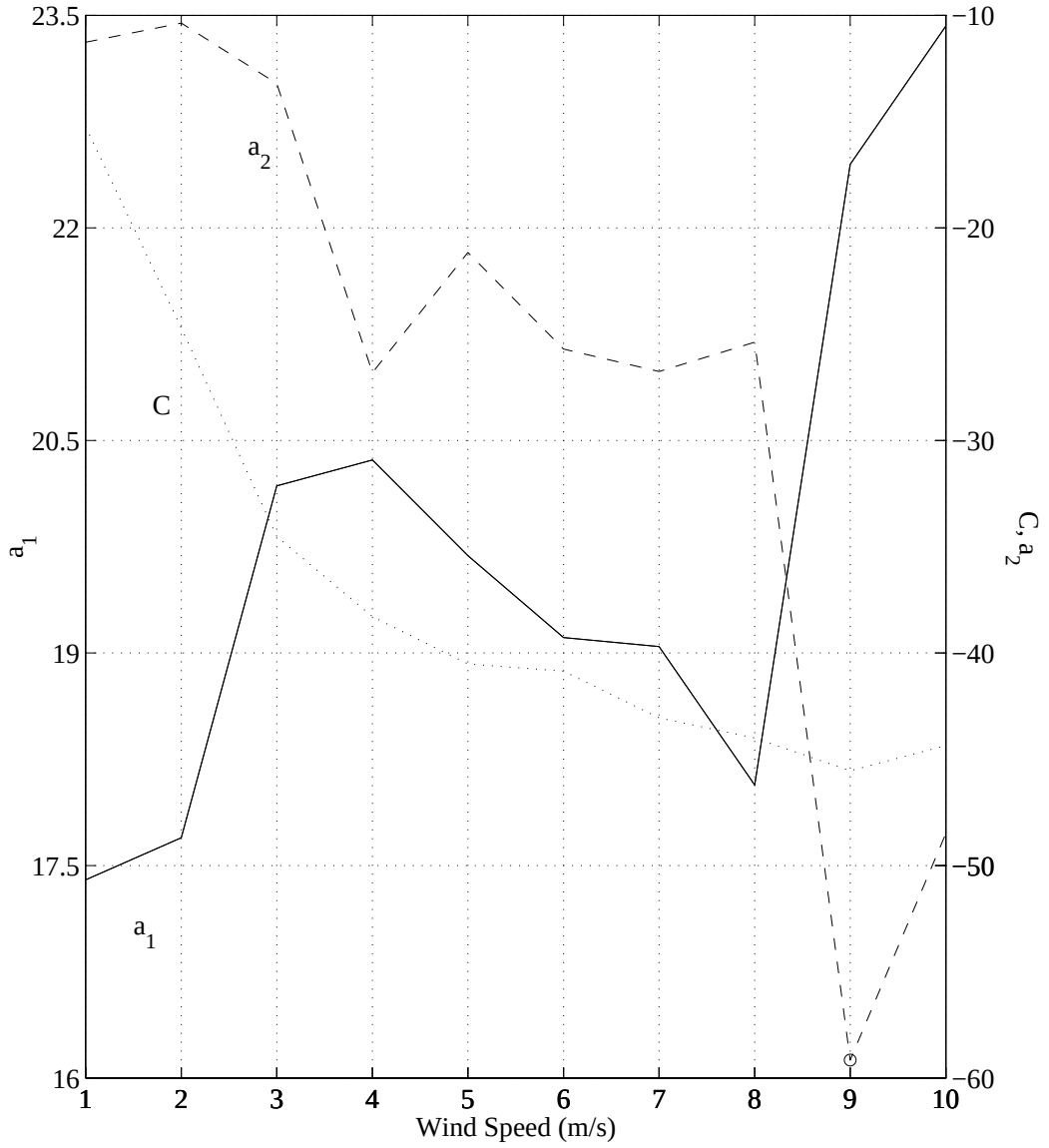

Figure 5.21: a_1, a_2, and C values for the Rayleigh/generalized log-normal distribution for 10 GHz, v-pol, downwind, 20°, wind speed 1-10 m/s. C values are scaled by the relation $20log_{10}(C) - 100$. Solid line represents a_1 values. Dashed line represents a_2 values. Dotted line represents C values.

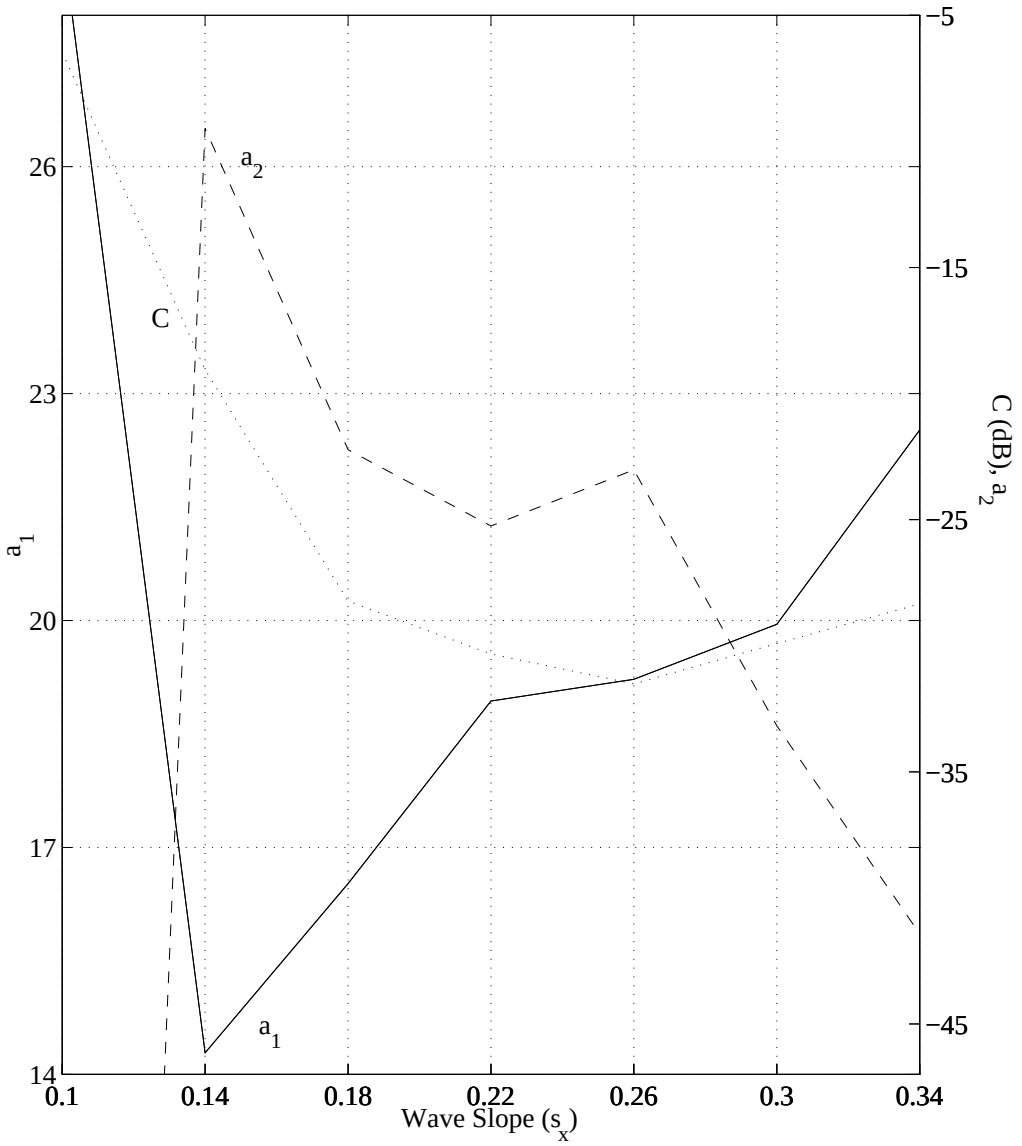

Figure 5.22: a_1, a_2, and C values for the Rayleigh/generalized log-normal distribution for 10 GHz, v-pol, downwind, 20°, mean wave slope 0.1-0.7. C values are scaled by the relation $20log_{10}(C) - 100$. Solid line represents a_1 values. Dashed line represents a_2 values. Dotted line represents C values.

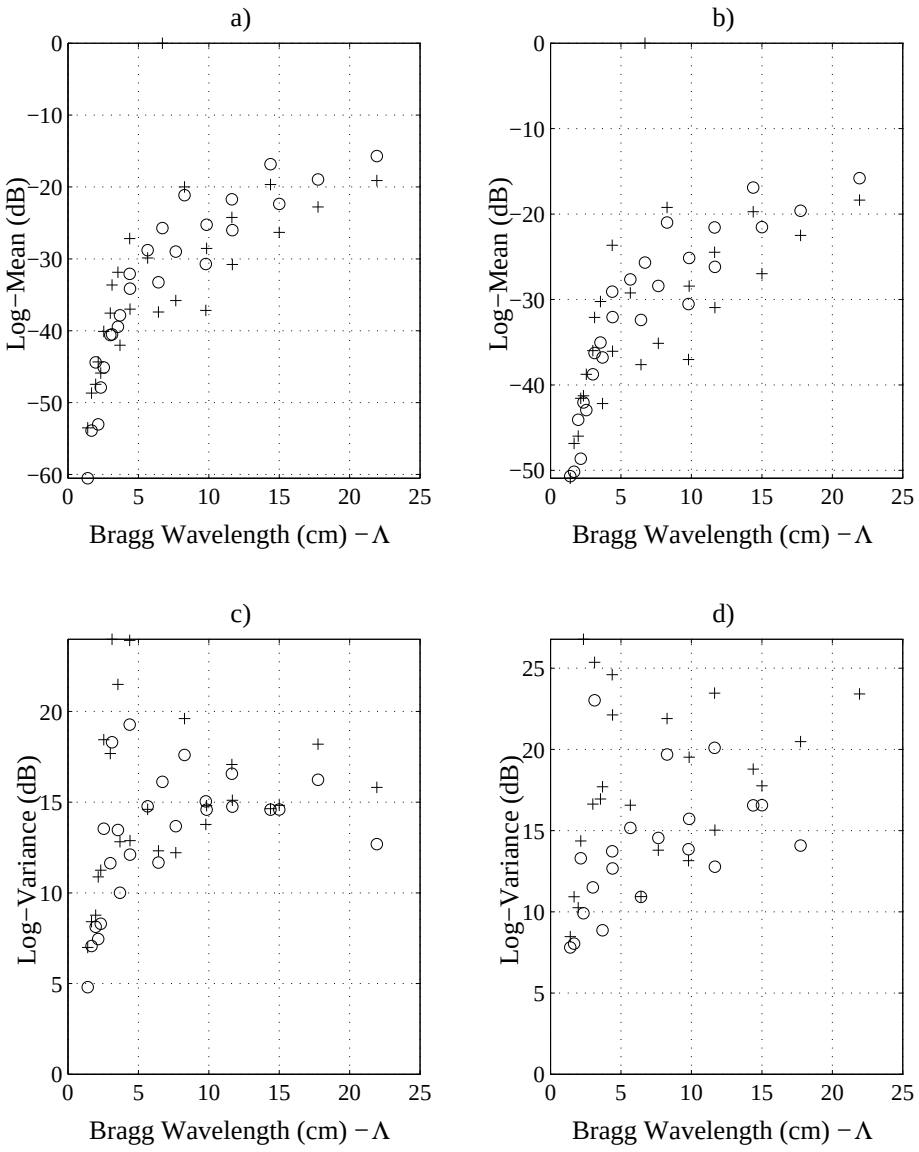

Figure 5.23: Log-mean (μ) and log-variance (σ^2) according to Bragg wavelength (Λ). a) and b) show the mean according to the Bragg wavelength for a (a) wind speed of 4 m/s, and (b) mean wave slope of 0.2. c) and d) show the log-variance according to the Bragg wavelength for the same cases. Circles indicate v-pol, upwind values. Pluses indicate h-pol, upwind values.

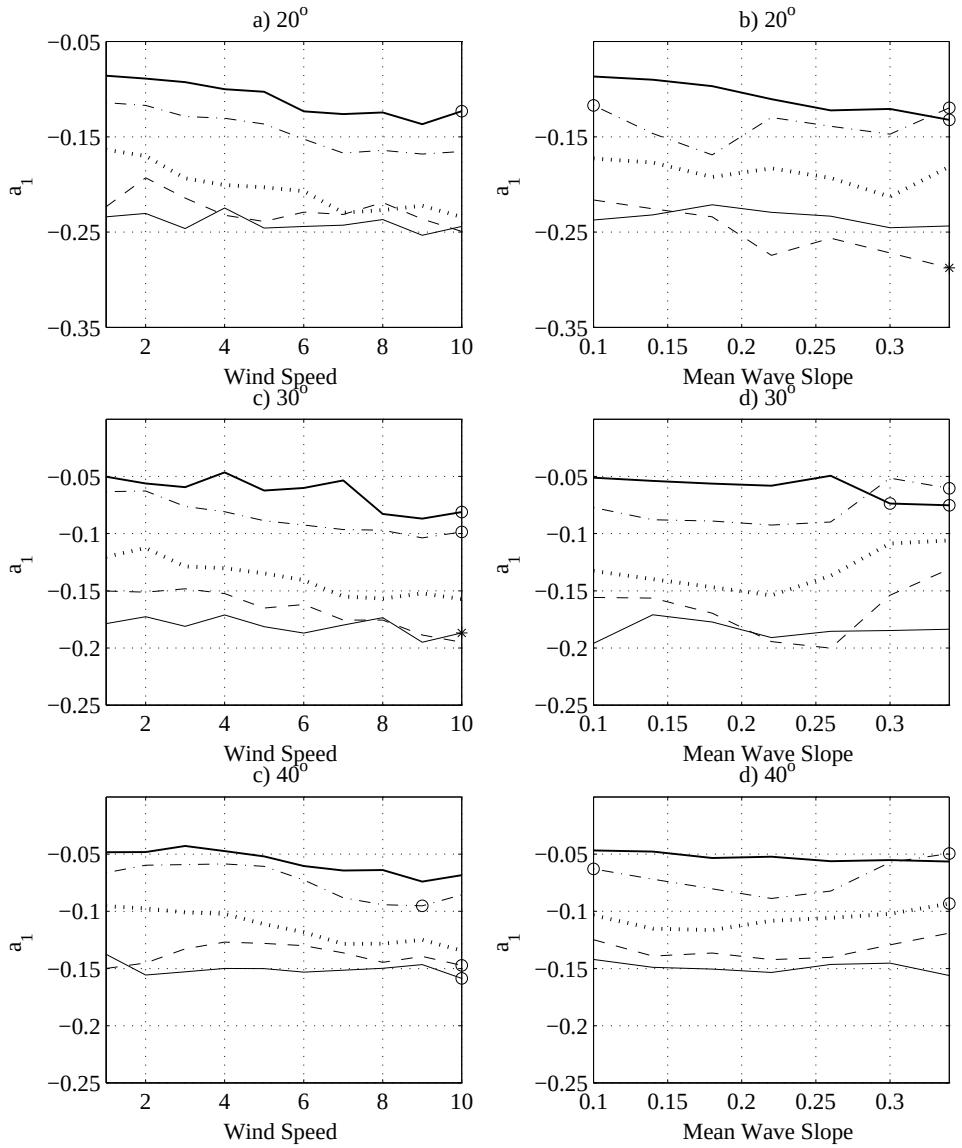

Figure 5.24: Trend in a_1 values for the log-normal distribution. a) and b) are for 20°, c) and d) are for 30°, e) and f) are for 40° incidence angle. Data is for v-pol, upwind case. Thin solid line corresponds to 2 GHz, dashed line corresponds to 3 GHz, dotted line corresponds to 5 GHz, dash/dot line corresponds to 10 GHz, and the bold solid line corresponds to 14 GHz. Asterisks correspond to interpolated values in bins with no data, and circles indicate bins with only one or two minutes of data.

versus mean wave slope (as opposed to the upward trend when plotted versus wind speed). In fact in the vast majority of data cases, the values of C for the log-normal distribution and the log-mean values are less than 1 dB apart. This is not surprising because of the structure of the expression for the mean of the log-normal distribution. An example of these similar trends is given in Fig. 5.25.

The generalized log-normal distribution was also fit to logged YSCAT94 data. The distribution's mean increases predictably as wind speed increases while the means are closely spaced and remaining the same as mean wave slope increases. a_1 values of a generalized log-normal distribution are somewhat noisy, but a flat (especially according to mean wave slope) to slightly upward trend in the parameter is noticeable. a_1 values get larger for larger incidence angles and smaller for higher frequencies. Figure 5.26 illustrates trends in a_1 values for the generalized log-normal distribution. a_2 values of the generalized log-normal distributions are both positive and negative and have a downward trend, often around zero, when plotted versus wind speed and mean wave slope (see Fig. 5.27). C values for the generalized log-normal distribution are almost identical with the corresponding C the values of the log-normal distribution.

5.6 Poor Fits

The Rayleigh/generalized log-normal distribution fits most of the backscatter distributions from YSCAT94 quite well. However, in cases of higher frequencies and higher incidence angles, the Rayleigh/generalized log-normal distribution is not able to fit the backscatter distribution as closely. Figure 5.28 shows one example for 14 GHz, horizontal polarization, 50° incidence angle, and 5 m/s wind speed. Note to the inability of the Rayleigh/generalized log-normal distribution to fit the very low amplitude part of the backscatter distribution. Seeking to find a distribution which better fits the extremely low amplitude section of the backscatter distribution, I considered the Weibull/generalized log-normal distribution.

The Rayleigh/generalized log-normal distribution fits many of the mid-range incidence angle cases extremely well. However, poor fits like those of Fig. 5.28, suggest that some other mechanism may be causing $p(a|\sigma^\circ)$ to be non-Rayleigh.

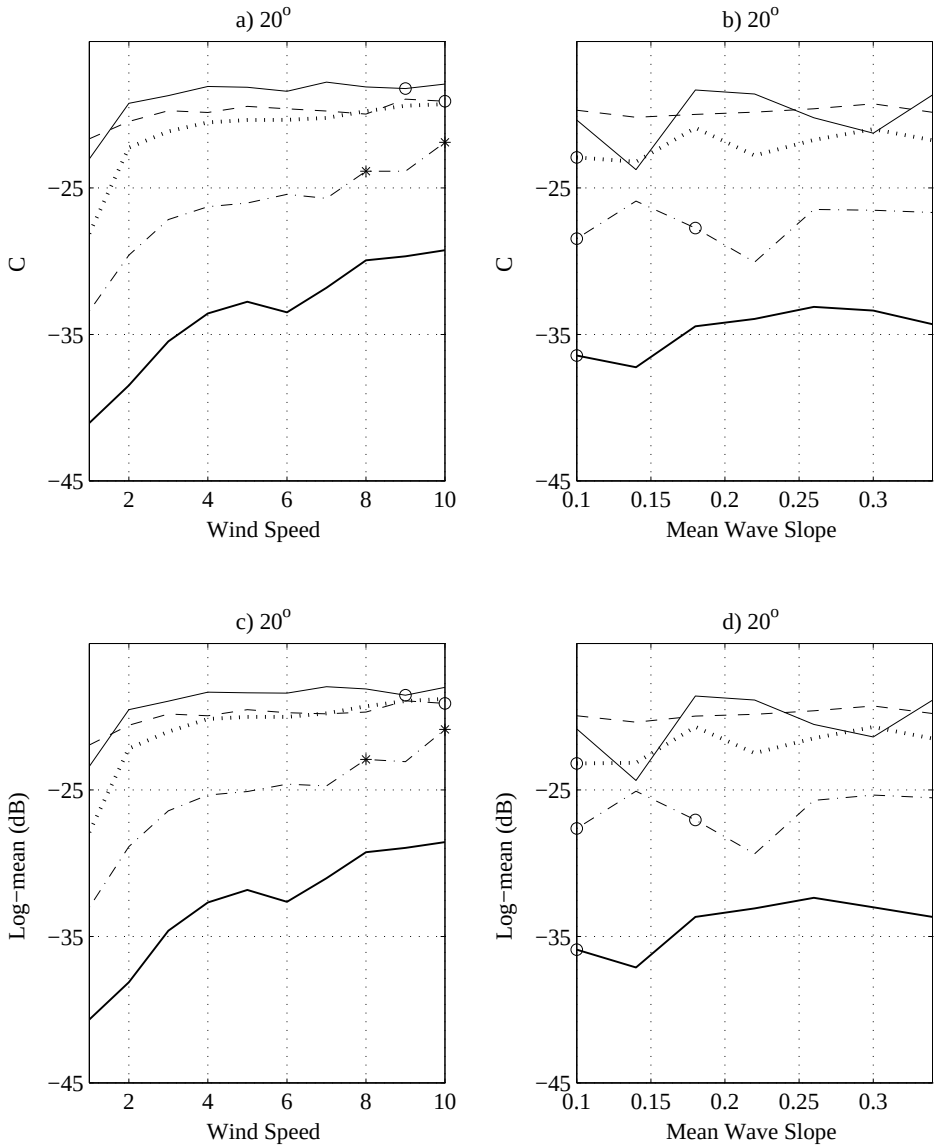

Figure 5.25: Comparison of C values for the log-normal distribution and the log-mean. All subplots are for 20° incidence angle. Data is for h-pol, downwind case. Thin solid line corresponds to 2 GHz, dashed line corresponds to 3 GHz, dotted line corresponds to 5 GHz, dash/dot line corresponds to 10 GHz, and the bold solid line corresponds to 14 GHz. Asterisks correspond to interpolated values in bins with no data, and circles indicate bins with only one or two minutes of data.

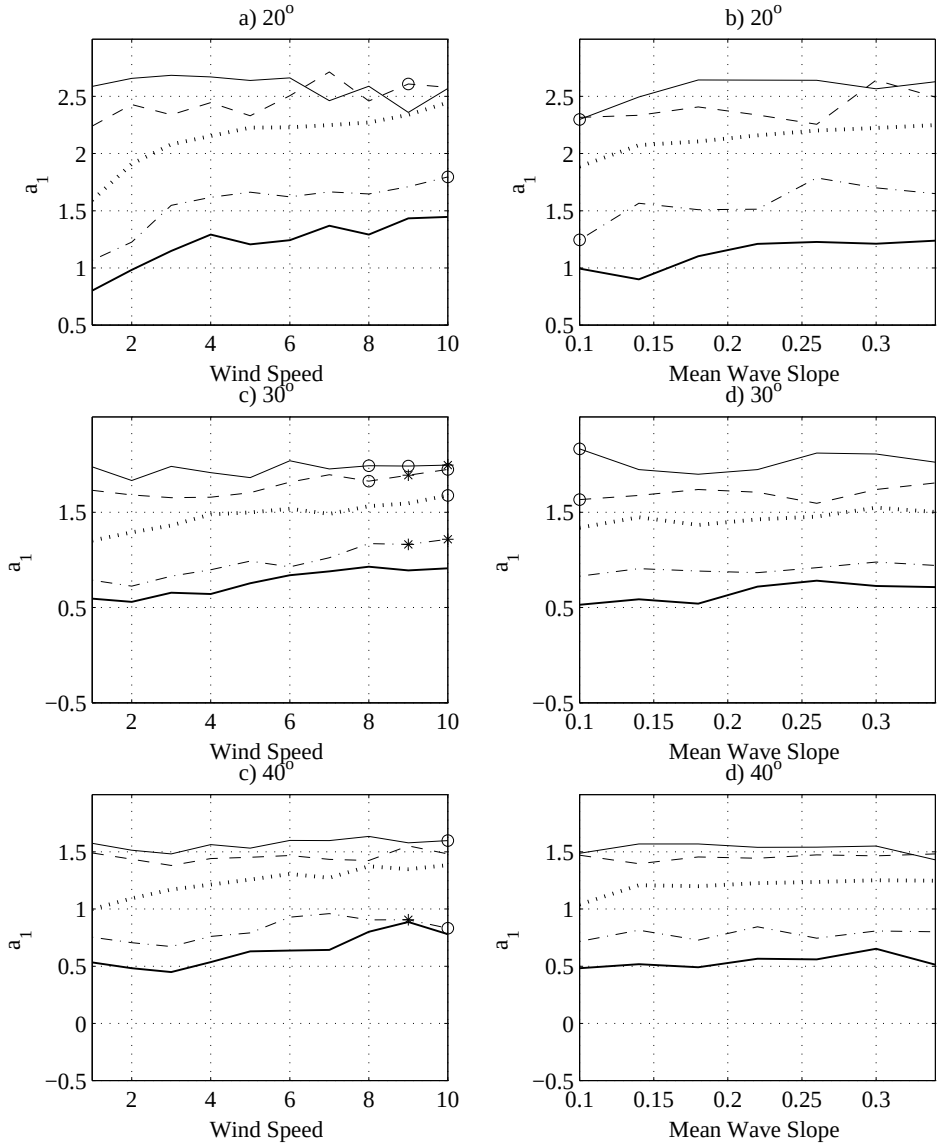

Figure 5.26: Trend in a_1 values for the generalized log-normal distribution. a) and b) are for 20°, c) and d) are for 30°, e) and f) are for 40° incidence angle. Data is for v-pol, downwind case. Thin solid line corresponds to 2 GHz, dashed line corresponds to 3 GHz, dotted line corresponds to 5 GHz, dash/dot line corresponds to 10 GHz, and the bold solid line corresponds to 14 GHz. Asterisks correspond to interpolated values in bins with no data, and circles indicate bins with only one or two minutes of data.

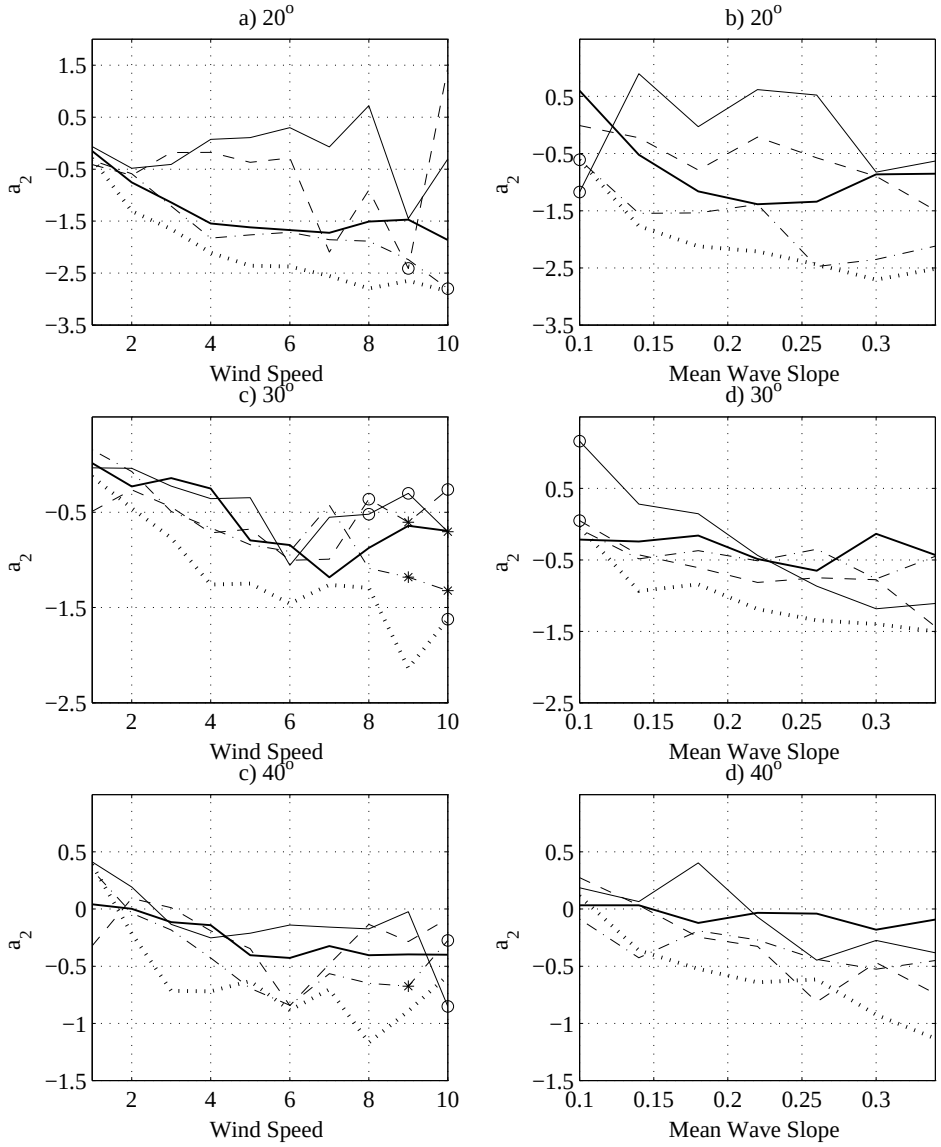

Figure 5.27: Trend in a_2 values for the generalized log-normal distribution. a) and b) are for 20°, c) and d) are for 30°, e) and f) are for 40° incidence angle. Data is for v-pol, downwind case. Thin solid line corresponds to 2 GHz, dashed line corresponds to 3 GHz, dotted line corresponds to 5 GHz, dash/dot line corresponds to 10 GHz, and the bold solid line corresponds to 14 GHz. Asterisks correspond to interpolated values in bins with no data, and circles indicate bins with only one or two minutes of data.

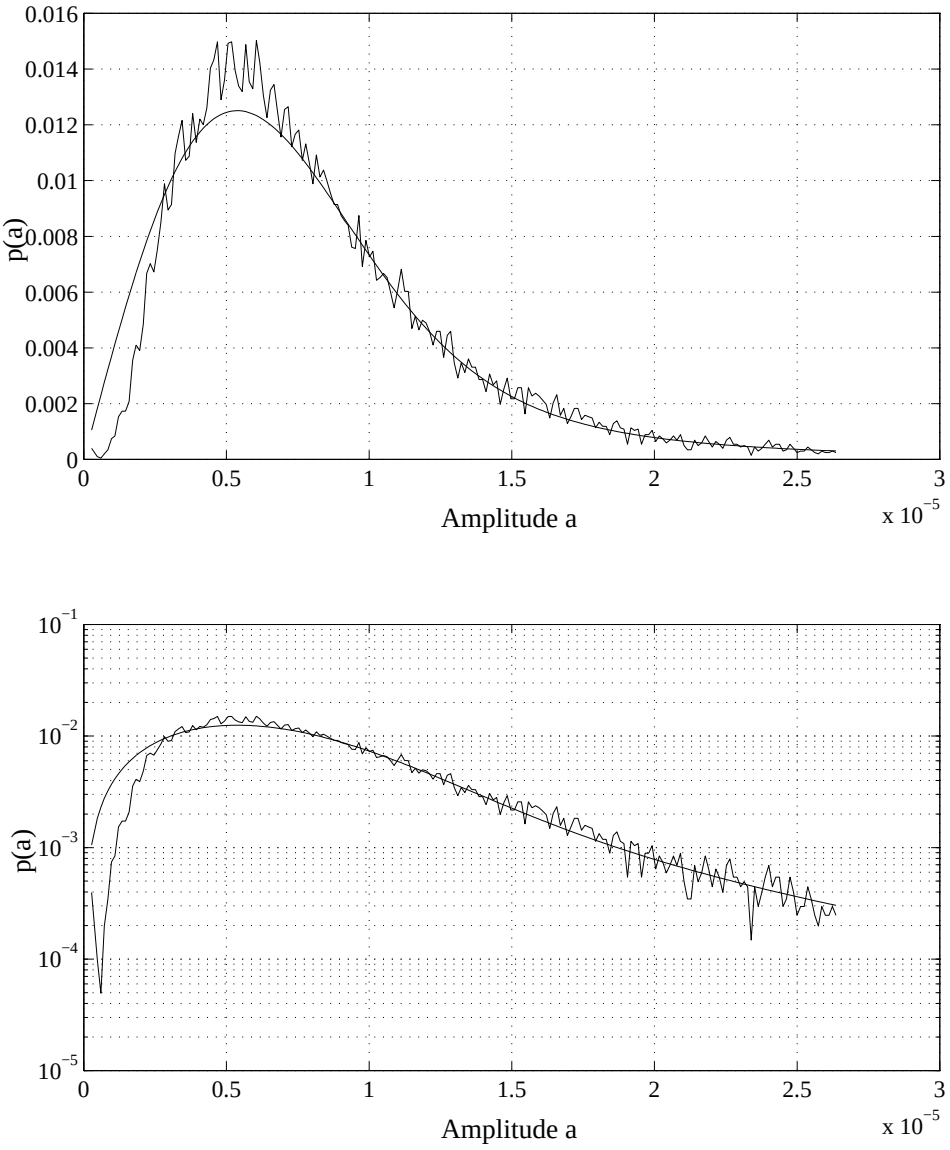

Figure 5.28: Example of the Rayleigh/generalized log-normal distribution as a poor fit. This occurs at higher incidence angles and higher frequencies. Data is for 14 GHz, h-pol, upwind, 50°, and 5 m/s wind speed. Kullback-Liebler distance is 0.108. Parameter values are a_1=5.66, a_2=-49.47, and C=1.9078e10.

Noting that a Rayleigh distribution is a special case of the Weibull distribution, a Weibull/generalized log-normal distribution is considered to determine if it can better match the empirical distributions from YSCAT94.

A Weibull distribution is commonly defined as

$$p(x|\alpha,\beta) = \frac{\beta}{\alpha^\beta}(x)^{\beta-1}e^{(-\frac{x}{\alpha})^\beta}, \tag{5.33}$$

but if the substitutions

$$\sigma^o = \frac{1}{\alpha^2} \quad \text{and} \quad x \mapsto a \tag{5.34}$$

are made, then leaving β as a free parameter, Eq. (5.33) may be written as

$$p(a|\sigma^o,\beta) = \beta(\sigma^o)^{\frac{\beta}{2}}(a)^{\beta-1}e^{-(a)^\beta(\sigma^o)^{\frac{\beta}{2}}}. \tag{5.35}$$

Equation (5.35) reduces directly to the Rayleigh distribution for the case $\beta = 2$. Consequently, if β is left as a free parameter, then $p(a)$ can be expressed as

$$\begin{aligned} p(a) &= \int_0^\infty \underbrace{p(a|\sigma^\circ)}_{\substack{Weibull \\ Eq.\ (5.35)}} \underbrace{p(\sigma^\circ)}_{Eq.\ (5.18)}\ d\sigma^\circ \\ &= \int_0^\infty \underbrace{\frac{\beta(\sigma^o)^{\frac{\beta}{2}}a^\beta}{ae^{(a)^\beta(\sigma^o)^{\frac{\beta}{2}}}}}_{\substack{p(a|\sigma^\circ,\beta) \\ Weibull}} \underbrace{\left(\frac{\exp\left(\frac{a_1^2}{4\sigma_x^2a_2^2}\right)\exp\left(\pm\frac{a_1\sqrt{a_1^2+4a_2\ln\frac{\sigma^\circ}{C}}}{4\sigma_x^2a_2^2}\right)\left(\frac{\sigma^\circ}{C}\right)^{\frac{1}{2a_2\sigma_x^2}}}{\sigma_x\sigma^\circ\sqrt{\pi}\sqrt{a_1^2+4a_2\ln\frac{\sigma^\circ}{C}}}\right)}_{p(\sigma^\circ)\ \ [Eq.\ (5.18)]} d\sigma^\circ. \end{aligned} \tag{5.36}$$

In terms of s_x, Eq. (5.36) becomes

$$p(a) = \int_{-\infty}^\infty \underbrace{\left(\frac{\beta}{a}a^\beta\frac{C^{\frac{\beta}{2}}\exp\left(\beta\frac{a_1s_x+a_2s_x^2}{2}\right)}{\exp\left(a^2C^{\frac{\beta}{2}}\exp\left(\beta\frac{a_1s_x+a_2s_x^2}{2}\right)\right)}\right)}_{p(a|\sigma^o(s_x),\beta)} \underbrace{\frac{e^{\frac{-s_x^2}{2\sigma_x^2}}}{\sqrt{2\pi}\sigma_x}}_{p(s_x)} ds_x. \tag{5.37}$$

Equation (5.36) will be referred to as the Weibull/generalized log-normal distribution. This distribution is fit to the data in Fig. 5.28 using a procedure similar to the one described in Section 5.4. The resulting fit to the data shown in Fig. 5.28 is shown in Fig. 5.29 as a solid line while the Rayleigh/generalized log-normal distribution fit is shown as a dashed line. The Weibull/generalized log-normal distribution

possesses the added flexibility necessary to fit the indented shape the empirical distribution exhibits at extremely low amplitudes. The Kullback-Leibler distance is improved by 38% by using the Weibull/generalized log-normal distribution rather than the Rayleigh/generalized log-normal distribution.

The Weibull/generalized log-normal distribution is needed in cases where the backscatter distribution indents at extremely low amplitudes instead of rising immediately. One convenient measure of whether the Weibull/generalized log-normal distribution is suited to a given backscatter distribution is the β parameter. If β is near 2, then the Weibull/generalized log-normal distribution is essentially Rayleigh/generalized log-normal distribution. For the distribution illustrated in Fig. 5.29, β is 3.24. This indicates a significant departure from the Rayleigh/generalized log-normal distribution.

For mid-range incidence angles, β is indeed nearly equal to two. For example, for the case of 10 GHz, vertical polariztion, upwind, and 20° incidence angle, β values for 1-10 m/s wind speeds have an mean value of 2.05, with a standard deviation of 0.057. β values for other frequencies at mid-range incidence angles are similar.

For higher incidence angles, β values tend to increase to within the three to four range. For the same data case above, but at 40° incidnece angle, the mean of β is 3.00 with a standard deviation of 0.47. Thus, the Weibull/generalized log-normal distribution captures the behavior of YSCAT94 backscatter distributions for mid-range and higher range incidence angles. Since the maximum incidence angle for the YSCAT94 experiment is 60°, there is no information as to the accuracy of the Weibull/generalized log-normal distribution for modelling backscatter at the grazing or near-grazing incidence angle regime. Figure 5.30 illustrates how β changes according to incidence angle for incidence angles of 0° (nadir), 10°, 20°, 25°, 30°, 40°, 50°, and 60°. The solid line represents mean β values (averaged over 1-10 m/s wind speeds), with errorbars indicating the standard deviation.

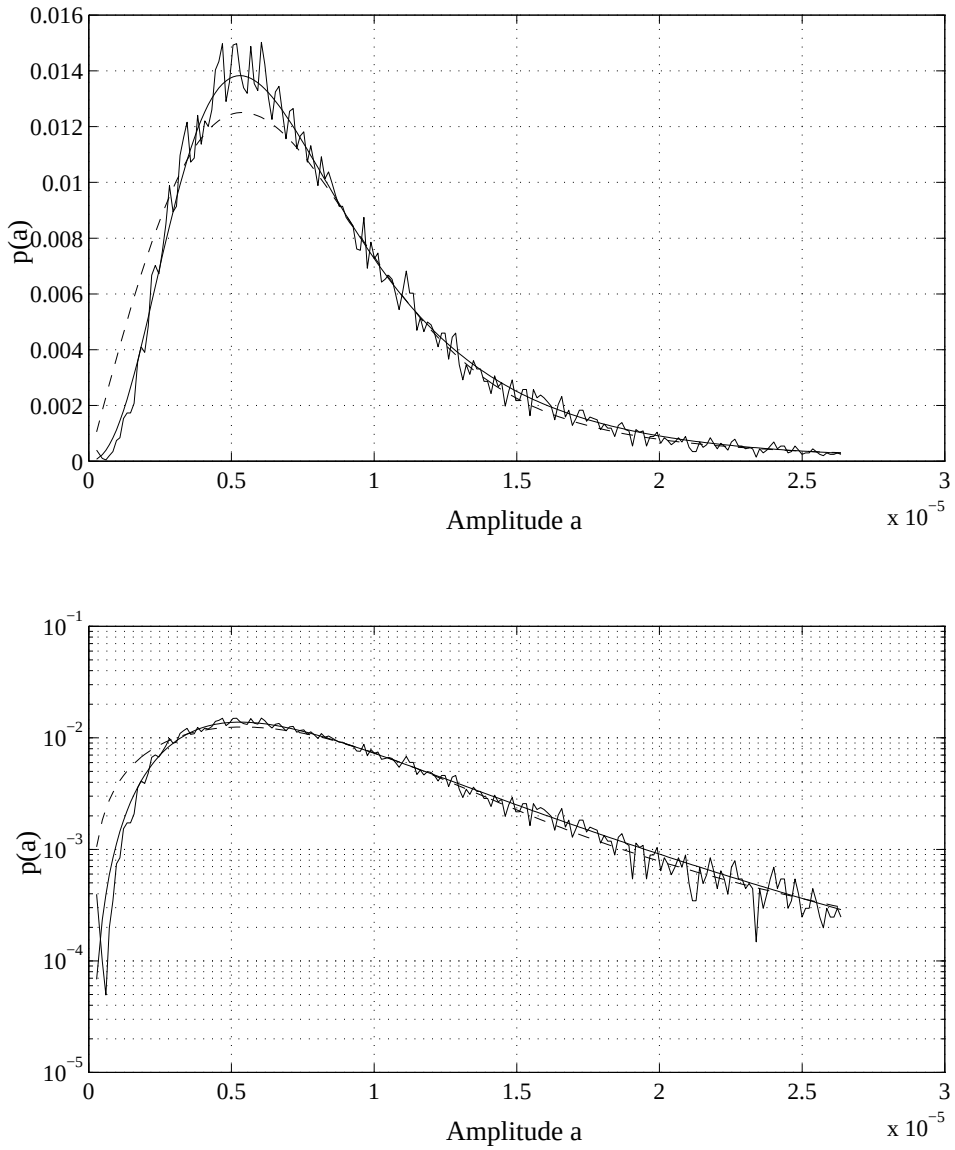

Figure 5.29: Weibull/generalized log-normal distribution (solid curve) fit to data at 14 GHz, h-pol, upwind, 50°, and 5 m/s wind speed. Dashed line is Rayleigh/generalized log-normal distribution fit. Kullback-Liebler distance is 0.067 as opposed to 0.108 using the Rayleigh/generalized log-normal distribution (dashed line). Parameter values are a_1=4.76, a_2=-5.77, C=3.25e6, and β=3.24.

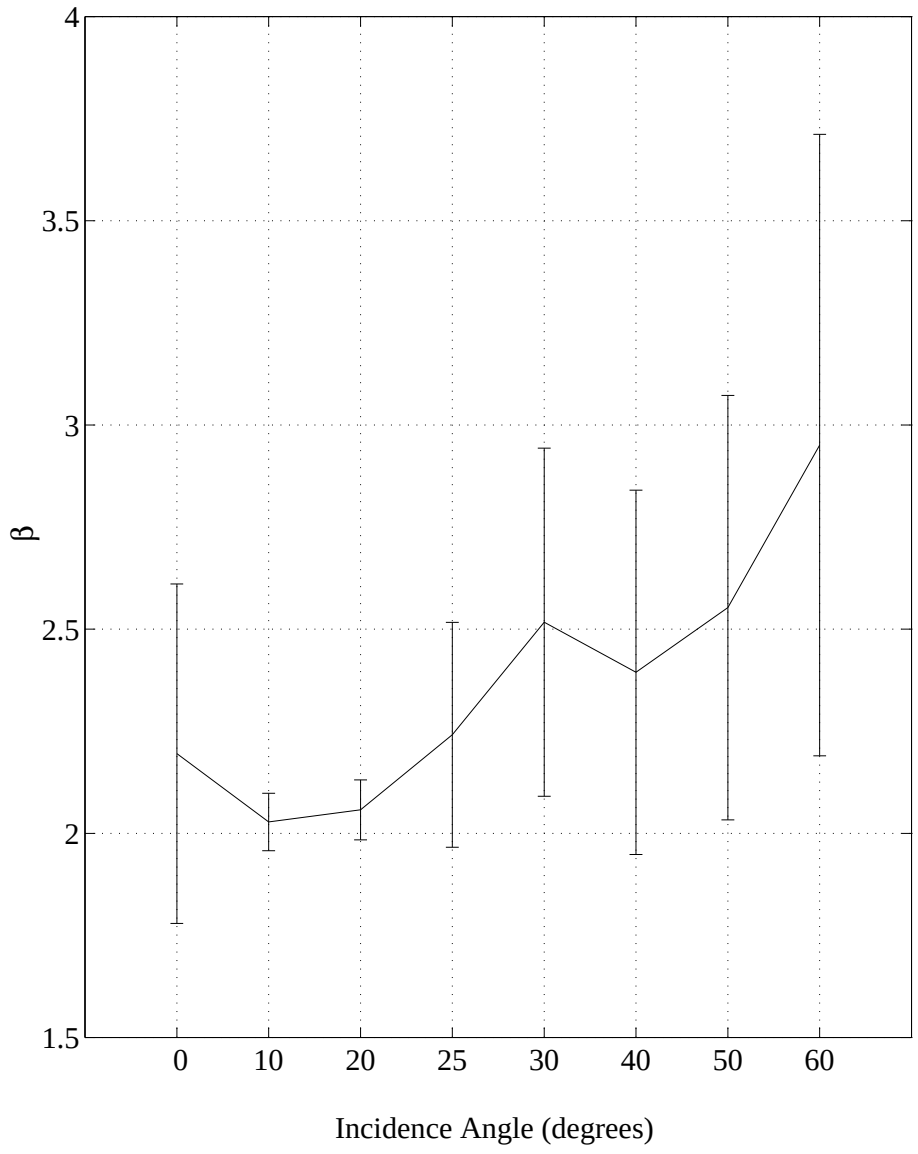

Figure 5.30: Change in β values according to incidence angle. Solid line represents mean β values (averaged over 1-10 m/s wind speeds), with errorbars indicating the standard deviation. Data is for the 10 GHz, v-pol, downwind case.

Chapter 6

Summary

The purpose of this thesis is to present a study of the microwave backscatter distributions from the sea surface. By parameterizing and classifying radar backscatter distributions, a better understanding of the air-sea interface is obtained. When trends in parameters characterizing microwave backscatter distributions are identified and tabulated versus wind speed and mean wave slope, a clearer understanding of the relationship between the environmental parameters and radar backscatter statistics emerges. Understanding this relationship is key in interpreting data from both tower-mounted and spaceborne microwave scatterometers.

The radar backscatter analyzed in this thesis was collected by the YSCAT radar scatterometer during the six month long YSCAT94 experiment which lasted from June to November, 1994. The experiment location was the WAVES research platform owned by the Canada Centre for Inland Waters (CCIW) located 1 km east of Hamilton, Ontario, Canada. The water depth is about twelve meters at this location, and YSCAT was mounted about ten meters above the water surface. The prevailing winds are westerly and generally produce fetches of 1-9 km. RMS wave heights during this experiment were generally less than 0.5 m except under unusual wind conditions.

YSCAT is a coherent, continuous wave, ultrawideband scatterometer which provided radar backscatter measurements at center frequencies of 2, 3.05, 5.3, 10.02, and 14 GHz. Data was collected at both horizontal and vertical polarizations. YSCAT also recorded data at incidence angles of 0° (nadir), 10°, 20°, 25°, 30°, 40°, 50°, and 60°. YSCAT94 data collected when the radar was pointed within 20° of the true when direction are classified as downwind, and data collected when the radar was pointed

within 20° of the opposite of the true wind direction are classified as upwind. Thus, YSCAT collected data under a wide variety of radar and environmental parameters during the YSCAT94 experiment.

A low wind speed rolloff was observed in YSCAT94 data. Previously, this rolloff had been observed only in airship [6] and carefully controlled wave tank [5] scatterometer data. The wind speed at which this rolloff occurs (Υ) was tabulated using a regression estimation analysis. An Epanechnikov kernel was used to smooth the one minute averages of YSCAT94 data for for each case. Υ was calculated using a heuristic method and determined to be in the range of 3-6 m/s for YSCAT94 data.

The mean, variance, log-mean, and log-variance were all tabulated versus wind speed and mean wave slope. The full report of these parameters are calculated for wind speed and mean wave slope in Appendices B and C respectively. While the mean, variance, and log-mean generally increase in a power relationship with wind speed, the log-variance remains remarkably unresponsive to wind speed. These and other general trends were identified and are comparable to trends of similar data sets.

The log-normal and generalized log-normal distributions were fit to empirical histograms of YSCAT94 logged data. General trends and typical values for the a_1 and C parameters (in the case of the log-normal) and the a_1, a_2, and C parameters (in the case of the generalized log-normal) were identified. C values for both cases followed the trends of the mean for the same data set, while the other parameters controlled the shape. The fit of the generalized log-normal distribution to YSCAT94 logged data was better than the fit for the lognormal distribution in all cases as measured by the Kullback-Leibler distance.

Following Gotwols and Thompson [8], the probability distribution function for the amplitude of the backscatter was calculated based on conditional probabilities as

$$p(a) = \int_0^\infty p(a|\sigma^\circ)p(\sigma^\circ)\ d\sigma^\circ \tag{6.1}$$

where $p(a|\sigma^\circ)$ was assumed to be Rayleigh distributed, and the distribution for $p(\sigma^\circ)$ was shown to be either the log-normal distribution for the case of horizontal polarization, or the generalized log-normal distribution for the case of vertical polarization. This model was based on a second degree polynomial in log space which modeled the normalized radar cross section (σ°) predicted by the composite model of a sea containing waves modeled by the Donelan spectrum. Therefore, the combined Rayleigh/generalized log-normal distribution derived from Eq. (6.1) was fit to YSCAT94 empirical unlogged data distributions.

The fitting method used a combination of bounded unconstrained, unbounded unconstrained, and random perturbation methods in order to find the "best" fit according to the Kullback-Leibler distance. To provide good seed values to the fitting methods, the mean and variance of the generalized log-normal distribution were derived. The fitting method described in detail in Section 5.4 proved to find the best fit for YSCAT94 data in over 99% of the data cases.

Trends in the Rayleigh/generalized log-normal distribution parameters a_1, a_2, and C were identified. C displayed a surprising, very distinct trend with an inverse relationship to the mean: data cases with greater means corresponded to smaller values for C. The a_1 and a_2 parameters also displayed trends when considered versus wind speed and mean wave slope (see Section 5.5 for a discussion of the observed trends of these parameters). Using parameters extracted from the backscatter distributions, a more direct link may be forged between radar system parameters and environmental parameters.

The Rayleigh/generalized log-normal distribution model was found to fit YSCAT94 backscatter distributions quite well at mid-range incidence angles. However, it was also found that the Rayleigh/generalized log-normal distribution is unable to capture the behavior in the extremely low amplitude portions of the high incidence angle backscatter distributions. To fit these low amplitude portions better, a more general distribution, the Weibull/generalized log-normal distribution, was developed. The Weibull/generalized log-normal distribution reduces to the Rayleigh generalized log-normal distribution for mid-range incidence angles. At the same time, the

Weibull/generalized log-normal distribution was able to capture the behavior of the extremely low amplitude portions of the backscatter distributions at high incidence angles. β values extracted by fitting the Weibull/generalized log-normal distribution to YSCAT94 data are tabulated in Appendix D.

6.1 Future Research

The main effort of this thesis is to observe, identify, tabulate, and characterize trends and patterns in the YSCAT94 backscatter distributions. Much research is still needed in order to understand the causes behind the observations made in this thesis. While noticing the low wind speed rolloff is potentially useful result, it is left to future researchers to discover more exactly the causes and consequences of that phenomenon. Similarly, while noticing that the Weibull/generalized log-normal distribution fit the empirical histograms better under some conditions may be interesting, research is needed to explain why this is the case. Wedge scattering, wave breaking or some other scatterer may be causing the backscatter distribution to change shape. In addition, a method which parameterizes backscatter distributions according to both wind speed and mean wave slope simultaneously may prove fruitful.

Specifically, the physics which cause the shape of the backscatter distribution to change at higher incidence angles, and the fundamental principles involved in the low wind speed rolloff need to be studied. Questions such as: What factors are important in determining at what wind speed the rolloff of the normalized radar cross section starts and stops and what scattering mechanisms become either more or less dominant as the incidence angle increases and causes the backscatter distribution to more closely resemble a Weibull/generalized log-normal distribution rather than a Rayleigh/generalized log-normal distribution will need to be the topic of future research.

Appendix A

Estimated Low Wind Speed Rolloff Υ

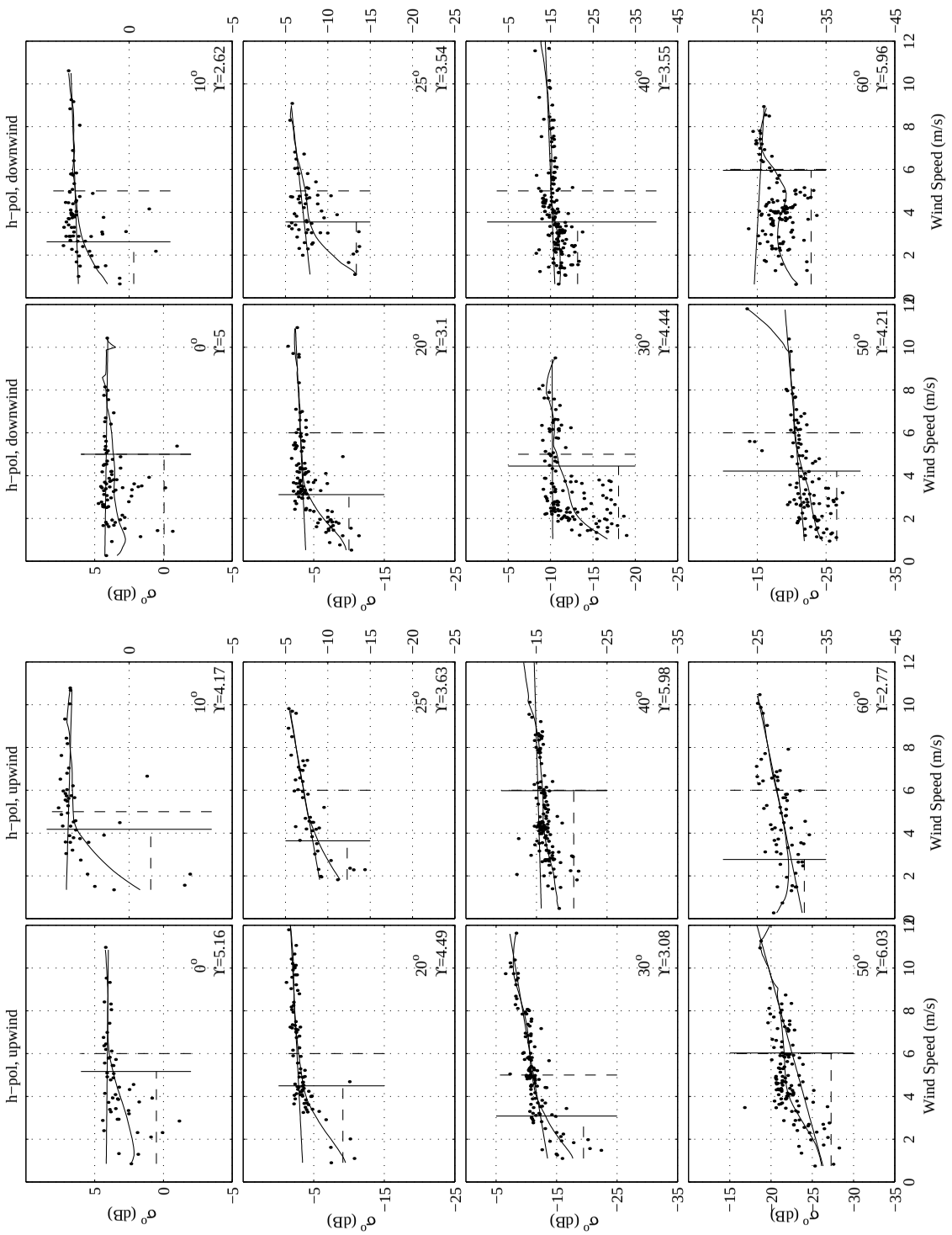

Figure A.1: Low wind speed rolloff (Υ) values for 2 GHz, h-pol, upwind and downwind. Υ is indicated by the solid vertical line. Solid curved line is the regression fit using an Epanechnikov kernel. Dashed vertical line is high wind speed delineation. The solid horizontal line is the linear fit to high wind speed σ° values. Dashed horizontal line is the mean of the five lowest σ° values.

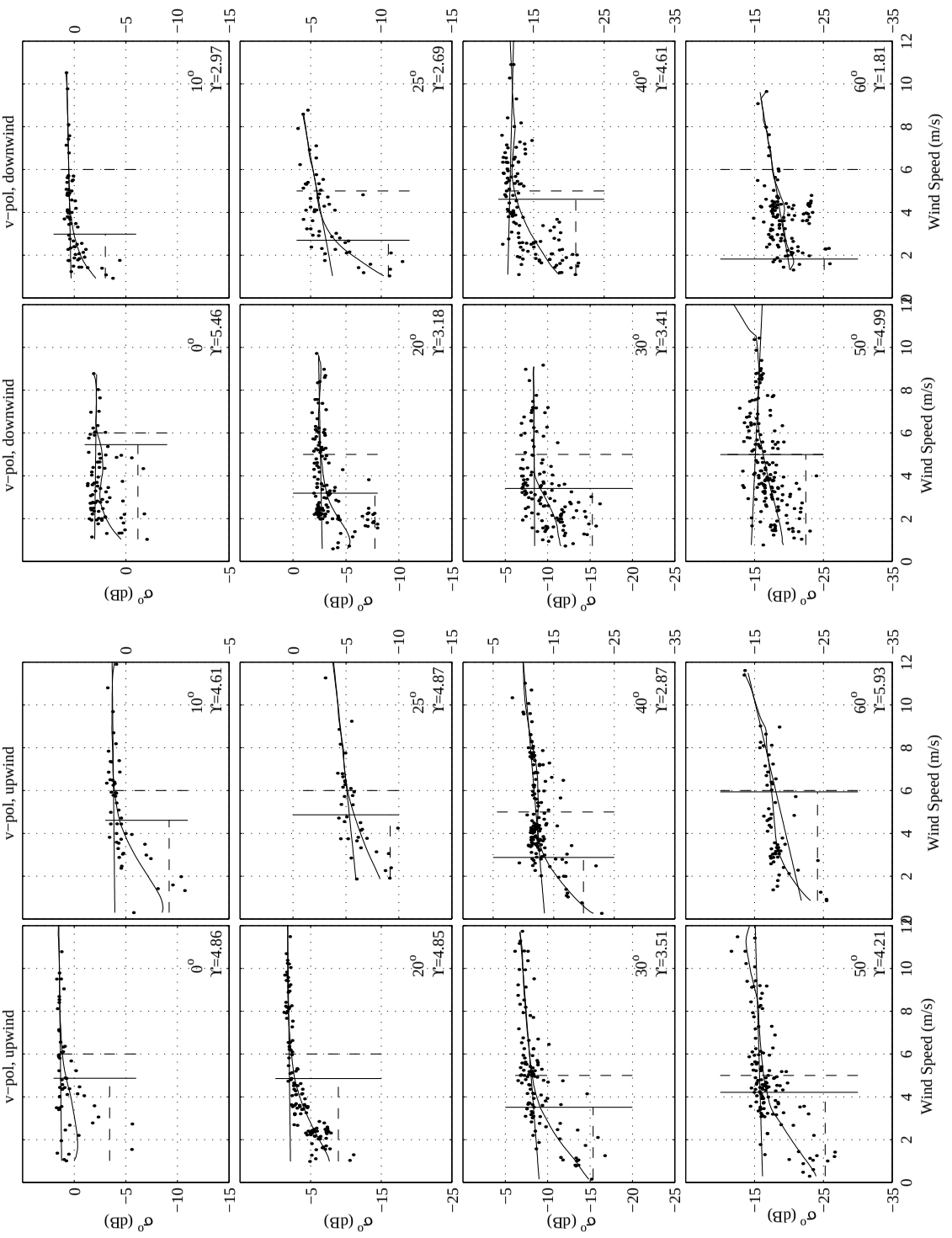

Figure A.2: Low wind speed rolloff (Υ) values for 2 GHz, v-pol, upwind and downwind. Υ is indicated by the solid vertical line. Solid curved line is the regression fit using an Epanechnikov kernel. Dashed vertical line is high wind speed delineation. The solid horizontal line is the linear fit to high wind speed σ° values. Dashed horizontal line is the mean of the five lowest σ° values.

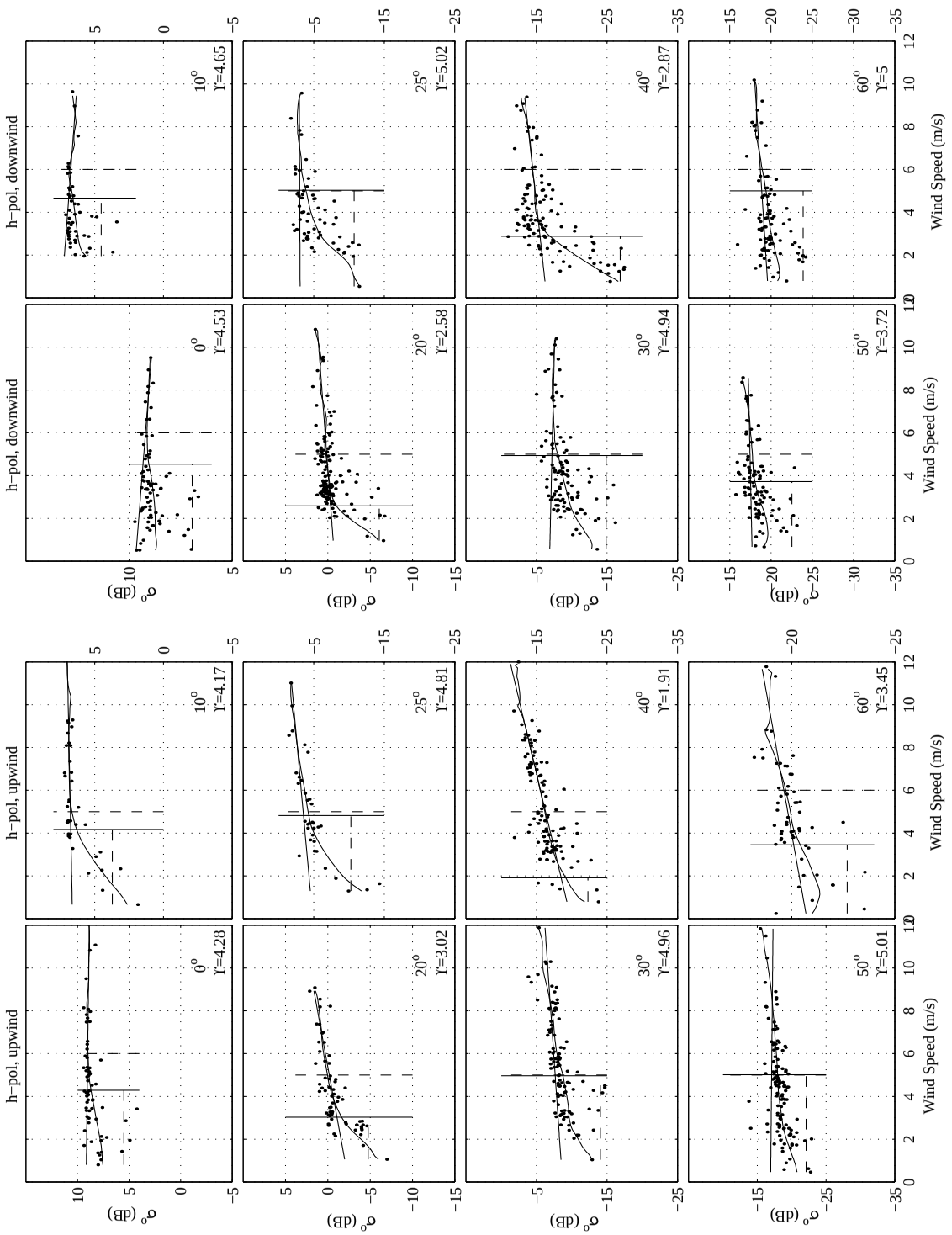

Figure A.3: Low wind speed rolloff (Υ) values for 3 GHz, h-pol, upwind and downwind. Υ is indicated by the solid vertical line. Solid curved line is the regression fit using an Epanechnikov kernel. Dashed vertical line is high wind speed delineation. The solid horizontal line is the linear fit to high wind speed σ° values. Dashed horizontal line is the mean of the five lowest σ° values.

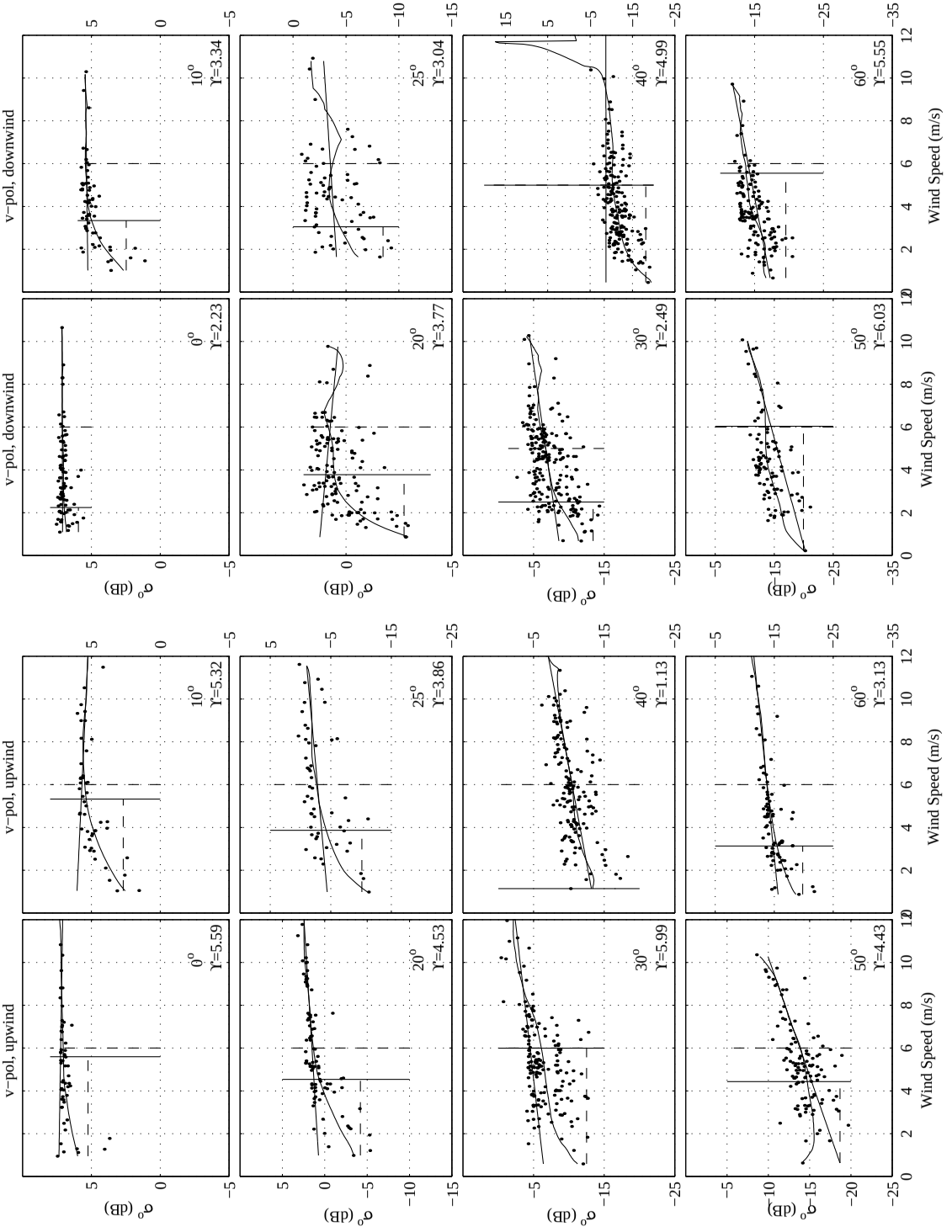

Figure A.4: Low wind speed rolloff (Υ) values for 3 GHz, v-pol, upwind and downwind. Υ is indicated by the solid vertical line. Solid curved line is the regression fit using an Epanechnikov kernel. Dashed vertical line is high wind speed delineation. The solid horizontal line is the linear fit to high wind speed σ° values. Dashed horizontal line is the mean of the five lowest σ° values.

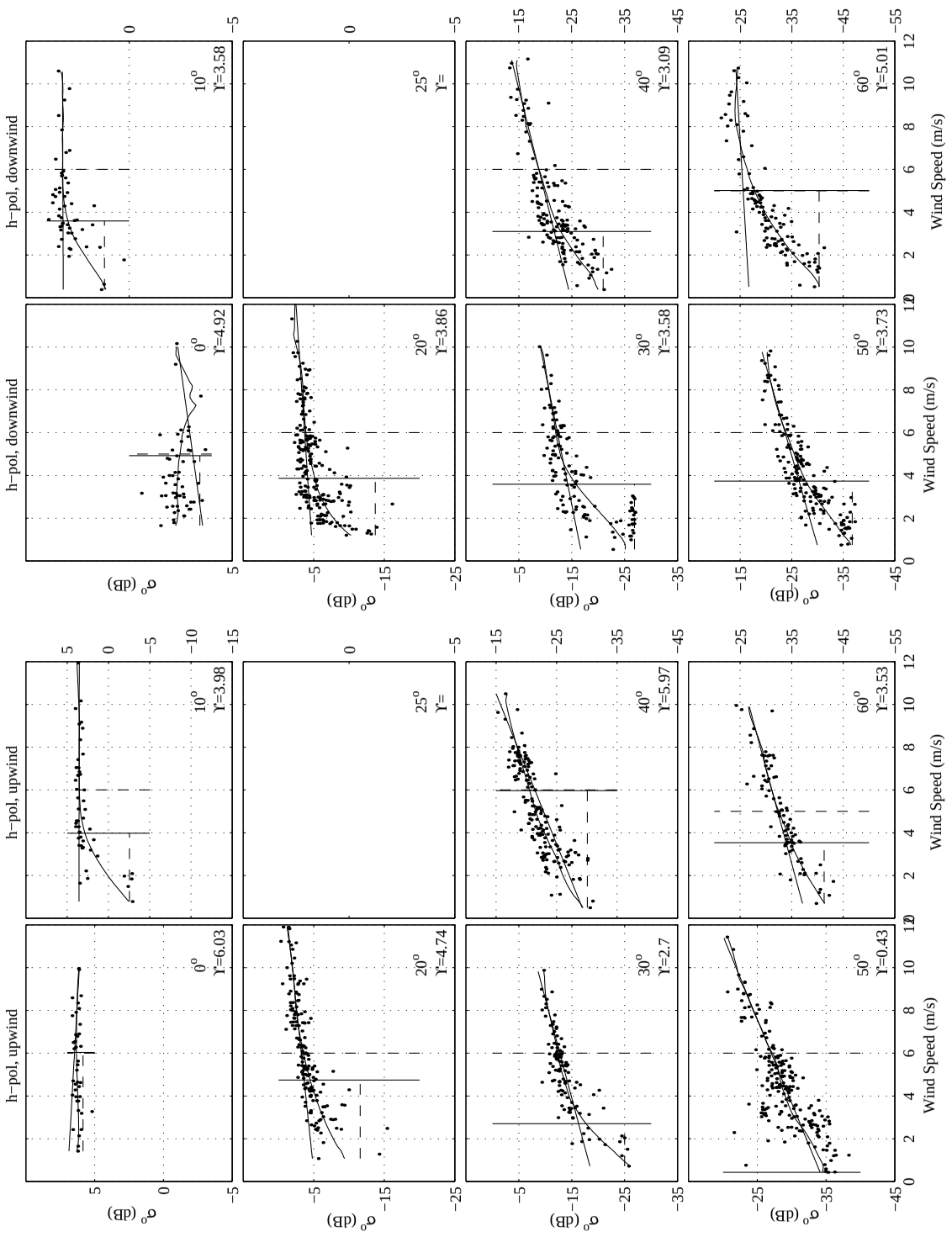

Figure A.5: Low wind speed rolloff (Υ) values for 5 GHz, h-pol, upwind and downwind. Υ is indicated by the solid vertical line. Solid curved line is the regression fit using an Epanechnikov kernel. Dashed vertical line is high wind speed delineation. The solid horizontal line is the linear fit to high wind speed σ° values. Dashed horizontal line is the mean of the five lowest σ° values.

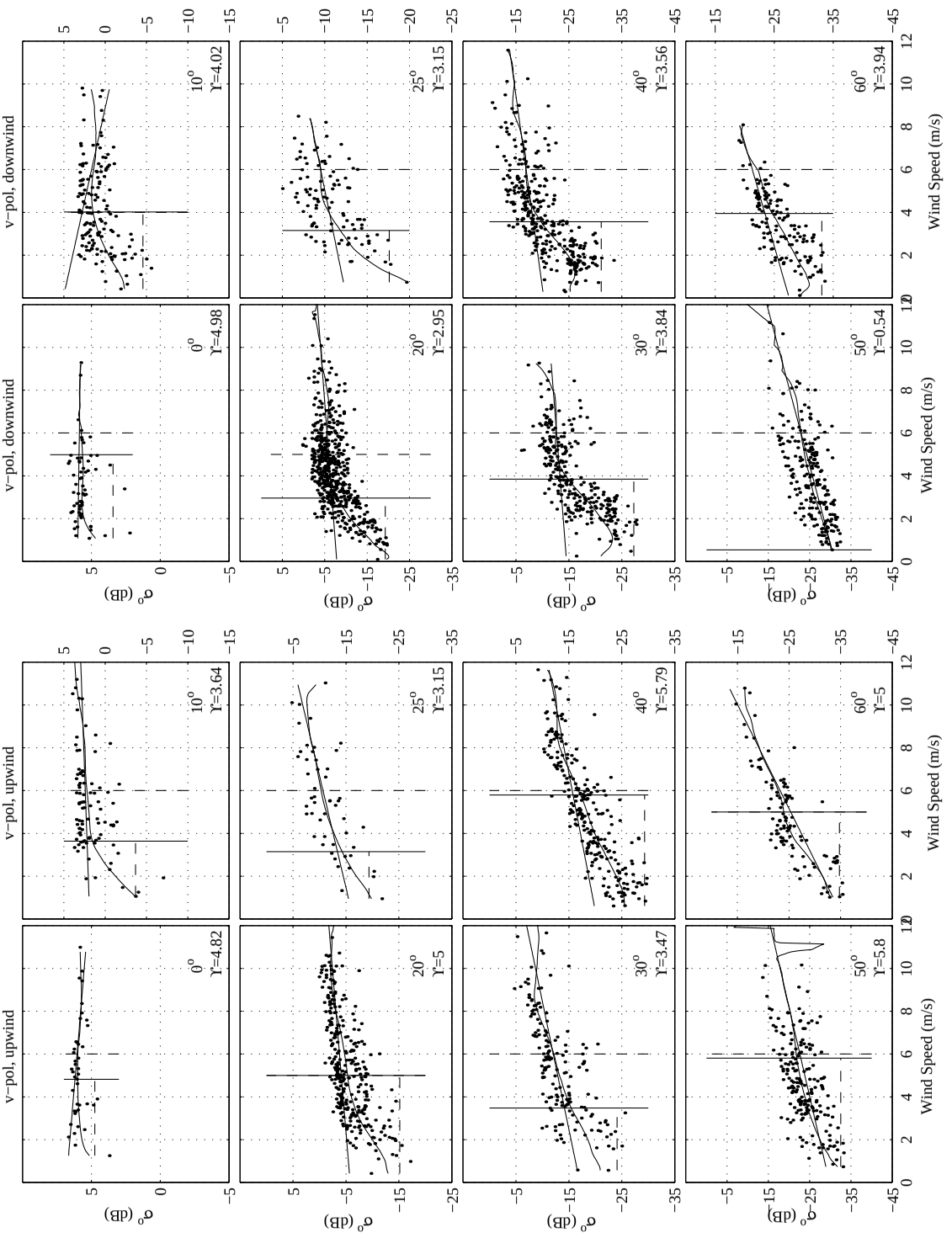

Figure A.6: Low wind speed rolloff (Υ) values for 5 GHz, v-pol, upwind and downwind. Υ is indicated by the solid vertical line. Solid curved line is the regression fit using an Epanechnikov kernel. Dashed vertical line is high wind speed delineation. The solid horizontal line is the linear fit to high wind speed σ° values. Dashed horizontal line is the mean of the five lowest σ° values.

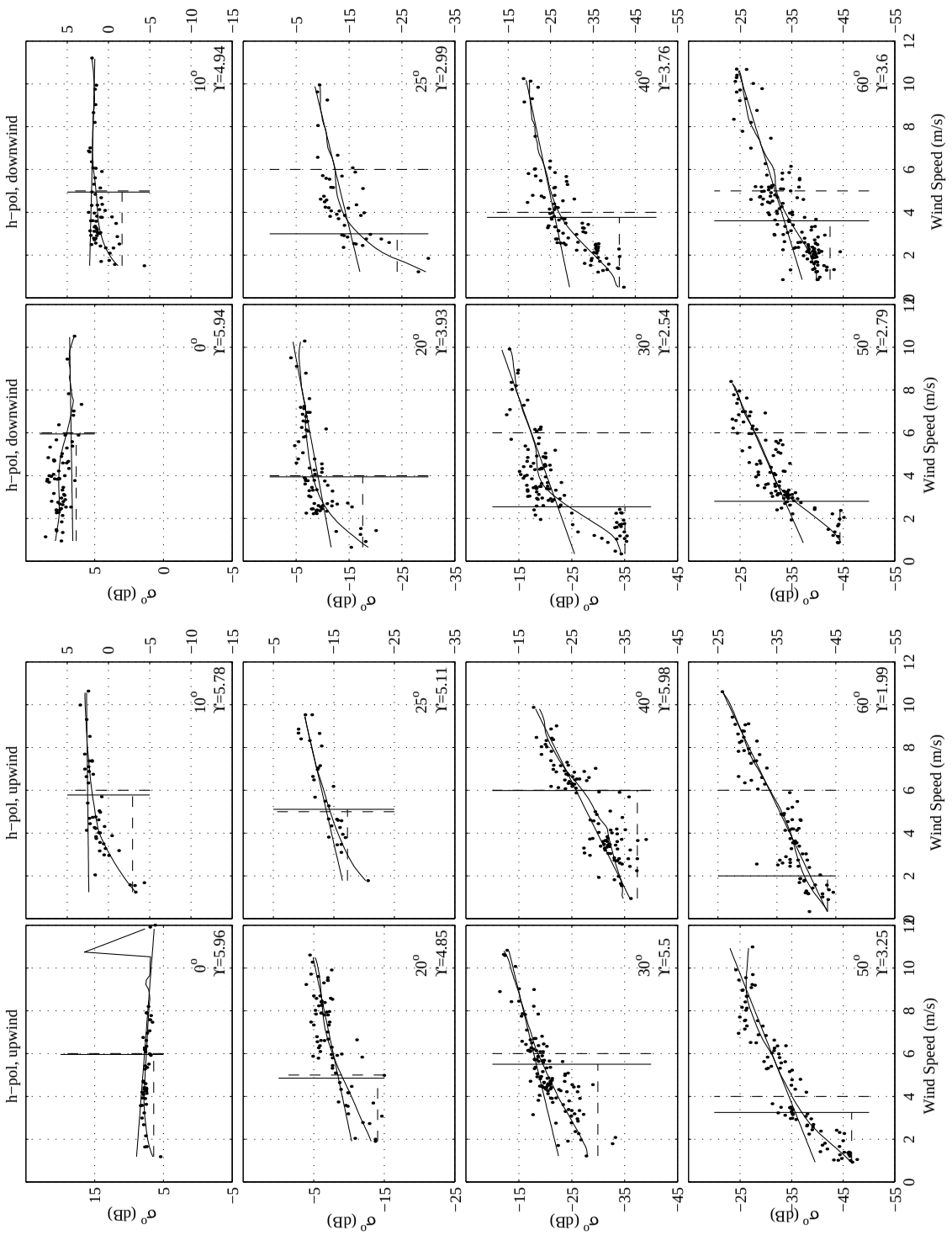

Figure A.7: Low wind speed rolloff (Υ) values for 10 GHz, h-pol, upwind and downwind. Υ is indicated by the solid vertical line. Solid curved line is the regression fit using an Epanechnikov kernel. Dashed vertical line is high wind speed delineation. The solid horizontal line is the linear fit to high wind speed σ° values. Dashed horizontal line is the mean of the five lowest σ° values.

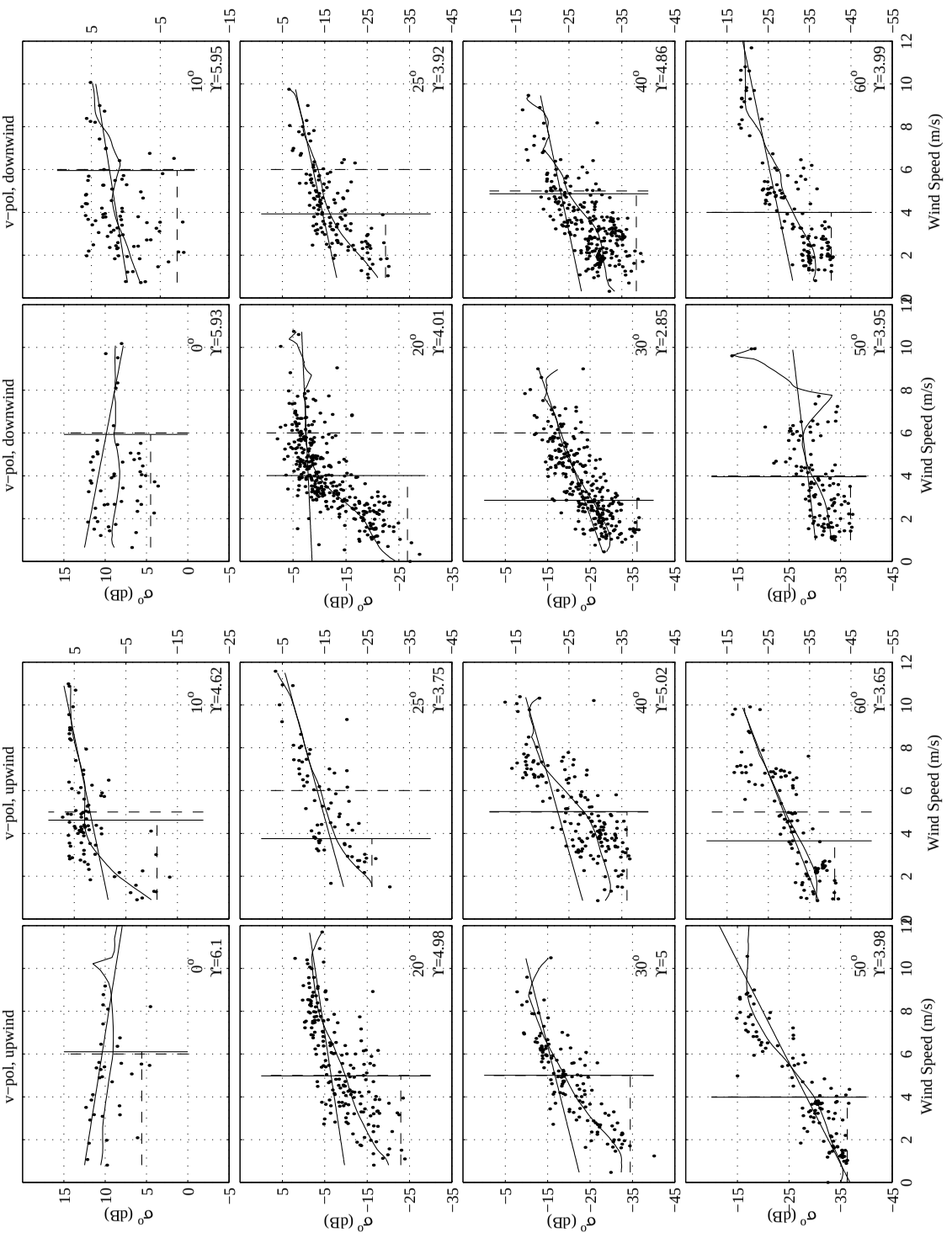

Figure A.8: Low wind speed rolloff (Υ) values for 10 GHz, v-pol, upwind and downwind. Υ is indicated by the solid vertical line. Solid curved line is the regression fit using an Epanechnikov kernel. Dashed vertical line is high wind speed delineation. The solid horizontal line is the linear fit to high wind speed σ° values. Dashed horizontal line is the mean of the five lowest σ° values.

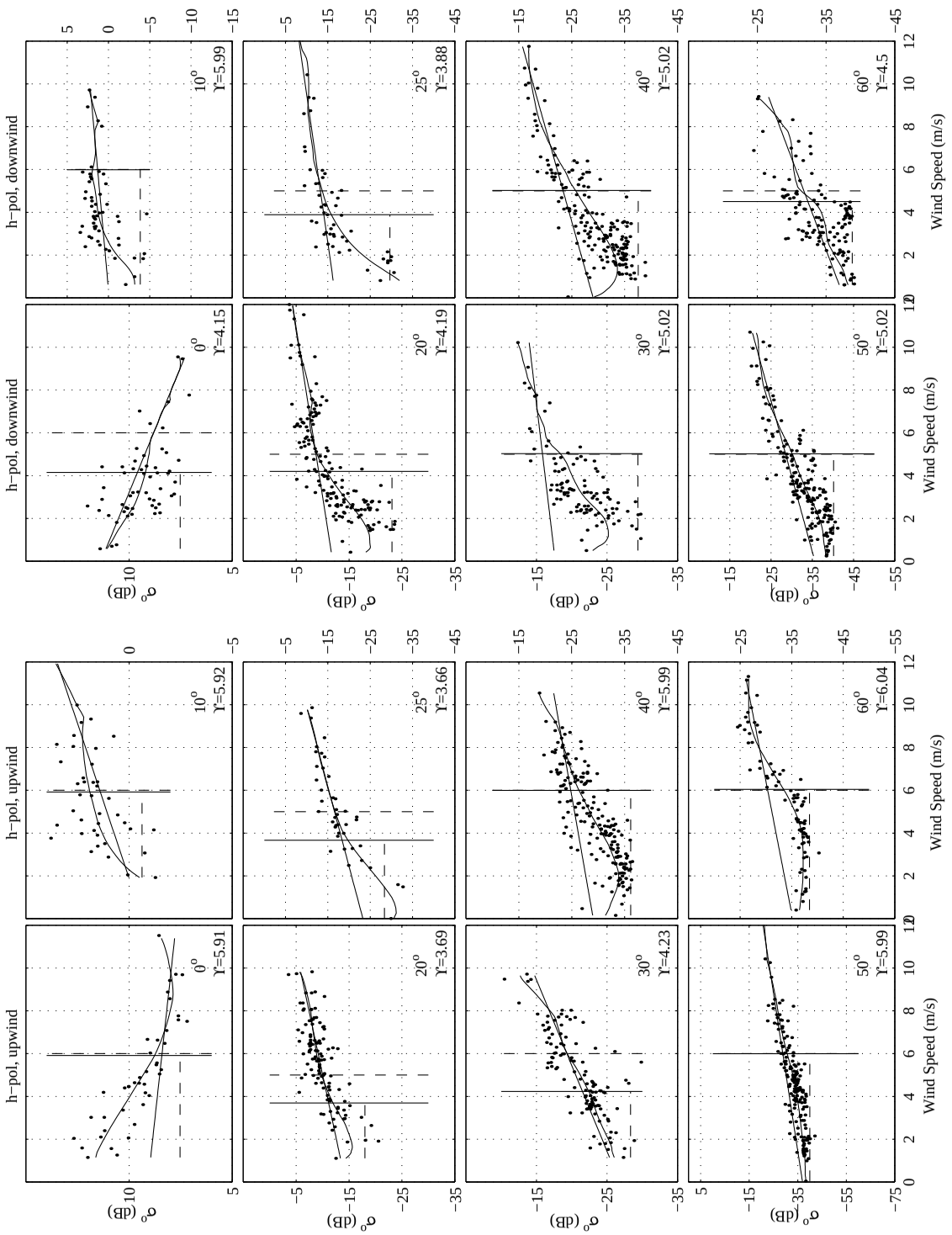

Figure A.9: Low wind speed rolloff (Υ) values for 14 GHz, h-pol, upwind and downwind. Υ is indicated by the solid vertical line. Solid curved line is the regression fit using an Epanechnikov kernel. Dashed vertical line is high wind speed delineation. The solid horizontal line is the linear fit to high wind speed σ° values. Dashed horizontal line is the mean of the five lowest σ° values.

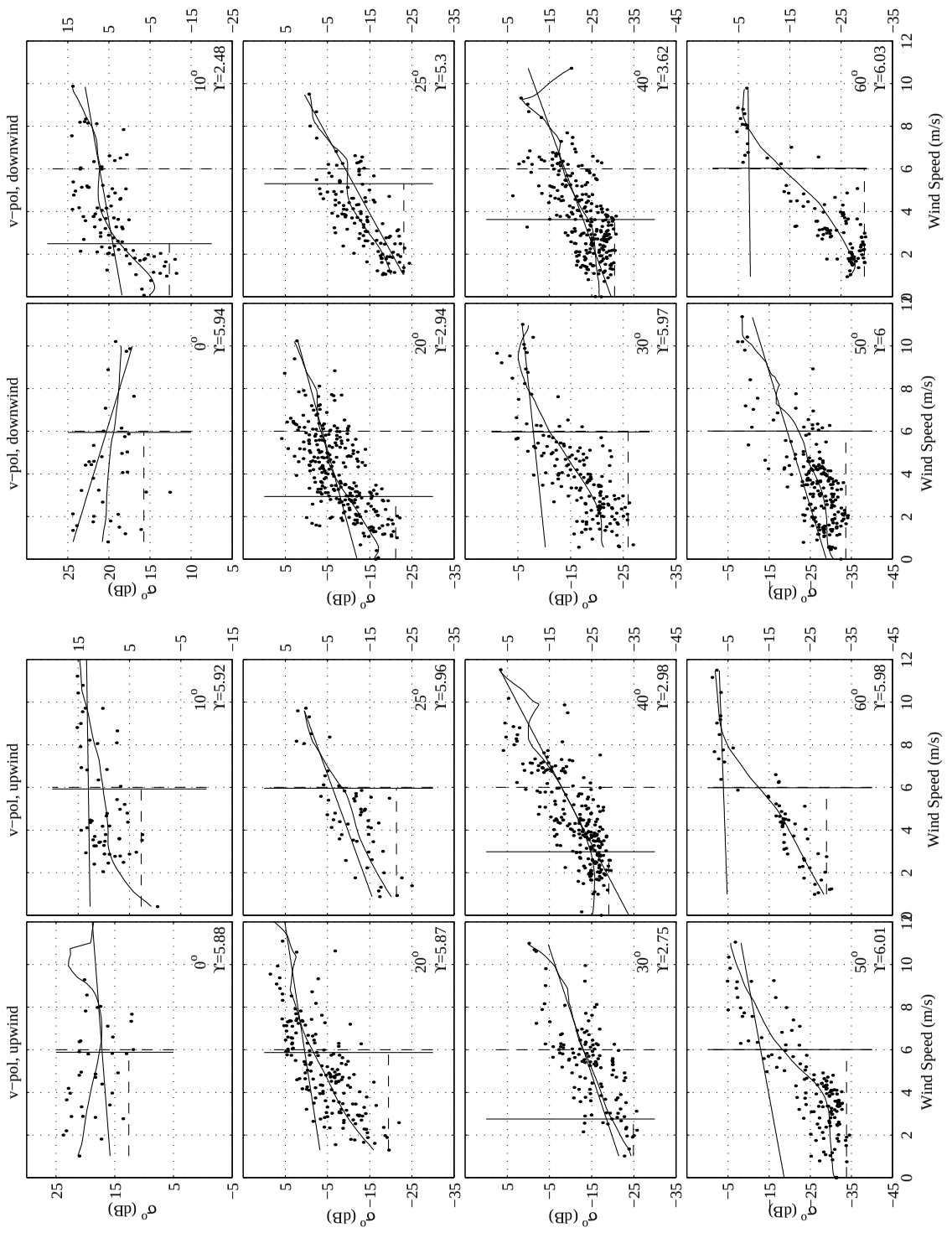

Figure A.10: Low wind speed rolloff (Υ) values for 14 GHz, v-pol, upwind and downwind. Υ is indicated by the solid vertical line. Solid curved line is the regression fit using an Epanechnikov kernel. Dashed vertical line is high wind speed delineation. The solid horizontal line is the linear fit to high wind speed σ° values. Dashed horizontal line is the mean of the five lowest σ° values.

Appendix B

Parameters for YSCAT94 Data According to Wind Speed

Parameters occur in the following order:

- Mean. Figs. B.1 to B.2
- Variance. Figs. B.3 to B.4
- a_1 for the Rayleigh/generalized log-normal distribution. Figs. B.5 to B.6
- a_2 for the Rayleigh/generalized log-normal distribution. Figs. B.7 to B.8
- C for the Rayleigh/generalized log-normal distribution. Figs. B.9 to B.10
- Log-mean. Figs. B.11 to B.12
- Log-variance. Figs. B.13 to B.14
- a_1 for the log-normal distribution. Figs. B.15 to B.16
- C for the log-normal distribution. Figs. B.17 to B.18
- a_1 for the generalized log-normal distribution. Figs. B.19 to B.20
- a_2 for the generalized log-normal distribution. Figs. B.21 to B.22
- C for the generalized log-normal distribution. Figs. B.23 to B.24
- α for the Weibull distribution. Figs. B.25 to B.26

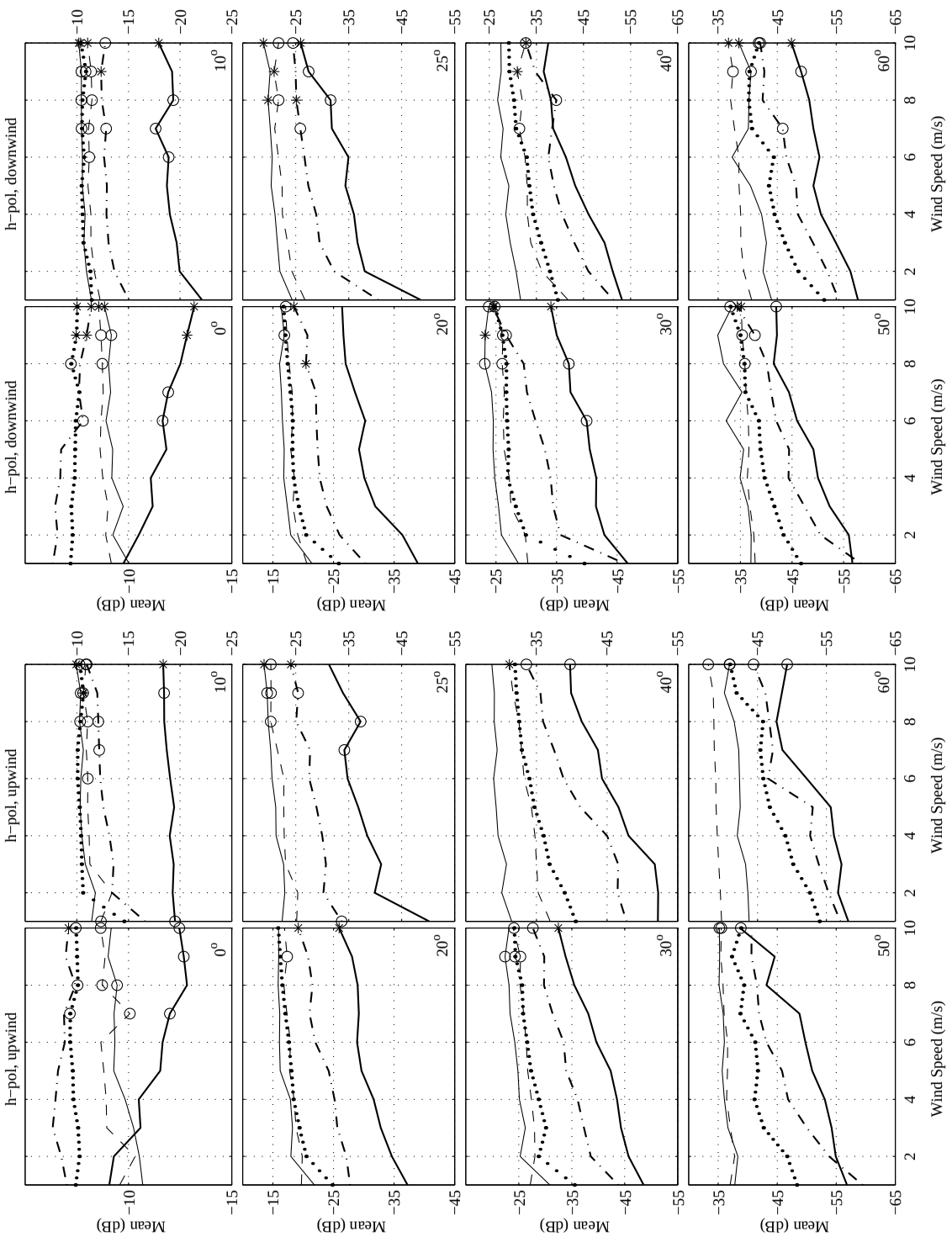

Figure B.1: Mean values for h-pol, upwind and downwind data versus wind speed for YSCAT94. Incidence angle is located at the bottom right corner of each plot. thin solid line → 2 GHz, dashed line → 3 GHz, dotted line → 5 GHz, dash/dot line → 10 GHz, and the bold solid line → 14 GHz. Asterisks correspond to bins with no data, and circles indicate bins with only one or two minutes of data.

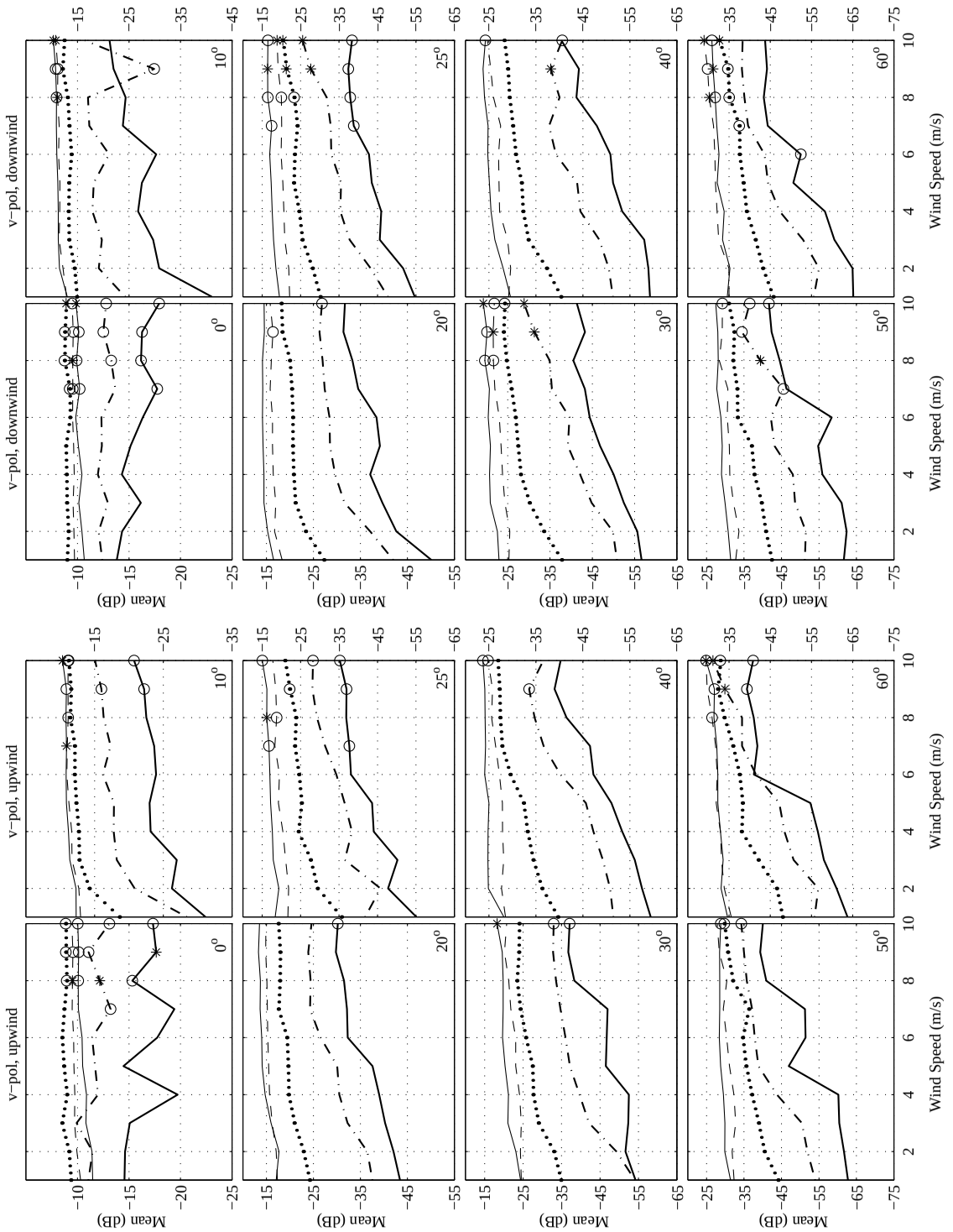

Figure B.2: Mean values for v-pol, upwind and downwind data versus wind speed for YSCAT94. Incidence angle is located at the bottom right corner of each plot. Thin solid line → 2 GHz, dashed line → 3 GHz, dotted line → 5 GHz, dash/dot line → 10 GHz, and the bold solid line → 14 GHz. Asterisks correspond to bins with no data, and circles indicate bins with only one or two minutes of data.

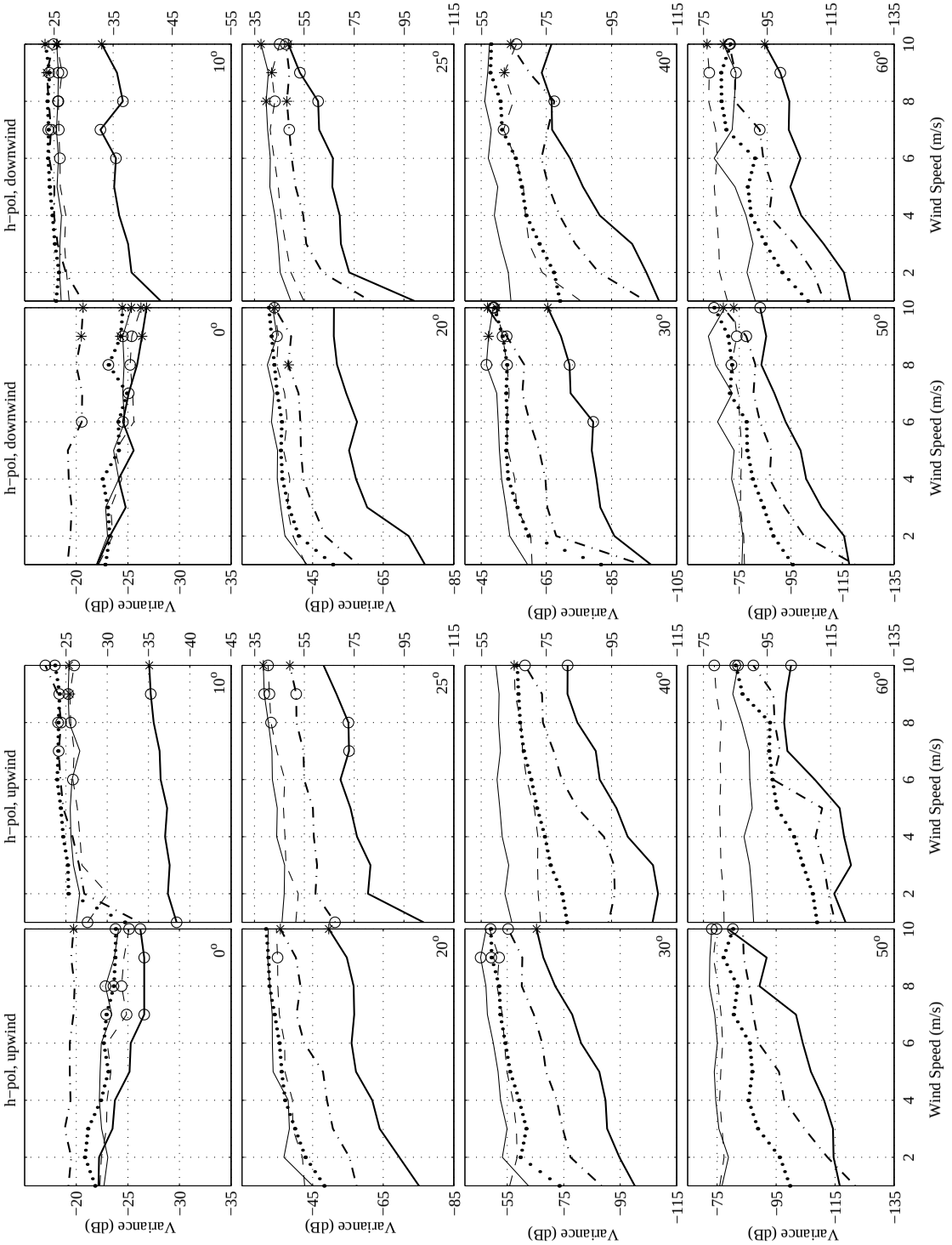

Figure B.3: Variance values for h-pol, upwind and downwind data versus wind speed for YSCAT94. Incidence angle is located at the bottom right corner of each plot. Thin solid line → 2 GHz, dashed line → 3 GHz, dotted line → 5 GHz, dash/dot line → 10 GHz, and the bold solid line → 14 GHz. Asterisks correspond to bins with no data, and circles indicate bins with only one or two minutes of data.

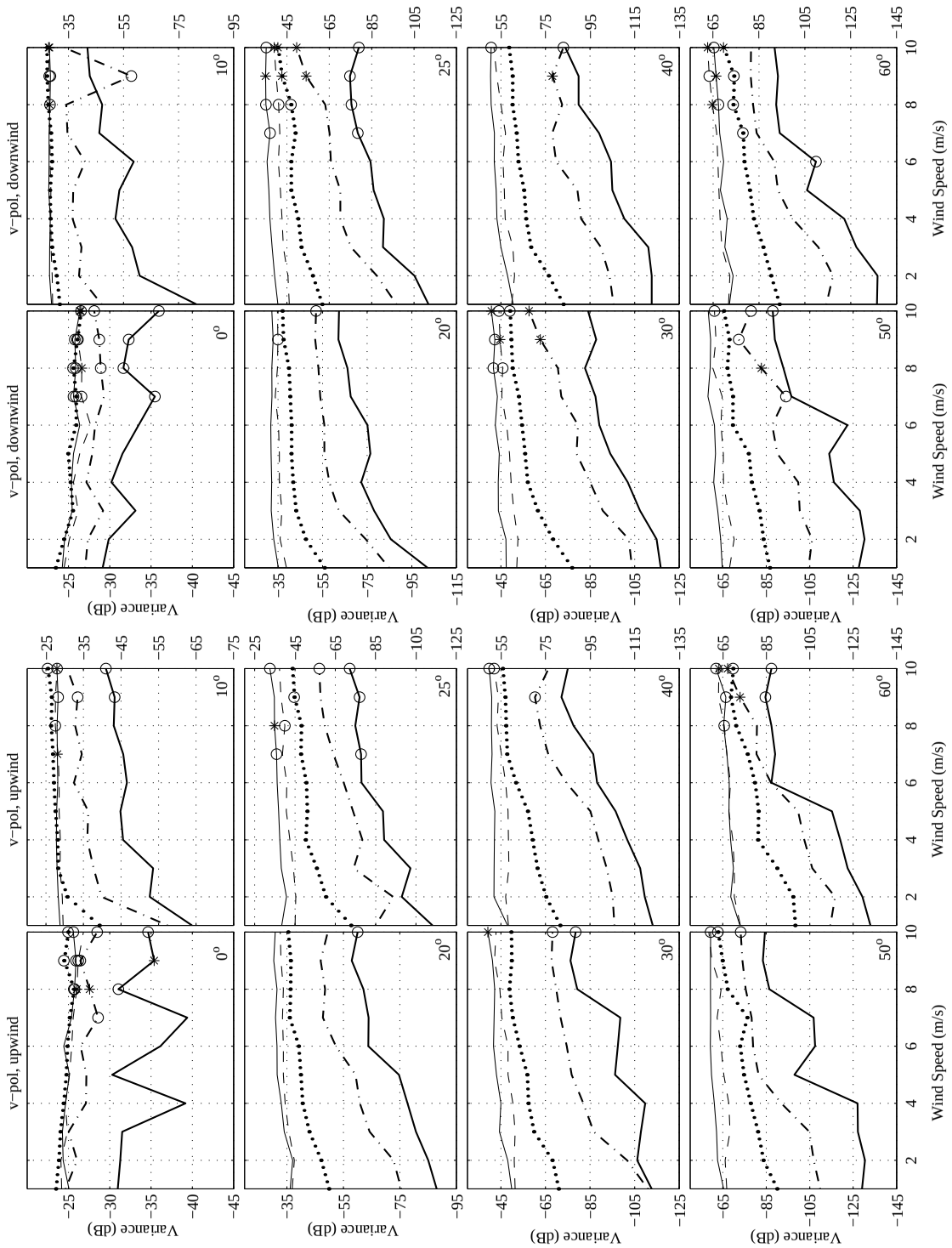

Figure B.4: Variance values for v-pol, upwind and downwind data versus wind speed for YSCAT94. Incidence angle is located at the bottom right corner of each plot. Thin solid line → 2 GHz, dashed line → 3 GHz, dotted line → 5 GHz, dash/dot line → 10 GHz, and the bold solid line → 14 GHz. Asterisks correspond to bins with no data, and circles indicate bins with only one or two minutes of data.

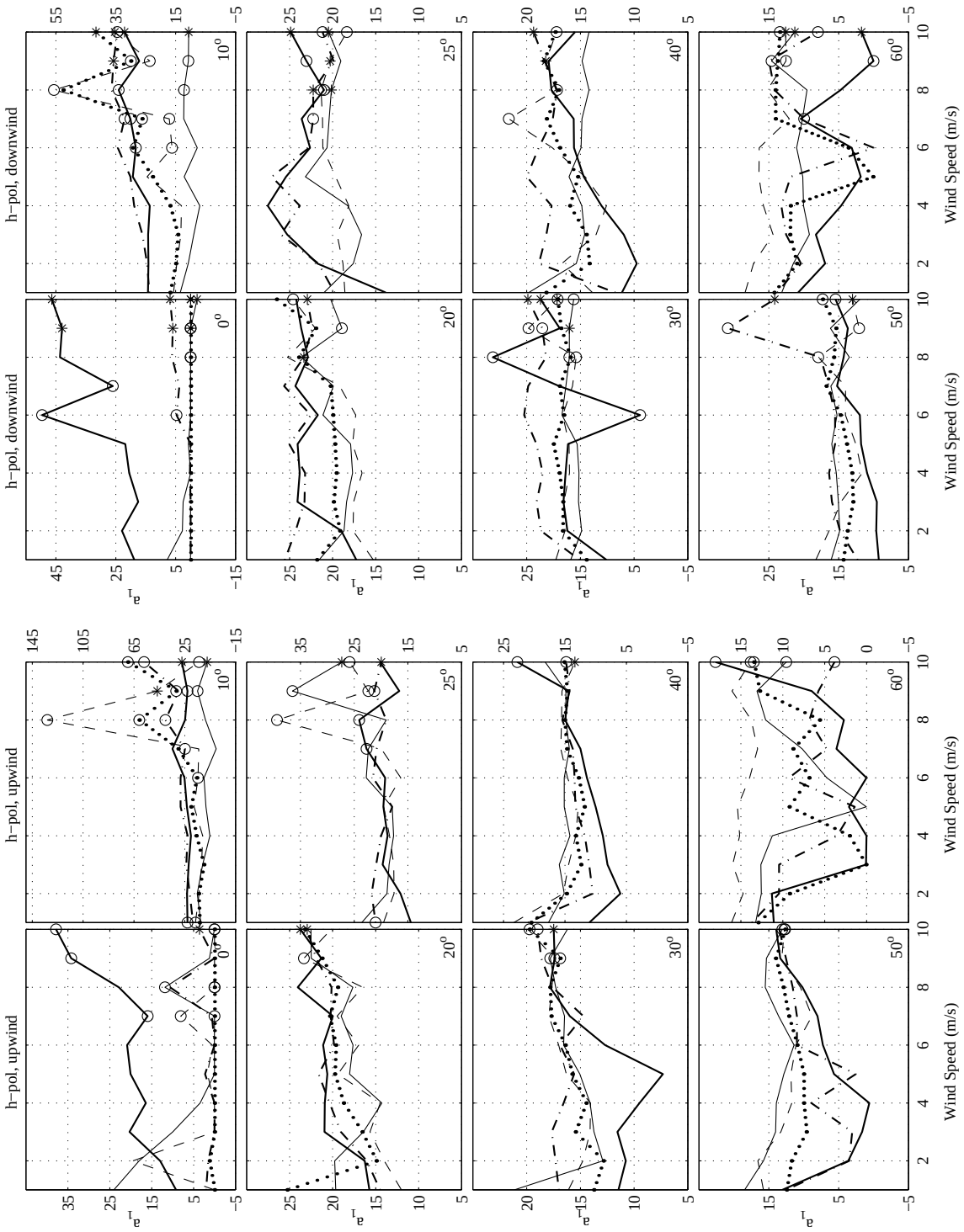

Figure B.5: a_1 values for h-pol, upwind and downwind data versus wind speed for YSCAT94 for the Rayleigh/generalized log-normal distribution. Incidence angle is located at the bottom right corner of each plot. Thin solid line → 2 GHz, dashed line → 3 GHz, dotted line → 5 GHz, dash/dot line → 10 GHz, and the bold solid line → 14 GHz. Asterisks correspond to bins with no data, and circles indicate bins with only one or two minutes of data.

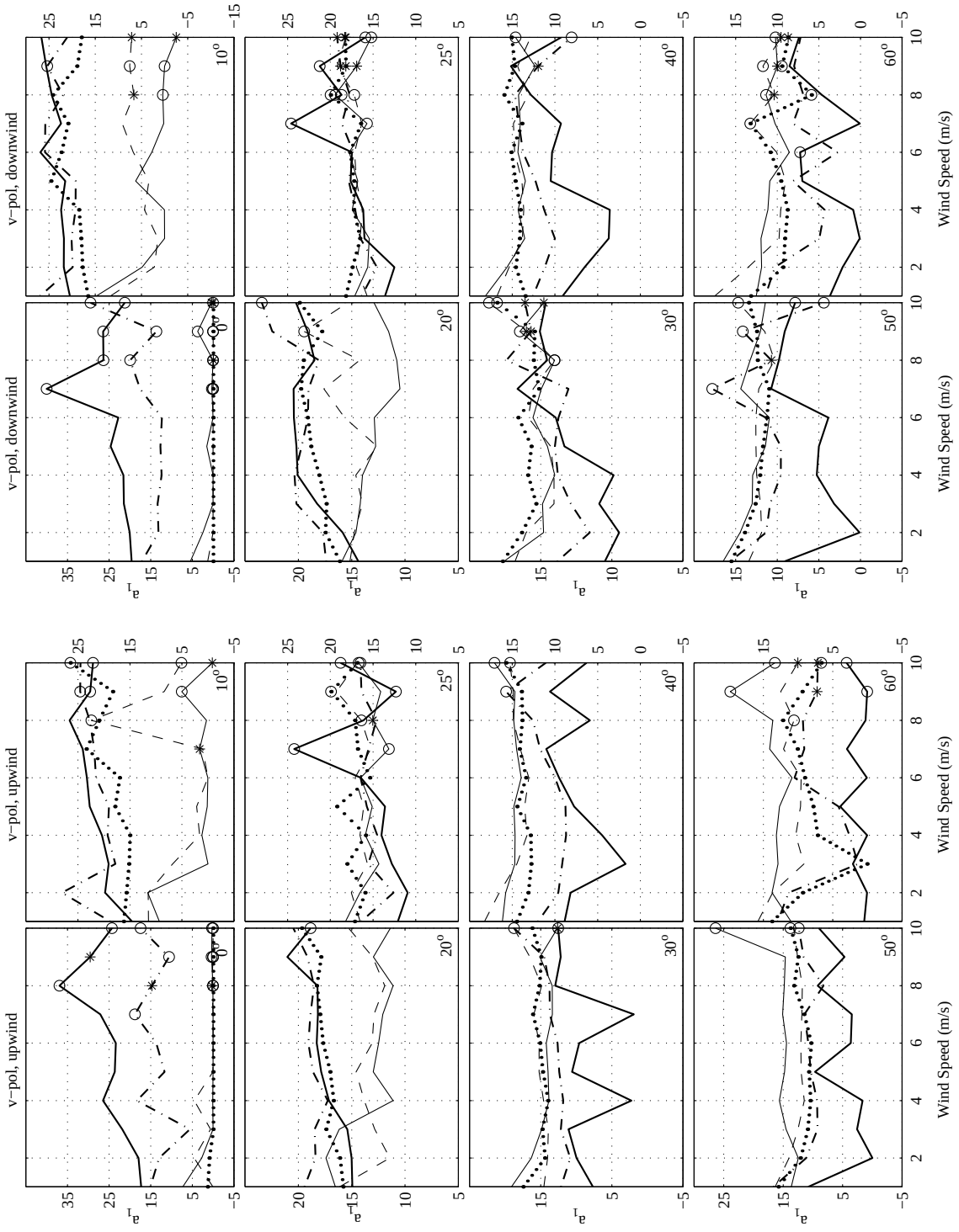

Figure B.6: a_1 values for v-pol, upwind and downwind data versus wind speed for YSCAT94 for the Rayleigh/generalized log-normal distribution. Incidence angle is located at the bottom right corner of each plot. Thin solid line → 2 GHz, dashed line → 3 GHz, dotted line → 5 GHz, dash/dot line → 10 GHz, and the bold solid line → 14 GHz. Asterisks correspond to bins with no data, and circles indicate bins with only one or two minutes of data.

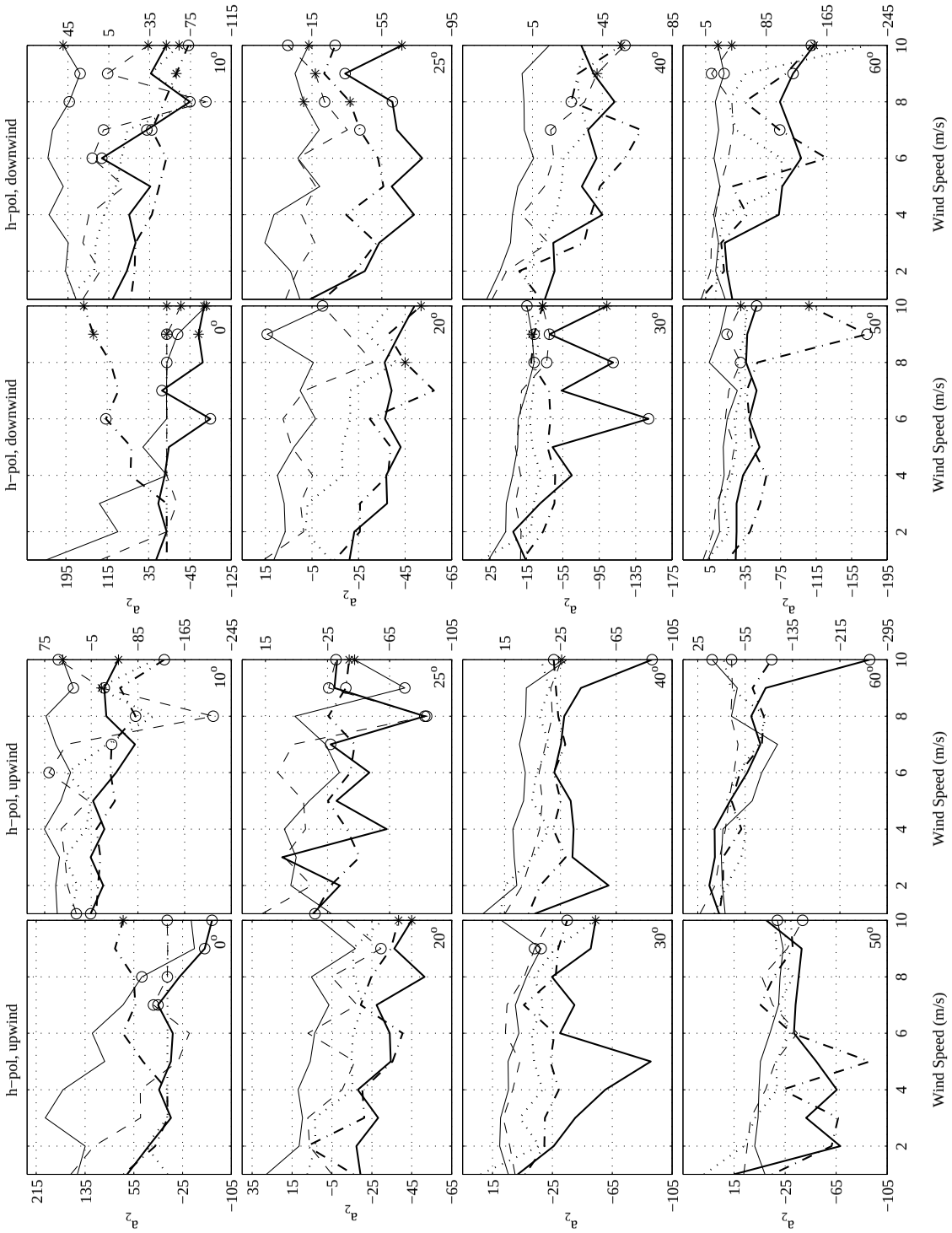

Figure B.7: a_2 values for h-pol, upwind and downwind data versus wind speed for YSCAT94 for the Rayleigh/generalized log-normal distribution. Incidence angle is located at the bottom right corner of each plot. Thin solid line → 2 GHz, dashed line → 3 GHz, dotted line → 5 GHz, dash/dot line → 10 GHz, and the bold solid line → 14 GHz. Asterisks correspond to bins with no data, and circles indicate bins with only one or two minutes of data.

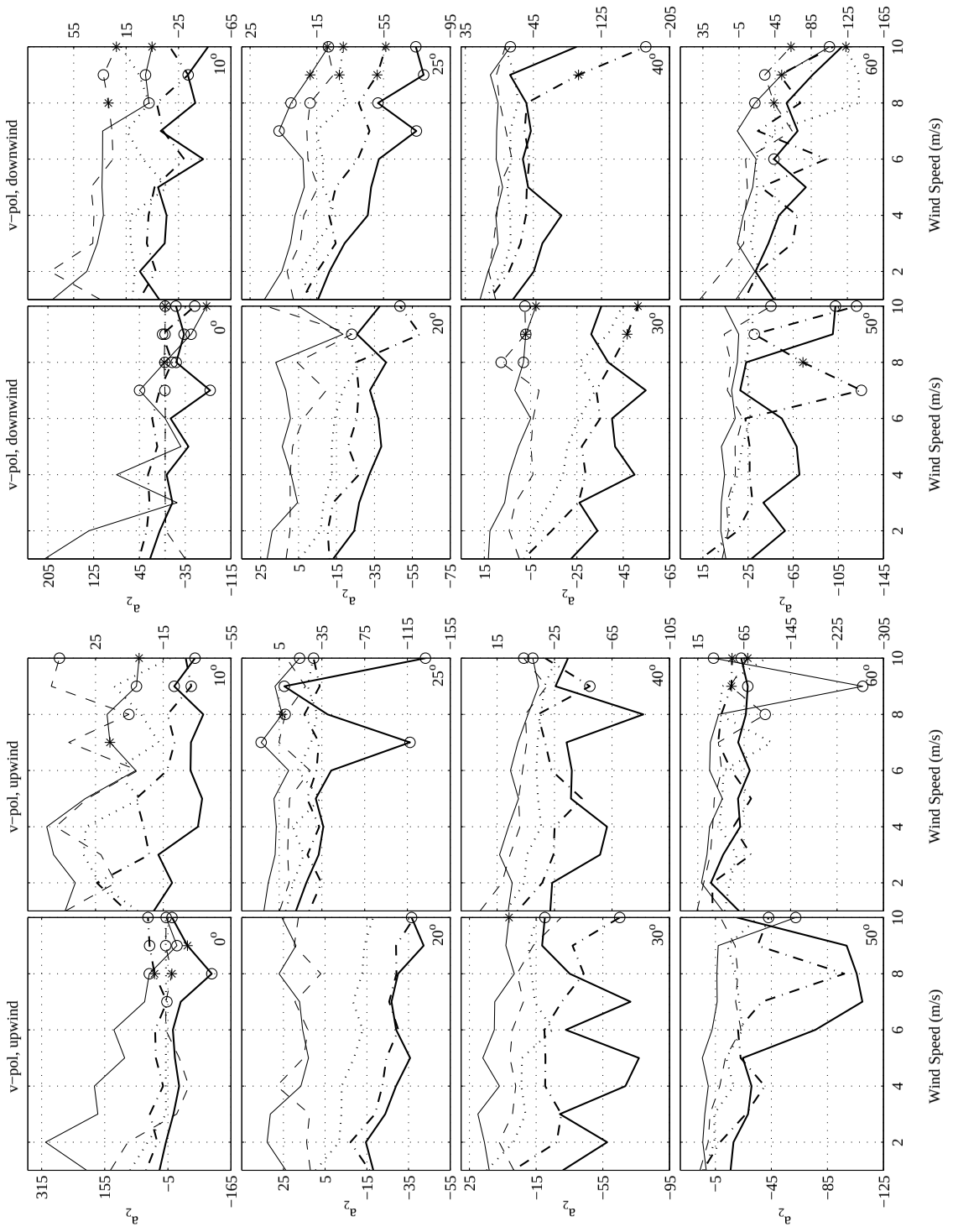

Figure B.8: a_2 values for v-pol, upwind and downwind data versus wind speed for YSCAT94 for the Rayleigh/generalized log-normal distribution. Incidence angle is located at the bottom right corner of each plot. Thin solid line → 2 GHz, dashed line → 3 GHz, dotted line → 5 GHz, dash/dot line → 10 GHz, and the bold solid line → 14 GHz. Asterisks correspond to bins with no data, and circles indicate bins with only one or two minutes of data.

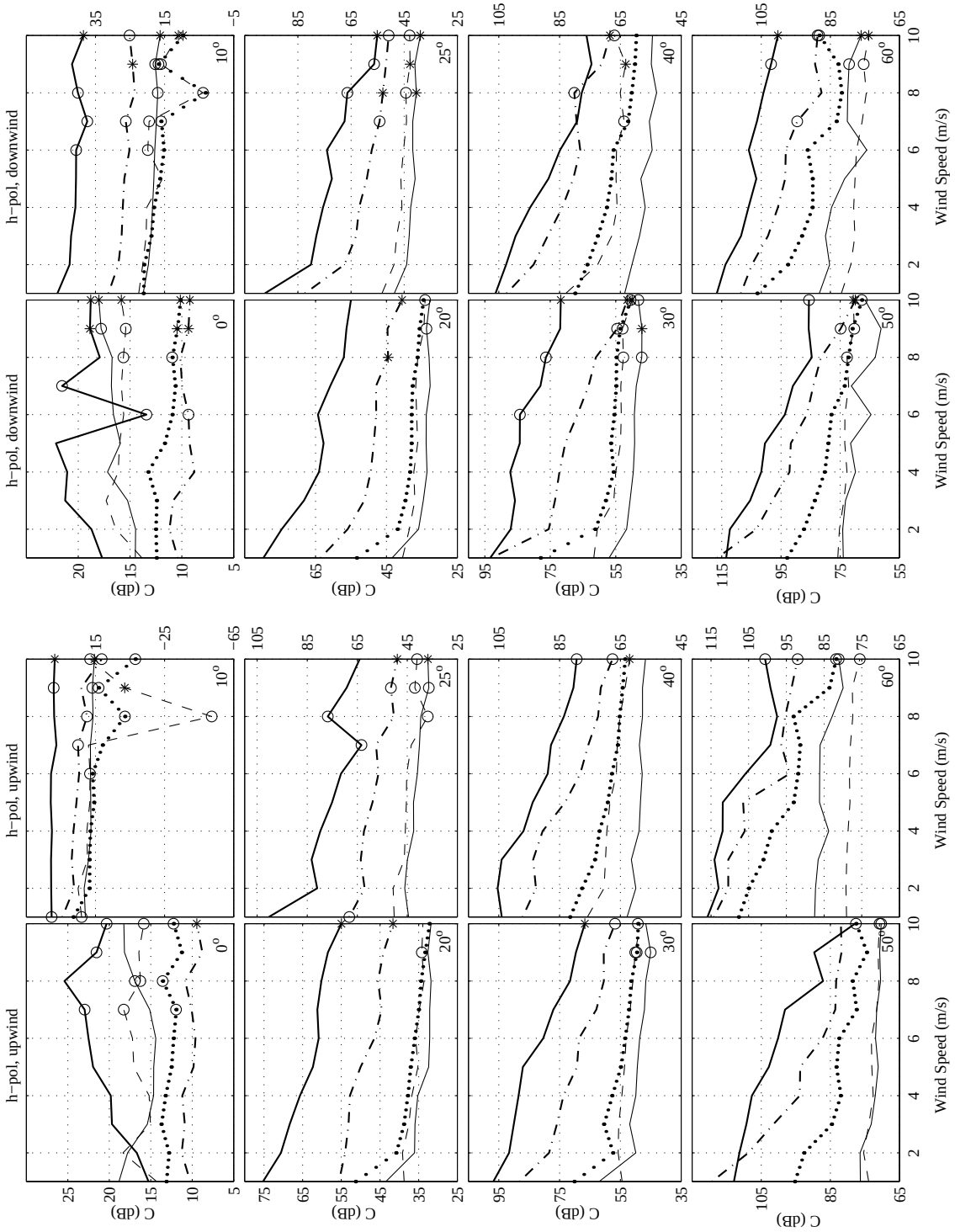

Figure B.9: C values for h-pol, upwind and downwind data versus wind speed for YSCAT94 for the Rayleigh/generalized log-normal distribution. Incidence angle is located at the bottom right corner of each plot. Thin solid line → 2 GHz, dashed line → 3 GHz, dotted line → 5 GHz, dash/dot line → 10 GHz, and the bold solid line → 14 GHz. Asterisks correspond to bins with no data, and circles indicate bins with only one or two minutes of data.

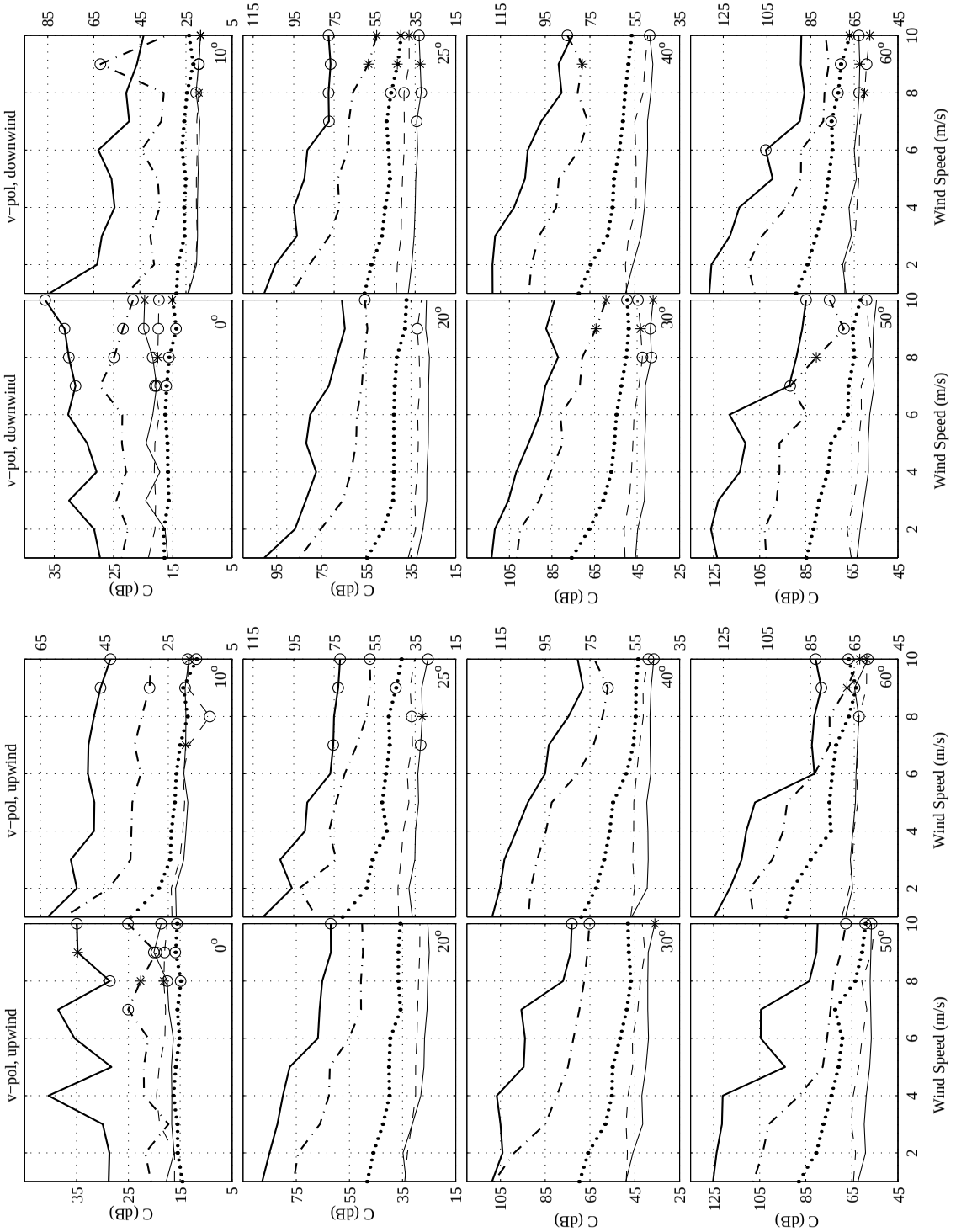

Figure B.10: C values for v-pol, upwind and downwind data versus wind speed for YSCAT94 for the Rayleigh/generalized log-normal distribution. Incidence angle is located at the bottom right corner of each plot. Thin solid line $\rightarrow$ 2 GHz, dashed line $\rightarrow$ 3 GHz, dotted line $\rightarrow$ 5 GHz, dash/dot line $\rightarrow$ 10 GHz, and the bold solid line $\rightarrow$ 14 GHz. Asterisks correspond to bins with no data, and circles indicate bins with only one or two minutes of data.

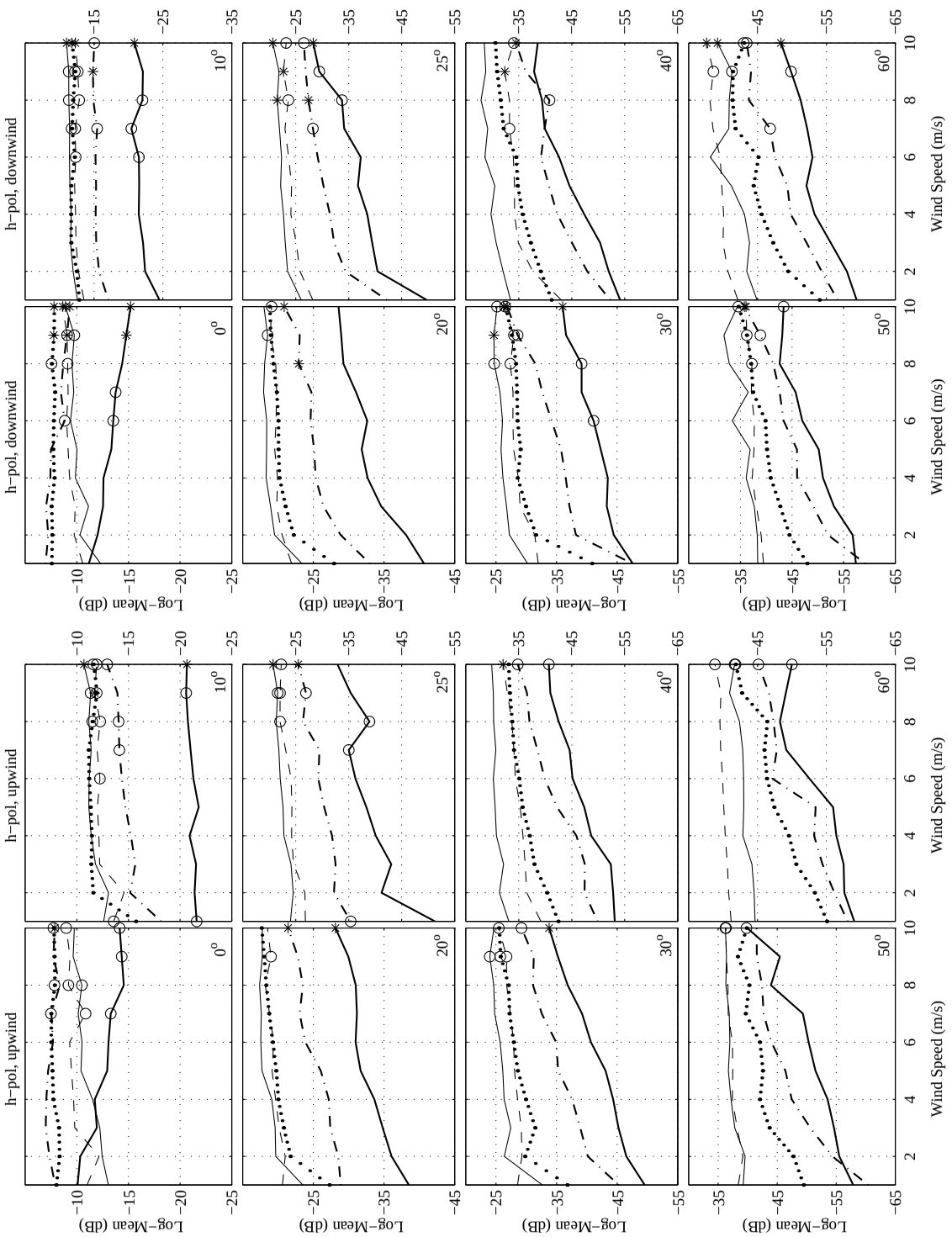

Figure B.11: Log-mean values for h-pol, upwind and downwind data versus wind speed for YSCAT94. Incidence angle is located at the bottom right corner of each plot. Thin solid line → 2 GHz, dashed line → 3 GHz, dotted line → 5 GHz, dash/dot line → 10 GHz, and the bold solid line → 14 GHz. Asterisks correspond to bins with no data, and circles indicate bins with only one or two minutes of data.

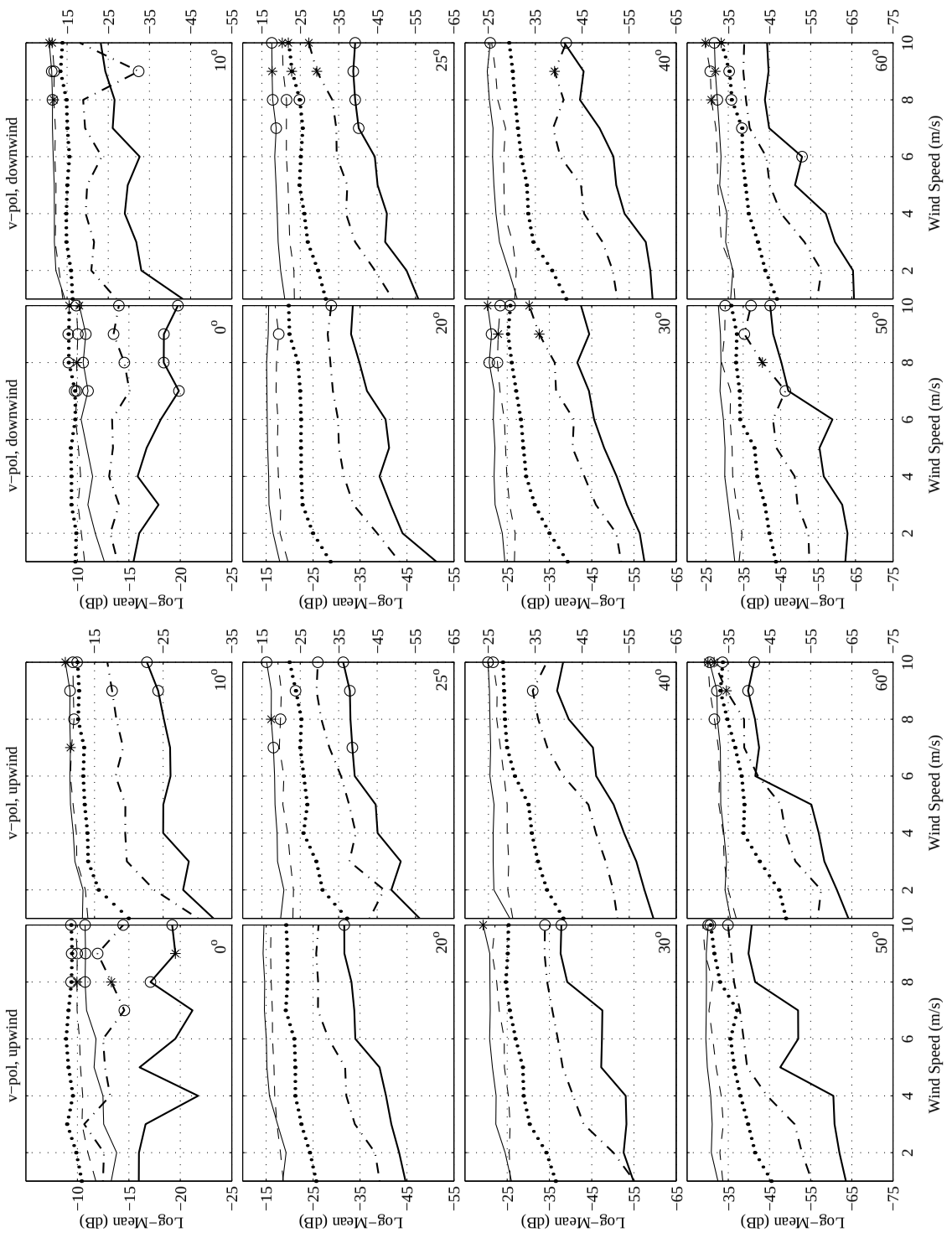

Figure B.12: Log-mean values for v-pol, upwind and downwind data versus wind speed for YSCAT94. Incidence angle is located at the bottom right corner of each plot. Thin solid line → 2 GHz, dashed line → 3 GHz, dotted line → 5 GHz, dash/dot line → 10 GHz, and the bold solid line → 14 GHz. Asterisks correspond to bins with no data, and circles indicate bins with only one or two minutes of data.

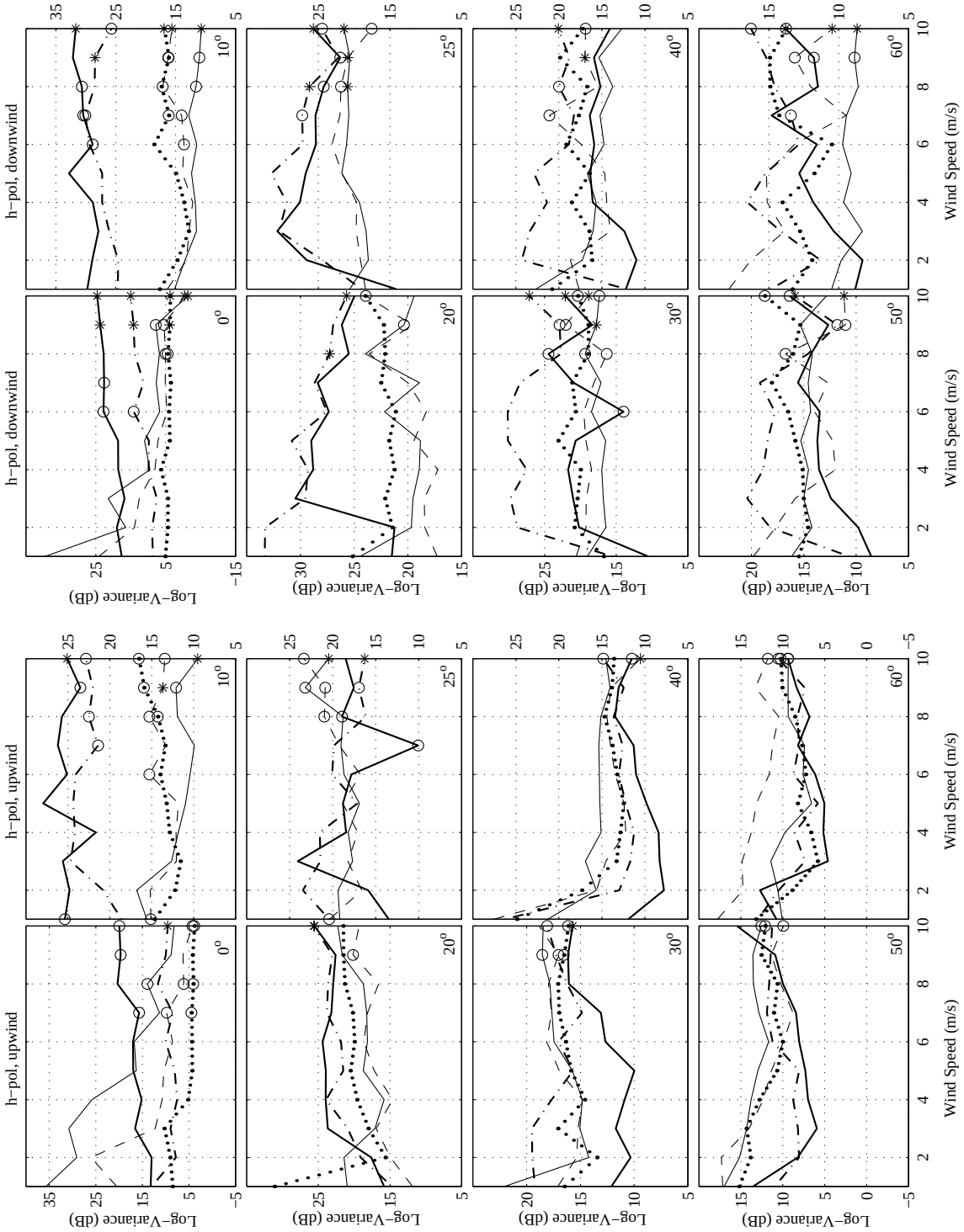

Figure B.13: Log-variance values for h-pol, upwind and downwind data versus wind speed for YSCAT94. Incidence angle is located at the bottom right corner of each plot. Thin solid line → 2 GHz, dashed line → 3 GHz, dotted line → 5 GHz, dash/dot line → 10 GHz, and the bold solid line → 14 GHz. Asterisks correspond to bins with no data, and circles indicate bins with only one or two minutes of data.

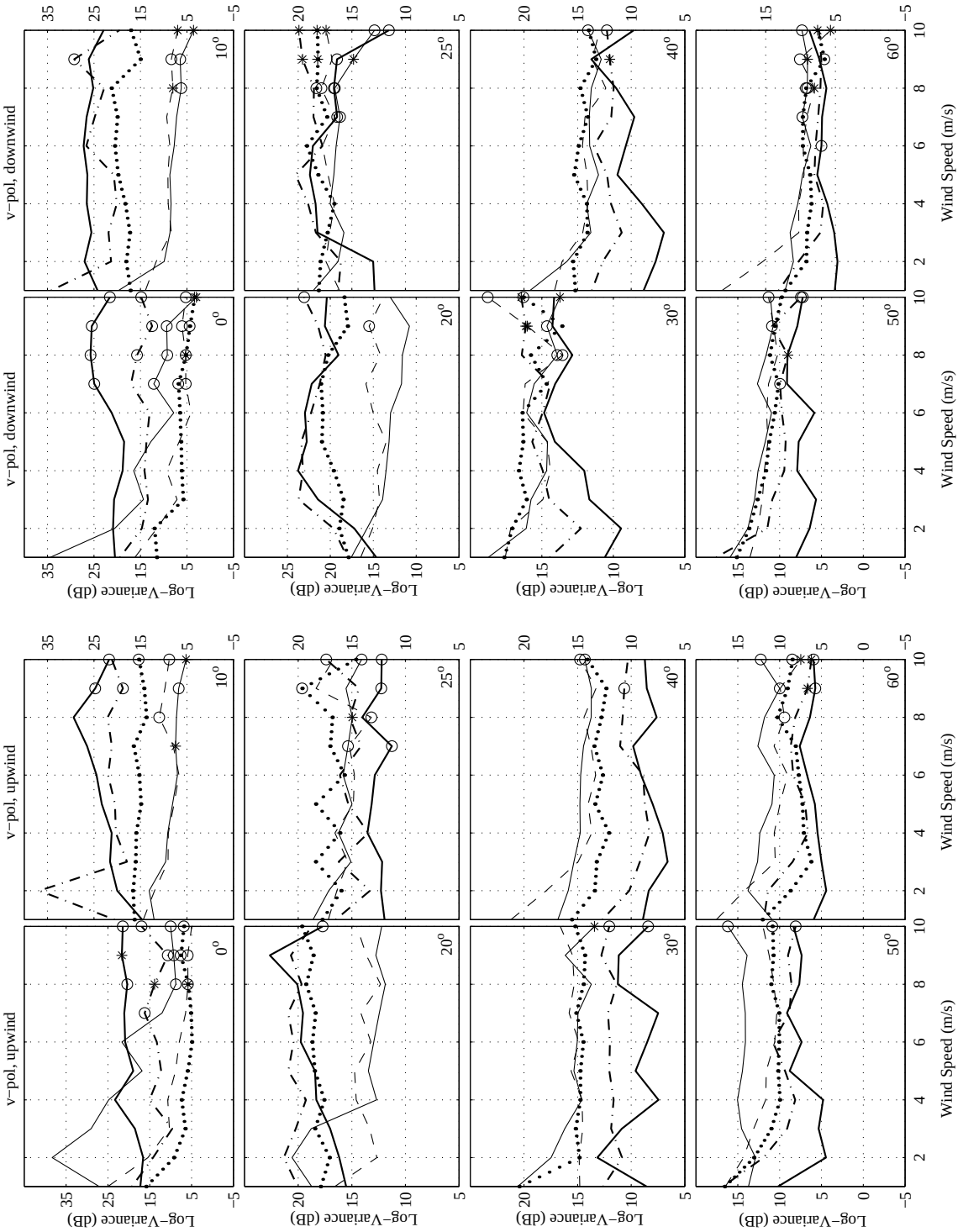

Figure B.14: Log-variance values for v-pol, upwind and downwind data versus wind speed for YSCAT94. Incidence angle is located at the bottom right corner of each plot. Thin solid line → 2 GHz, dashed line → 3 GHz, dotted line → 5 GHz, dash/dot line → 10 GHz, and the bold solid line → 14 GHz. Asterisks correspond to bins with no data, and circles indicate bins with only one or two minutes of data.

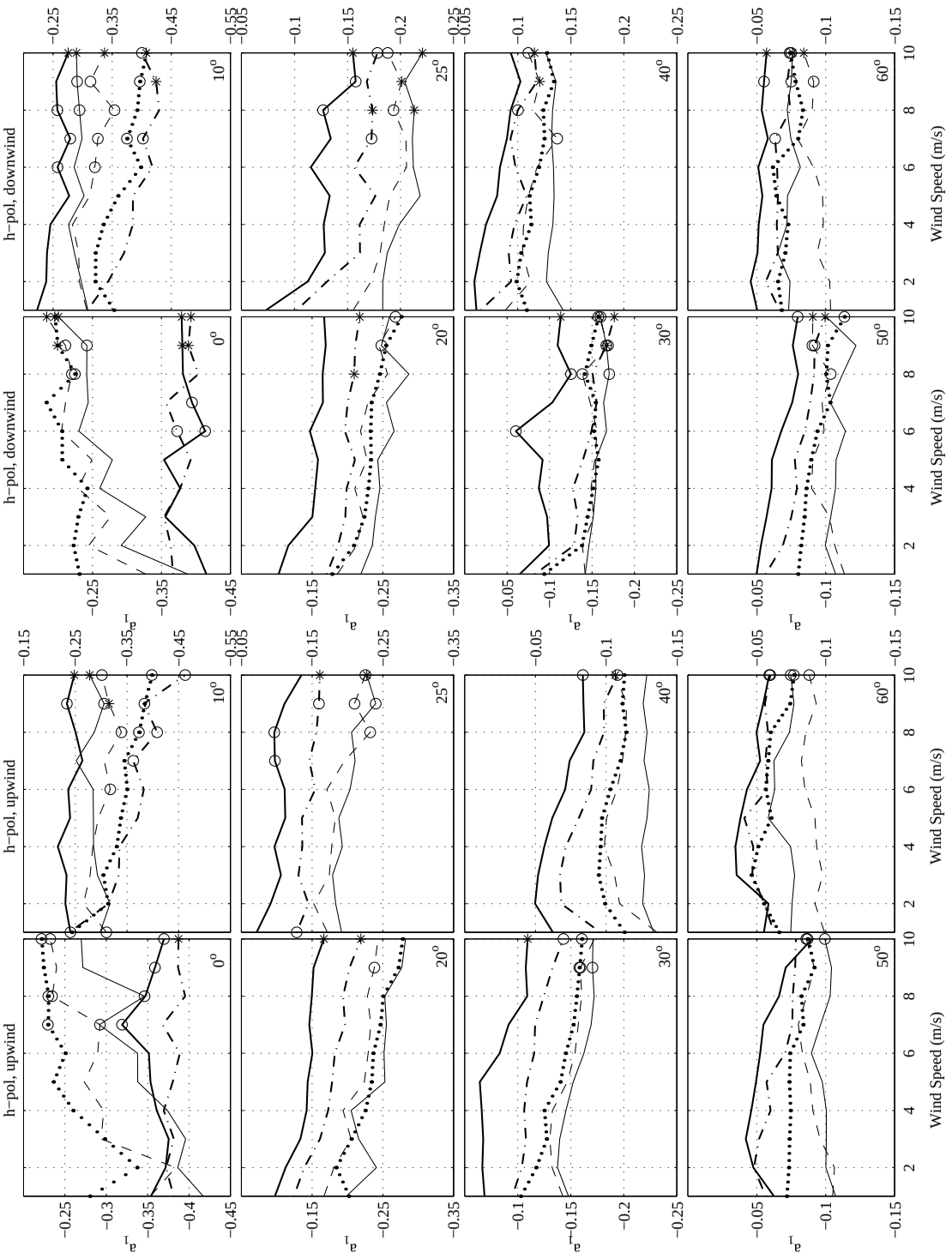

Figure B.15: a_1 values for h-pol, upwind and downwind data versus wind speed for YSCAT94 for the log-normal distribution. Incidence angle is located at the bottom right corner of each plot. Thin solid line $\rightarrow$ 2 GHz, dashed line $\rightarrow$ 3 GHz, dotted line $\rightarrow$ 5 GHz, dash/dot line $\rightarrow$ 10 GHz, and the bold solid line $\rightarrow$ 14 GHz. Asterisks correspond to bins with no data, and circles indicate bins with only one or two minutes of data.

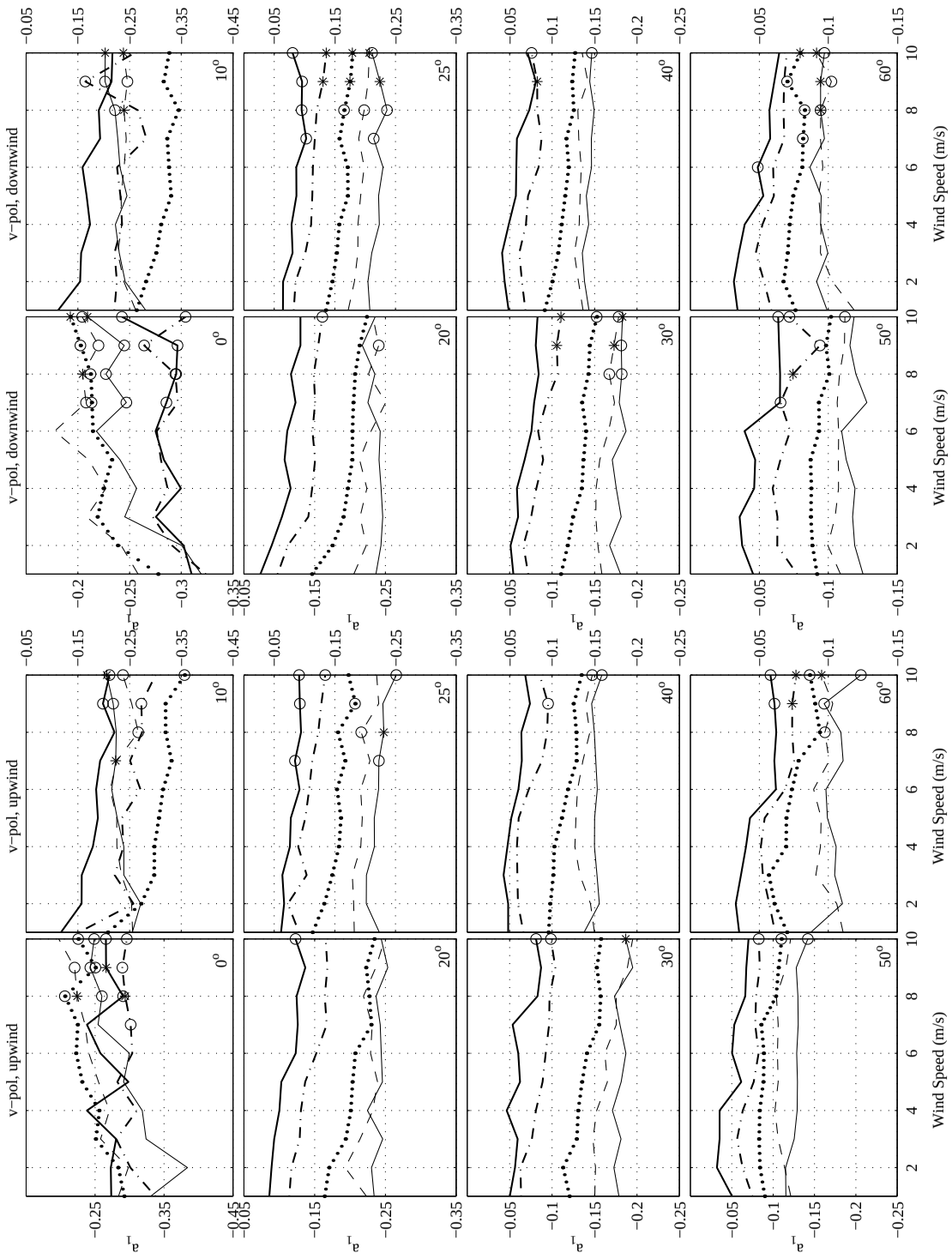

Figure B.16: a_1 values for v-pol, upwind and downwind data versus wind speed for YSCAT94 for the log-normal distribution. Incidence angle is located at the bottom right corner of each plot. Thin solid line $\rightarrow$ 2 GHz, dashed line $\rightarrow$ 3 GHz, dotted line $\rightarrow$ 5 GHz, dash/dot line $\rightarrow$ 10 GHz, and the bold solid line $\rightarrow$ 14 GHz. Asterisks correspond to bins with no data, and circles indicate bins with only one or two minutes of data.

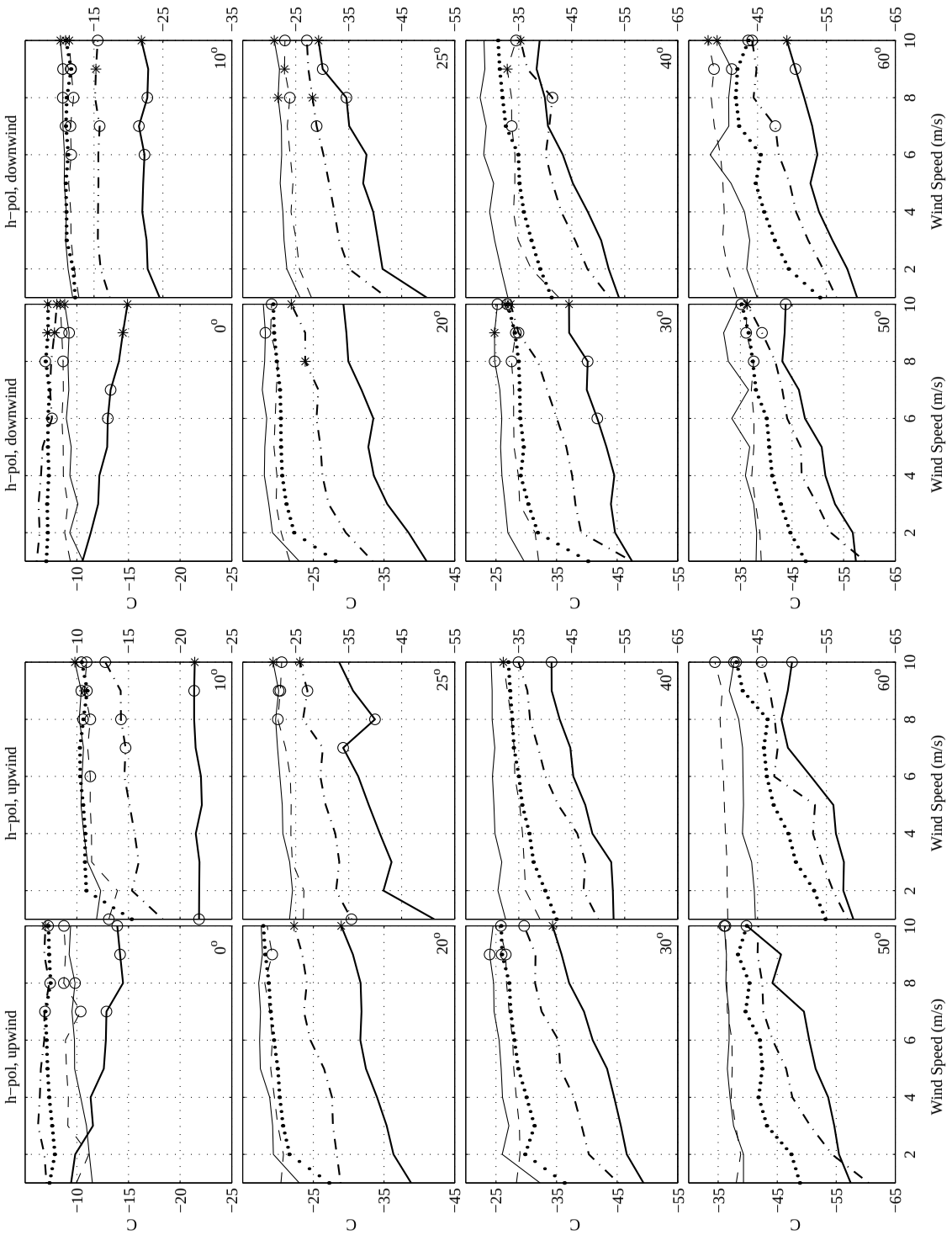

Figure B.17: C values for h-pol, upwind and downwind data versus wind speed for YSCAT94 for the log-normal distribution. Incidence angle is located at the bottom right corner of each plot. Thin solid line $\rightarrow$ 2 GHz, dashed line $\rightarrow$ 3 GHz, dotted line $\rightarrow$ 5 GHz, dash/dot line $\rightarrow$ 10 GHz, and the bold solid line $\rightarrow$ 14 GHz. Asterisks correspond to bins with no data, and circles indicate bins with only one or two minutes of data.

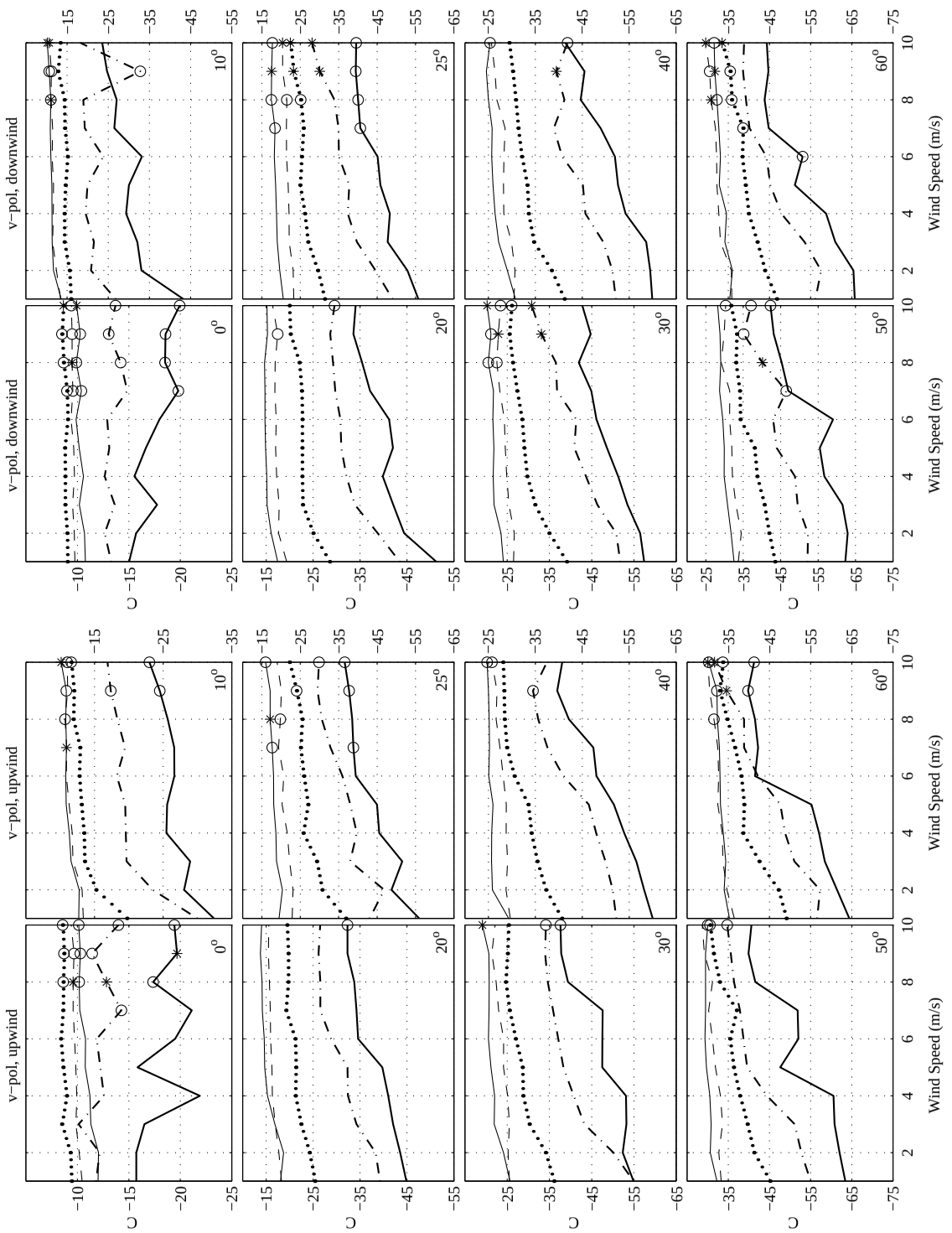

Figure B.18: C values for v-pol, upwind and downwind data versus wind speed for YSCAT94 for the log-normal distribution. Incidence angle is located at the bottom right corner of each plot. Thin solid line $\rightarrow$ 2 GHz, dashed line $\rightarrow$ 3 GHz, dotted line $\rightarrow$ 5 GHz, dash/dot line $\rightarrow$ 10 GHz, and the bold solid line $\rightarrow$ 14 GHz. Asterisks correspond to bins with no data, and circles indicate bins with only one or two minutes of data.

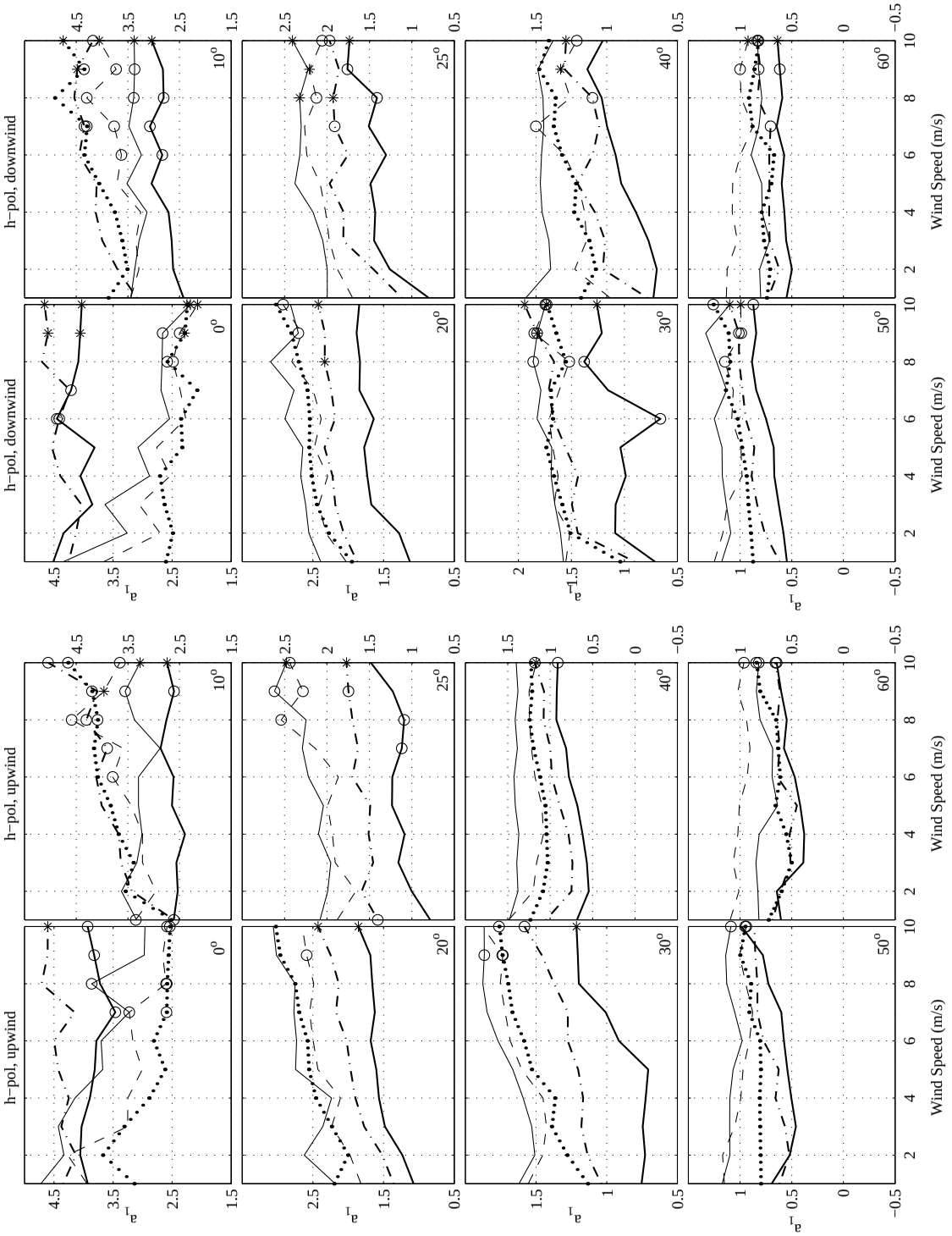

Figure B.19: a_1 values for h-pol, upwind and downwind data versus wind speed for YSCAT94 for the generalized log-normal distribution. Incidence angle is located at the bottom right corner of each plot. Thin solid line → 2 GHz, dashed line → 3 GHz, dotted line → 5 GHz, dash/dot line → 10 GHz, and the bold solid line → 14 GHz. Asterisks correspond to bins with no data, and circles indicate bins with only one or two minutes of data.

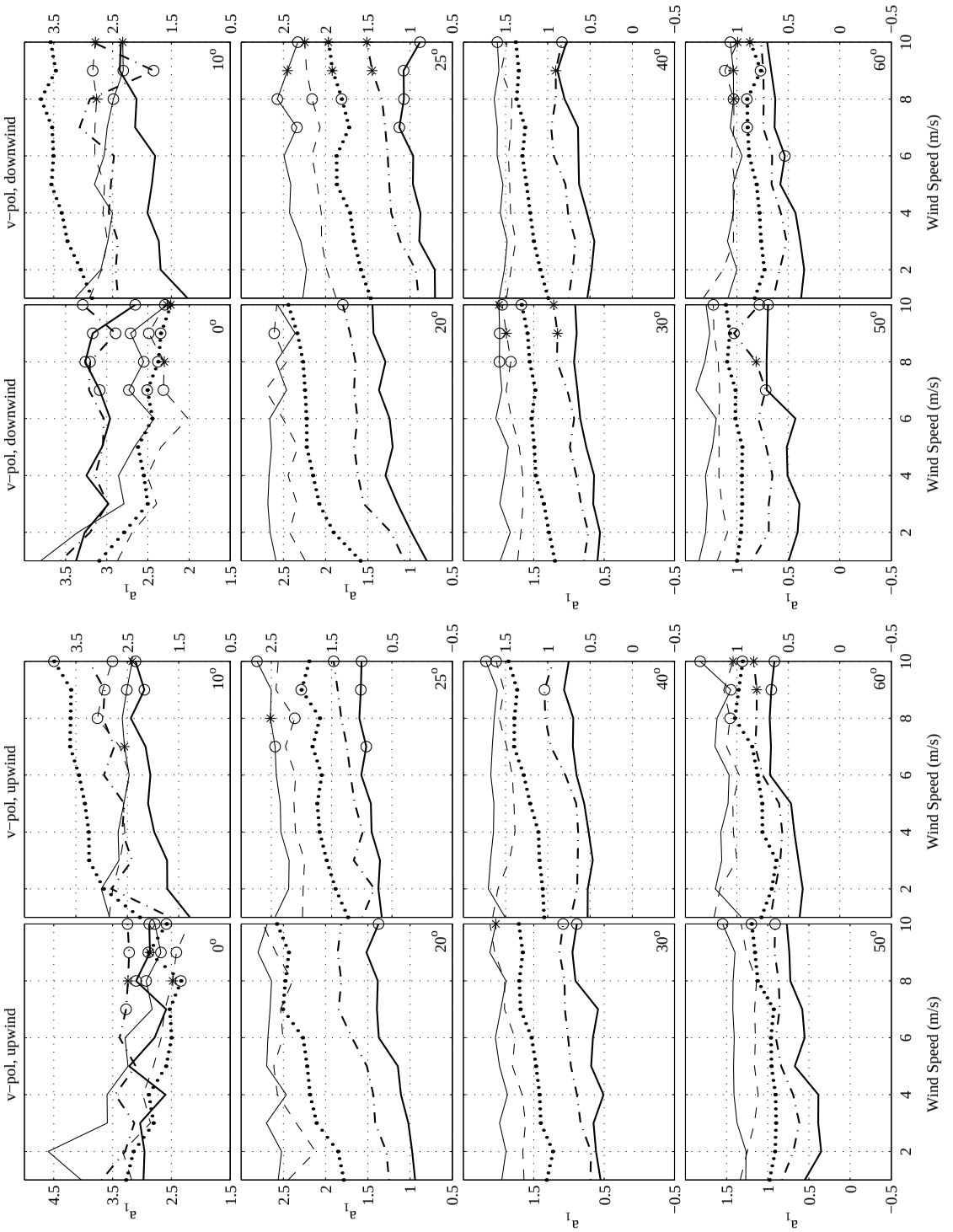

Figure B.20: a_1 values for v-pol, upwind and downwind data versus wind speed for YSCAT94 for the generalized log-normal distribution. Incidence angle is located at the bottom right corner of each plot. Thin solid line → 2 GHz, dashed line → 3 GHz, dotted line → 5 GHz, dash/dot line → 10 GHz, and the bold solid line → 14 GHz. Asterisks correspond to bins with no data, and circles indicate bins with only one or two minutes of data.

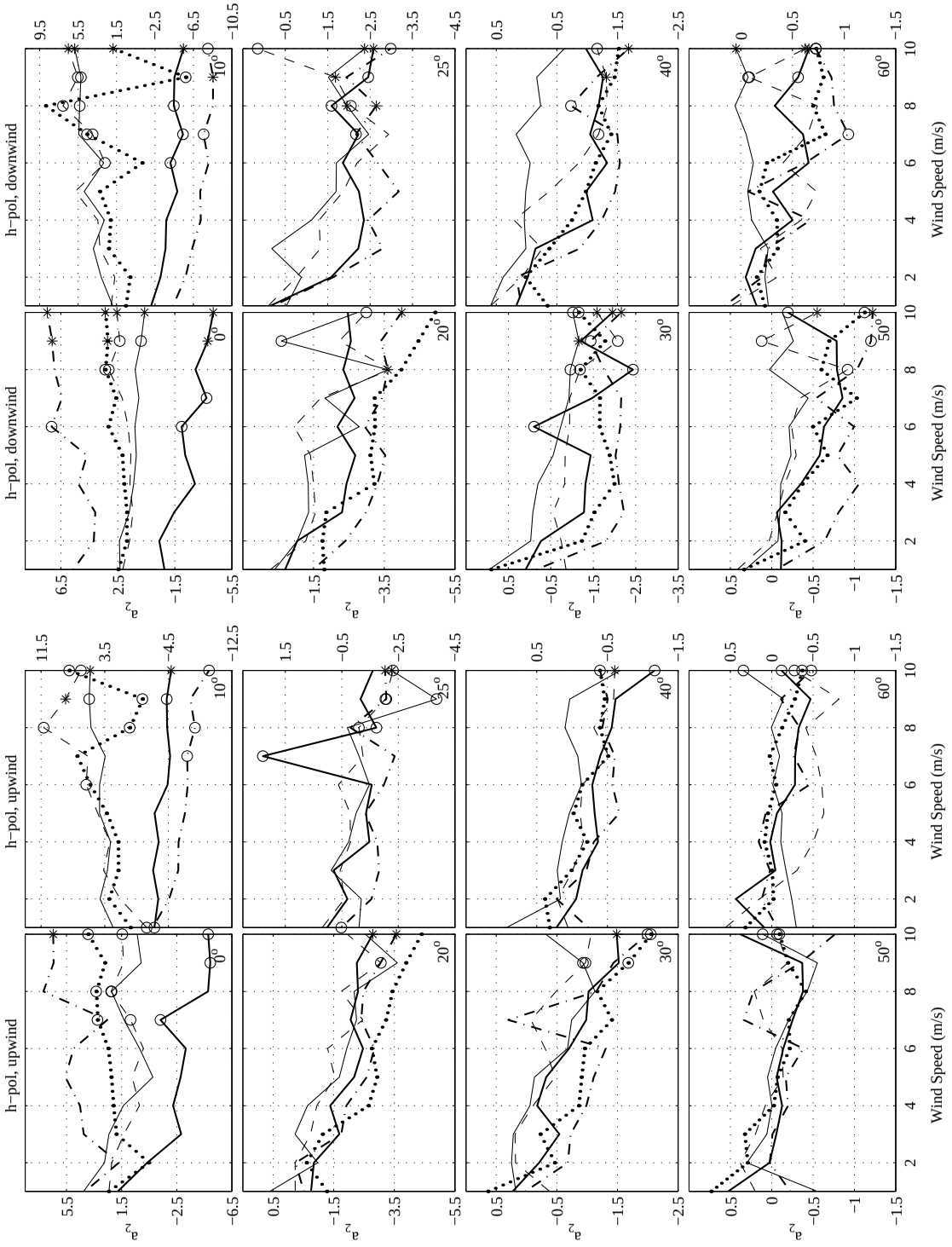

Figure B.21: a_2 values for h-pol, upwind and downwind data versus wind speed for YSCAT94 for the generalized log-normal distribution. Incidence angle is located at the bottom right corner of each plot. Thin solid line → 2 GHz, dashed line → 3 GHz, dotted line → 5 GHz, dash/dot line → 10 GHz, and the bold solid line → 14 GHz. Asterisks correspond to bins with no data, and circles indicate bins with only one or two minutes of data.

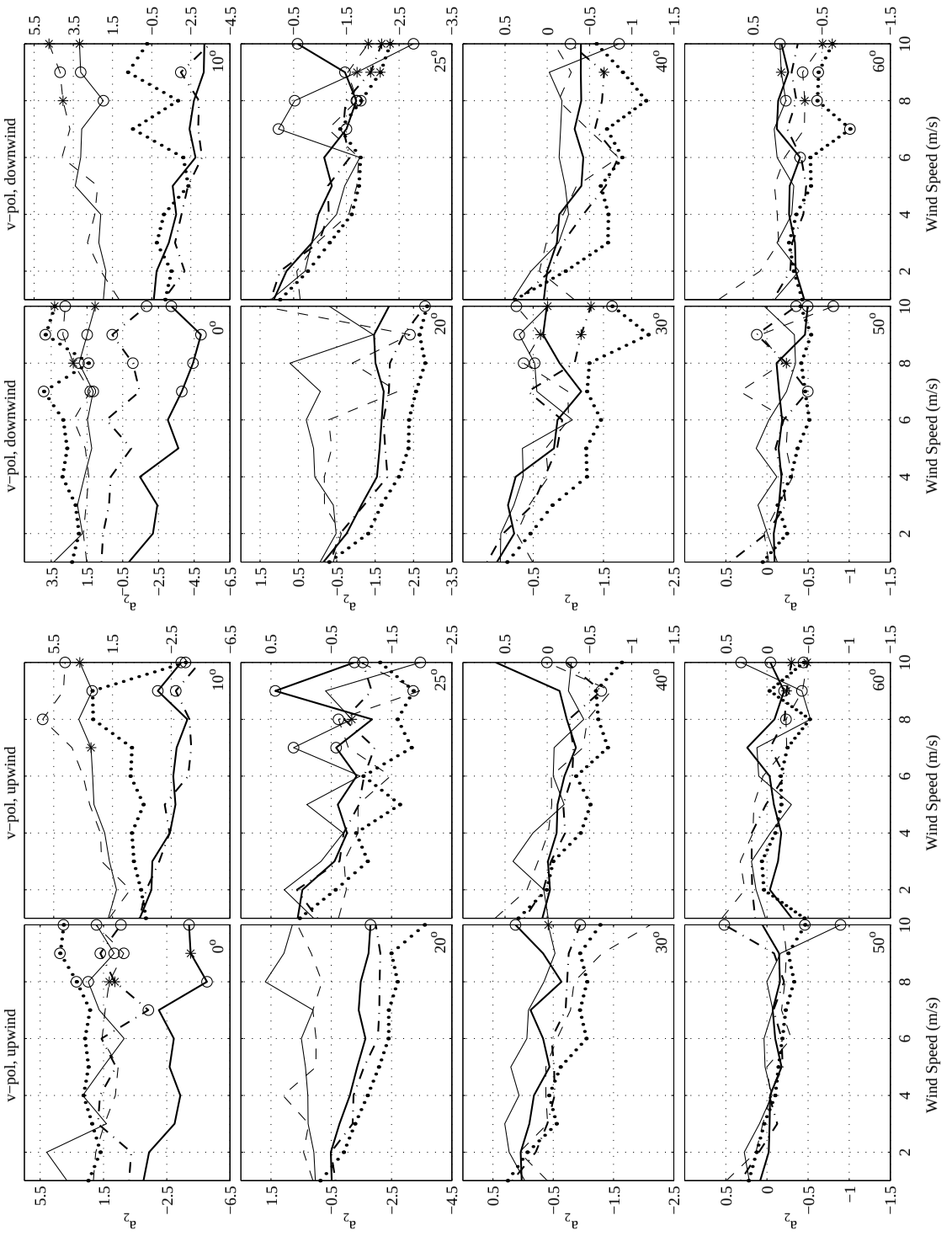

Figure B.22: a_2 values for v-pol, upwind and downwind data versus wind speed for YSCAT94 for the generalized log-normal distribution. Incidence angle is located at the bottom right corner of each plot. Thin solid line → 2 GHz, dashed line → 3 GHz, dotted line → 5 GHz, dash/dot line → 10 GHz, and the bold solid line → 14 GHz. Asterisks correspond to bins with no data, and circles indicate bins with only one or two minutes of data.

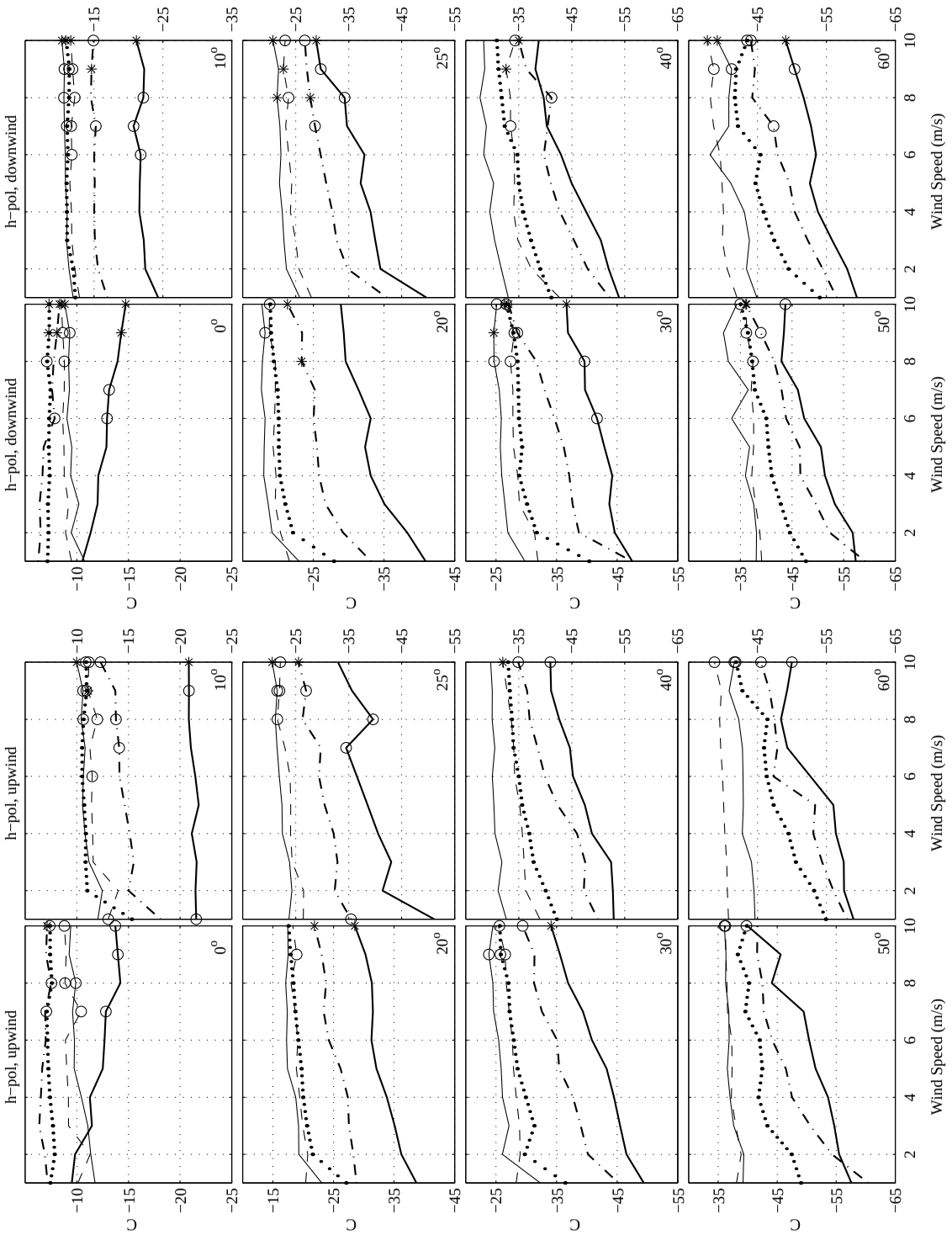

Figure B.23: C values for h-pol, upwind and downwind data versus wind speed for YSCAT94 for the generalized log-normal distribution. Incidence angle is located at the bottom right corner of each plot. Thin solid line $\rightarrow$ 2 GHz, dashed line $\rightarrow$ 3 GHz, dotted line $\rightarrow$ 5 GHz, dash/dot line $\rightarrow$ 10 GHz, and the bold solid line $\rightarrow$ 14 GHz. Asterisks correspond to bins with no data, and circles indicate bins with only one or two minutes of data.

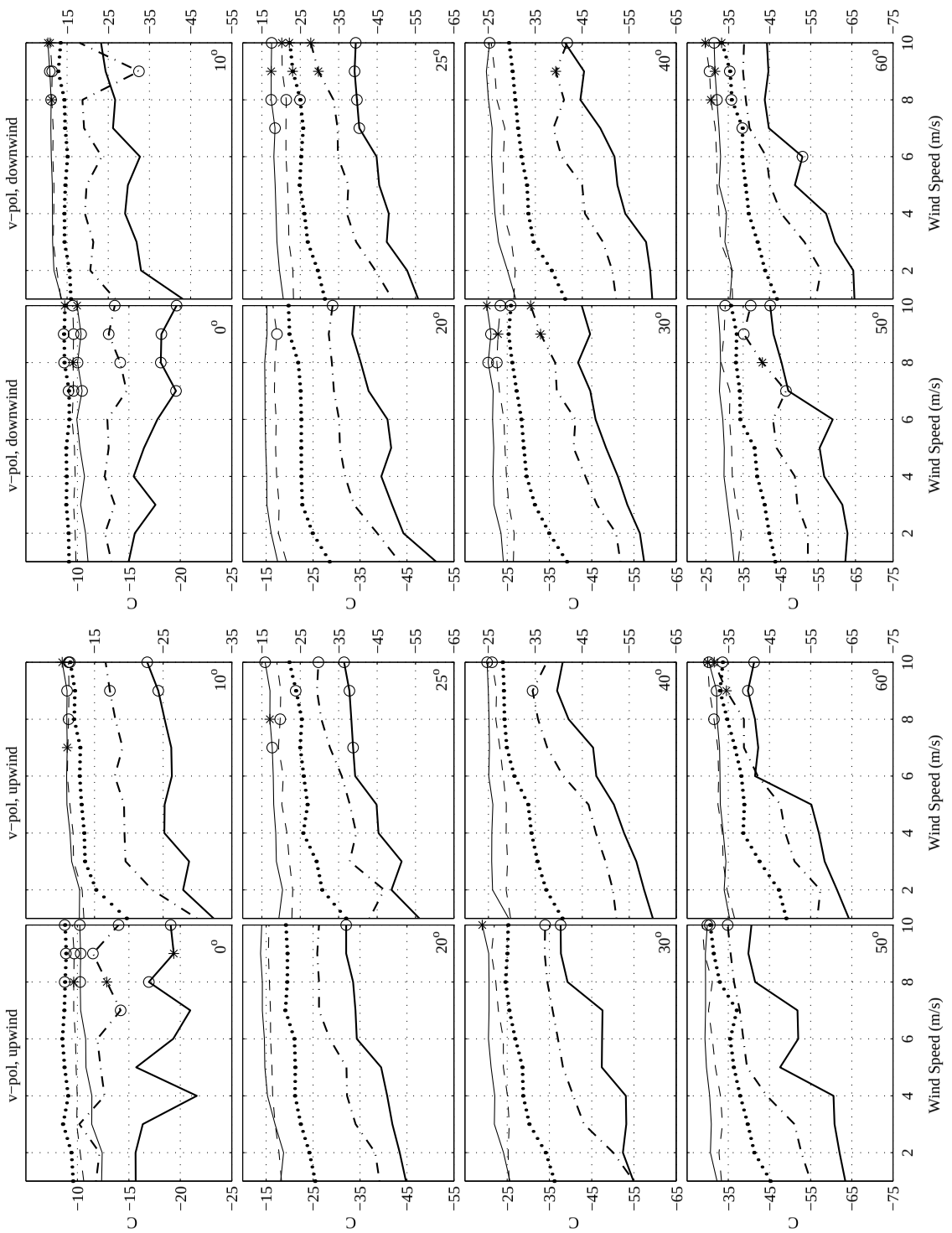

Figure B.24: C values for v-pol, upwind and downwind data versus wind speed for YSCAT94 for the generalized log-normal distribution. Incidence angle is located at the bottom right corner of each plot. Thin solid line $\rightarrow$ 2 GHz, dashed line $\rightarrow$ 3 GHz, dotted line $\rightarrow$ 5 GHz, dash/dot line $\rightarrow$ 10 GHz, and the bold solid line $\rightarrow$ 14 GHz. Asterisks correspond to bins with no data, and circles indicate bins with only one or two minutes of data.

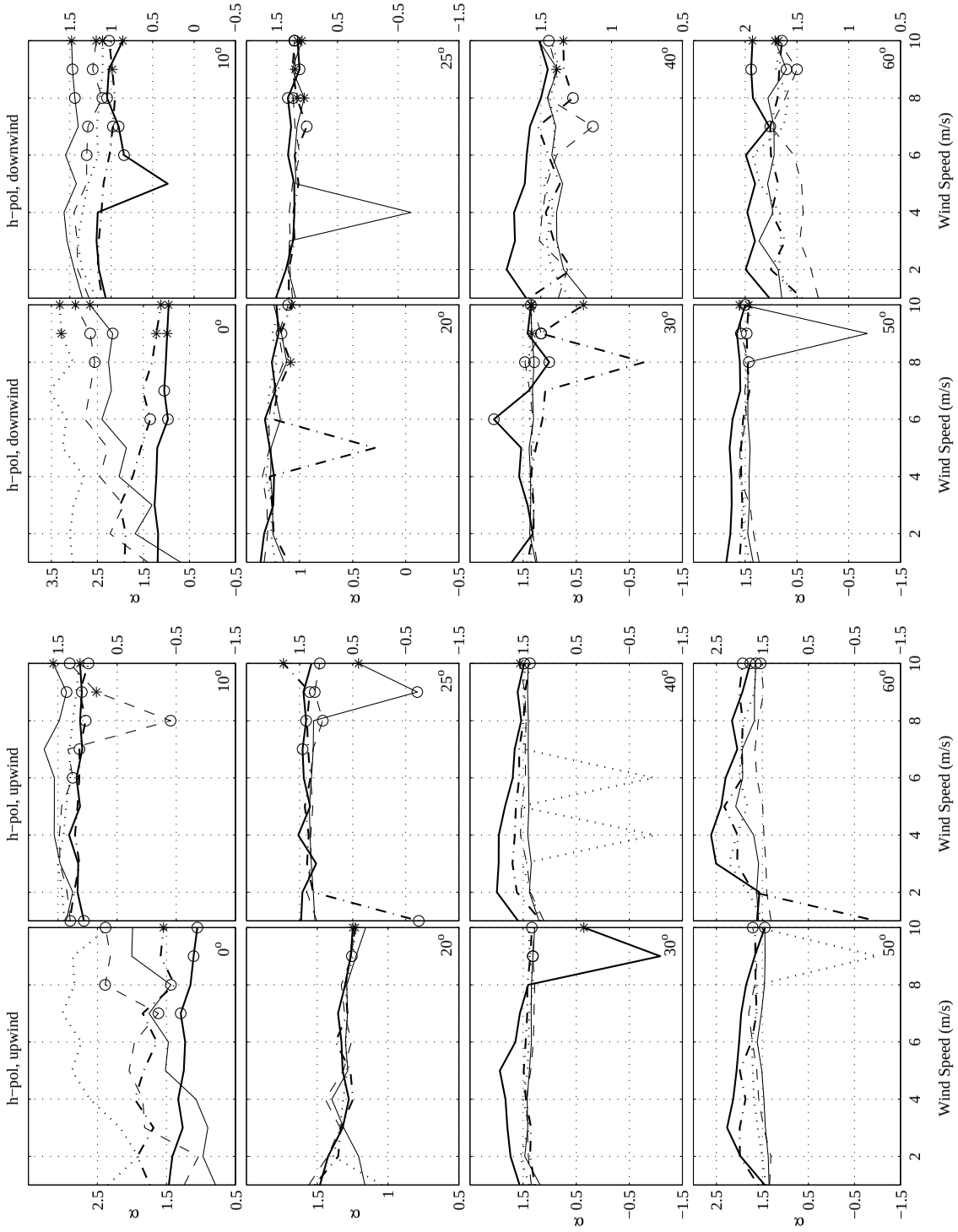

Figure B.25: α values for h-pol, upwind and downwind data versus wind speed for YSCAT94 for the Weibull distribution. Incidence angle is located at the bottom right corner of each plot. Thin solid line $\rightarrow$ 2 GHz, dashed line $\rightarrow$ 3 GHz, dotted line $\rightarrow$ 5 GHz, dash/dot line $\rightarrow$ 10 GHz, and the bold solid line $\rightarrow$ 14 GHz. Asterisks correspond to bins with no data, and circles indicate bins with only one or two minutes of data.

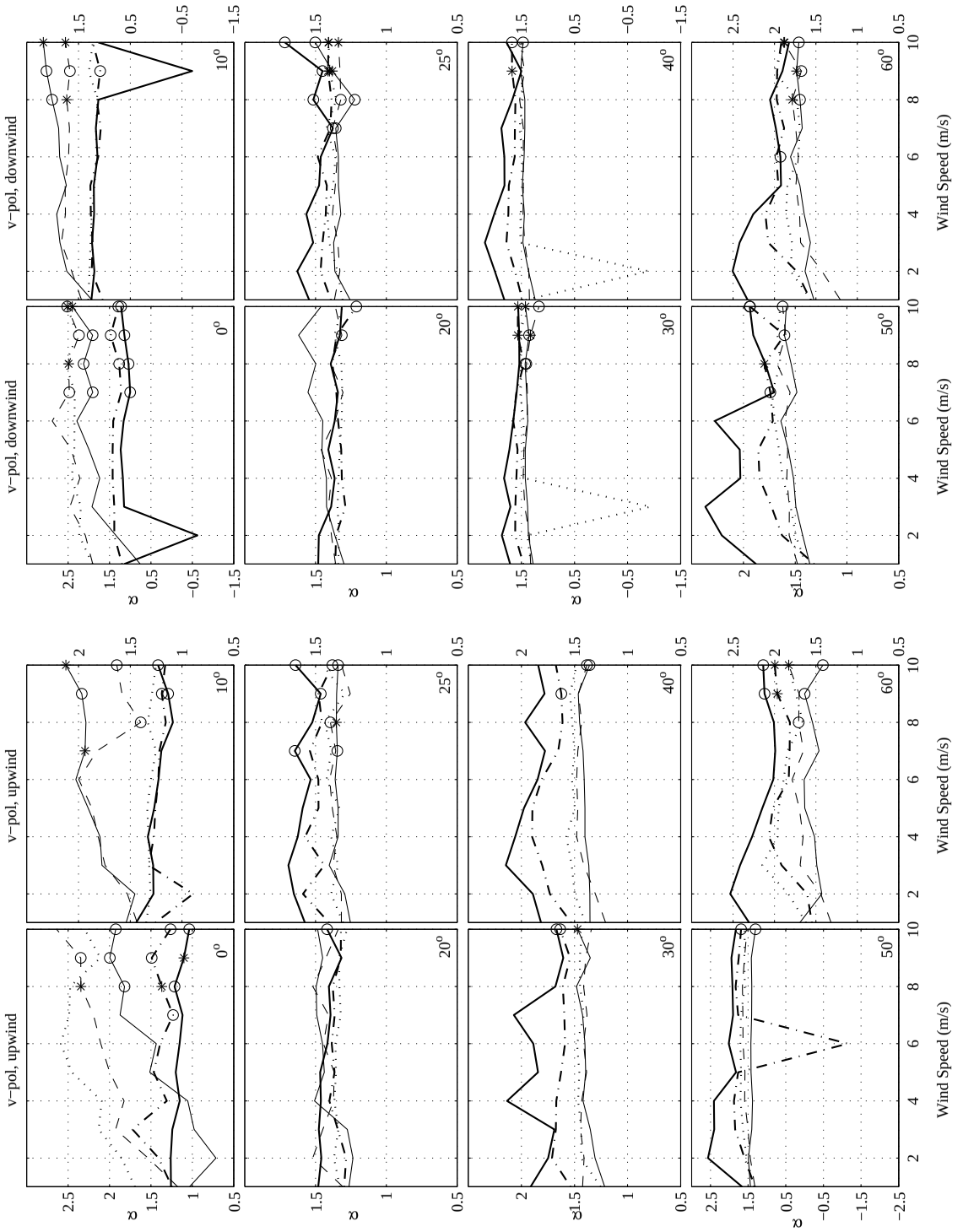

Figure B.26: α values for v-pol, upwind and downwind data versus wind speed for YSCAT94 for the Weibull distribution. Incidence angle is located at the bottom right corner of each plot. Thin solid line $\rightarrow$ 2 GHz, dashed line $\rightarrow$ 3 GHz, dotted line $\rightarrow$ 5 GHz, dash/dot line $\rightarrow$ 10 GHz, and the bold solid line $\rightarrow$ 14 GHz. Asterisks correspond to bins with no data, and circles indicate bins with only one or two minutes of data.

Appendix C

Parameters for YSCAT94 Data According to Mean Wave Slope

Parameters occur in the following order:

- Mean. Figs. C.1 to C.2
- Variance. Figs. C.3 to C.4
- a_1 for the Rayleigh/generalized log-normal distribution. Figs. C.5 to C.6
- a_2 for the Rayleigh/generalized log-normal distribution. Figs. C.7 to C.8
- C for the Rayleigh/generalized log-normal distribution. Figs. C.9 to C.10
- Log-mean. Figs. C.11 to C.12
- Log-variance. Figs. C.13 to C.14
- a_1 for the log-normal distribution. Figs. C.15 to C.16
- C for the log-normal distribution. Figs. C.17 to C.18
- a_1 for the generalized log-normal distribution. Figs. C.19 to C.20
- a_2 for the generalized log-normal distribution. Figs. C.21 to C.22
- C for the generalized log-normal distribution. Figs. C.23 to C.24

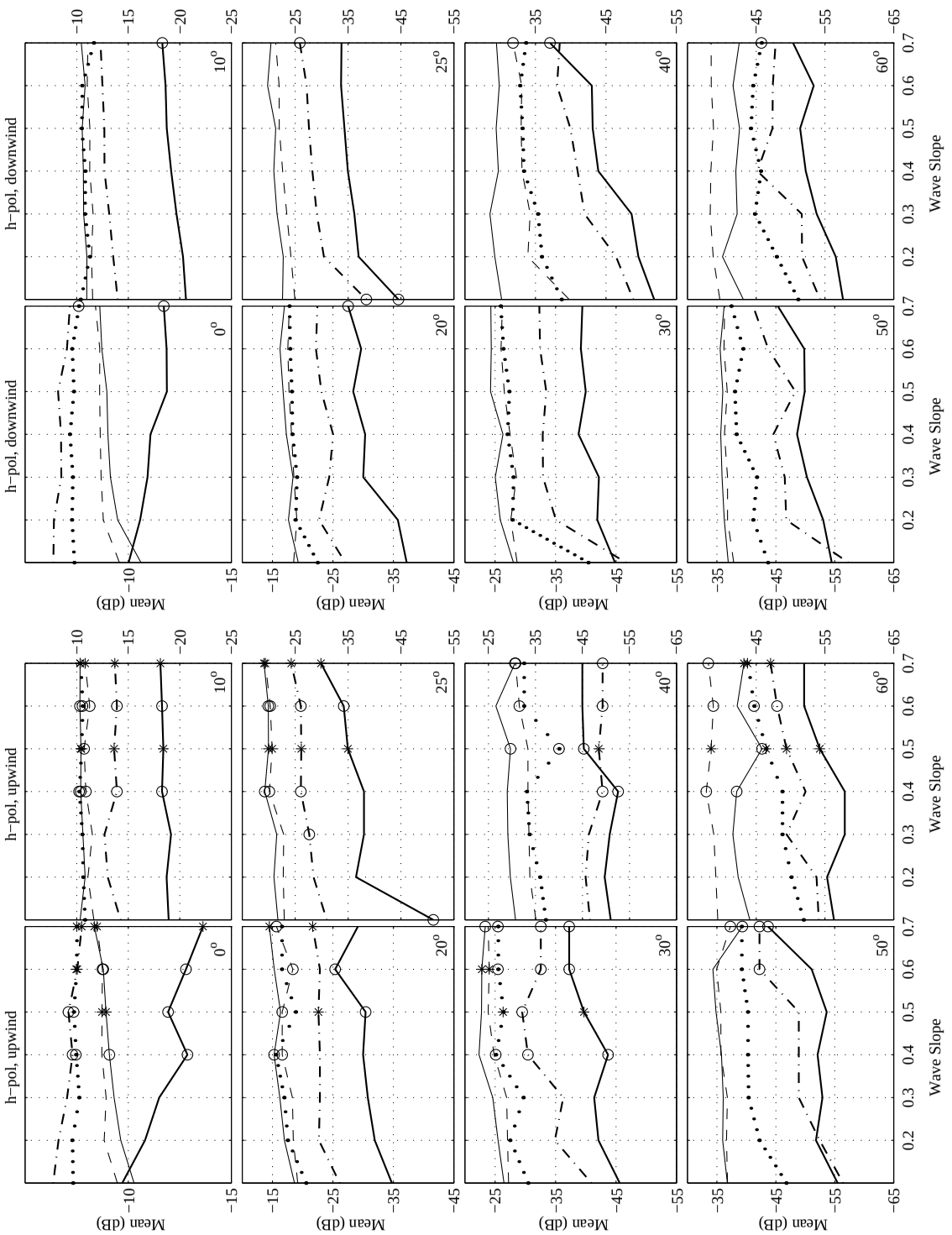

Figure C.1: Mean values for h-pol, upwind and downwind data versus mean wave slope for YSCAT94. Incidence angle is located at the bottom right corner of each plot. Thin solid line → 2 GHz, dashed line → 3 GHz, dotted line → 5 GHz, dash/dot line → 10 GHz, and the bold solid line → 14 GHz. Asterisks correspond to bins with no data, and circles indicate bins with only one or two minutes of data.

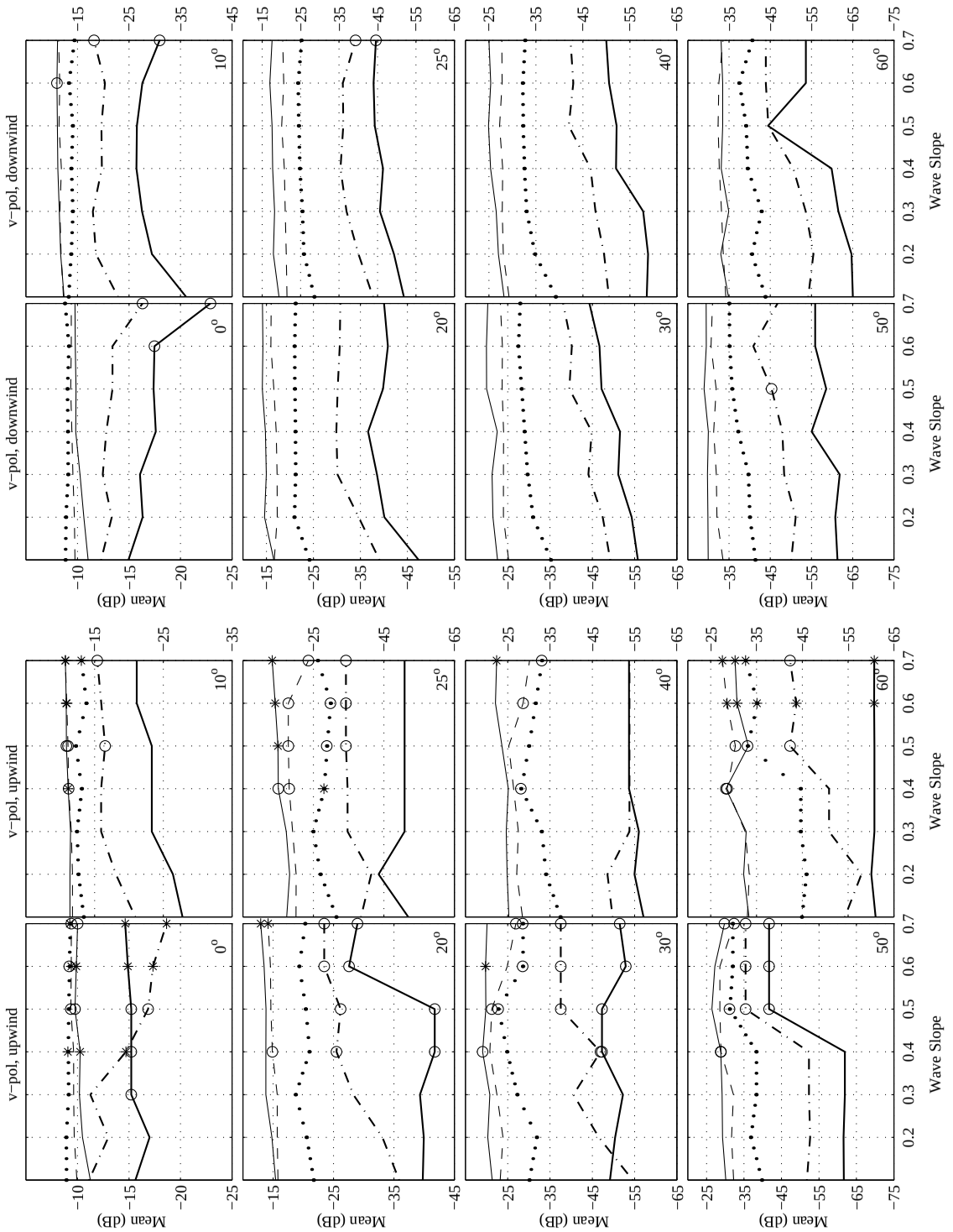

Figure C.2: Mean values for v-pol, upwind and downwind data versus mean wave slope for YSCAT94. Incidence angle is located at the bottom right corner of each plot. Thin solid line → 2 GHz, dashed line → 3 GHz, dotted line → 5 GHz, dash/dot line → 10 GHz, and the bold solid line → 14 GHz. Asterisks correspond to bins with no data, and circles indicate bins with only one or two minutes of data.

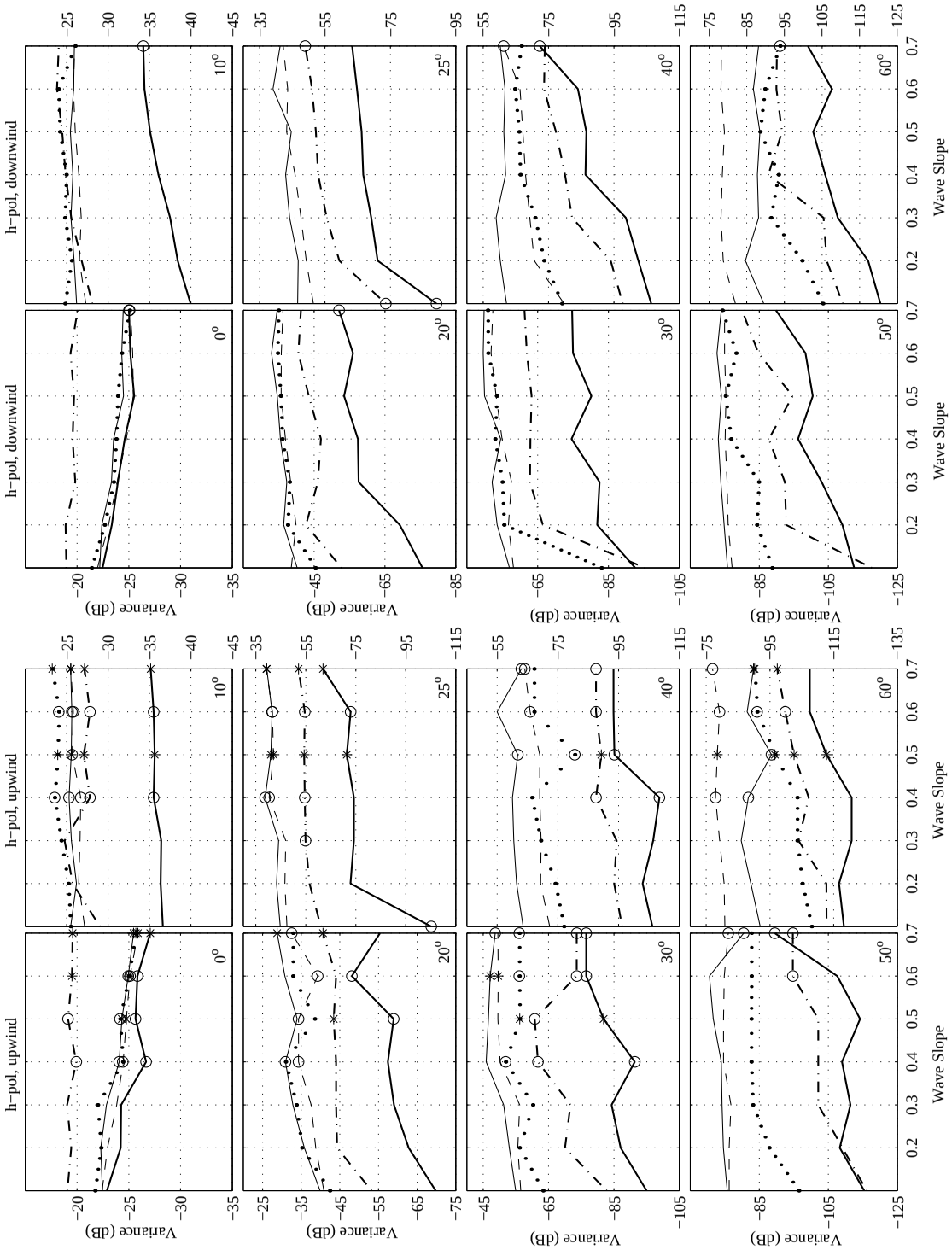

Figure C.3: Variance values for h-pol, upwind and downwind data versus mean wave slope for YSCAT94. Incidence angle is located at the bottom right corner of each plot. Thin solid line → 2 GHz, dashed line → 3 GHz, dotted line → 5 GHz, dash/dot line → 10 GHz, and the bold solid line → 14 GHz. Asterisks correspond to bins with no data, and circles indicate bins with only one or two minutes of data.

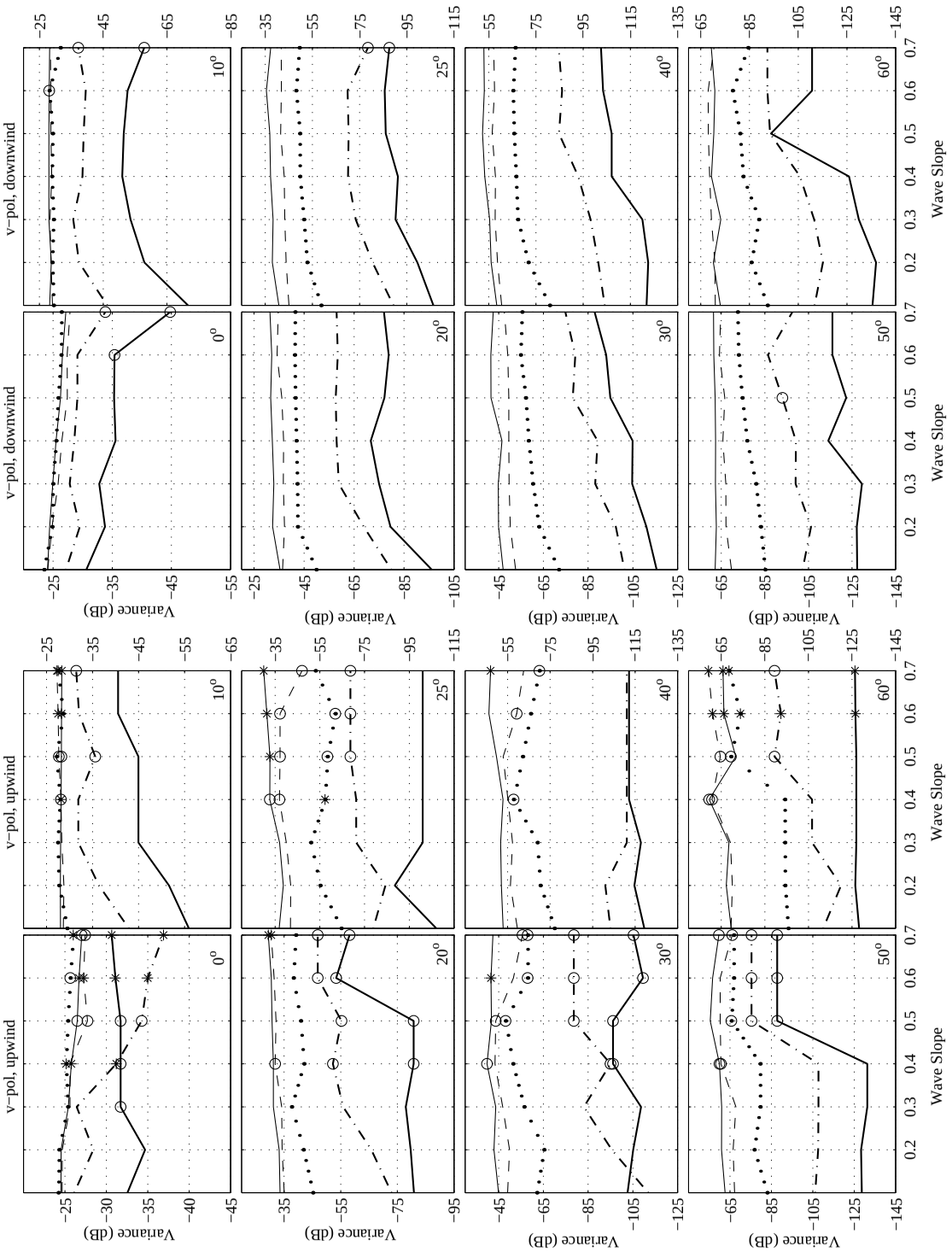

Figure C.4: Variance values for v-pol, upwind and downwind data versus mean wave slope for YSCAT94. Incidence angle is located at the bottom right corner of each plot. Thin solid line → 2 GHz, dashed line → 3 GHz, dotted line → 5 GHz, dash/dot line → 10 GHz, and the bold solid line → 14 GHz. Asterisks correspond to bins with no data, and circles indicate bins with only one or two minutes of data.

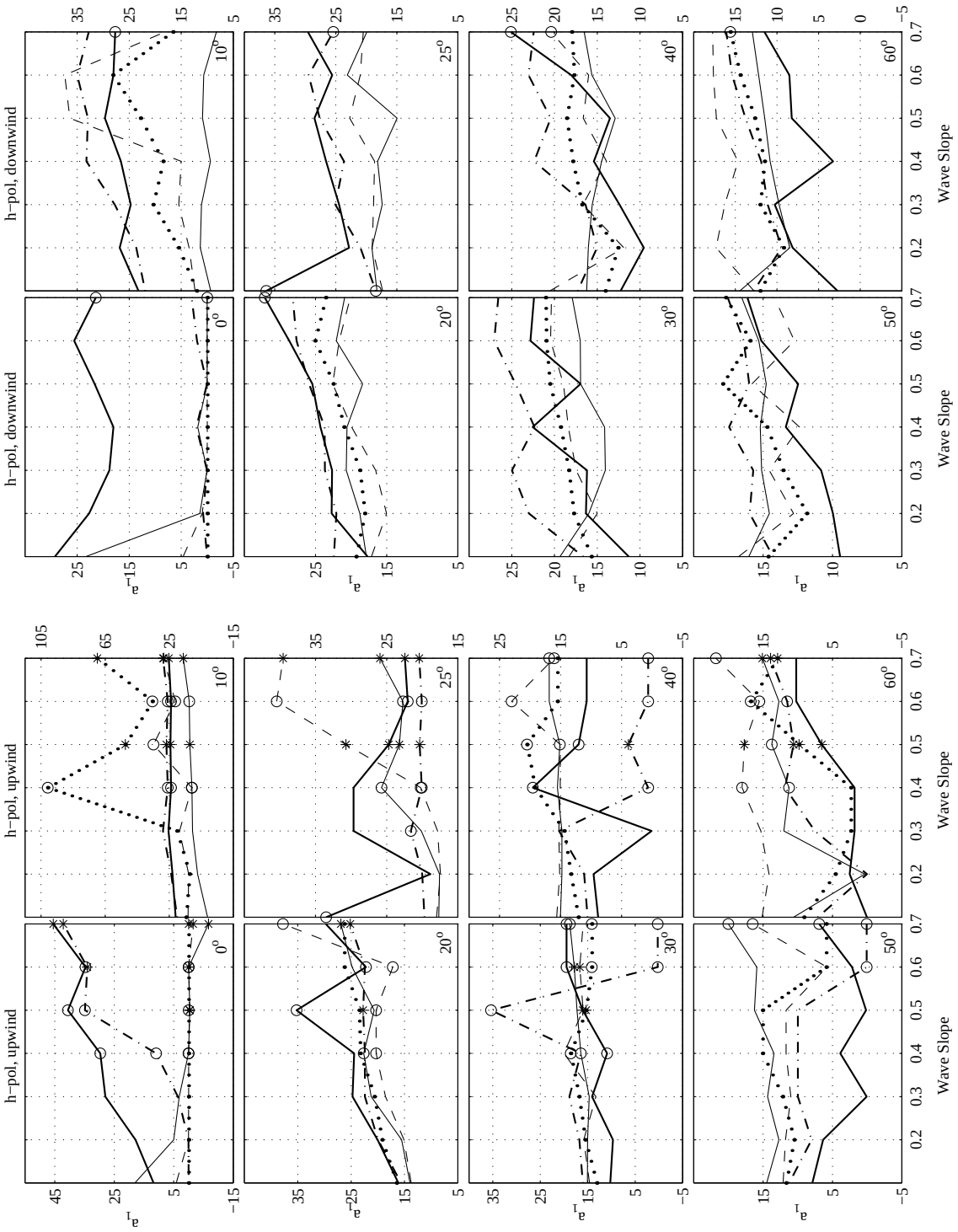

Figure C.5: a_1 values for h-pol, upwind and downwind data versus mean wave slope for YSCAT94 for the Rayleigh/generalized log-normal distribution. Incidence angle is located at the bottom right corner of each plot. Thin solid line → 2 GHz, dashed line → 3 GHz, dotted line → 5 GHz, dash/dot line → 10 GHz, and the bold solid line → 14 GHz. Asterisks correspond to bins with no data, and circles indicate bins with only one or two minutes of data.

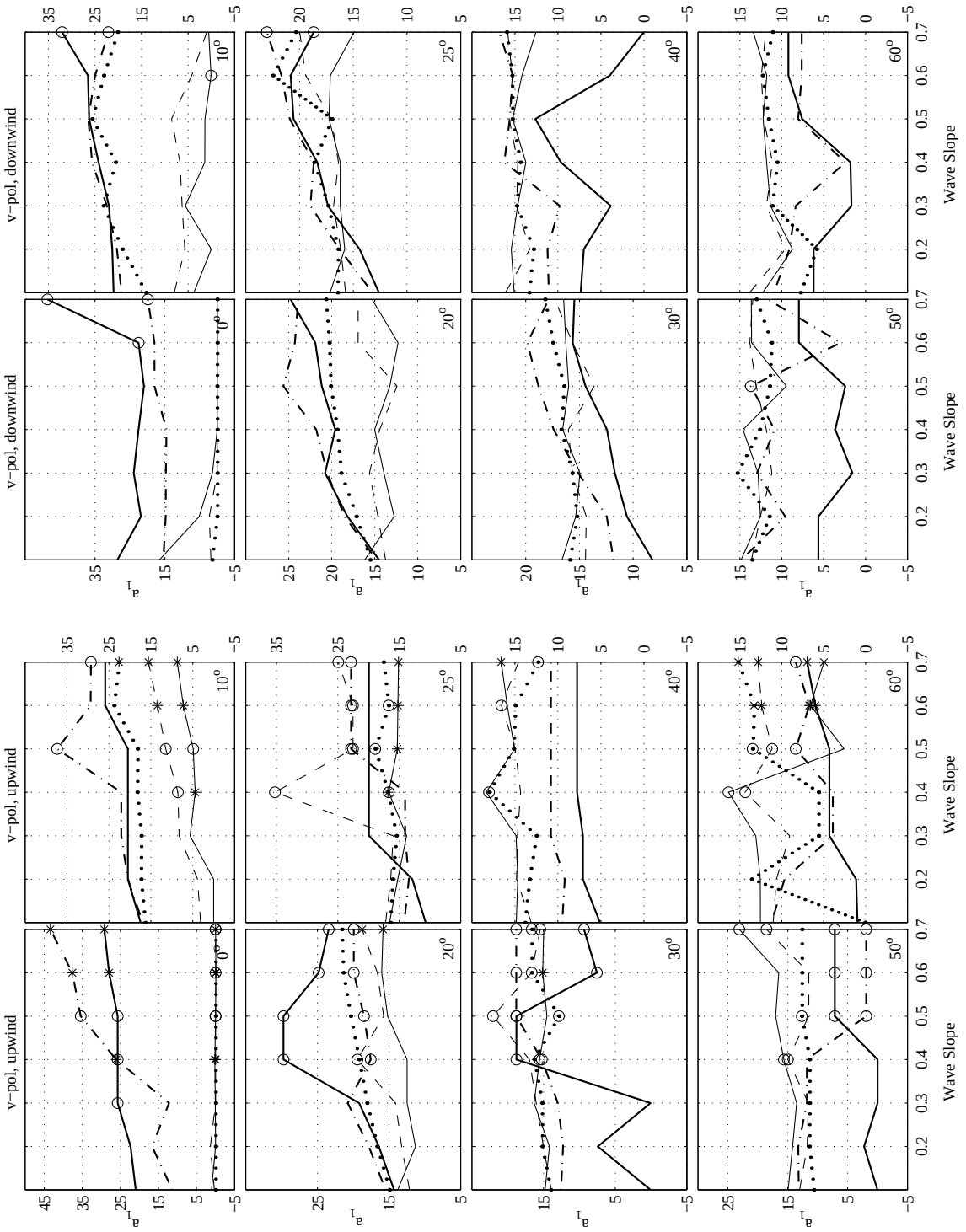

Figure C.6: a_1 values for v-pol, upwind and downwind data versus mean wave slope for YSCAT94 for the Rayleigh/generalized log-normal distribution. Incidence angle is located at the bottom right corner of each plot. Thin solid line → 2 GHz, dashed line → 3 GHz, dotted line → 5 GHz, dash/dot line → 10 GHz, and the bold solid line → 14 GHz. Asterisks correspond to bins with no data, and circles indicate bins with only one or two minutes of data.

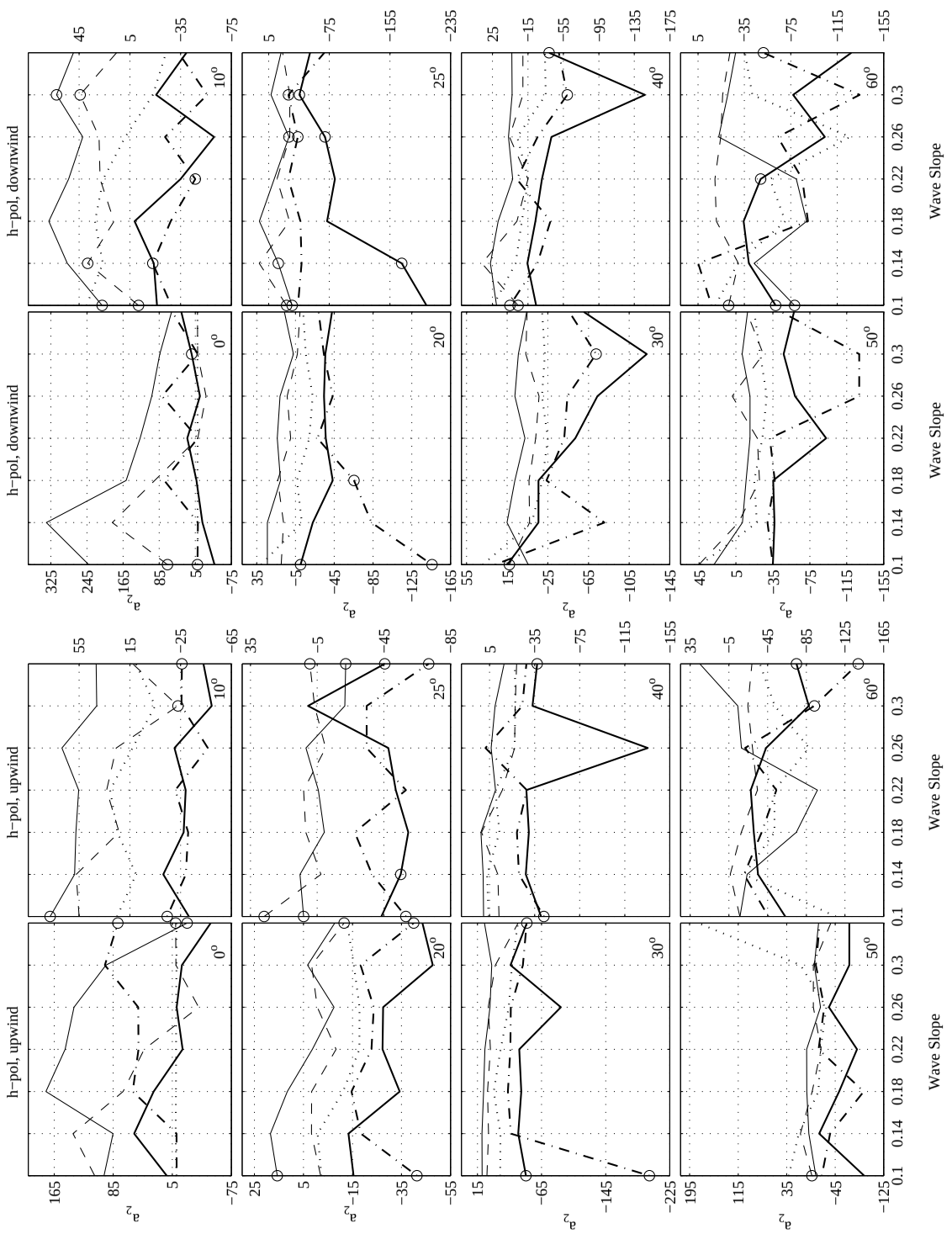

Figure C.7: a_2 values for h-pol, upwind and downwind data versus mean wave slope for YSCAT94 for the Rayleigh/generalized log-normal distribution. Incidence angle is located at the bottom right corner of each plot. Thin solid line → 2 GHz, dashed line → 3 GHz, dotted line → 5 GHz, dash/dot line → 10 GHz, and the bold solid line → 14 GHz. Asterisks correspond to bins with no data, and circles indicate bins with only one or two minutes of data.

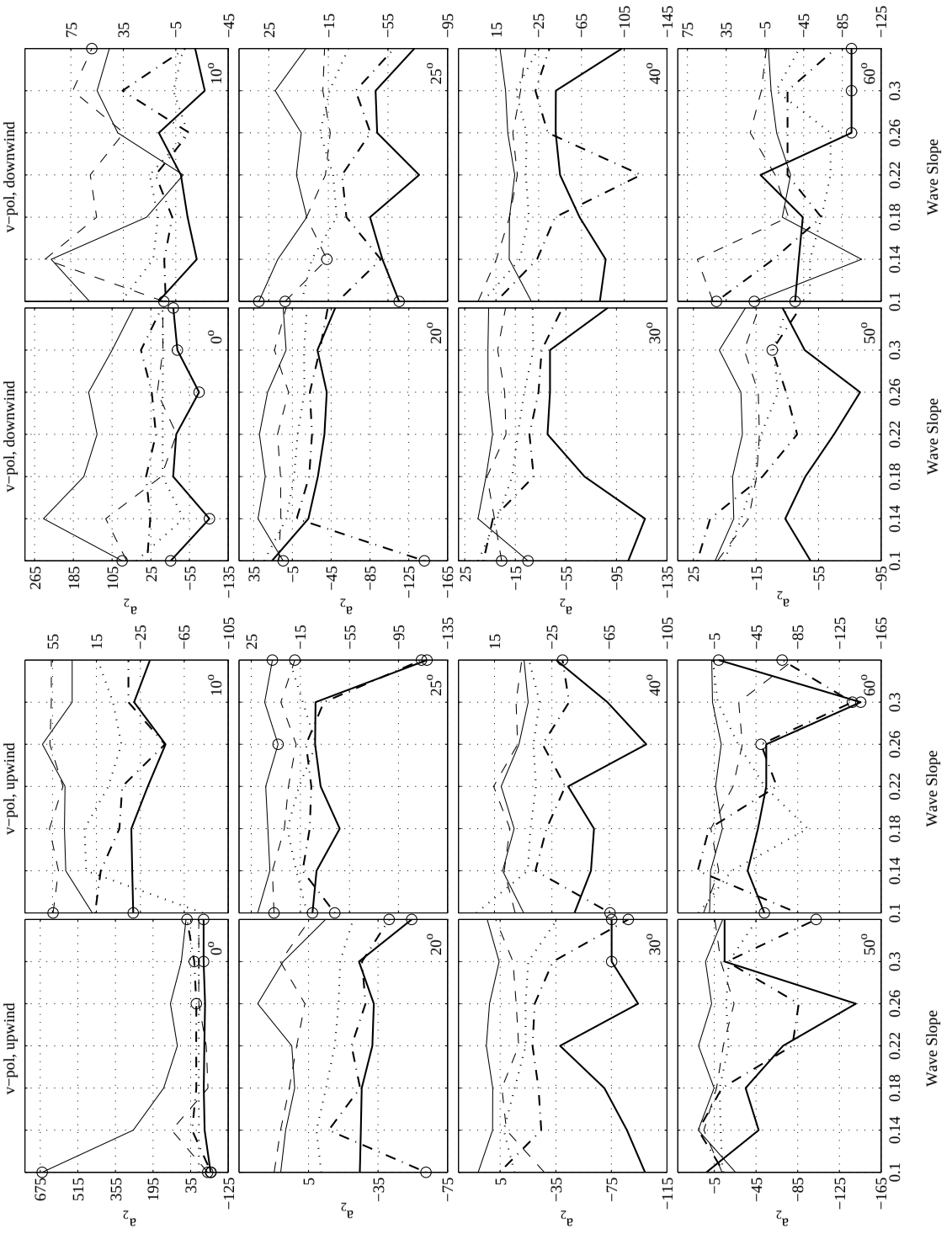

Figure C.8: a_2 values for v-pol, upwind and downwind data versus mean wave slope for YSCAT94 for the Rayleigh/generalized log-normal distribution. Incidence angle is located at the bottom right corner of each plot. Thin solid line → 2 GHz, dashed line → 3 GHz, dotted line → 5 GHz, dash/dot line → 10 GHz, and the bold solid line → 14 GHz. Asterisks correspond to bins with no data, and circles indicate bins with only one or two minutes of data.

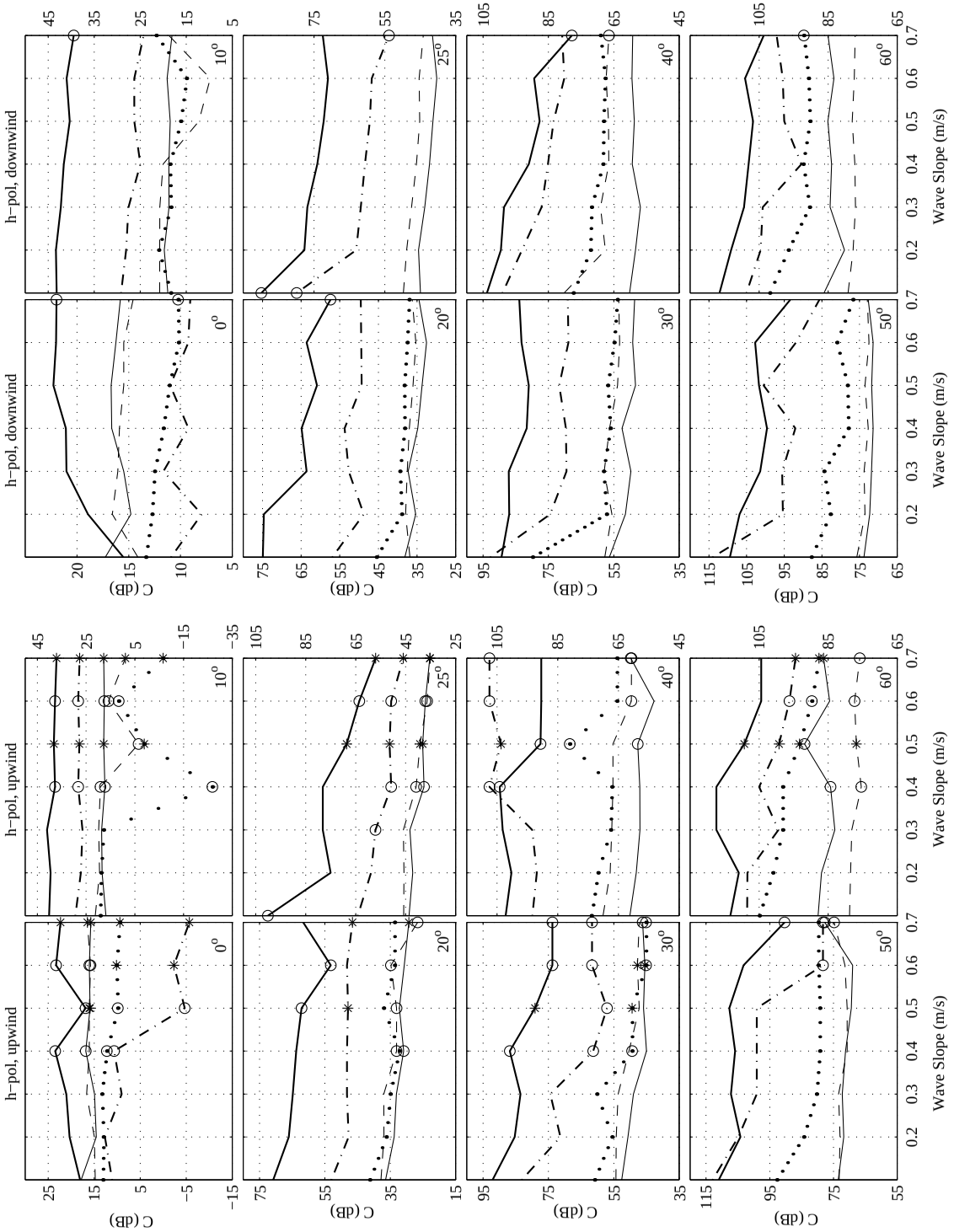

Figure C.9: C values for h-pol, upwind and downwind data versus mean wave slope for YSCAT94 for the Rayleigh/generalized log-normal distribution. Incidence angle is located at the bottom right corner of each plot. Thin solid line $\rightarrow$ 2 GHz, dashed line $\rightarrow$ 3 GHz, dotted line $\rightarrow$ 5 GHz, dash/dot line $\rightarrow$ 10 GHz, and the bold solid line $\rightarrow$ 14 GHz. Asterisks correspond to bins with no data, and circles indicate bins with only one or two minutes of data.

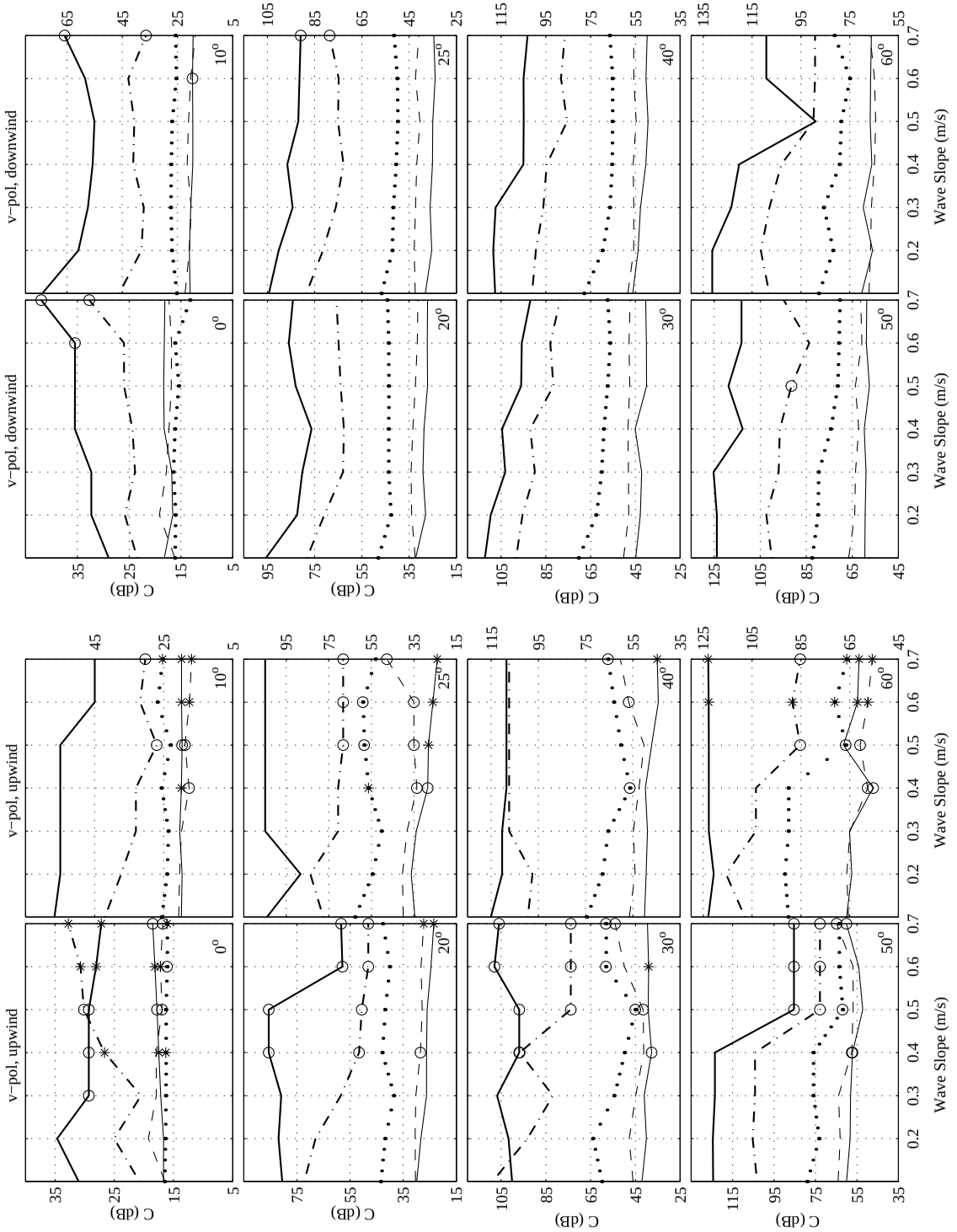

Figure C.10: C values for v-pol, upwind and downwind data versus mean wave slope for YSCAT94 for the Rayleigh/generalized log-normal distribution. Incidence angle is located at the bottom right corner of each plot. Thin solid line $\rightarrow$ 2 GHz, dashed line $\rightarrow$ 3 GHz, dotted line $\rightarrow$ 5 GHz, dash/dot line $\rightarrow$ 10 GHz, and the bold solid line $\rightarrow$ 14 GHz. Asterisks correspond to bins with no data, and circles indicate bins with only one or two minutes of data.

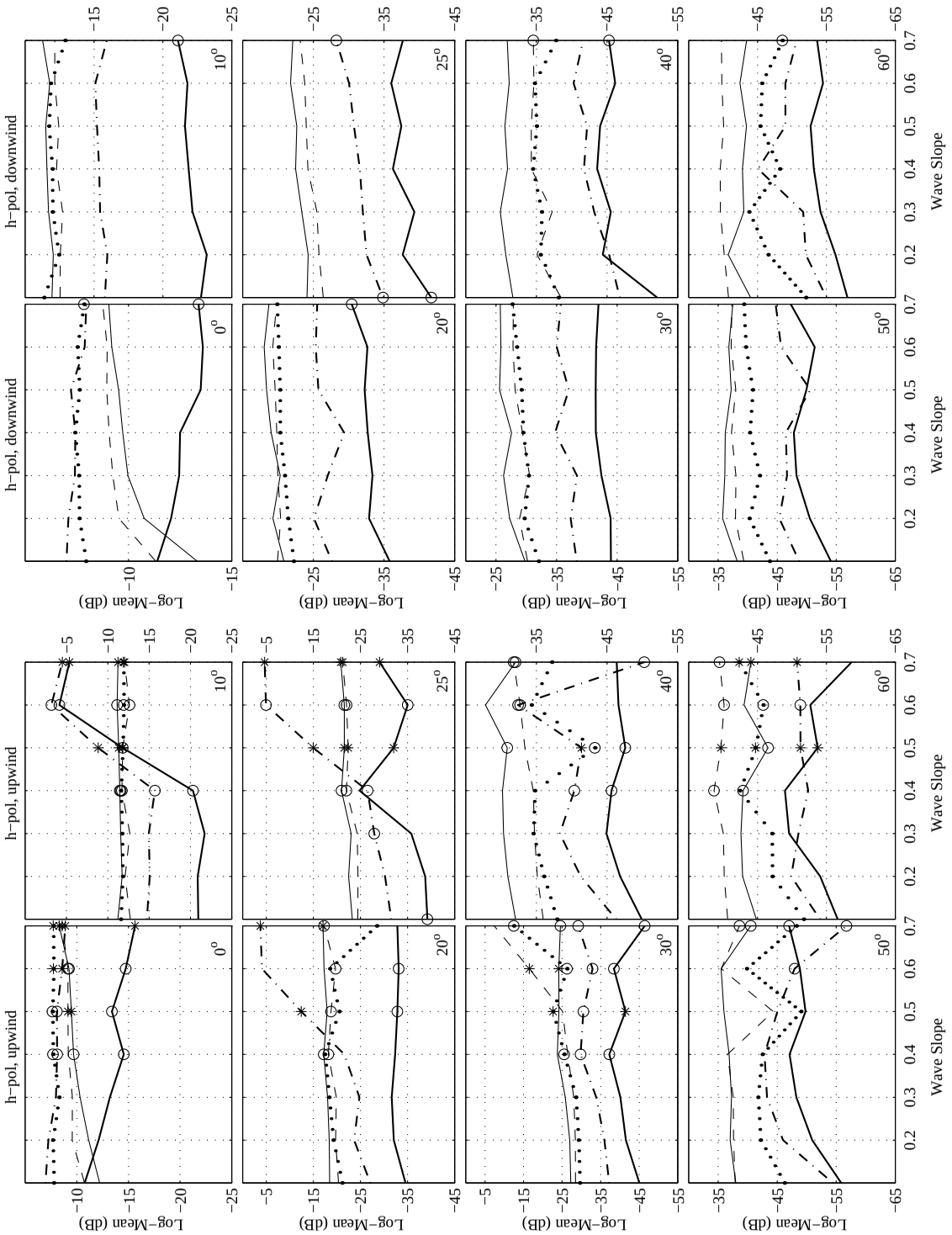

Figure C.11: Log-mean values for h-pol, upwind and downwind data versus mean wave slope for YSCAT94. Incidence angle is located at the bottom right corner of each plot. Thin solid line → 2 GHz, dashed line → 3 GHz, dotted line → 5 GHz, dash/dot line → 10 GHz, and the bold solid line → 14 GHz. Asterisks correspond to bins with no data, and circles indicate bins with only one or two minutes of data.

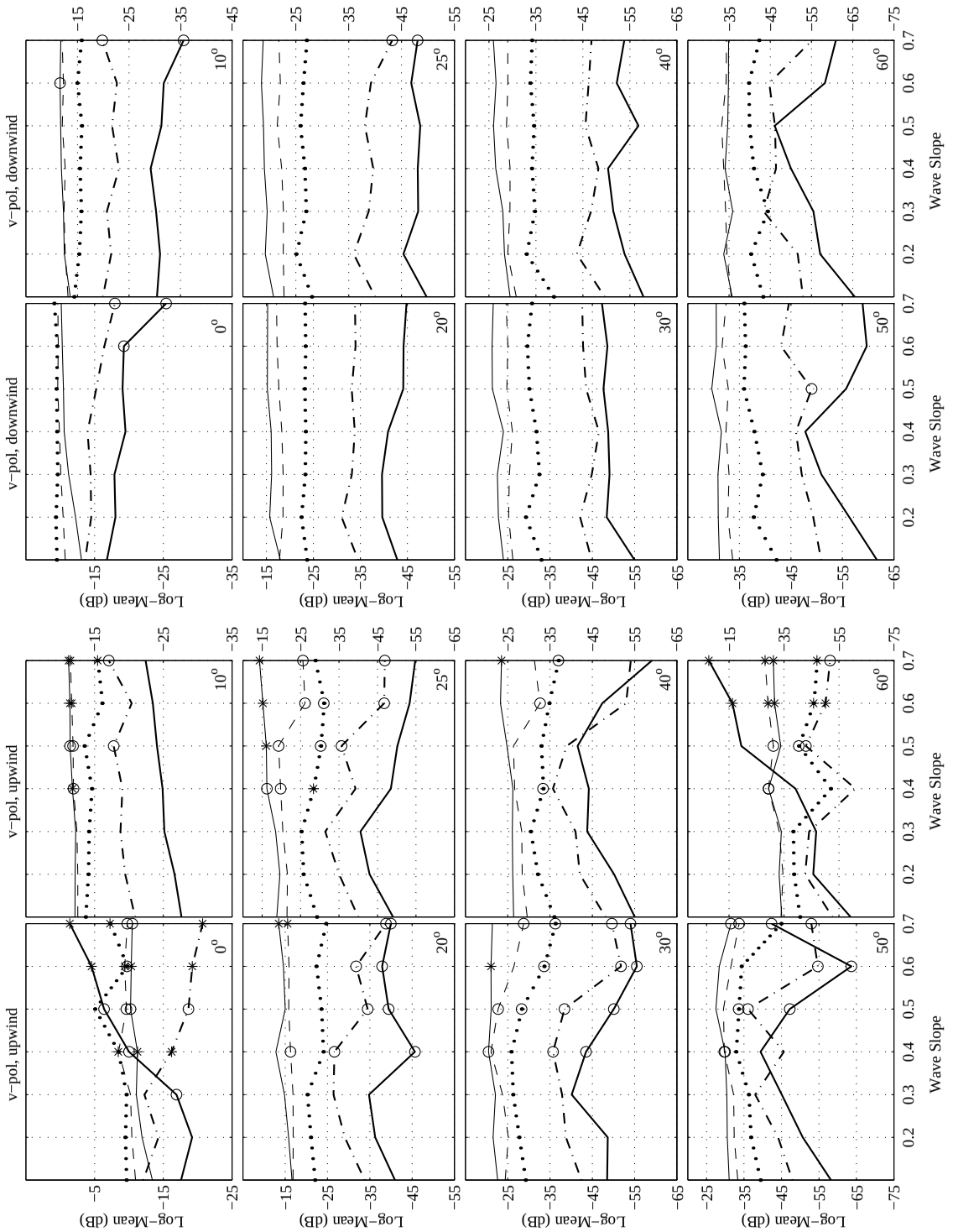

Figure C.12: Log-mean values for v-pol, upwind and downwind data versus mean wave slope for YSCAT94. Incidence angle is located at the bottom right corner of each plot. Thin solid line → 2 GHz, dashed line → 3 GHz, dotted line → 5 GHz, dash/dot line → 10 GHz, and the bold solid line → 14 GHz. Asterisks correspond to bins with no data, and circles indicate bins with only one or two minutes of data.

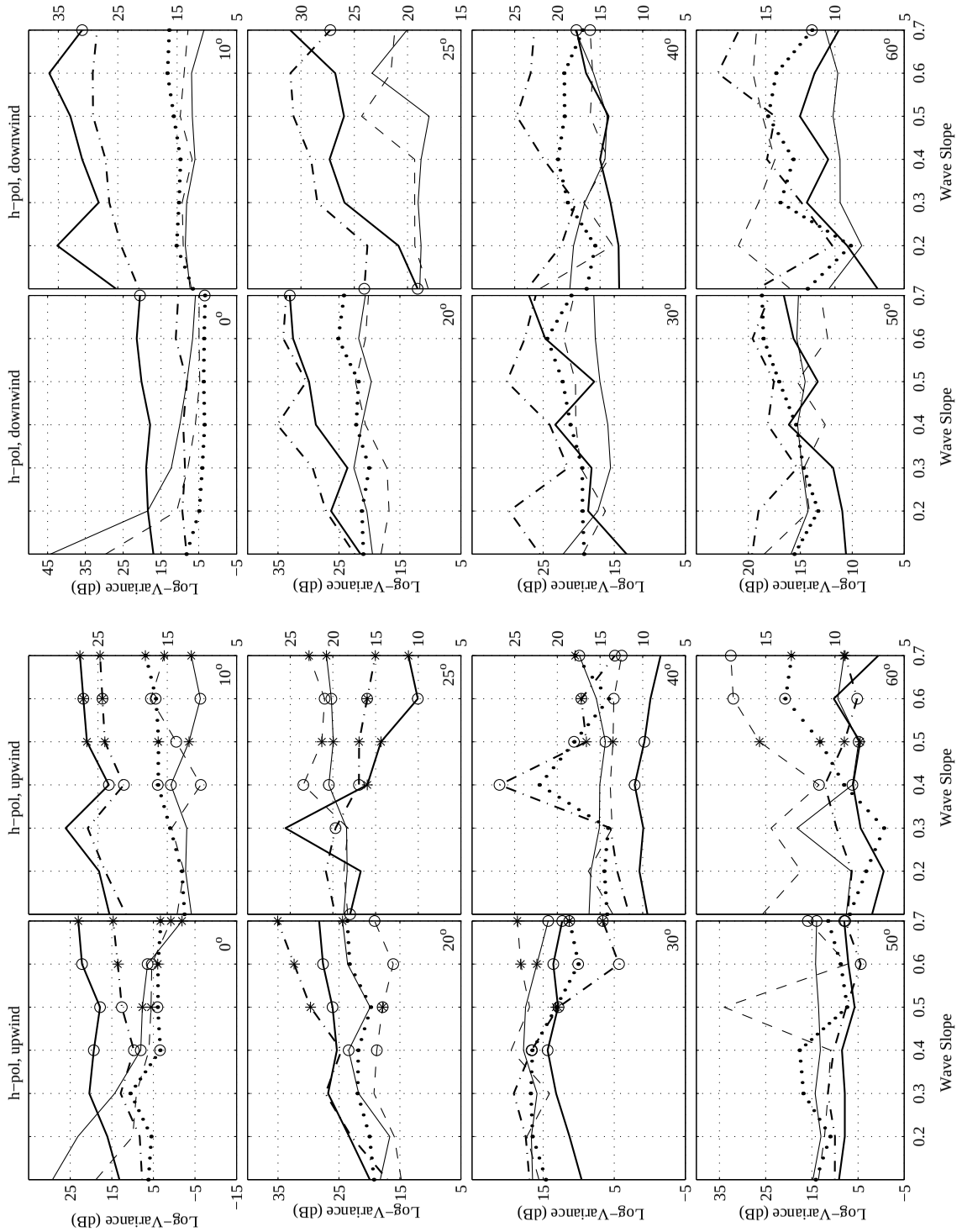

Figure C.13: Log-variance values for h-pol, upwind and downwind data versus mean wave slope for YSCAT94. Incidence angle is located at the bottom right corner of each plot. Thin solid line → 2 GHz, dashed line → 3 GHz, dotted line → 5 GHz, dash/dot line → 10 GHz, and the bold solid line → 14 GHz. Asterisks correspond to bins with no data, and circles indicate bins with only one or two minutes of data.

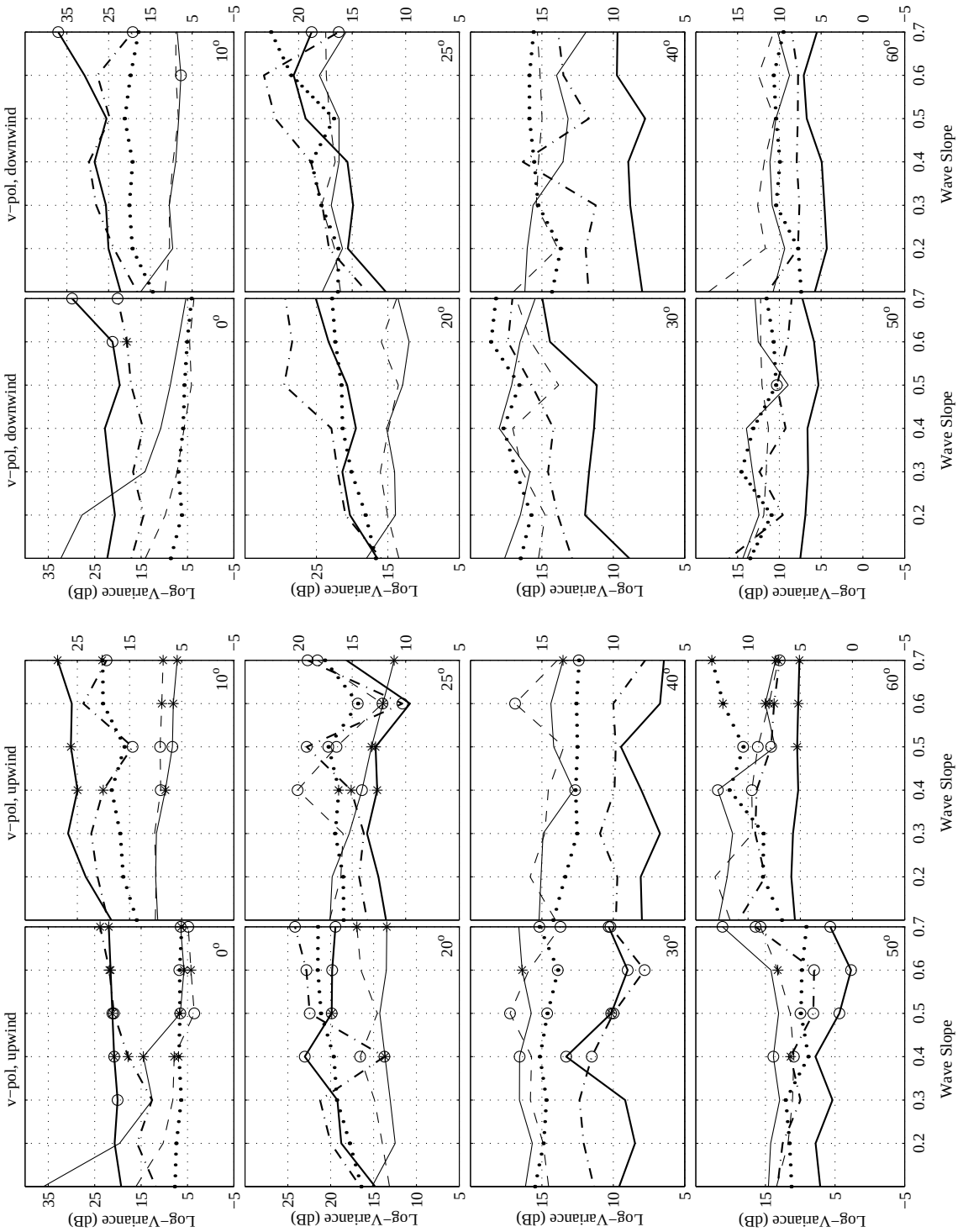

Figure C.14: Log-variance values for v-pol, upwind and downwind data versus mean wave slope for YSCAT94. Incidence angle is located at the bottom right corner of each plot. Thin solid line → 2 GHz, dashed line → 3 GHz, dotted line → 5 GHz, dash/dot line → 10 GHz, and the bold solid line → 14 GHz. Asterisks correspond to bins with no data, and circles indicate bins with only one or two minutes of data.

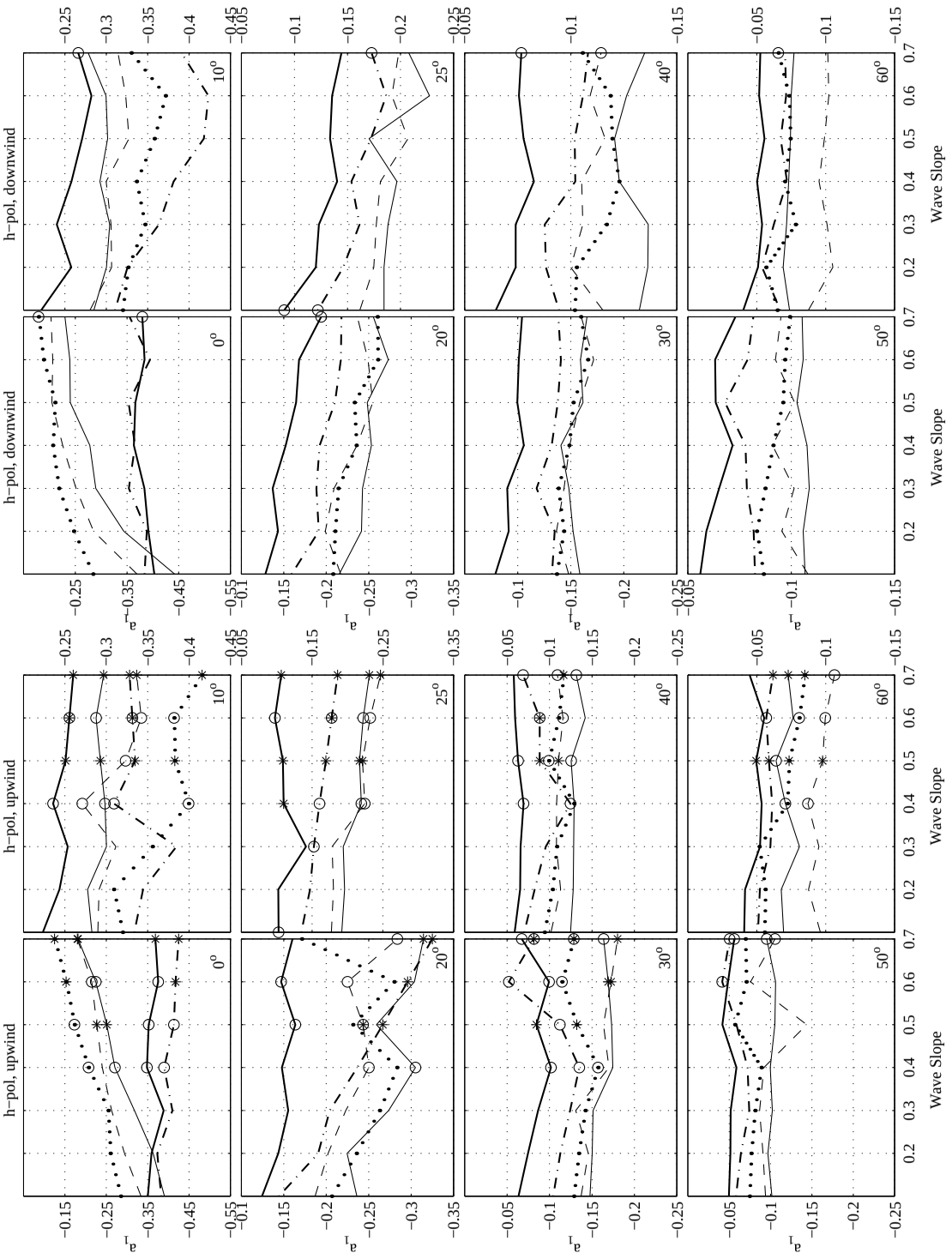

Figure C.15: a_1 values for h-pol, upwind and downwind data versus mean wave slope for YSCAT94 for the log-normal distribution. Incidence angle is located at the bottom right corner of each plot. Thin solid line → 2 GHz, dashed line → 3 GHz, dotted line → 5 GHz, dash/dot line → 10 GHz, and the bold solid line → 14 GHz. Asterisks correspond to bins with no data, and circles indicate bins with only one or two minutes of data.

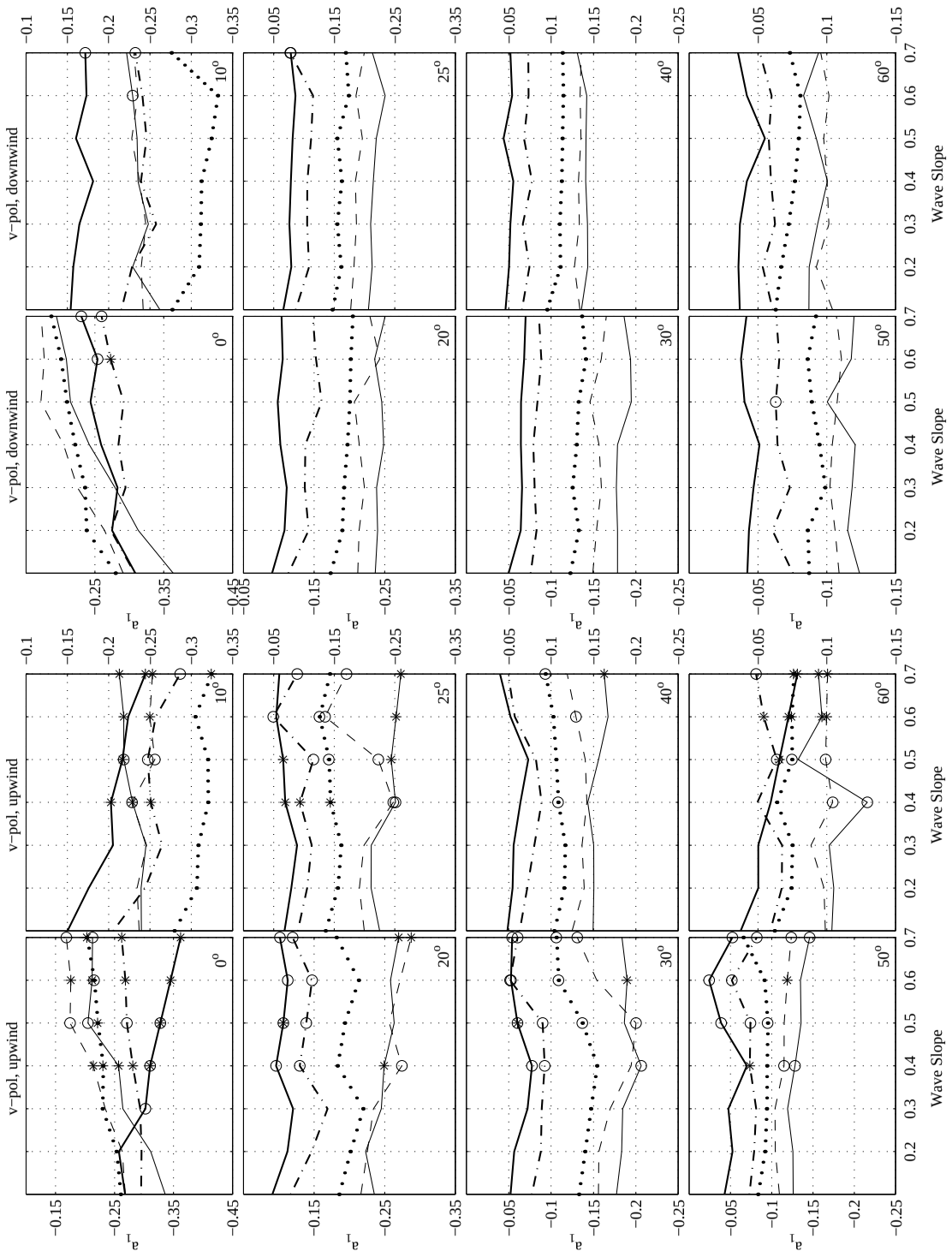

Figure C.16: a_1 values for v-pol, upwind and downwind data versus mean wave slope for YSCAT94 for the log-normal distribution. Incidence angle is located at the bottom right corner of each plot. Thin solid line $\rightarrow$ 2 GHz, dashed line $\rightarrow$ 3 GHz, dotted line $\rightarrow$ 5 GHz, dash/dot line $\rightarrow$ 10 GHz, and the bold solid line $\rightarrow$ 14 GHz. Asterisks correspond to bins with no data, and circles indicate bins with only one or two minutes of data.

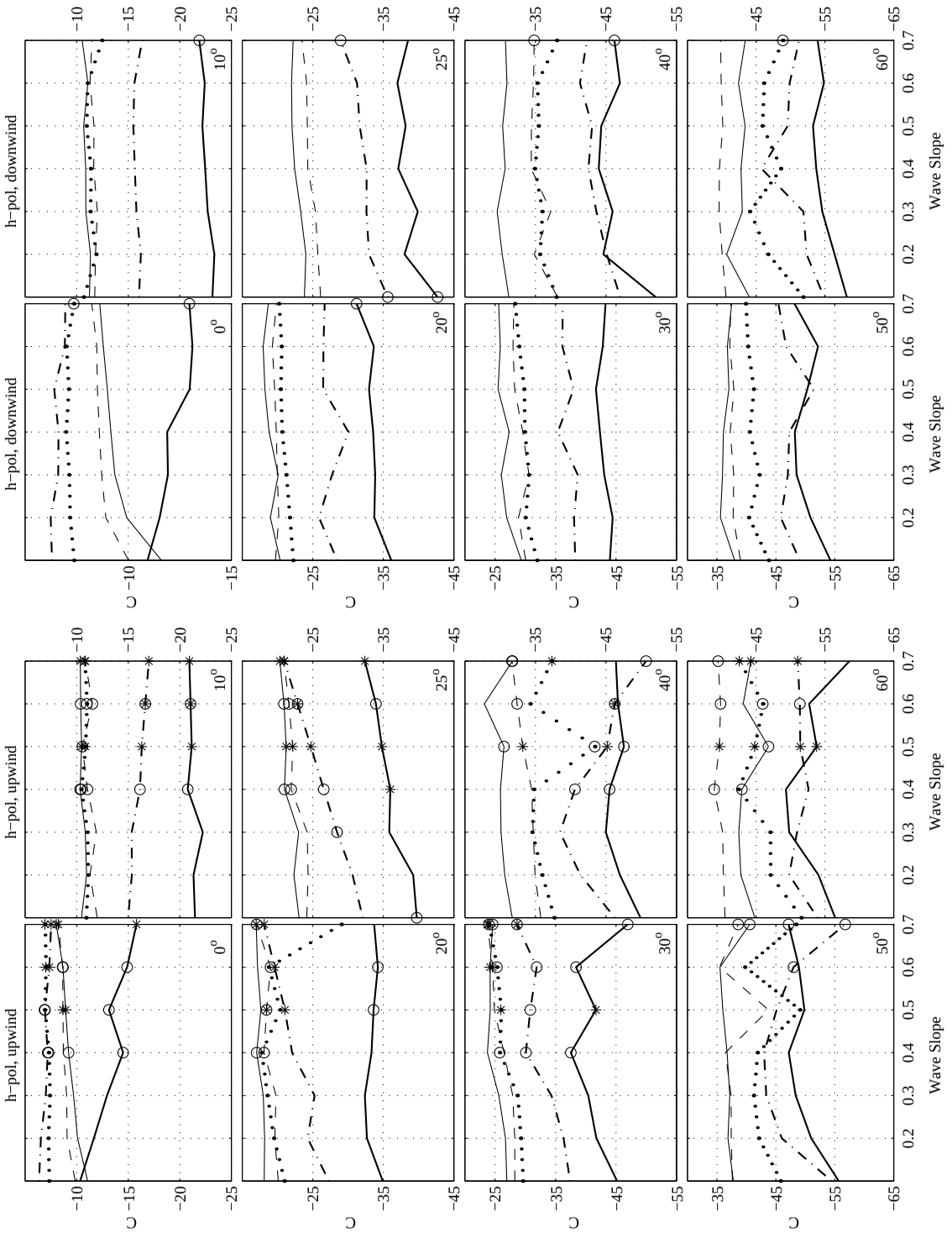

Figure C.17: C values for h-pol, upwind and downwind data versus mean wave slope for YSCAT94 for the log-normal distribution. Incidence angle is located at the bottom right corner of each plot. Thin solid line $\rightarrow$ 2 GHz, dashed line $\rightarrow$ 3 GHz, dotted line $\rightarrow$ 5 GHz, dash/dot line $\rightarrow$ 10 GHz, and the bold solid line $\rightarrow$ 14 GHz. Asterisks correspond to bins with no data, and circles indicate bins with only one or two minutes of data.

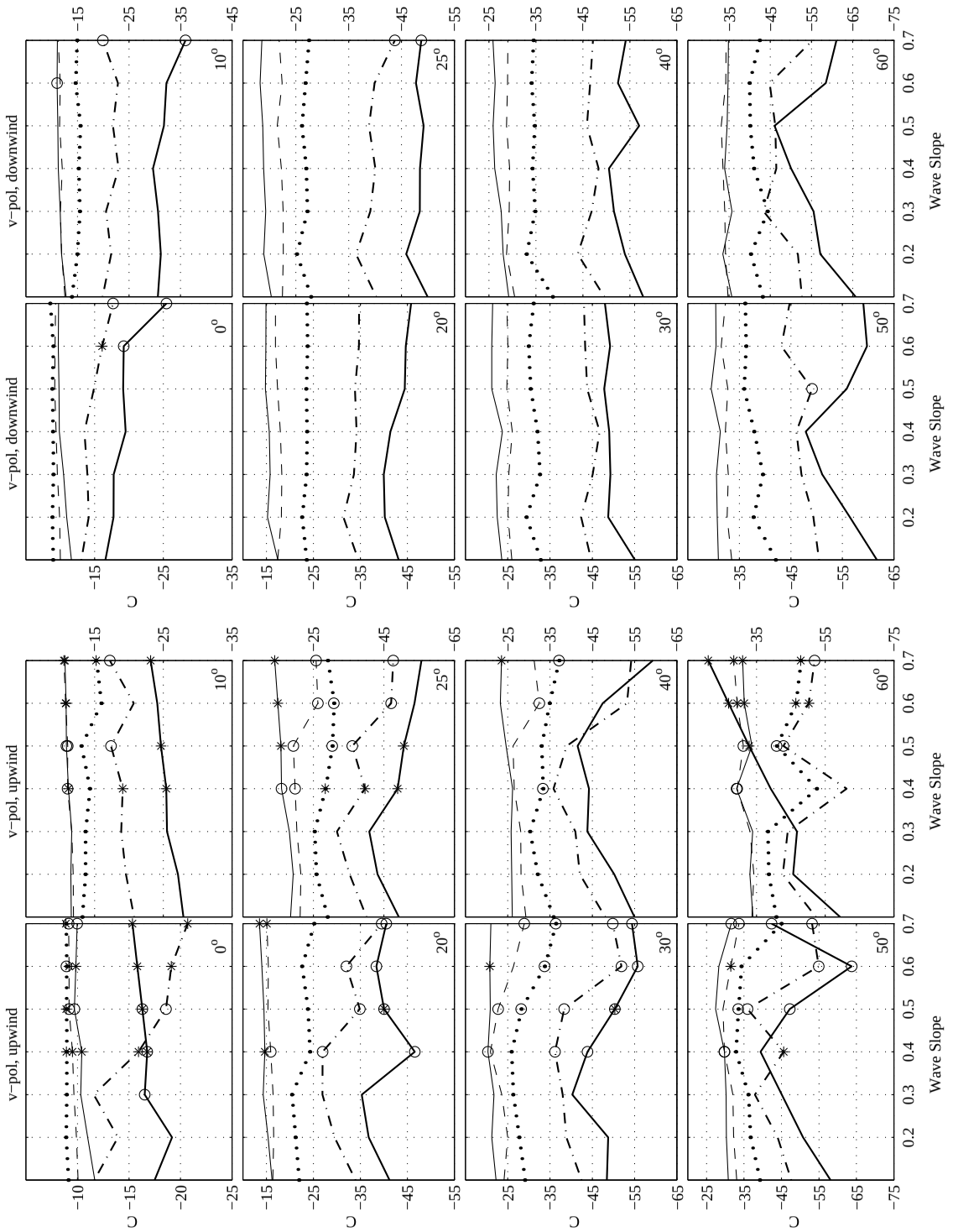

Figure C.18: C values for v-pol, upwind and downwind data versus mean wave slope for YSCAT94 for the log-normal distribution. Incidence angle is located at the bottom right corner of each plot. Thin solid line $\rightarrow$ 2 GHz, dashed line $\rightarrow$ 3 GHz, dotted line $\rightarrow$ 5 GHz, dash/dot line $\rightarrow$ 10 GHz, and the bold solid line $\rightarrow$ 14 GHz. Asterisks correspond to bins with no data, and circles indicate bins with only one or two minutes of data.

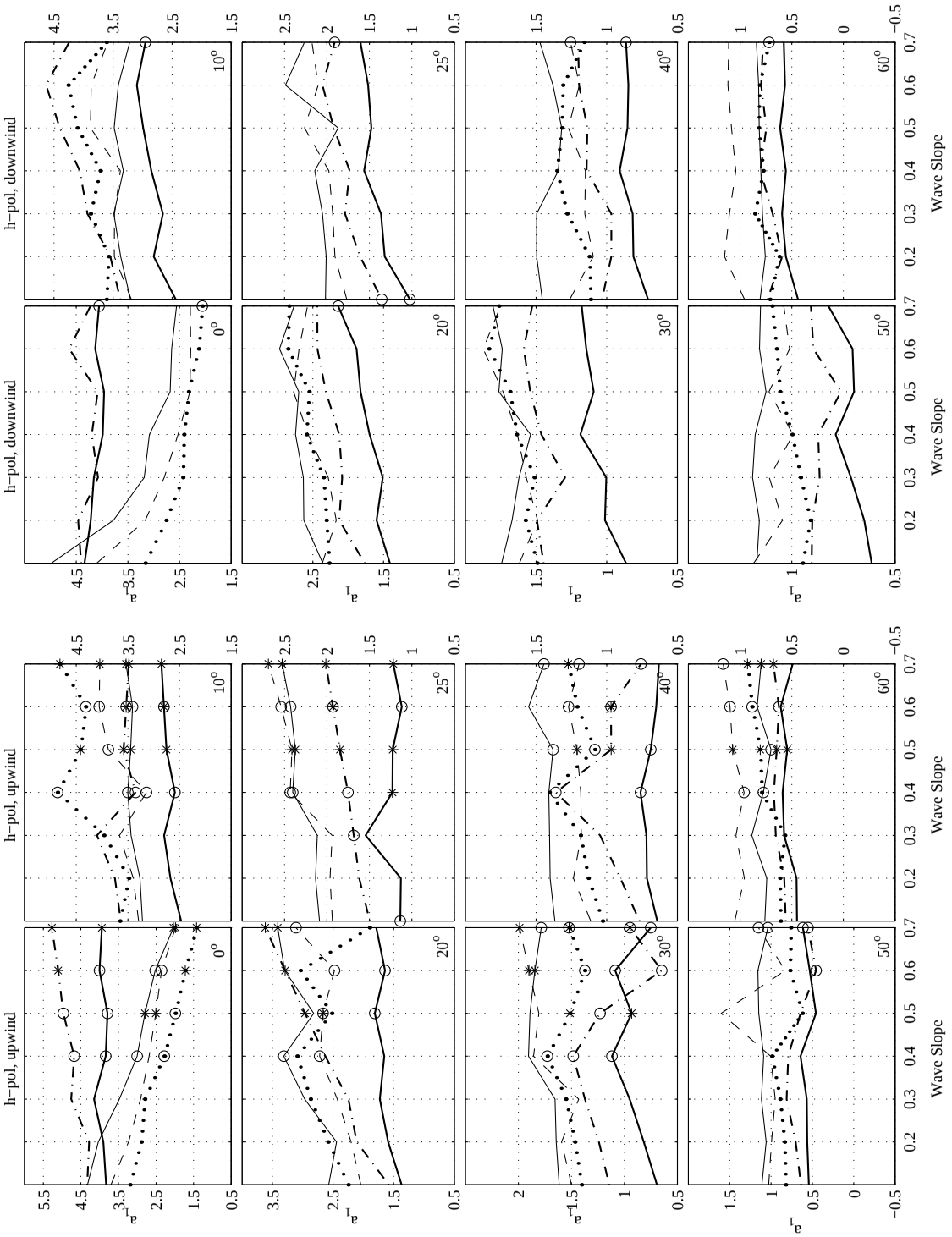

Figure C.19: a_1 values for h-pol, upwind and downwind data versus mean wave slope for YSCAT94 for the generalized log-normal distribution. Incidence angle is located at the bottom right corner of each plot. Thin solid line → 2 GHz, dashed line → 3 GHz, dotted line → 5 GHz, dash/dot line → 10 GHz, and the bold solid line → 14 GHz. Asterisks correspond to bins with no data, and circles indicate bins with only one or two minutes of data.

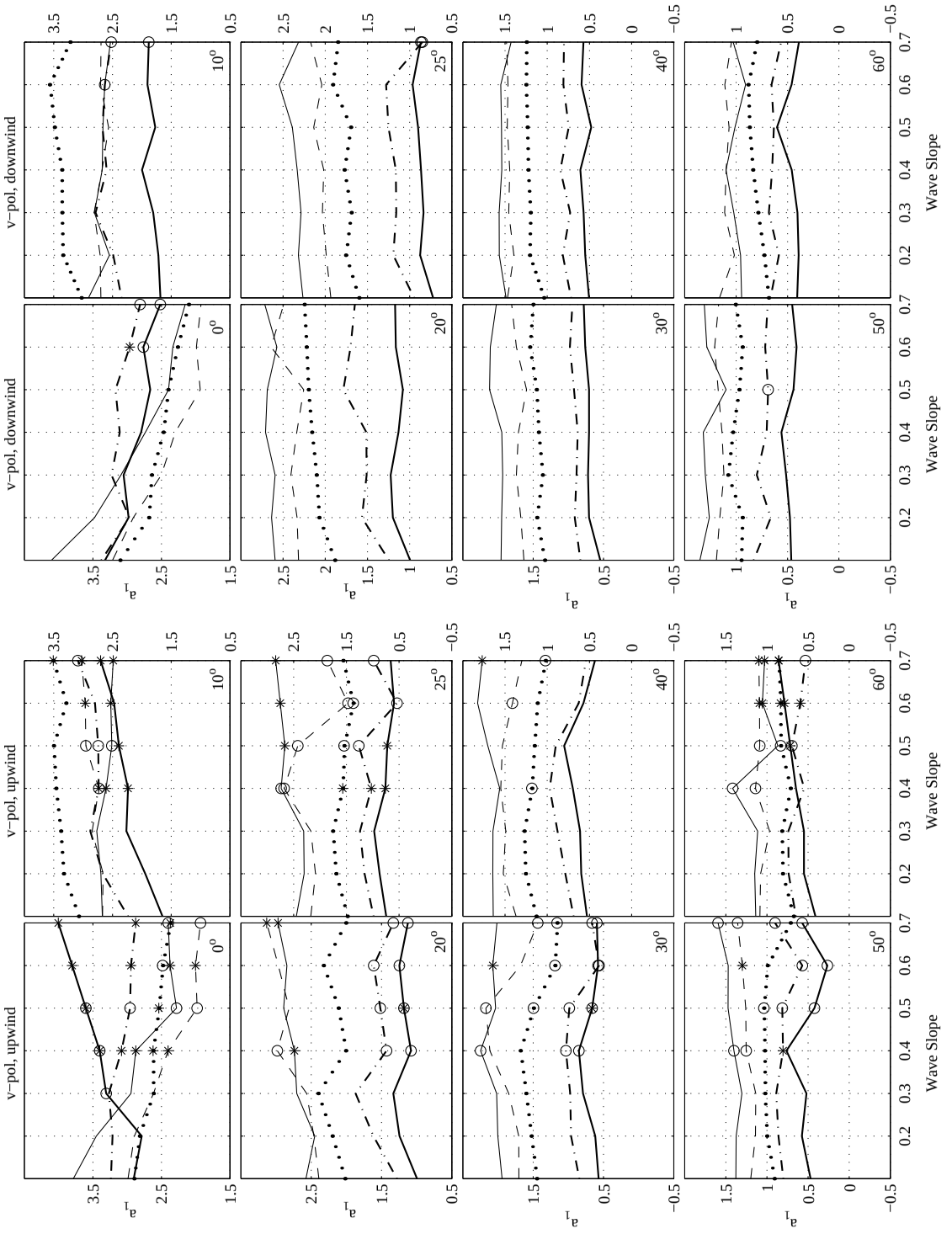

Figure C.20: a_1 values for v-pol, upwind and downwind data versus mean wave slope for YSCAT94 for the generalized log-normal distribution. Incidence angle is located at the bottom right corner of each plot. Thin solid line $\rightarrow$ 2 GHz, dashed line $\rightarrow$ 3 GHz, dotted line $\rightarrow$ 5 GHz, dash/dot line $\rightarrow$ 10 GHz, and the bold solid line $\rightarrow$ 14 GHz. Asterisks correspond to bins with no data, and circles indicate bins with only one or two minutes of data.

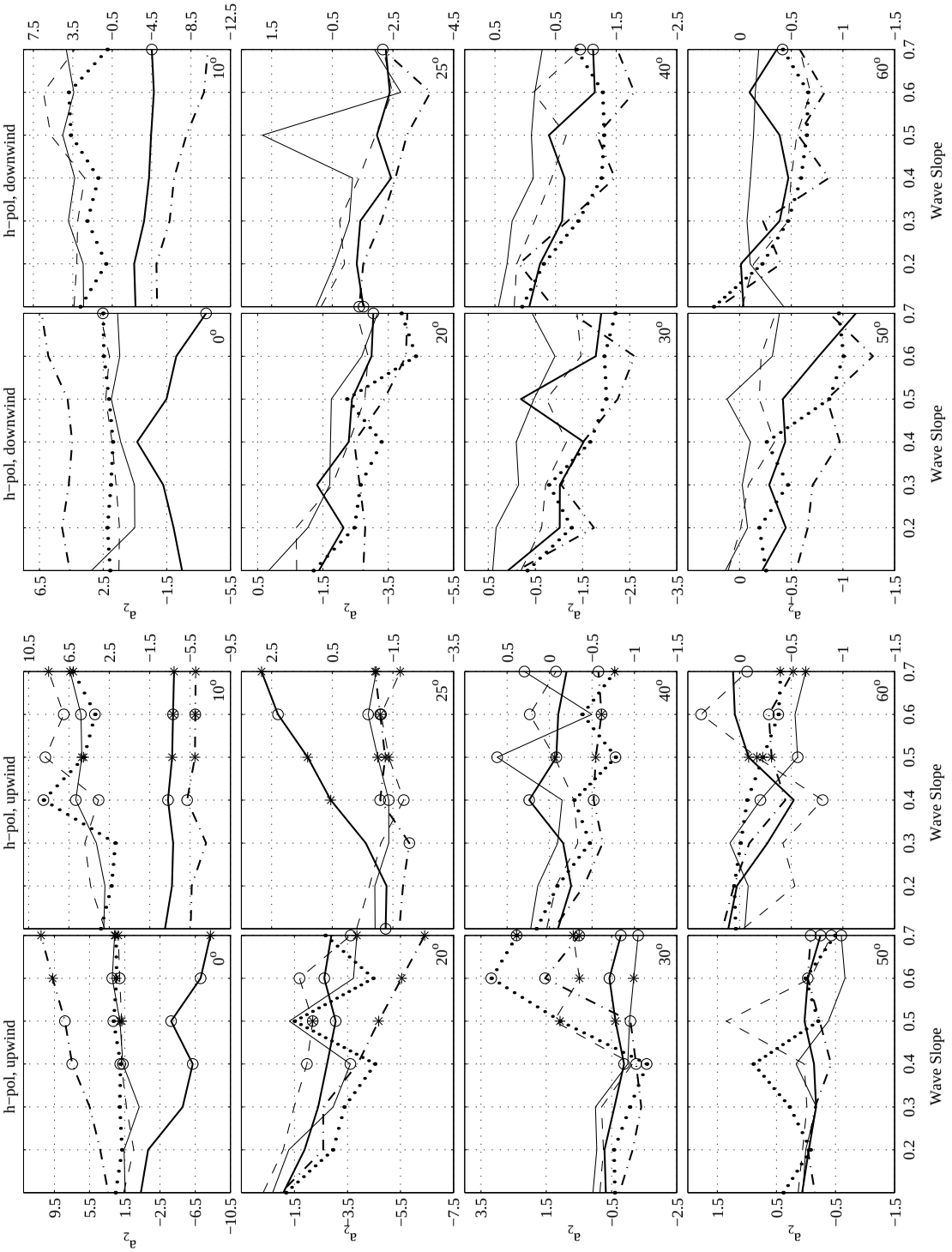

Figure C.21: a_2 values for h-pol, upwind and downwind data versus mean wave slope for YSCAT94 for the generalized log-normal distribution. Incidence angle is located at the bottom right corner of each plot. Thin solid line → 2 GHz, dashed line → 3 GHz, dotted line → 5 GHz, dash/dot line → 10 GHz, and the bold solid line → 14 GHz. Asterisks correspond to bins with no data, and circles indicate bins with only one or two minutes of data.

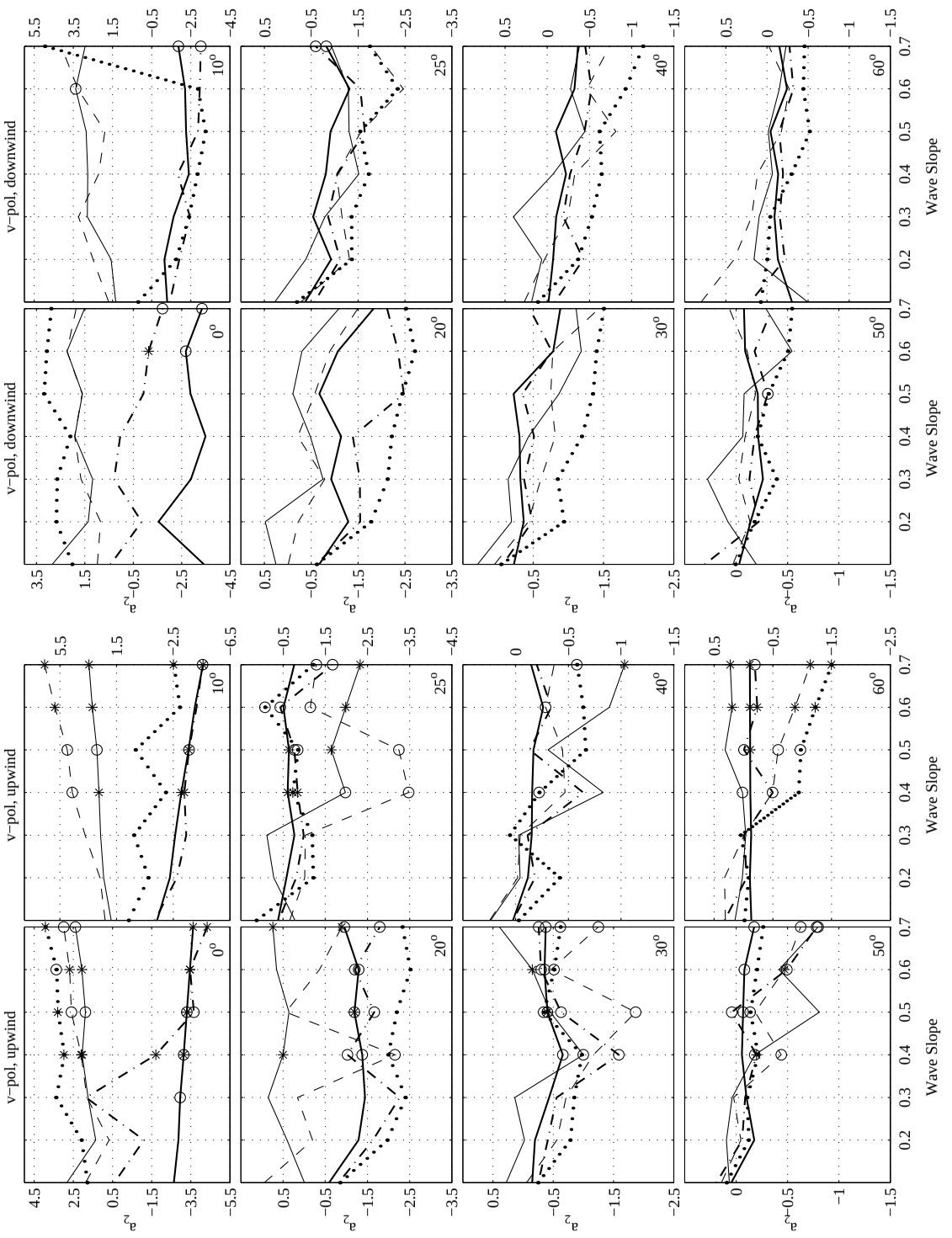

Figure C.22: a_2 values for v-pol, upwind and downwind data versus mean wave slope for YSCAT94 for the generalized log-normal distribution. Incidence angle is located at the bottom right corner of each plot. Thin solid line → 2 GHz, dashed line → 3 GHz, dotted line → 5 GHz, dash/dot line → 10 GHz, and the bold solid line → 14 GHz. Asterisks correspond to bins with no data, and circles indicate bins with only one or two minutes of data.

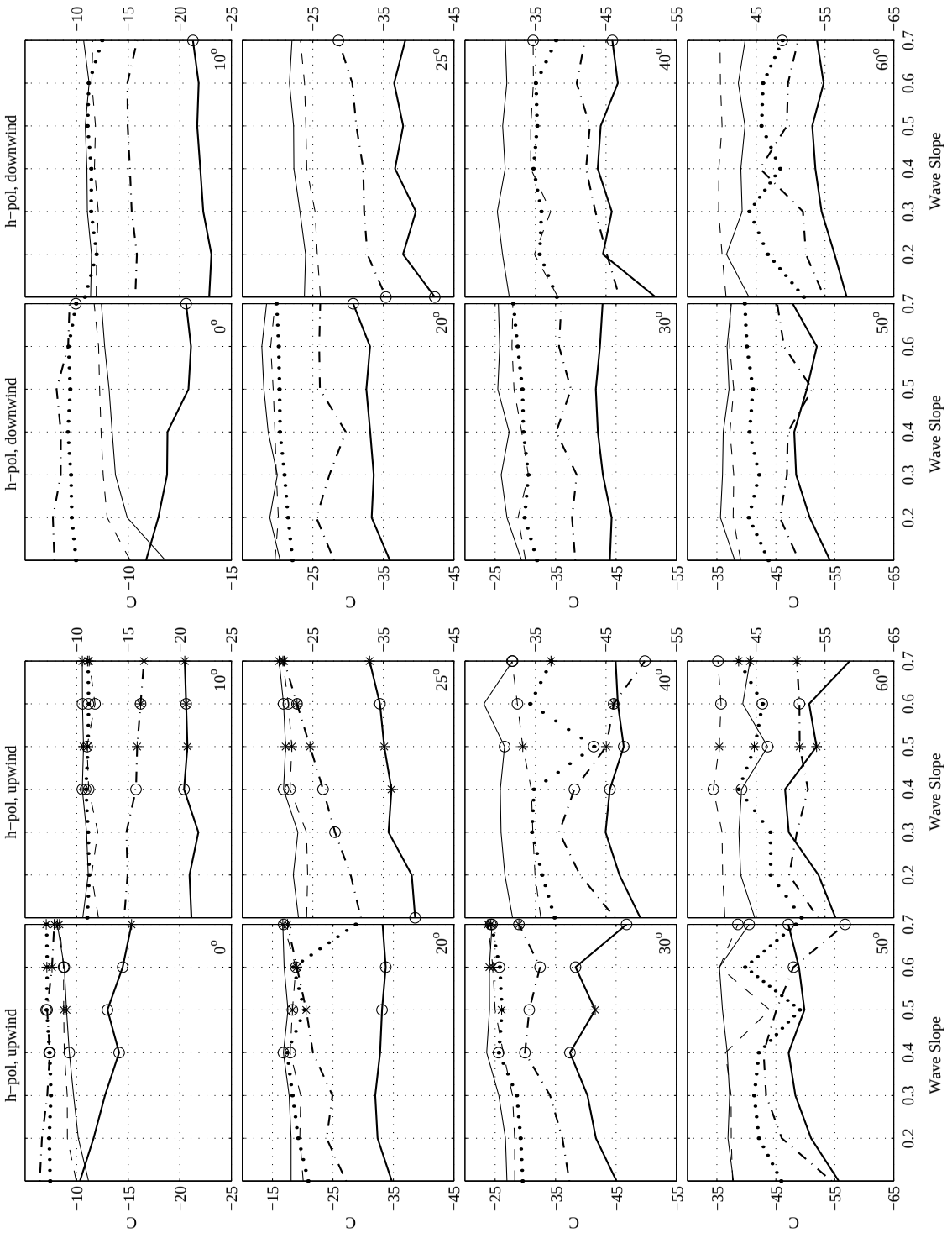

Figure C.23: C values for h-pol, upwind and downwind data versus mean wave slope for YSCAT94 for the generalized log-normal distribution. Incidence angle is located at the bottom right corner of each plot. Thin solid line $\rightarrow$ 2 GHz, dashed line $\rightarrow$ 3 GHz, dotted line $\rightarrow$ 5 GHz, dash/dot line $\rightarrow$ 10 GHz, and the bold solid line $\rightarrow$ 14 GHz. Asterisks correspond to bins with no data, and circles indicate bins with only one or two minutes of data.

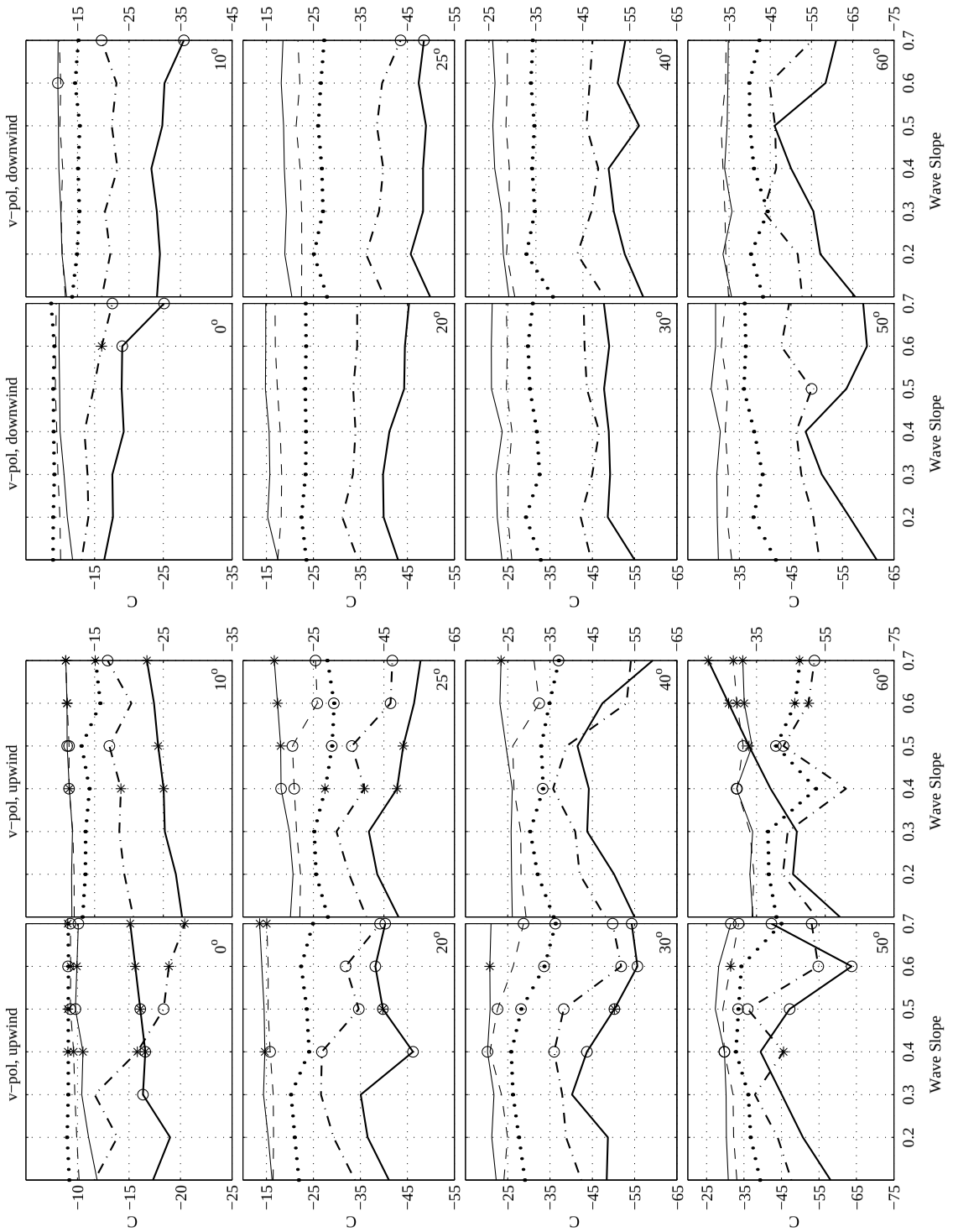

Figure C.24: C values for v-pol, upwind and downwind data versus mean wave slope for YSCAT94 for the generalized log-normal distribution. Incidence angle is located at the bottom right corner of each plot. Thin solid line $\rightarrow$ 2 GHz, dashed line $\rightarrow$ 3 GHz, dotted line $\rightarrow$ 5 GHz, dash/dot line $\rightarrow$ 10 GHz, and the bold solid line $\rightarrow$ 14 GHz. Asterisks correspond to bins with no data, and circles indicate bins with only one or two minutes of data.

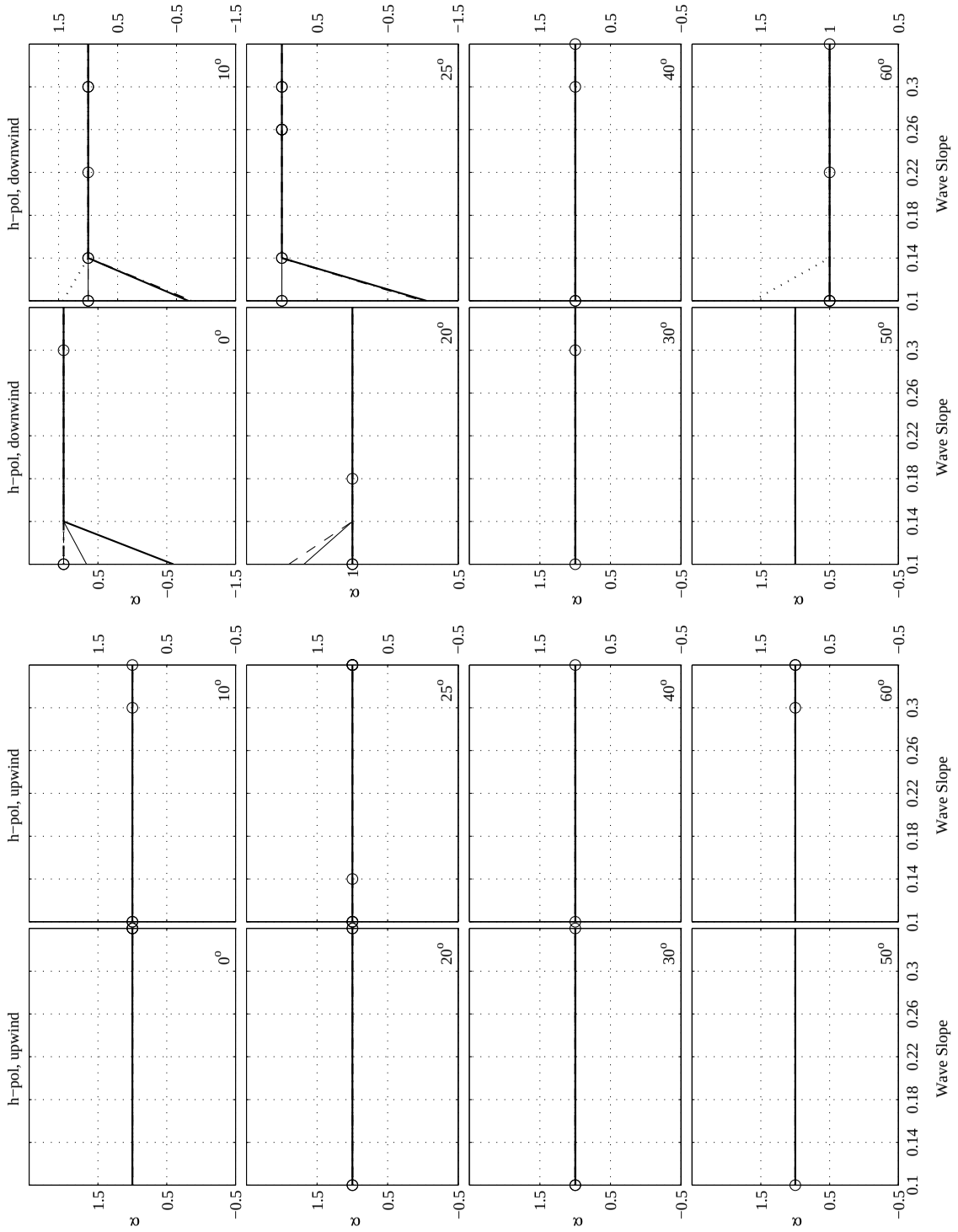

Figure C.25: α values for h-pol, upwind and downwind data versus mean wave slope for YSCAT94 for the Weibull distribution. Incidence angle is located at the bottom right corner of each plot. Thin solid line $\rightarrow$ 2 GHz, dashed line $\rightarrow$ 3 GHz, dotted line $\rightarrow$ 5 GHz, dash/dot line $\rightarrow$ 10 GHz, and the bold solid line $\rightarrow$ 14 GHz. Asterisks correspond to bins with no data, and circles indicate bins with only one or two minutes of data.

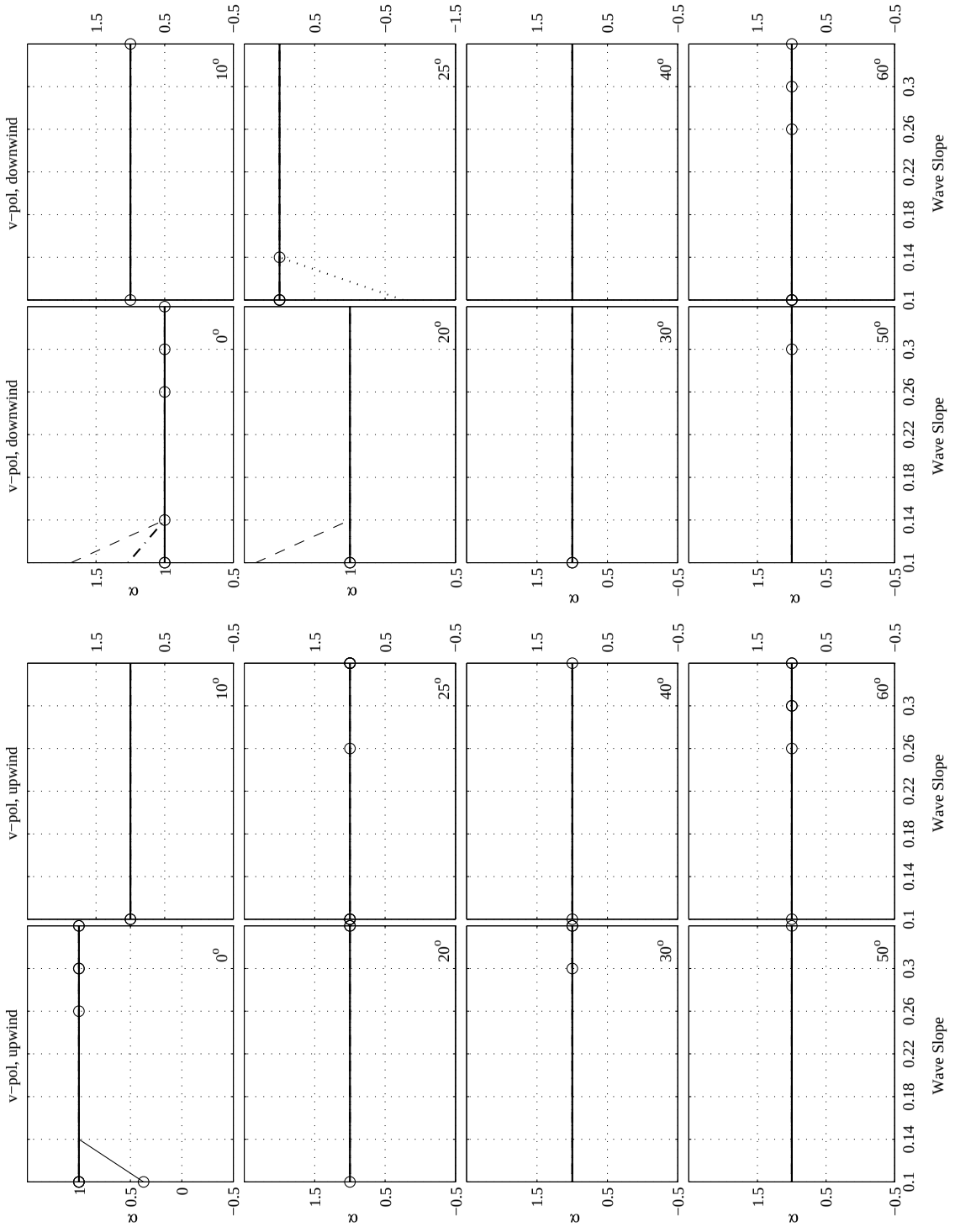

Figure C.26: α values for v-pol, upwind and downwind data versus mean wave slope for YSCAT94 for the Weibull distribution. Incidence angle is located at the bottom right corner of each plot. Thin solid line $\rightarrow$ 2 GHz, dashed line $\rightarrow$ 3 GHz, dotted line $\rightarrow$ 5 GHz, dash/dot line $\rightarrow$ 10 GHz, and the bold solid line $\rightarrow$ 14 GHz. Asterisks correspond to bins with no data, and circles indicate bins with only one or two minutes of data.

Appendix D

β Values from the Weibull/Generalized Log-Normal Distribution

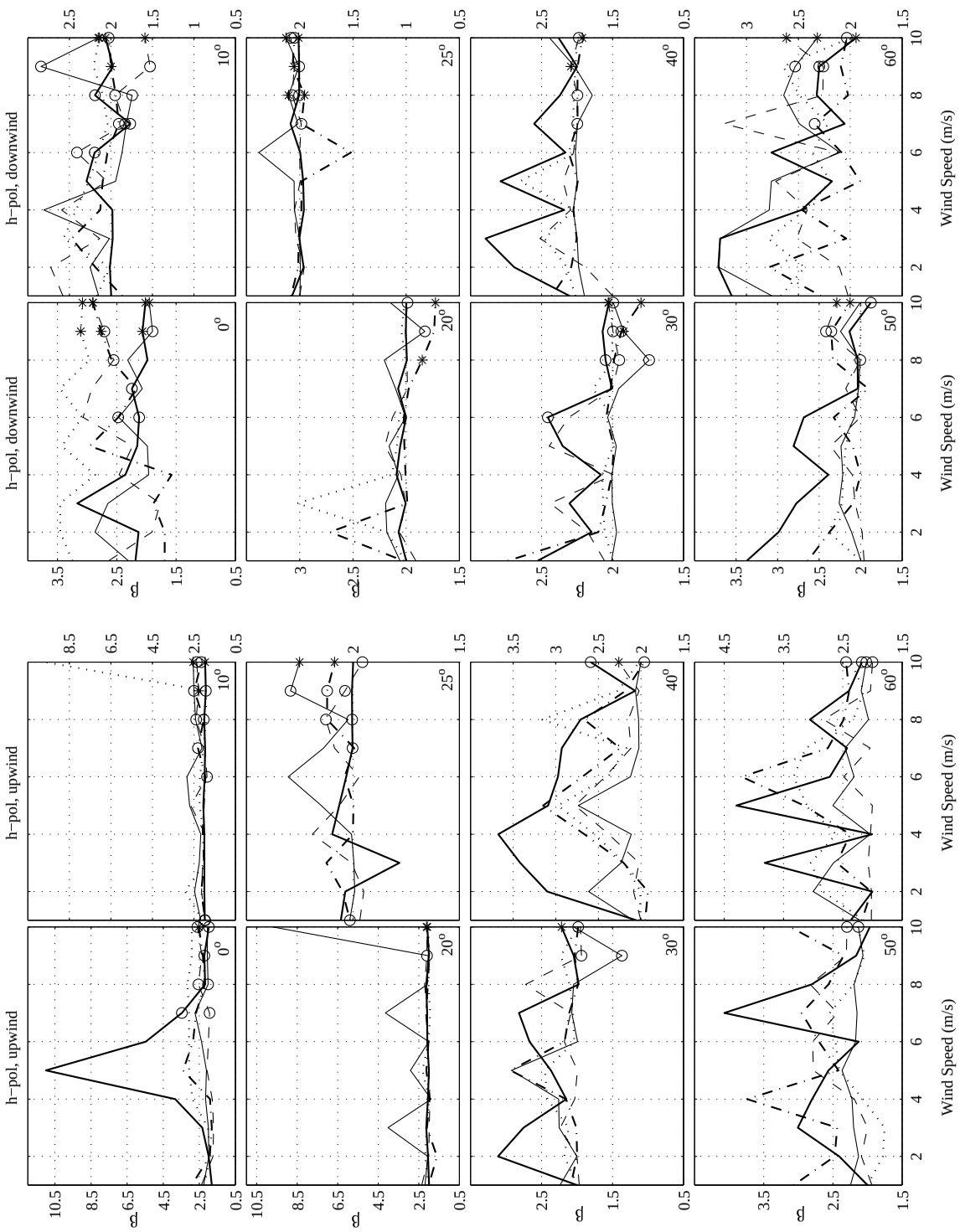

Figure D.1: β values for h-pol, upwind and downwind data versus wind speed for YSCAT94 for the Weibull/generalized log-normal distribution. Incidence angle is located at the bottom right corner of each plot. Thin solid line $\rightarrow$ 2 GHz, dashed line $\rightarrow$ 3 GHz, dotted line $\rightarrow$ 5 GHz, dash/dot line $\rightarrow$ 10 GHz, and the bold solid line $\rightarrow$ 14 GHz. Asterisks correspond to bins with no data, and circles indicate bins with only one or two minutes of data.

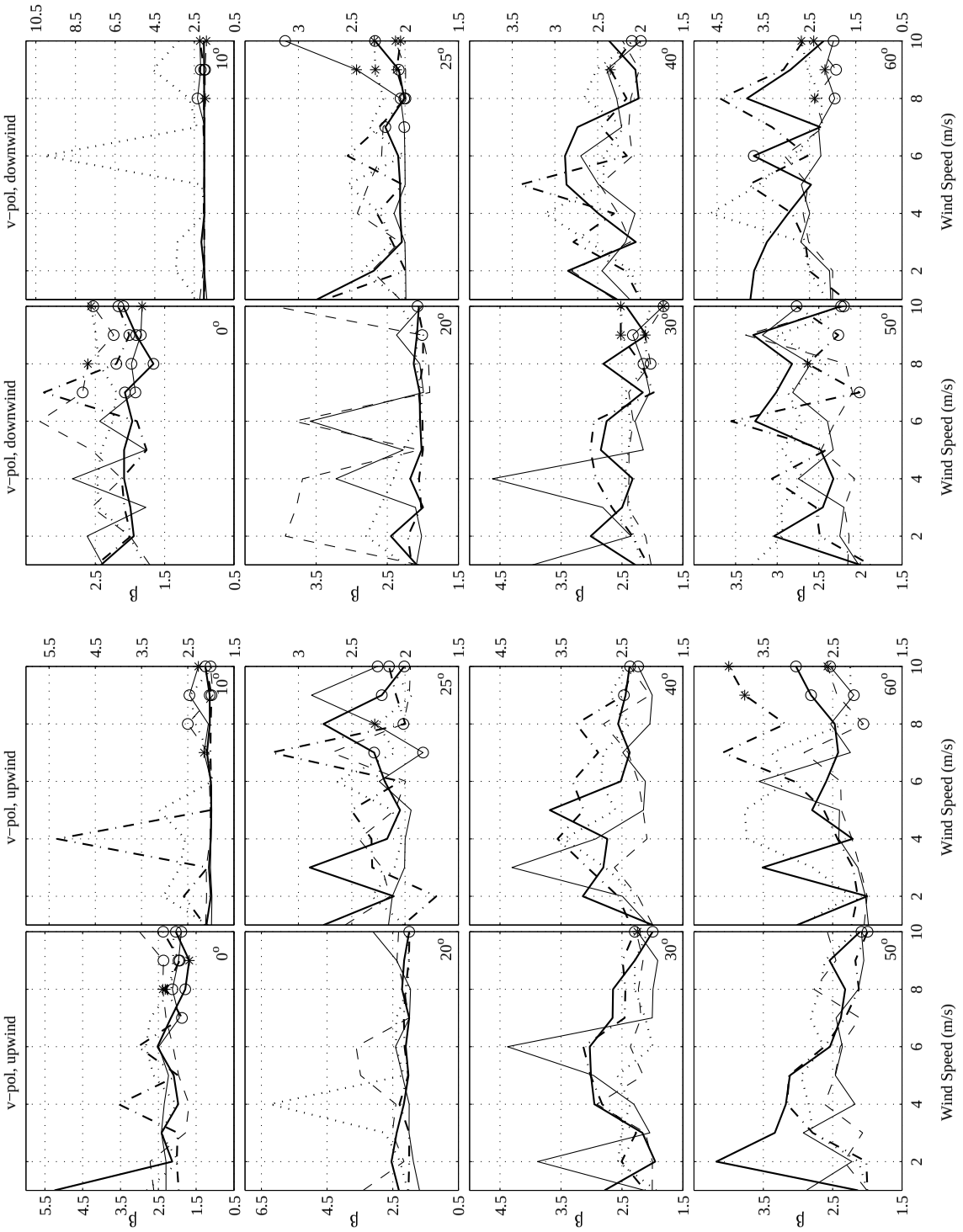

Figure D.2: β values for v-pol, upwind and downwind data versus wind speed for YSCAT94 for the Weibull/generalized log-normal distribution. Incidence angle is located at the bottom right corner of each plot. Thin solid line $\rightarrow$ 2 GHz, dashed line $\rightarrow$ 3 GHz, dotted line $\rightarrow$ 5 GHz, dash/dot line $\rightarrow$ 10 GHz, and the bold solid line $\rightarrow$ 14 GHz. Asterisks correspond to bins with no data, and circles indicate bins with only one or two minutes of data.

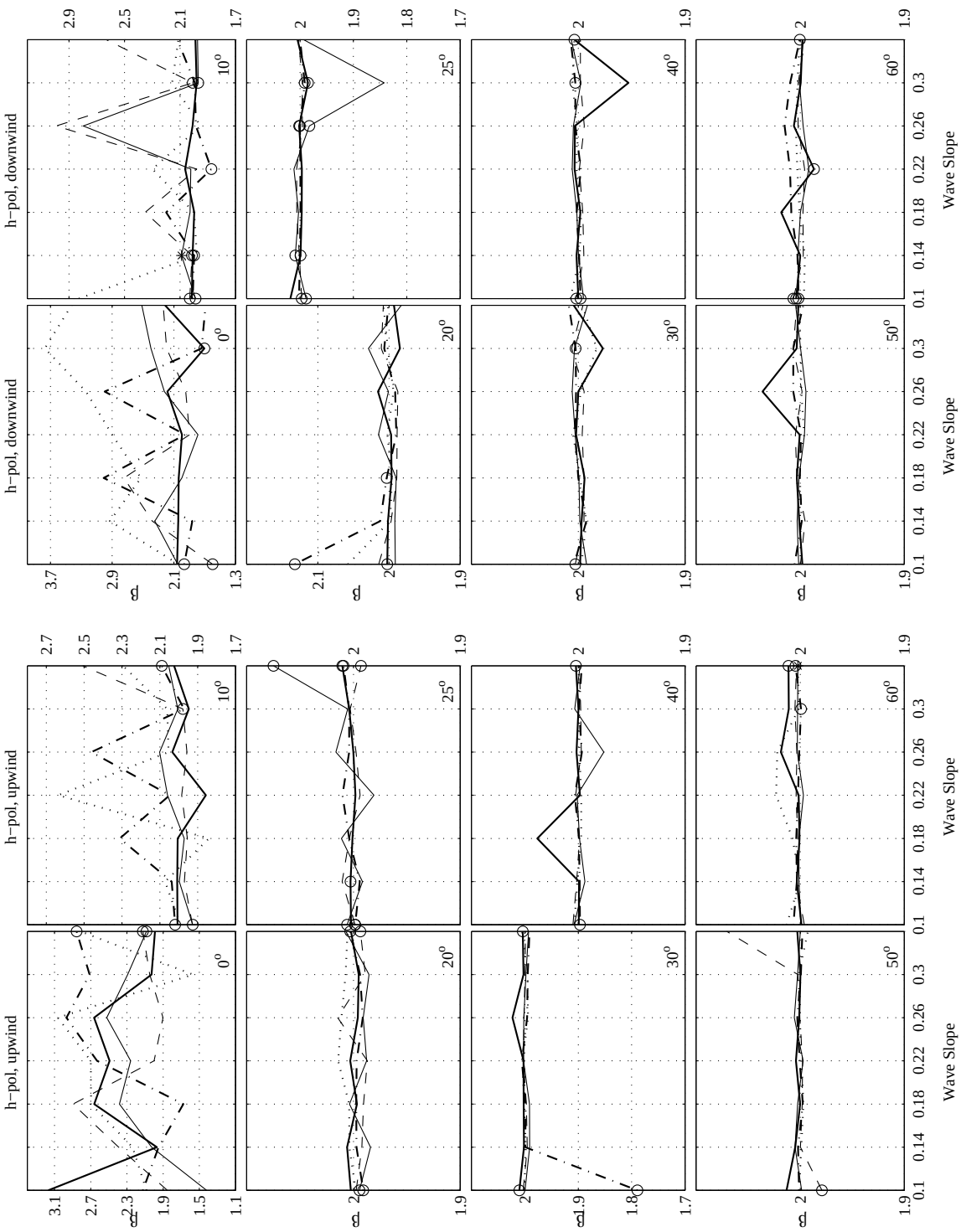

Figure D.3: β values for h-pol, upwind and downwind data versus mean wave slope for YSCAT94 for the Weibull/generalized log-normal distribution. Incidence angle is located at the bottom right corner of each plot. Thin solid line $\rightarrow$ 2 GHz, dashed line $\rightarrow$ 3 GHz, dotted line $\rightarrow$ 5 GHz, dash/dot line $\rightarrow$ 10 GHz, and the bold solid line $\rightarrow$ 14 GHz. Asterisks correspond to bins with no data, and circles indicate bins with only one or two minutes of data.

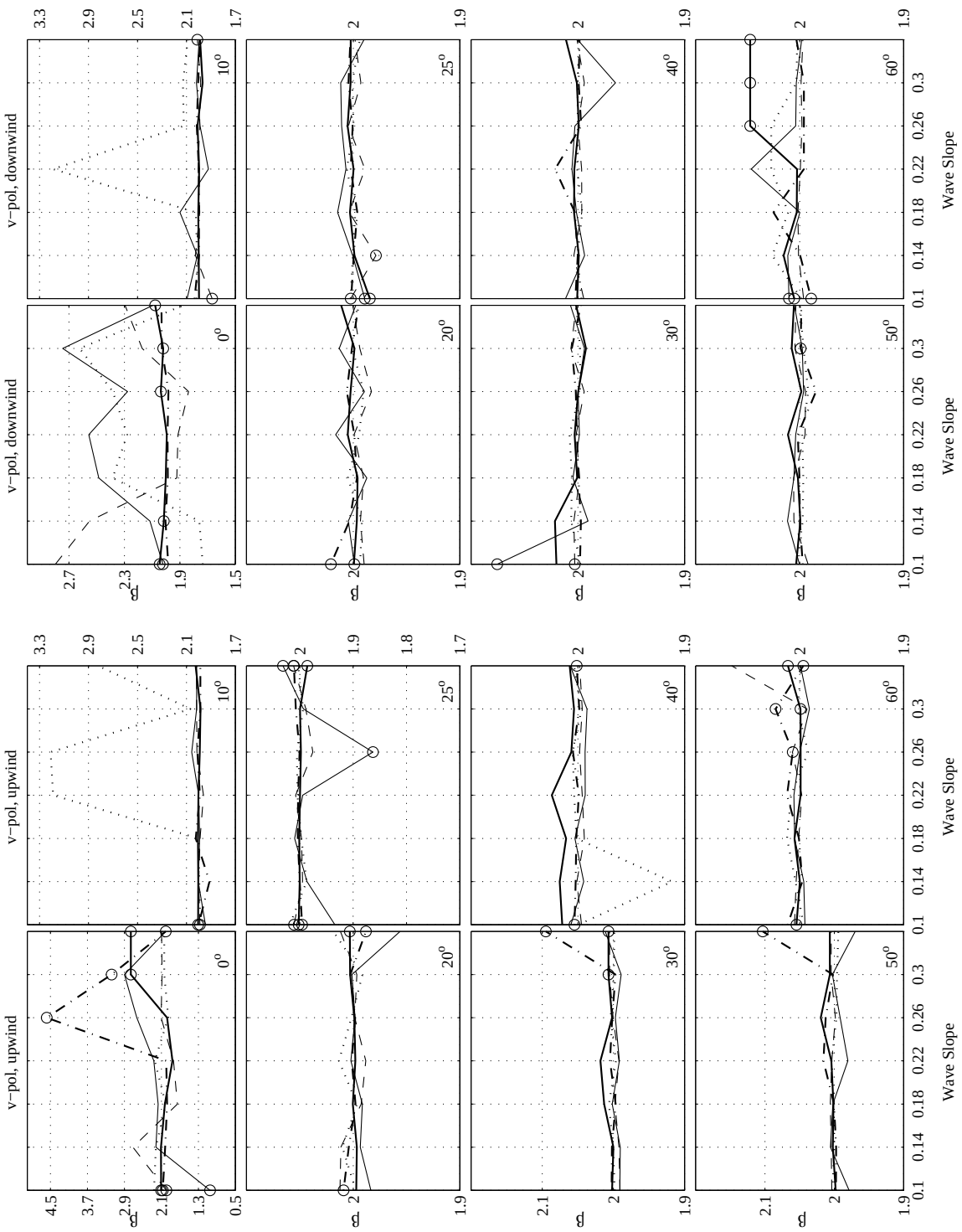

Figure D.4: β values for v-pol, upwind and downwind data versus mean wave slope for YSCAT94 for the Weibull/generalized log-normal distribution. Incidence angle is located at the bottom right corner of each plot. Thin solid line $\rightarrow$ 2 GHz, dashed line $\rightarrow$ 3 GHz, dotted line $\rightarrow$ 5 GHz, dash/dot line $\rightarrow$ 10 GHz, and the bold solid line $\rightarrow$ 14 GHz. Asterisks correspond to bins with no data, and circles indicate bins with only one or two minutes of data.

Bibliography

[1] F. M. Naderi, M. H. Freilich, and David G. Long, "Spaceborne radar measurements of wind velocity over the ocean–an overview of the nscat scatterometer system", *Proceedings of the IEEE*, vol. 79, no. 6, pp. 850–866, June 1991.

[2] Stanislaw R. Massel, *Ocean Surface Waves: Their Physics and Prediction*, Number 11 in Advanced Series on Ocean Engineering. World Scientific Publishing Co., 1996.

[3] G. J. Komen, L. Cavaleri, M. Donelan, K. Hasselmann, S. Hasselmann, and P.A.E.M. Janssen, *Dynamics and Modelling of Ocean Waves*, Cambridge University Press, Cambridge, 1994.

[4] D. G. Long, "Current progress in ku band model functions", NSCAT Project Office, Jet Propulsion Laboratory, Pasedena, CA, May 1995, 1994.

[5] M. A. Donelan, W. J. Plant, W. C. Keller, and D. E. Weissman, "A wind speed threshold in microwave scattering from the ocean", URSI Meeting, Boulder, CO, 1999.

[6] W. J. Plant, D.E. Weissman, W.C. Keller, V. Hesany, K. Hayes, , and K.W. Hoppel, "Air/sea momentum transfer and the microwave cross section of the sea", *Journal of Geophysical Research*, 1999.

[7] Charles Cox and Walter H. Munk, "Slopes of the sea surface deduced from photographs of sun glitter", *Bulletin of the Scripps Institute of Oceanography of the University of California*, vol. 6, no. 9, pp. 401–488, September 1956.

[8] B. L. Gotwols and D. R. Thompson, "Ocean microwave backscatter distributions", *Journal of Geophysical Research*, vol. c5, no. 99, pp. 9741–9750, May 1994.

[9] O. M. Phillips, *The Dynamics of the Upper Ocean*, Cambridge University Press, second edition, 1977.

[10] W. J. Plant, "A relationship between wind stress and wave slope", *Journal of Geophysical Research*, vol. 87, no. C3, pp. 1961–1967, March 1982.

[11] J. A. Kong, *Electromagnetic Wave Theory*, Artech House, 1992.

[12] F. T. Ulaby, *Microwave Remote Sensing*, vol. 2, Artech House, 1983.

[13] O. M. Phillips, "The equilibrium range in the spectrum of wind-generated waves", *Journal of Fluid Mechanics*, vol. 4, pp. 426–434, 1958.

[14] S. L. Durden and J. F. Vesecky, "A physical radar cross-section model for a wind-driven sea with swell", *IEEE Journal of Oceanic Engineering*, vol. 10, no. 4, pp. 445–452, October 1985.

[15] W. J. Pierson and L. Moskowitz, "A proposed spectral form for fully developed wind seas based on the similarity theory os s. a. kitaigorodskii", *Journal of Geophysical Research*, vol. 69, pp. 5181–5190, 1964.

[16] William J. Plant, "A two scale model of short wind-generated waves and scatterometery", *IEEE Journal of Geoscience and Remote Sensing*, vol. 91, no. 9, pp. 10735–10749, September 1986.

[17] K. Hasselmann, T. P. Barnett, E. Bouws, H. Carlson, D. E. Cartwright, K. Enke, J. A. Ewing, H. Gienapp, D. E. Hasselmann, P. Kruseman, A. Meerburg, P. Müller, D. J. Olbers, K. Richter, W. Sell, and H. Walden, "Measurements of wind-wave growth and swell decay during the joint north sea wave project", *Deutsches Hydr. Zeit.*, vol. A12, pp. 1–95, 1973.

[18] M. A. Donelan, J. Hamilton, and W. H. Hui, "Directional spectra of wind-generated waves", *Philosophical Transactions of the Royal Society of London*, vol. 315, no. A, pp. 509–562, 1985.

[19] John W. Wright, "Backscattering from capillary waves with application to sea clutter", *IEEE Transactions on Antennas and Propagation*, vol. 14, no. 6, pp. 749–754, Nov 1966.

[20] R. S. Collyer, "Wind speed dependence of the normalized radar cross section", Master's thesis, Brigham Young University, Provo, UT, Aug 1994.

[21] R. Reed, *Statistical Properties of the Sea Scattered Radar Return*, Dissertation, Brigham Young University, December 1995.

[22] M. A. Donelan and W. J. Pierson, "Radar scattering and equilibrium ranges in wind generated waves with application to scatterometry", *IEEE Journal of Geoscience and Remote Sensing*, vol. 92, no. C5, pp. 4971–5029, May 1987.

[23] J. Fan and I. Gijbels, *Local Polynomial Modelling and Its Applications*, Chapman & Hall, Inc., 1996.

[24] Jeffrey S. Sminoff, *Smoothing Methods in Statistics*, Springer-Verlag New York, Inc., 1996.

[25] W. Kendall Melville and F. C. Felizardo, "The influence of wave slope and elevation on EM bias", Author provided a rough draft.

[26] Justin. D. Smith, "Studies to improve the estimation of the electromagnetic bias in radar altimitry", Master's thesis, Brigham Young University, 1999.

[27] W. K. Melville, A. Rozenburg, and P. Matusov, "Polarized microwave scattering by surface water waves and turbulence", *IEEE International Geoscience and Remote Sensing Symposium*, vol. 4, no. Part 5 (of 5), pp. 2273–2275, July 1998.

[28] G. R. Valenzuela and M. B. Laing, "On the statistics of sea clutter", Tech. Rep. 7349, U.S. Naval Research Lab., Washington D.C., 1971.

[29] H. R. Raemer, *Radar Systems Principles*, CRC Press, 1997.

[30] G. V. Trunk, "Radar properties of non-rayleigh sea clutter", *IEEE Transactions on Aerospace and Electronic Systems*, vol. AES-8, no. 2, pp. 196–204, March 1972.

[31] K. D. Ward, C. J. Baker, and S. Watts, "Maritime surveillance radar, 1, radar scattering from the ocean surface", in *IEEE Proc. Part F, Radar Signal Processing*, 1990, vol. 137, pp. 51–62.

[32] W. J. Plant, "Bragg scattering of electromagnetic waves from the air-sea interface", in *Surface Waves and Fluxes*, G. L. Geernaert and W. J. Plant, Eds., Norwell, Mass., 1990, Kluwer Academic.

[33] Charles Cox and Walter H. Munk, "Measurement of the roughness of the sea surface from photographs of the sun's glitter", *Journal of the Optical Society of America*, vol. 44, no. 11, pp. 838–850, November 1954.

[34] W. J. Plant, "The variance of the normalized radar cross section of the sea", *IEEE Journal of Geoscience and Remote Sensing*, vol. 96, no. C11, pp. 20643–20654, Nov 1991.

[35] D. G. Long, R. S. Collyer, R. Reed, and D. V. Arnold, "Dependance of the normalized radar cross section of water waves on bragg wavelength-wind speed sensitivity", *IEEE Transactions on Geoscience and Remote Sensing*, vol. 34, no. 3, pp. 656–666, May To appear March, 1996.

[36] T. M. Cover and J. M. Thomas, *Elements of Information Theory*, New York: Wiley, 1990.